

THE UNIVERSITY *of* EDINBURGH

This thesis has been submitted in fulfilment of the requirements for a postgraduate degree (e. g. PhD, MPhil, DClinPsychol) at the University of Edinburgh. Please note the following terms and conditions of use:

- This work is protected by copyright and other intellectual property rights, which are retained by the thesis author, unless otherwise stated.
- A copy can be downloaded for personal non-commercial research or study, without prior permission or charge.
- This thesis cannot be reproduced or quoted extensively from without first obtaining permission in writing from the author.
- The content must not be changed in any way or sold commercially in any format or medium without the formal permission of the author.
- When referring to this work, full bibliographic details including the author, title, awarding institution and date of the thesis must be given.

The Astrobiological Potential of Putative Aqueous Microenvironments on Mars

Ophelia Gunn



Doctor of Philosophy
The University of Edinburgh
2023

Abstract

Water is a fundamental requirement for life as we know it. Therefore, one approach to the search for extraterrestrial life is to look for environments where liquid water exists or has existed. This approach has led us to Mars, where liquid water once existed in abundance, but for billions of years has been subject to low pressure and low-temperature conditions, making liquid water on the planet's surface highly unstable.

There are however a number of surface microenvironments that have been proposed as potential habitats. In some of the terrestrial environments considered the closest analogues to Mars there exist complex communities of microorganisms inhabiting microenvironments whose physical and chemical properties buffer the polyextreme environmental conditions. As a result, these environments have been proposed as model systems for Martian surface habitats.

This work aims to explore the astrobiological potential of three of these microenvironments; brine evaporites, rock pores and fluid inclusions in ice. Using laboratory based analogue environment simulations this work investigates the formation and volatilisation of liquid water, and the effect of dissolved salts on these processes.

Firstly, we observe the formation of evaporites from saturated sulphate, chloride, and perchlorate salt solutions and their binary mixtures under Earth and Martian pressure conditions to qualitatively understand their physical behaviour and how this might influence their potential as habitats. The resultant evaporite morphologies are categorised into 'creeping' and 'crusting' structures, each with distinct astrobiological implications: self-expansion of habitats and the extension of liquid water lifetime respectively.

Secondly, we examine the impact of porous media on liquid water lifetime at low pressures. As a result of decreased evaporative surface area, the introduction of

porous media increased the lifetime of liquid water compared to free water, though the difference decreased with decreasing atmospheric pressure. The introduction of dissolved magnesium sulphate salt significantly enhanced the longevity of liquid water within porous media as a result of crystallised salt obstructing the pore openings.

Finally, we investigate the ability of solar-heated low-albedo material to melt ice under Martian north polar and Antarctic temperature conditions. Even under ideal Martian temperature conditions, no bulk melting occurs as a result of the solar-heating of a black aluminium disc or Martian analogue regolith. When highly deliquescent magnesium perchlorate salt was incorporated into the analogue regolith, sediment migration into the ice surface is observed.

These data show that although the presence of salts in high concentrations can challenge life, they also generate new habitat space and prolong the presence of liquid water with implications for the habitability of Martian environments.

Lay Summary

Water is essential for life as we know it so when searching for life beyond Earth we look for environments where liquid water exists or has existed in the past. One of our closest neighbours in the solar system is the planet Mars, whose surface is dry, barren, and appears to be completely devoid of life. The thin atmosphere and cold and dry environmental conditions mean that liquid water usually cannot persist on the surface of the planet. However, billions of years ago, Mars had a substantial atmosphere and large quantities of water flowed on its surface. If life ever emerged on Mars, there may still be traces of it to be discovered. Therefore, it is important we understand which environments could have been habitable throughout Mars' history so we can direct missions to these sites to investigate them in detail.

One of the ways we can understand the potential habitability of Mars is to look at organisms on Earth that live in environments that have conditions in common with Mars, for example being extremely cold and dry. In these environments, there are often surprisingly abundant communities of microorganisms living in small protective habitats known as microenvironments. These microenvironments have properties that facilitate the survival of living organisms. By studying these properties in the laboratory we can begin to determine whether similar environments on Mars could also have sustained habitats as conditions became progressively more extreme.

This thesis studies whether liquid water can form or how long it lasts under certain environmental conditions relevant to the surface of Mars. Three different potential liquid water harbouring microenvironments were studied: brine evaporites, rock pores and liquid water pockets in ice.

Firstly, structures that form as concentrated salt solutions evaporate - known as evaporites - were studied. On Earth, evaporites host communities of

microorganisms in otherwise hostile environments such as the Atacama desert in Chile. We investigated whether salts abundant on Mars have properties that could contribute to habitability. We did this by observing the formation of their evaporite macrostructures from concentrated salt solutions and their 1:1 mixtures. We found that the structures fell broadly into three categories: crusts, creeping structures and a combination of the two. Some of the crusts were very effective at preventing further evaporation from the brine, preserving the liquid solution beneath. A creeping evaporite was able to transport micron-sized objects through its structure as it formed. The brines that produced the most distinctive evaporites were studied at low atmospheric pressure to see how this affected their formation and properties. We found that evaporite crusts were effective at reducing evaporation at low atmospheric pressure. The creeping structure we examined was only able to form at low pressure in the presence of porous material and the maximum extent of the structures decreased at lower pressures. These results suggest that evaporite environments on Mars could have extended the lifetime liquid water and created new habitat spaces as the conditions on Mars transitioned from Earth-like to inhospitable. Distinctive evaporite structures may have the potential to tell us about the environmental conditions of the planet at the time they formed, since their maximum extent is limited by pressure.

Secondly, we investigated the habitability of porous rock under Mars pressure conditions. On Earth, porous rocks are inhabited by microorganisms called endoliths. These rocky environments allow organisms to live in extremely dry environments like the Antarctic cold desert and the hot Atacama desert. One of the properties that allows life to persist is the ability of porous rocks to retain liquid water and humidity in otherwise arid environments. We investigated whether liquid water in porous rock and other porous materials would take longer to evaporate than free water (water not in porous materials). This was done at Earth and Mars atmospheric pressures. We also dissolved salts into the water to determine if the lifetime of liquid water in porous materials would be affected by the formation of pore-clogging salt crystals. We found that liquid water persisted for longer in porous media than free water at all pressures studied but that the proportionate difference in liquid water lifetime decreased with decreasing pressure. The introduction of salt significantly increased liquid water lifetime under current Mars pressure conditions. This suggests that porous rocks on the surface of Mars associated with salts that form crusts could be a good place to search for biosignatures.

Finally we investigated whether ice at the Martian north pole could be melted by the sun heating up dark-coloured material. Dark-coloured material can absorb more energy from the sun than lighter material like ice and snow. There are ice environments on Earth where dark material heats up enough to melt the ice beneath it. Microorganisms can inhabit these melt-water microenvironments. The addition of a salt detected on Mars called magnesium perchlorate may contribute to this melt process as it is effective at absorbing water at low temperatures. We used a lamp to simulate the sun shining onto blocks of ice at Antarctic and Martian temperatures to determine if a black aluminium disc could heat up sufficiently to melt the ice and form fluid inclusions. We found that fluid inclusions formed readily under Antarctic conditions but no measurable melt occurred at Mars temperatures. Only when magnesium perchlorate was mixed with an analogue Martian regolith material did a small amount of melt occur at Martian temperature. This suggests that the salt magnesium perchlorate can contribute to the production of liquid water in very cold ice environments when combined with regolith material and solar radiation.

The results presented in this thesis highlight that although salts are often associated with being detrimental to living organisms, they can also contribute to the formation and expansion of habitats and increase the lifetime of liquid water under environmental conditions relevant to the surface of Mars.

Declaration

I declare that this thesis was composed by myself, that the work contained herein is my own except where explicitly stated otherwise in the text, and that this work has not been submitted for any other degree or professional qualification except as specified.

(*Ophelia Gunn, 2023*)

Acknowledgements

Thank you to the Science and Technology Facilities Council and United Kingdom Research and Innovation for funding this research and affording me the opportunity to conduct this work.

I would like to express my sincere thanks to my supervisor, Professor Charles Cockell for giving me the opportunity to conduct research in such a fascinating field, facilitating my development and independence as a researcher, and who's enthusiasm for Astrobiology is truly aspirational. The many skills I have developed under Charles's supervision will be invaluable to me for the rest of my life for which I am extremely grateful.

I offer my sincere thanks to all members of the UK Centre for Astrobiology, past and present, for their support, insight, and encouragement. Special thanks to Stewart Gault, Annemiek Waajen and Philippe Reekie for your friendship, support and laughs. Thanks to Andy Dickinson, Liam Perera, and Rosie Cane for the excellent lunch chat, food recommendations, advice and willingness to help out. Thank you to Rosa Santomartino, Sean McMahon and Corentin Loron for your example, expertise and valuable advice. Thank you to Adam Stevens for your collaboration, expertise and guidance. Thank you to Scott McLaughlin for all your work in the Mars lab. Thank you to Sev Zielinska for your collaboration, diligent work and constant enthusiasm. Thanks also to Hector Leong for our many long and insightful conversations in the lab.

I would like to express my sincere gratitude to my friends and family for their unwavering support during the course of my PhD. Your encouragement has been instrumental in keeping me motivated and focused.

Finally, thank you to my partner Calum Buchanan. Thank you for your patience in listening to me reading out thesis sections repeatedly, by this point your familiarity with its contents may rival my own. Without your endless support and encouragement over the past few years, this thesis would not exist.

Contents

Abstract i

Lay Summary iii

Declaration vi

Acknowledgements vii

Contents viii

List of Figures xiv

List of Tables xxiv

1 Introduction 1

1.1 Thesis Outline 2

2 Background 4

2.1 Water on Mars 5

2.2 Life in Extreme Environments on Earth 6

2.3 The Astrobiological Potential of Putative Aqueous Microenvironments on Mars 10

3 General Methodology 11

3.1 The Planetary Environment Simulation Chamber 11

3.2 Fluorescence Microscopy 11

3.3 Data Analysis 13

3.3.1 Uncertainty in Mass Caused by Diurnal Environmental Variations 14

3.3.2 Salt Content of Saturated Brines 14

4 The Astrobiological Potential of Brine Evaporites 19

4.1 Introduction 19

4.2 Background 21

4.2.1 Terrestrial Hypersaline Habitats 21

4.2.2 Creeping Evaporites as Habitats and Paleoenvironmental Indicators 24

4.2.3 Limits to Life in Martian Brines 28

4.2.4 Salt Deposits on Mars 28

4.2.5 The Astrobiological Potential of Brine Evaporites 29

4.3 Materials and Methods 31

4.3.1 Preliminary Experiment: The Morphology of Evaporites Formed From Martian Brines 31

4.3.2 Main Experiment: The Morphology of Evaporites Formed From Martian Brines 33

4.3.3 The Morphology of Evaporites at Low Pressure 35

4.3.4 The Effect of a $MgSO_4$ Crust on Evaporation at Ambient and Low Pressure 36

4.3.5 Creeping Evaporites as Environmental Indicators 38

4.3.6 Analogue Microorganism Transport in Creeping Evaporites . 39

4.4 Results 41

4.4.1 Preliminary Experiment: The Morphology of Evaporites Formed From Martian Brines 41

4.4.2 Main Experiment: The Morphology of Evaporites Formed From Martian Brines 47

4.4.3 The Morphology of Evaporites at Low Pressure 80

4.4.4 The Effect of a $MgSO_4$ Crust on Evaporation at Ambient and Low Pressure 88

4.4.5 Creeping Evaporites as Environmental Indicators 92

4.4.6 Analogue Microorganism Transport in Creeping Evaporites . 99

4.5 Discussion 102

4.5.1 Crusts 103

4.5.2 Creeping Structures 106

4.5.3 Crusts and Creeping Structures 109

4.5.4 Deliquescence of Evaporite Structures 109

4.5.5 Limitations and Further Work 110

4.6 Conclusions 114

5 The Lifetime of Liquid Water in Porous Media at Low Pressure 115

5.1 Introduction 115

5.2 Background 117

5.2.1 Terrestrial Endolithic Habitats 117

5.2.2 Martian Vesicular Rock Environments 118

5.2.3 Water and Brines in Porous Media 121

5.3 Materials and Methods 126

5.3.1 Parameters and Materials 126

5.3.2 Protocol Development 129

5.3.3 Experimental Methods 133

5.3.4 Data Processing and Calculations 139

5.4 Results 144

5.4.1 Mass Loss of Water From Porous Media at Low Pressure 144

5.4.2 The Effect of Solution Position Within Porous Media on the Mass Loss of Water 166

5.4.3 The Effect of Flux Surface Area on the Mass Loss of Water. 168

5.4.4 The Effect of Crusting Brines on the Mass Loss of Water From Porous Media 174

5.5 Discussion 189

5.5.1 Diminishing Efficacy at Low Pressure 189

5.5.2 Water Position Within Porous Media and and Mass Loss Rate Evolution 190

5.5.3 Comparing Capillary Tube Lengths 191

5.5.4 Mass Loss Rate From the Rock Cube 192

5.5.5 Prevention of Freezing in 75 mm Tubes at 7 mb 193

5.5.6 Salt Crusts in Porous Media 193

5.5.7 Implications For Habitability 195

5.5.8 Limitations and Future Work 196

5.6 Conclusions 198

6 A Potential Aqueous Environment on the Martian North Polar Residual Cap 199

6.1 Introduction 199

6.2 Background 201
6.2.1 Terrestrial Ice Habitats 201
6.2.2 The Martian Cryosphere 205
6.2.3 Liquid Water on the NPRC 208
6.3 Materials and Methods 210
6.3.1 Materials and Experimental Parameters 210
6.3.2 Protocol Development and Apparatus 213
6.3.3 Experimental Methods 220
6.3.4 Measurements and Calculations 225
6.4 Results 227
6.4.1 Preliminary Experiments 227
6.4.2 Antarctic Temperature Experiments 235
6.4.3 Martian Temperature Experiments - Ideal Conditions 243
6.4.4 Martian Temperature Experiments - Typical Conditions 249
6.5 Discussion 252
6.5.1 Antarctic Temperature Conditions 252
6.5.2 Martian Temperature Conditions 253
6.5.3 Implications for Habitability 255
6.5.4 Limitations and Future Work 257
6.6 Conclusions 260

7 Conclusions 261

7.1 Chapter 4: The Astrobiological Potential of Brine Evaporites 263
7.2 Chapter 5: The Lifetime of Liquid Water in Porous Media at Low Pressure 264

7.3 Chapter 6: A Potential Aqueous Environment on the Martian North Polar Residual Cap 265

7.4 Closing Remarks 265

A Appendix 267

A.1 Pure Brines 267

A.1.1 No Evaporite Macrostructure Formation 267

A.1.2 Crusts 270

A.1.3 Creeping Structures 271

A.1.4 Crusts & Creeping Structures 272

A.2 Mixed Brines 273

A.2.1 Crusts 273

A.2.2 Creeping Structures 277

A.2.3 Crusts & Creeping Structures 279

Bibliography 287

List of Figures

2.1 Phase Diagram for Water at Mars Surface Pressures 7

2.2 Ancient Features Carved by Water on the Surface of Mars 8

2.3 Liquid Brine Droplets and Ice at Phoenix Lander Site 9

2.4 Map of the Distribution of Hydrated Minerals Detected on the Surface of Mars 9

3.1 Planetary Environment Simulation Chamber Apparatus 12

3.2 Microscopy Apparatus Schematic 13

3.3 Plots of Diurnal Variation in Measurements of a Fixed Mass at Each Experimental Pressure 15

4.1 Communities of Microorganisms in Antarctic Gypsum Salt Crusts 22

4.2 Communities of Microorganisms Living in Atacama Salt Crusts . 22

4.3 Salt Crust and Crust Formation Mechanism 23

4.4 Halite Evaporite Crust in UAE Sabkha 24

4.5 Microorganisms in a Fluid Inclusion in Ancient Halite 24

4.6 Dendritic Mineral Assemblages at Gale Crater, Mars 25

4.7 Creeping Structure and Salt Creeping Formation Mechanism . . . 27

4.8 Results of Preliminary Evaporite Experiment: Photographs of Pure Brines That Formed Interfacial Crust Evaporites 44

4.9 Results of Preliminary Evaporite Experiment: Photographs of a Pure Brine That Formed a Creeping Evaporite Structure 45

4.10 Results of Preliminary Evaporite Experiment: Photographs of a Pure Brine That Formed both a Crust and Creeping Evaporites . 45

4.11 Results of Preliminary Evaporite Experiment: Photographs of a Mixed Brine That Formed Creeping Evaporites 45

4.12 Results of Preliminary Evaporite Experiment: Photographs of Mixed Brines That Formed Both Crusts and Creeping Evaporites 46

4.13 Main Evaporite Experiment Results: Overall Mean Mass and Bulk Volume of Brines That Formed a Particularly Clear Example of an Evaporite Structure From Each Category 52

4.14 Main Evaporite Experiment Results: Mass and Bulk Volume of Pure Brines That Formed Interfacial Crusts 53

4.15 Main Evaporite Experiment Results: Photographs of Pure Brines That Formed Interfacial Crusts 54

4.16 Main Evaporite Experiment Results: Mass and Bulk Volume of Pure Brines That Formed Creeping Evaporites 55

4.17 Main Evaporite Experiment Results: Photographs of Pure Brines That Formed Creeping Evaporites 55

4.18 Main Evaporite Experiment Results: Mass and Bulk Volume of Pure Brines That Formed Both Crusts and Creeping Evaporites . 56

4.19 Main Evaporite Experiment Results: Photographs of Pure Brines That Formed Both Crusts and Creeping Evaporites 56

4.20 **(Part 1/2)** 67

4.20 (Part 2/2) Results of Main Evaporite Experiment: Mass and Bulk Volume of Mixed Brines That Formed Interfacial Crusts 68

4.21 **(Part 1/2)** 69

4.21 (Part 2/2) Results of Main Evaporite Experiment: Photographs of Mixed Brines That Formed Interfacial Crusts 70

4.22 Results of Main Evaporite Experiment: Mass and Bulk Volume of Mixed Brines That Formed Creeping Evaporites 71

4.23 Results of Main Evaporite Experiment: Photographs of Mixed Brines That Formed Creeping Evaporites 72

4.24 **Part (1/3)** 73

4.24 **(Part 2/3)** 74

4.24 (Part 3/3) Results of Main Evaporite Experiment: Mass and Bulk Volume of Mixed Brines That Formed Interfacial Crusts and Creeping Evaporites 75

4.25 **(Part 1/4)** 76

4.25 **(Part 2/4)** 77

4.25 **(Part 3/4)** 78

4.25 (Part 4/4) Results of Main Evaporite Experiment: Photographs of Pure Brines That Formed Interfacial Crusts and Creeping Evaporites 79

4.26 Results of Evaporite Morphology at Low Pressure Experiment: Plots of Brine and Water Mass Over 4 Days at 50 mb Pressure . . 84

4.27 Results of Evaporite Morphology at Low Pressure Experiment: Example of $MgSO_4$ Crust Forming and Changing over 4 Days at 50 mb Pressure 85

4.28 Results of Evaporite Morphology at Low Pressure Experiment: Examples of Each Evaporite Structure After 4 Days at 50 mb Pressure 86

4.29 Results of Evaporite Morphology at Low Pressure Experiment: Example of Na_2SO_4 Crust Forming over 4 Days at 50 mb Pressure 87

4.30 Results of Effect of $MgSO_4$ Crust on Evaporation at Ambient Pressure Experiment: Plots of Mass of Solution over 300 Minutes at 1000 mb 89

4.31 Results of Effect of $MgSO_4$ Crusts on Evaporation at Low Pressure Experiment: Plots of Mass of Solution over 300 Minutes at 50 mb 90

4.32 Results of Creeping Evaporites as Environmental Indicators Experiment: Photographs of Secondary Creep Structures Formed on Porous Rock During 4 Days at 7 mb 94

4.33 Results of Creeping Evaporites as Environmental Indicators Experiment: Photographs of Secondary Creep Structures Formed on Porous Rock at 50 mb 95

4.34 Results of Creeping Evaporites as Environmental Indicators Experiment: Secondary Creep Structures Formed on Porous Rock at 1000 mb 96

4.35 Dendritic Martian Mineral Assemblage Compared to Secondary Creeping Structures 98

4.36 Results of Analogue Microorganism Transport in Creeping Evaporites Experiment: Photographs of $MgSO_4$ & Na_2SO_4 Evaporite Structures 100

4.37 Results of Analogue Microorganism Transport in Creeping Evaporites Experiment: Photographs of $MgSO_4$ & Na_2SO_4 Evaporite Structures on Porous Rock 100

4.38 Results of Analogue Microorganism Transport in Creeping Evaporites Experiment: Fluorescent Micrograph of Salt Samples Taken From Rock Interior 101

4.39 Summary Representation of Potential Evaporite Environments on the Surface of Mars 102

5.1 Endolithic Habitats 119

5.2 Endolithic Microorganisms in Various Lithic Environments 120

5.3 Vesicular Basalt on the Surface of Mars 122

5.4 Pinnacle Island - A Salt Encrusted Rock at Endeavour Crater, Mars 123

5.5 Salt Crystals Precipitating From Brine in Capillary Tubes 125

5.6 The Lifetime of Liquid Water in Porous Media Experimental Apparatus 133

5.7 Solution Position Within Porous Media Experimental Apparatus . 135

5.8 Parameters and Flux Area of Each Substrate 143

5.9 Results of the Lifetime of Liquid Water in Porous Media at Low Pressure Experiment: Mass of Water Over Time at 1000 mb . . . 156

5.10 Results of The Lifetime of Liquid Water in Porous Media Experiment: Overall Mean Mass of Water Across Triplicate Experiments Over Time at 1000 mb 157

5.11 Results of The Lifetime of Liquid Water in Porous Media Experiment: Mass of Water Over Time at 100 mb 158

5.12 Results of The Lifetime of Liquid Water in Porous Media Experiment: Overall Mean Mass of Water Across Triplicate Experiments Over Time at 100 mb 159

5.13 Results of the Lifetime of Liquid Water in Porous Media Experiment: Mass of Water Over Time at 1000 mb 160

5.14 Results of the Lifetime of Liquid Water in Porous Media Experiment: Overall Mean Mass of Water Across Triplicate Experiments Over Time at 10 mb 161

5.15 Results of the Lifetime of Liquid Water in Porous Media Experiment: Mass of Water Over Time at 1000 mb 162

5.16 Results of the Lifetime of Liquid Water in Porous Media Experiment: Overall Mean Mass of Water Across Triplicate Experiments Over Time at 1000 mb 163

5.17 Results of the Lifetime of Liquid Water in Porous Media Experiment: Summary of Overall Mean Mass of Water Over Time at Each Pressure 164

5.18 Results of the Lifetime of Liquid Water in Porous Media Experiment: Summary of Mean Mass Loss Rate and Mean Mass Flux From Each Substrate at Each Experimental Pressure 165

5.19 Results of the Effect of Solution Position Within Porous Media Experiment: Plot of Mass of Water in Capillary Tubes Containing Water at Different Positions Within the Tube 167

5.20 Results of the Effect of Flux Surface Area on the Mass Loss of Water Experiment: Plots of Mass Loss Rate From Each Substrate at Each Pressure 171

5.21 Results of the Effect of Flux Surface Area on the Mass Loss of Water Experiment: Plots of Mass Loss Rate and Mass Flux From Each Substrate Vs Pressure 172

5.22 Results of the Effect of Crusting Brines on the Mass Loss of Water From Porous Media Experiment: Capillary Tubes That Contained Liquid $MgSO_4$ Solution After 4 Days at 7 mb 182

5.23 Results of the Effect of Crusting Brines on the Mass Loss of Water From Porous Media Experiment: Plot of Mass of $MgSO_4$ Brine and Precipitated Salt in 75 mm Tube Bundle Over 4 days at 7 mb 183

5.24 Results of the Effect of Crusting Brines on the Mass Loss of Water From Porous Media Experiment: Mass of $MgSO_4$ Brine and Precipitated Salt in Porous Rock Over 4 Days at 7 mb 184

5.25 Results of the Effect of Crusting Brines on the Mass Loss of Water From Porous Media Experiment: Porous Rock PM-2 Interior Containing Liquid $MgSO_4$ Solution After 4 Days at 7 mb 185

5.26 Results of the Effect of Crusting Brines on the Mass Loss of Water From Porous Media Experiment: Mass of $FeSO_4$ & $MgSO_4$ Brine and Precipitated Salt in Porous Rock Over 4 Days at 7 mb 186

5.27 Results of the Effect of Crusting Brines on the Mass Loss of Water From Porous Media Experiment: Porous Rock PF-1 Interior Containing Liquid $FeSO_4$ & $MgSO_4$ Solution After 4 days at 7 mb 187

6.1 Formation of Inhabited Fluid Inclusion Environments in Antarctic Lake Ice . . . 202
6.2 An Ice-Lidded Cryoconite Hole on Taylor Glacier, Antarctica . . . 203
6.3 Algal Bloom on the Greenland Ice Sheet . . . 204
6.4 Mars Global Surveyor Images of the Martian Poles . . . 205
6.5 Radargram Showing North Polar Layered Deposits . . . 207
6.6 South Polar Eruptions . . . 208
6.7 Duration and Depth of Melt From Losiak Model . . . 209
6.8 Directional Freezing Method . . . 214
6.9 Bubbly Ice Comparison Photographs . . . 215
6.10 Ice Production Apparatus . . . 215
6.11 Bubble-Free Ice Block Embedded with Black Disc . . . 216
6.12 Ice Block Embedded with JSC Mars-1 Regolith . . . 217
6.13 Mean Ice Temperature Plots . . . 218
6.14 Ice Irradiation Experiment Apparatus . . . 219
6.15 Ice Block and Melt Measurements . . . 225
6.16 Results of Preliminary Antarctic Temperature Experiment: Black Disc Atop Ice Block . . . 229
6.17 Results of Preliminary Antarctic Temperature Experiment: Black Disc Embedded Within Ice Block . . . 230
6.18 Results of Preliminary Antarctic Temperature Experiment: Regolith Atop Ice Block . . . 231
6.19 Results of Preliminary Antarctic Temperature Experiment: Regolith Embedded Within Ice Block . . . 231
6.20 Results of Preliminary Mars Temperature Experiment: Black Disc Atop Ice Block . . . 232
6.21 Results of Preliminary Mars Temperature Experiment: Black Disc Embedded Within Ice Block . . . 232
6.22 Results of Antarctic Temperature Experiments: Black Disc Atop Ice 237
6.23 Results of Antarctic Temperature Experiments: Black Disc Embedded Within Ice . . . 238

6.24 Results of Antarctic Temperature Experiments: Black Disc Embedded Within Ice - Halved Ice Blocks. 239

6.25 Results of Antarctic Temperature Control Experiments: Irradiated Without Black Disc 240

6.26 Results of Antarctic Temperature Control Experiments: Unirradiated Black Disc Atop Ice 241

6.27 Results of Antarctic Temperature Control Experiments: Unirradiated Black Disc Embedded Within Ice 242

6.28 Results of Ideal Martian Temperature Experiments: Black Disc Atop Ice 244

6.29 Results of Ideal Martian Temperature Experiments: Black Disc Embedded Within Ice 245

6.30 Results of Ideal Martian Temperature Experiments: JSC Mars-1 Regolith and $Mg(ClO_4)_2$ Atop Ice Surface Before and After Irradiation 245

6.31 Results of Ideal Martian Temperature Experiments: JSC Mars-1 Regolith and $Mg(ClO_4)_2$ Atop Halved Ice Block 246

6.32 Results of Ideal Martian Temperature Control Experiments: JSC Mars-1 Regolith Atop Halved Ice 247

6.33 Results of Ideal Martian Temperature Control Experiments: Unirradiated JSC Mars-1 Regolith and $Mg(ClO_4)_2$ Atop Ice 248

6.34 Results of Typical Martian Temperature Experiments: Black Disc Atop Ice 249

6.35 Results of Typical Martian Temperature Experiments: Black Disc Embedded Within Ice 250

6.36 Results of Typical Martian Temperature Experiments: Black Disc Embedded Within Ice - Halved Ice Blocks 251

7.1 Summary Representation of Potential Aqueous Microenvironments on the Surface of Mars 262

A.1 Results of Main Evaporite Experiment: Plots of Mass and Bulk Volume of Pure Brines That Did Not Form Evaporite Macrostructures Over 11 Months 268

A.2 Results of Main Evaporite Experiment: Photographs of Pure Brines That Did Not Form Evaporite Macrostructures Over 11 Months 269

A.3 Results of Main Evaporites Experiment: Evaporites Forming From $FeSO_4$ Brine (Sample T3) Over 11 months 270

A.4 Results of Main Evaporites Experiment: Evaporites Forming From $MgSO_4$ Brine (Sample T2) Over 11 months 270

A.5 Results of Main Evaporites Experiment: Evaporites Forming From Na_2SO_4 Brine (Sample T1) Over 49 days 271

A.6 Results of Main Evaporites Experiment: Evaporites Forming From $MgCl_2$ Brine (Sample T3) Over 11 months 271

A.7 Results of Main Evaporites Experiment: Evaporites Forming From NaCl Brine (Sample T2) Over 28 days 272

A.8 Results of Main Evaporites Experiment: Evaporites Forming From $Mg(ClO_4)_2$ Brine (Sample T1) Over 11 months 272

A.9 Results of Main Evaporites Experiment: Evaporites Forming From $NaClO_4$ Brine (Sample T1) Over 11 months 273

A.10 Results of Main Evaporites Experiment: Evaporites Forming From $CaCl_2$ & $FeSO_4$ Brine (Sample T1) Over 11 months 273

A.11 Results of Main Evaporites Experiment: Evaporites Forming From $CaCl_2$ & $MgSO_4$ Brine (Sample T2) Over 11 months 274

A.12 Results of Main Evaporites Experiment: Evaporites Forming From $CaCl_2$ & Na_2SO_4 Brine (Sample T3) Over 11 months 274

A.13 Results of Main Evaporites Experiment: Evaporites Forming From $Ca(ClO_4)_2$ & $FeSO_4$ Brine (Sample T1) Over 11 months 274

A.14 Results of Main Evaporites Experiment: Evaporites Forming From $Ca(ClO_4)_2$ & Na_2SO_4 Brine (Sample T1) Over 11 months 275

A.15 Results of Main Evaporites Experiment: Evaporites Forming From $CaSO_4$ & $FeSO_4$ Brine (Sample T2) Over 11 months 275

A.16 Results of Main Evaporites Experiment: Evaporites Forming From $CaSO_4$ & $MgSO_4$ Brine (Sample T1) Over 11 months 276

A.17 Results of Main Evaporites Experiment: Evaporites Forming From $CaSO_4$ & Na_2SO_4 Brine (Sample T2) Over 63 Days 276

A.18 Results of Main Evaporites Experiment: Evaporites Forming From $FeSO_4$ & $MgCl_2$ Brine (Sample T1) Over 11 months 276

A.19 Results of Main Evaporites Experiment: Evaporites Forming From $FeSO_4$ & $MgSO_4$ Brine (Sample T2) Over 11 months 277

A.20 Results of Main Evaporites Experiment: Evaporites Forming From $CaSO_4$ & $MgCl_2$ Brine (Sample T2) Over 11 months 277

A.21 Results of Main Evaporites Experiment: Evaporites Forming From $MgCl_2$ & NaCl Brine (Sample T1) Over 11 months 278

A.22 Results of Main Evaporites Experiment: Evaporites Forming From $MgSO_4$ & Na_2SO_4 Brine (Sample T2) Over 21 days 278

A.23 Results of Main Evaporites Experiment: Evaporites Forming From $Ca(ClO_4)_2$ & $MgSO_4$ Brine (Sample T1) Over 11 months 279

A.24 Results of Main Evaporites Experiment: Evaporites Forming From $CaSO_4$ & $Mg(ClO_4)_2$ Brine (Sample T1) Over 11 months 279

A.25 Results of Main Evaporites Experiment: Evaporites Forming From $CaSO_4$ & $NaClO_4$ Brine (Sample T1) Over 11 Months 280

A.26 Results of Main Evaporites Experiment: Evaporites Forming From $FeSO_4$ & $Mg(ClO_4)_2$ Brine (Sample T1) Over 11 months 280

A.27 Results of Main Evaporites Experiment: Evaporites Forming From $FeSO_4$ & NaCl Brine (Sample T3) Over 11 months 280

A.28 Results of Main Evaporites Experiment: Evaporites Forming From $FeSO_4$ & $NaClO_4$ Brine (Sample T3) Over 11 months 281

A.29 Results of Main Evaporites Experiment: Evaporites Forming From $MgCl_2$ & $Mg(ClO_4)_2$ Brine (Sample T1) Over 11 months 281

A.30 Results of Main Evaporites Experiment: Evaporites Forming From $MgCl_2$ & $MgSO_4$ Brine (Sample T2) Over 11 months 281

A.31 Results of Main Evaporites Experiment: Evaporites Forming From $MgCl_2$ & $NaClO_4$ Brine (Sample T2) Over 11 months 282

A.32 Results of Main Evaporites Experiment: Evaporites Forming From $MgCl_2$ & Na_2SO_4 Brine (Sample T2) Over 11 months 282

A.33 Results of Main Evaporites Experiment: Evaporites Forming From $Mg(ClO_4)_2$ & $MgSO_4$ Brine (Sample T3) Over 11 months 283

A.34 Results of Main Evaporites Experiment: Evaporites Forming From $Mg(ClO_4)_2$ & NaCl Brine (Sample T2) Over 11 months 283

A.35 Results of Main Evaporites Experiment: Evaporites Forming From $Mg(ClO_4)_2$ & $NaClO_4$ Brine (Sample T1) Over 11 months 284

A.36 Results of Main Evaporites Experiment: Evaporites Forming From $Mg(ClO_4)_2$ & Na_2SO_4 Brine (Sample T1) Over 11 months 284

A.37 Results of Main Evaporites Experiment: Evaporites Forming From $MgSO_4$ & NaCl Brine (Sample T1) Over 35 days 285

A.38 Results of Main Evaporites Experiment: Evaporites Forming From $MgSO_4$ & $NaClO_4$ Brine (Sample T1) Over 11 months 285

A.39 Results of Main Evaporites Experiment: Evaporites Forming From NaCl & $NaClO_4$ Brine (Sample T3) Over 11 months 285

A.40 Results of Main Evaporites Experiment: Evaporites Forming From $NaClO_4$ & Na_2SO_4 Brine (Sample T3) Over 11 months 286

List of Tables

3.1 Diurnal Variation in Fixed Mass Measurement at Each Experimental Pressure 16

3.2 Brine Salt and Water Fractions 18

4.1 Parameters and Nomenclature 31

4.2 Results of Preliminary Evaporite Experiment: Evaporite Structures Formed From Each Pure and Mixed Brine 43

4.3 Main Evaporite Experiment Results: Evaporite Structures Formed From Each Pure and Mixed Brine 51

4.4 Results of Evaporite Morphology at Low Pressure Experiment: Mass Loss Rates From Brines and Water at 50 mb 82

4.5 Results of Evaporite Morphology at Low Pressure Experiment: Breakdown of Mass Loss Rates During Different Stages of the Evaporite Formation Process 83

4.6 Results of Effect of $MgSO_4$ Crust on Evaporation at Ambient Pressure Experiment: Mass Loss Rates From 40 mL of Solution at 1000 mb Over 300 Minutes 89

4.7 Results of Effect of $MgSO_4$ Crust on Evaporation at Low Pressure Experiment: Mass Loss Rates From 40 mL of Solution at 50 mb over 300 Minutes 90

4.8 Results of Effect of $MgSO_4$ Crusts on Evaporation at Low Pressure Experiment: Breakdown of Mass Loss Rate of $MgSO_4$ over 300 Minutes at 50 mb 91

4.9 Results of Creeping Evaporites as Environmental Indicators Experiment: Maximum Vertical Extent of Secondary Creep Evaporite Structures Formed in the Presence of Porous Rock at Different Pressures 97

4.10 Results of Creeping Evaporites as Environmental Indicators Experiment: ANOVA Test Results for Maximum Structure Extent at Different Pressures 97

4.11 Results of Analogue Microorganism Transport in Creeping Evaporites Experiment: Mean Microsphere Counts 101

5.1 Parameters and Nomenclature 126

5.2 Free Water Glass Dish Parameters 126

5.3 Capillary Tube and Tube Bundle Parameters 127

5.4 Rock Cube Parameters 127

5.5 Flux Surface Area of Dishes and Single Capillary Tubes 136

5.6 Results of the Lifetime of Liquid Water in Porous Media at Low Pressure Experiment: Mass Loss Rate and Mass Flux of Free Water at Different Pressures 151

5.7 Results of the Lifetime of Liquid Water in Porous Media at Low Pressure Experiment: Mass Loss Rate and Mass Flux of Water From Rock Cube at Different Pressures 152

5.8 Results of the Lifetime of Liquid Water in Porous Media at Low Pressure Experiment: Mass Loss Rate and Mass Flux of Water From 20 mm Capillary Tube Bundle at Different Pressures 153

5.9 Results of the Lifetime of Liquid Water in Porous Media at Low Pressure Experiment: Mass Loss Rate and Mass Flux of Water From 75 mm Capillary Tube Bundle at Different Pressures 154

5.10 Results of the Lifetime of Liquid Water in Porous Media at Low Pressure Experiment: Summary of Mean Time Taken For Mass Loss to Complete 155

5.11 Results of the Lifetime of Liquid Water in Porous Media at Low Pressure Experiment: Summary of Mean Mass Loss Rates 155

5.12 Results of the Lifetime of Liquid Water in Porous Media at Low Pressure Experiment: Summary of Mean Mass Flux 155

5.13 Results of the Effect of Solution Position Within Porous Media Experiment: Mass Loss Rate and Mass Flux From Capillary Tubes Bundles Containing Water at Different Positions Within the Tubes 166

5.14 Results of the Effect of Flux Surface Area on the Mass Loss of Water Experiment: Mass Loss Rate and Mass Flux From Each Substrate at 1000 mb 170

5.15 Results of the Effect of Flux Surface Area on the Mass Loss of Water Experiment: Mass Loss Rate and Mass Flux From Each Substrate at 100 mb 170

5.16 Results of the Effect of Flux Surface Area on the Mass Loss of Water Experiment: Mass Loss Rate and Mass Flux From Each Substrate at 10 mb 170

5.17 Results of the Effect of Flux Surface Area on the Mass Loss of Water Experiment: Mass Loss Rate and Mass Flux From Each Substrate at 7 mb 173

5.18 Results of the Effect of Crusting Brines on the Mass Loss of Water From Porous Media Experiment: Summary of $MgSO_4$ Salt Crusted Porous Media Preparation 178

5.19 Results of the Effect of Crusting Brines on the Mass Loss of Water From Porous Media Experiment: Mass Loss Rate and Mass Flux of $MgSO_4$ Brine From Porous Media at 7 mb 179

5.20 Results of the Effect of Crusting Brines on the Mass Loss of Water From Porous Media Experiment: Summary of $FeSO_4$ & $MgSO_4$ Salt Crusted Rock Preparation 188

5.21 Results of the Effect of Crusting Brines on the Mass Loss of Water From Porous Media Experiment: Summary of $FeSO_4$ & $MgSO_4$ Mass Loss Rate From Porous Rock at 7 mb 188

6.1 Parameters and Nomenclature 210

6.2 Regolith Material Parameters 223

6.3 Results of Preliminary Ice Experiments Under Antarctic and Mars Temperature Conditions: Depth, Rate and Volume of Ice Melt . . 229

6.4 Results of Melt Caused by a Black Disc Atop Ice Under Each Experimental Temperature Condition 233

6.5 Results of Melt Caused by a Black Disc Embedded in Ice Under Each Experimental Temperature Condition 234

6.6 Mean Ablation Rate of Uncovered Ice Surface at Each Experimental Temperature Condition 235

6.7 Results of Antarctic Temperature Control Experiments 237

Chapter 1

Introduction

The question of whether life exists beyond Earth has fascinated humankind for at least centuries. The field of Astrobiology seeks to uncover how life originated on Earth and whether there are instances of life emerging or existing in extraterrestrial environments.

Mars has long been a focus in the search for life beyond Earth. One of our closest planetary neighbours and once home to a substantial atmosphere and enough liquid water to carve valleys and deltas into the surface, the red planet has long since withered into the desert-like landscape we know today. A number of probes and rovers have landed on and traversed the desolate landscape, searching for traces of life. Thus far, none have identified convincing evidence for the presence of life, extinct or extant. They have, however, contributed to the growing body of evidence that there were environments on Mars that may have once been habitable. There are still many environments to be investigated by current and future missions. Therefore it is essential to determine which sites are the most likely to yield positive results. This is achieved through multiple approaches including analysis of orbital data, computer modelling and physical experiments in simulated planetary environments.

'Follow the water' is a phrase often used when considering where to search for extraterrestrial life. We know that liquid water is a fundamental necessity for life as we know it. This presents a substantial challenge for putative Martian life as the atmospheric pressure is low and the surface of the planet is typically extremely cold and arid meaning any substantial quantity of water on or near the surface is frozen. The subsurface has been proposed as a more promising location

to search for life due more stable environmental conditions leading to a higher likelihood of liquid water stability. However, there are significant limitations in our current ability to explore these depths and we are presently restricted to the surface and shallow subsurface. It is therefore important to determine which surface environments may have harboured conditions favourable to life such that habitat and biosignature detection resources can be directed appropriately.

To contribute to this goal, we work towards understanding how factors that have been shown to generate and extend the lifetime of liquid water and habitat space in terrestrial environments are affected by Martian geophysical and environmental conditions. The work presented in this thesis contributes to our understanding of some Martian surface environments by exploring the interactions between water, salts, and lithic and analogue lithic material.

1.1 Thesis Outline

This work uses laboratory based environmental simulations to investigate the interactions between water, lithic and analogue lithic material and salts under Earth and Mars environmental conditions and how these interactions could lead to the generation or preservation of habitable spaces. The microenvironments investigated were brine evaporites, rock pores, and fluid inclusions in ice.

Chapter 2 will present background material to place this work into context. The current state and history of water on Mars and regions of astrobiological interest will be discussed. This chapter will also introduce the microenvironments studied and outline the terrestrial analogue environments that inspired their selection. More detailed background information pertaining to each specific environment investigated in this thesis will be presented at the beginning of the corresponding chapters. Chapter 3 will briefly outline the apparatus used throughout the work presented in this thesis as well as the general data analysis and error propagation methods used.

Chapter 4 will address the question of what properties putative Martian evaporites may have that contribute to their potential as habitats or as environmental indicators. The chapter will explore the macrostructure of evaporites formed from the evaporation of ten pure brines and forty-five binary mixtures of brines composed of ions detected on the surface of Mars. The

formation of some evaporite structures was also studied under low pressure conditions to determine how this factor affects their properties and morphologies. We show that the evaporites formed fall into three morphological categories: crusts, creeping structures and a combination of the two. We show that the interfacial crusts formed from $MgSO_4$ brine are effective at inhibiting evaporation under ambient and low pressure conditions. We show that micron-sized objects can be transported throughout creeping structures as they form. We also show that the extent of creeping structures formed from the mixture of $MgSO_4$ & Na_2SO_4 is limited under low pressure conditions.

Chapter 5 presents a study of the effect of porous media on the mass loss rate of water under ambient and low pressure conditions. The effect of pore-obstruction by the precipitation of salt from $MgSO_4$ brine on mass loss rate at current Martian surface pressure was also investigated. We found that the mass loss rate of water from some porous media could be reduced significantly compared to free water, though the proportionate difference between them generally decreased with decreasing atmospheric pressure. We found that the introduction of $MgSO_4$ salt had the most significant effect on reducing the mass loss rate of liquid water.

Chapter 6 presents a study on the ability of low-albedo material to facilitate the melting of ice under Antarctic and Martian north polar solar and temperature conditions. We also investigated the ability of the hygroscopic salt $Mg(ClO_4)_2$ mixed with analogue regolith material to facilitate ice melt under Martian north polar conditions. We found that ice melts readily under Antarctic conditions. However, under Mars temperatures, no detectable melt occurs except in the case of $Mg(ClO_4)_2$ mixed with analogue regolith material, where a small amount of regolith melt-migration took place.

Chapter 7 will summarise the principle findings and conclusions of this thesis.

Chapter 2

Background

The search for life and its origins involves work ranging from studying molecular interactions and microscopic organisms to observing the atmospheric signatures of distant exoplanets within our galaxy. Within our own solar system, there are several locations of astrobiological interest including the icy Jovian moon Europa, icy Saturnian moons such as Enceladus and Titan, and the planet Mars. The proximity of Mars to Earth and its apparent wet history make it a place of particular astrobiological interest.

Since the first flyby missions of the 1960's, many probes have been sent to the red planet including landers, rovers, orbiters, and as of NASA's successful Ingenuity flight in 2021, a helicopter. An objective of many of these missions was to investigate the habitability of Mars and search for signs of extinct and extant life. However, our interest in Mars as a host for life goes much further back than these missions. Mars has for centuries been an object of interest with regard to extraterrestrial life. In his 1784 work about his telescope observations of the Martian polar regions and atmosphere, William Herschel speculated that the inhabitants of Mars 'probably enjoy a situation in many respects, similar to ours' [1]. Later, nineteenth-century astronomer Percival Lowell erroneously interpreted the enigmatic surface features first observed by Giovanni Schiapperelli as canals created by intelligent Martians [2]. These canals, which Lowell suggested may be used for irrigation purposes were later found to be optical illusions. Over a century later we are yet to find convincing evidence of extinct or extant life on the red planet. There have however been many observations of the results of substantial volumes of liquid water flowing on the Martian surface, suggesting

that Mars was once somewhat Earth-like. This has led to speculation that life may have emerged on Mars at some time in its history and that signatures or vestiges of that life may yet be detectable.

2.1 Water on Mars

Mars once had an active hydrologic cycle and substantial volumes of water flowed on its surface [3–14]. Over time, Mars lost much of its atmosphere to space leading to liquid water becoming unstable on the surface [15]. In the present, low temperatures, low humidity and an average atmospheric pressure of ∼6.5 mb (∼650 Pa) mean that any surface water is locked away as ice or hydrated minerals (Figure 2.1). Evidence of past water remains etched into the surface in the form of deltas, alluvial fans, valley networks and outflow channels like those in Figure 2.2 [16–19].

There is evidence that transient liquid water may exist on the present Martian surface in the form of brine when the deliquescence relative humidity and eutectic temperature of hygroscopic salts are exceeded [3, 20–26]. This can occur at surprisingly low temperatures due to the low eutectic point of the perchlorate salts present on the Martian surface, with calcium perchlorate having a eutectic temperature of ∼199 K [27–29]. This has been proposed as a potential explanation of the mysterious 'recurring slope lineae' [20, 25], though they have also been attributed to the flow of granular material [30, 31]. The appearance, merging, and dripping of small spheroids on the struts of the Phoenix lander over a period of weeks, as shown in Figure 2.3a, suggested they were formed of liquid brine that was deliquescing [21].

Abundant and widespread deposits of hydrated minerals on the surface and also point towards a once-wet Mars as they usually require liquid water to form [32–35]. Deposits of sulphates, chlorides and perchlorate salts are among those that have been detected at many locations across the Martian surface. Figure 2.4 is a map of the many hydrated mineral deposits detected by the Mars Express orbiter. Additionally, there is evidence of water in the subsurface, sequestered within hydrated minerals [36, 37]. Rocks analysed at Endeavour crater, Meridiani Planum, exhibit signs of recent and ongoing aqueous alteration, depositing magnesium-bearing minerals into voids in the rocks [38]. There are also signs of the aqueous alteration of rocks at Jezero crater, leaving behind perchlorate

and sulphate minerals within the rock interiors [39, 40]. Polygonal, topographic features have been observed at many locations on the Martian surface, indicating periods of recurring ephemeral lacustrine environments causing desiccation cracks similar to many observed on terrestrial salt flats. Polygonal features interpreted as desiccation cracks have been observed at Gale crater by Curiosity [41]. Similar features have been observed by the Mars Reconnaissance Orbiter across the southern highlands and are associated with chloride deposits [42]. Phillips et al. (2023) identified 16 Martian chloride-bearing salars (salt flats) that harboured potential salt constructs, indicated by the topographic polygonal features [43]. These features indicate the repeated interaction of the terrain with liquid water after the lakes have dried up. This, combined with the presence of salts, makes them regions of particularly high potential as habitats and sites of biosignature preservation.

Layered deposits at both of the Martian poles presently contain substantial volumes of perennially frozen water. The presence of late Amazonian gypsum deposits at the north polar region suggests that liquid water must have formed in the recent past, potentially by melt processes at the north polar ice cap [44–46]. Furthermore, ice has been observed beneath a few centimetres of loose soil at the Phoenix lander site as shown in Figure 2.3b and models and observational data point to a widespread layer of shallow ice at high and mid latitudes [47, 48].

The observations of water and its historical presence on the Martian surface can point towards sites of astrobiological importance, particularly if those environments have inhabited terrestrial analogues with good preservation potential.

2.2 Life in Extreme Environments on Earth

Complex and diverse communities of microorganisms survive in many extreme environments on Earth. In environments that initially appear barren, including those considered the closest terrestrial analogues to Mars, communities of microorganisms can be found. These microorganisms inhabit microenvironments with properties that buffer the extreme conditions, providing a refuge for life. In some of the driest and hottest locations on the planet - the Atacama and the Mojave deserts, endoevaporitic and endolithic organisms persist in evaporite deposits and rocks respectively [49, 50]. In the cold desert of the dry valleys of Antarctica, communities of microorganisms are found in a number

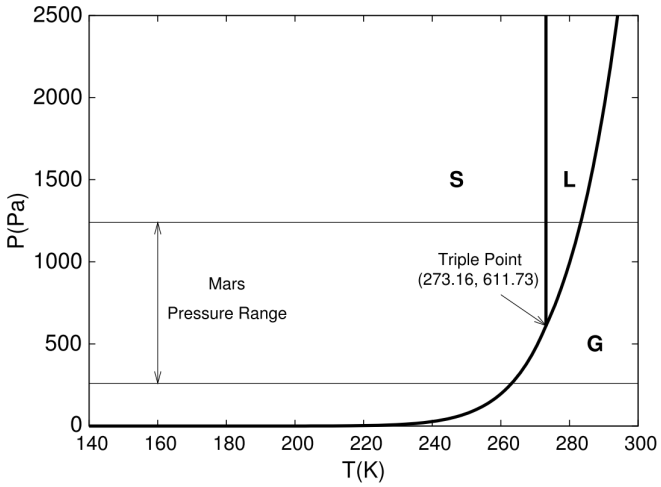

Figure 2.1: Phase Diagram for Water at Mars Surface Pressures. Under present Mars surface pressures, liquid water is unstable and can typically only exist as ice or gas (from Martinez and Reno (2013) [3]).

of microenvironments including within rock pores, in ice covered lakes, and within fluid inclusions in the ice that perennially caps those lakes [51–53]. Similar fluid inclusion environments called cryoconite holes are found on glacier ice throughout the terrestrial cryosphere [54] (cryoconite is a dark-coloured material of mineral and biological composition). Organisms can live in such extreme environments through a combination of adaption mechanisms and taking advantage of the environmental buffering properties that microenvironments can provide. Rock interiors and evaporites can sustain liquid water or high humidity in arid environments, provide protection from UV radiation, and lessen extreme variations in temperature that the exterior environment experiences [55–57]. Lake ice inclusions and cryoconite holes provide a relatively warm, liquid water environment compared to the freezing exterior conditions. Life can be preserved in some of these environments too, potentially over geologic timescales. Viable microorganisms and biosignatures have reportedly been extracted from fluid inclusions in ancient evaporite deposits and from ancient permafrost and glacial ice environments [58–61]. Ancient endolithic life has reportedly been preserved in rock as fossils [62, 63] though the biogenicity of some samples has been called into question by recent work on the cultivation of similar structures in chemical gardens (mixtures of a metal salt and an aqueous silicate or carbonate solution that abiotically form structures with biological-appearing morphologies) [64, 65].

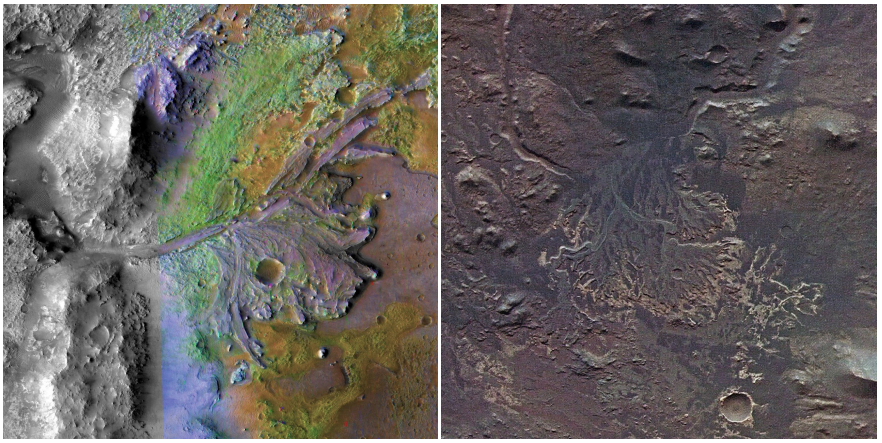

(a) **(b)**



(c)

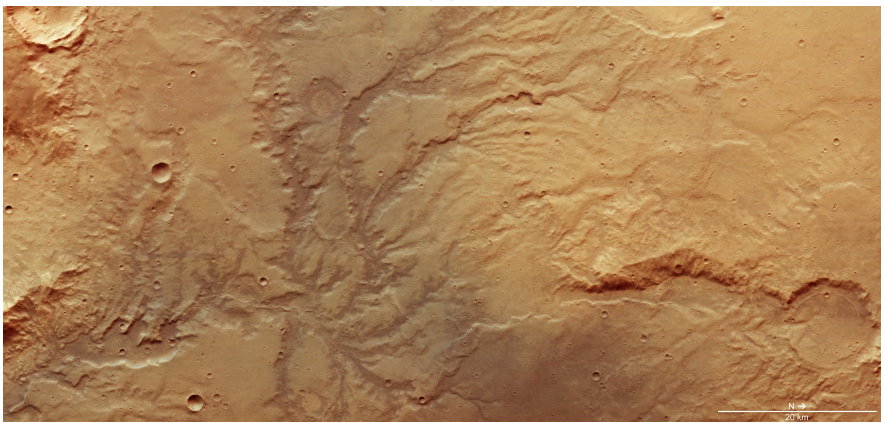

(d)

Figure 2.2: Ancient Features Carved by Water on the Surface of Mars. (a) Delta in Jezero Crater (NASA/JPL-Caltech/MSSS/JHU-APL). (b) Delta in Eberswalde crater (ESA/DLR/FU Berlin). (c) Osuga Valles, an outflow channel thought to be carved by catastrophic flooding (ESA/DLR/FU Berlin). (d) Valley network in the southern highlands (ESA/DLR/FU Berlin).

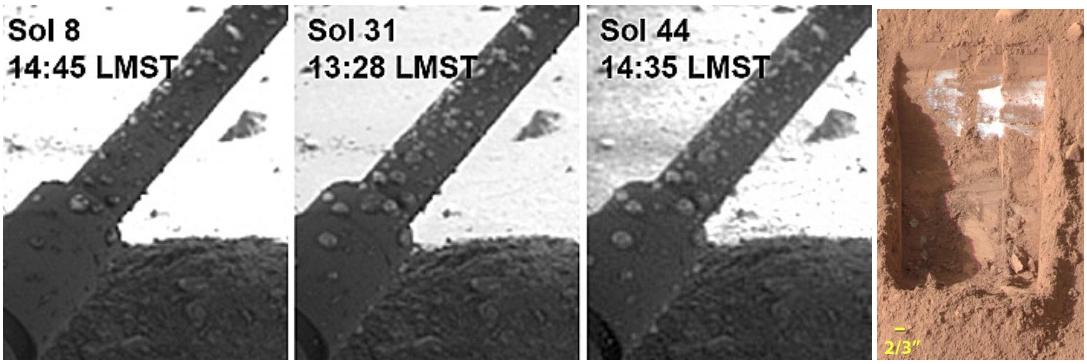

(a) **(b)**

Figure 2.3: Brine Droplets and Ice at the Phoenix Lander Site. (a) Potential liquid brine droplets on the Phoneix lander struts. The droplets merged over time and one dripped off the strut (From Rennó et al. (2009) [21]). (b) Water ice beneath a few centimetres of regolith, uncovered by the Phoenix lander's robotic arm (NASA/JPL-Caltech/University of Arizona/Texas A&M University).

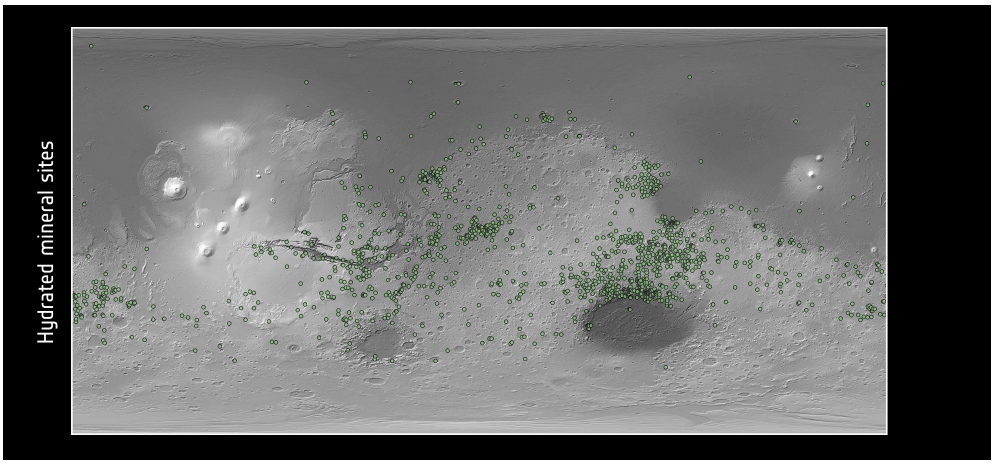

Figure 2.4: Map of the Distribution of Hydrated Minerals on the Surface of Mars. The green dots are sites where hydrated minerals that formed in the presence of water were detected by OMEGA on Mars Express (ESA/CNES/CNRS/IAS/Université Paris-Sud, Orsay; NASA/JPL/JHUAPL; Background image: NASA MOLA).

2.3 The Astrobiological Potential of Putative Aqueous Microenvironments on Mars

This work investigates the potential habitability of putative aqueous Martian microenvironments. Habitability in this context refers to the ability of an environment to support the survival of at least one organism [66, 67]. Life as we know it has several requirements for survival including the presence of essential CHNOPS elements, a source of energy, clement environmental conditions and liquid water to act as a solvent. To understand the habitability of past and present Mars we need to understand if, when, and where these requirements converged. This work will focus on the formation or longevity of liquid water in three environments that exist on the surface of Mars and have terrestrial analogues populated with communities of microorganisms: brine evaporites, rock pores and water ice. A detailed background for each environment investigated will be presented at the beginning of each chapter. By understanding how refugia in extreme terrestrial environments facilitates the survival of microorganisms and studying the effect of Martian geophysical and environmental conditions on those properties, we can improve our understanding of the limits of habitat formation under Martian environmental conditions and contribute to selection of appropriate sites for life, biosignature, and habitat seeking missions on the surface of the red planet.

Chapter 3

General Methodology

3.1 The Planetary Environment Simulation Chamber

The Planetary Environment Simulation (PES) Chamber (Figure 3.1) was used in several experiments presented in this thesis. It is a stainless steel, cylindrical vacuum chamber (Kurt J. Lesker, custom built). The pressure is maintained using a dry scroll pump (Edwards, nXDS), and measured using a pressure transducer (mks, 90B). A tray of silica beads in the base of the chamber was used to minimise the relative humidity. A precision balance (KERN, PCB 100-3) within the chamber could measure the mass of samples at set intervals. Data from the balance was recorded using a custom LabView programme. A removable manipulation arm could interact with samples in the chamber during experiments without change of pressure. The PES chamber maintains pressure at an accuracy of ± 1 mb.

3.2 Fluorescence Microscopy

Microscopy was performed using a digital microscope (Leica, DM4000B). Fluorescence microscopy was performed using a Leica EL6000 light source. Images were acquired using a microscope camera (Leica, DFC450 C). The apparatus is depicted in a schematic in Figure 3.2.

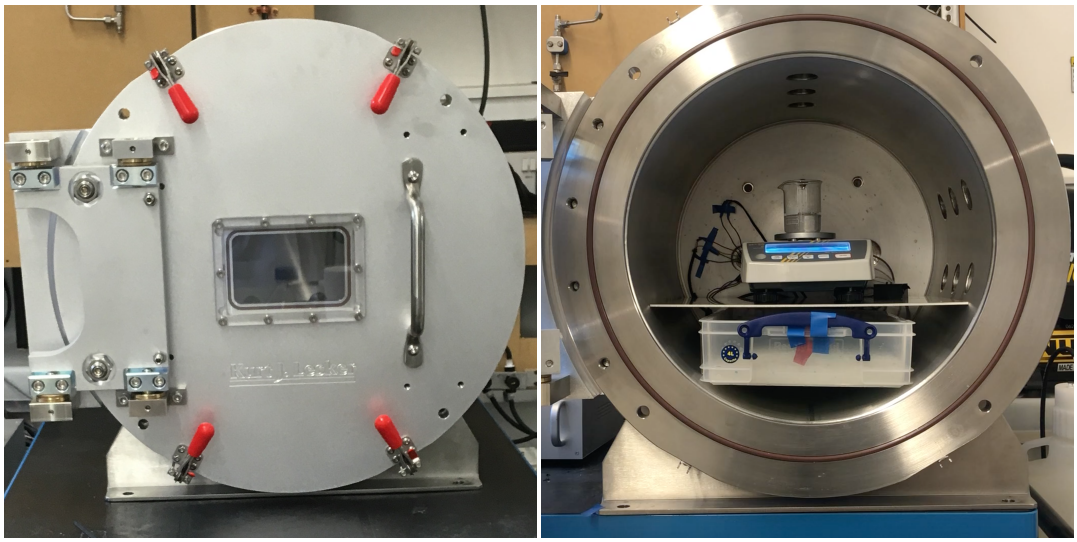

(a) (b)

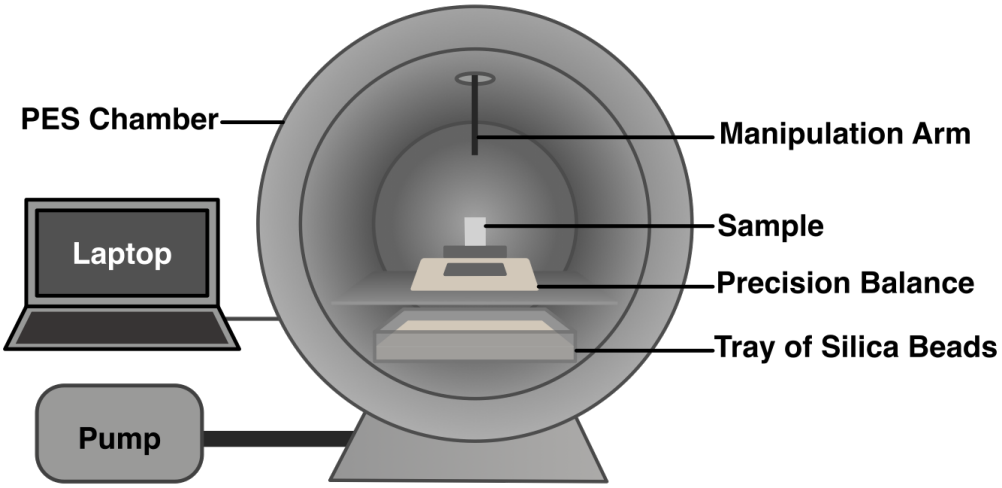

(c)

Figure 3.1: The Planetary Environment Simulation (PES) Chamber. The PES chamber is a low pressure pressure chamber maintained by a dry scroll pump. A balance inside the chamber measured sample mass over time, which was logged on the connected laptop. A tray of silica beads minimised humidity. A manipulation arm could be used to interact with samples without breaking pressure. Chamber (a) exterior and (b) interior. (c) A schematic of the PES chamber apparatus.

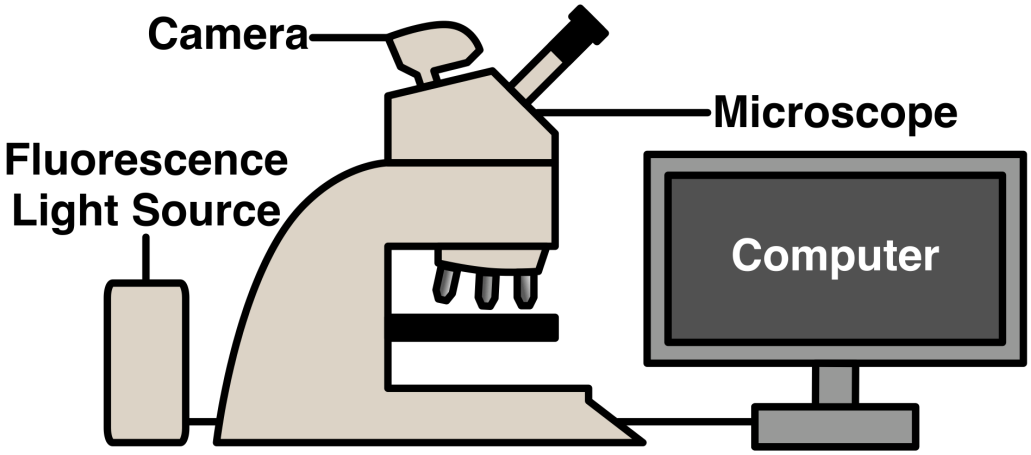

Figure 3.2: Microscopy Apparatus Schematic. The fluorescence light source connected to the microscope allowed for the counting of fluorescent microspheres. Images could be acquired using the connected microscope camera.

3.3 Data Analysis

Data analysis was performed in Microsoft Excel Version 16.72 [68] and Python 3.8 [69].

Mean values across repeated measurements and triplicates $\bar{x}$ and the uncertainty in the mean $\sigma_{\bar{x}}$ were calculated using

$$\bar{x} = \frac{\sum_{n=1}^{N} \frac{x_i}{\sigma_i^2}}{\sum_{n=1}^{N} \frac{1}{\sigma_i^2}} \tag{3.1}$$

and

$$\sigma_{\bar{x}} = \sqrt{\frac{1}{\sum_{n=1}^{N} \frac{1}{\sigma_i^2}}} \tag{3.2}$$

respectively. Where x_i is the ith measurement of a set of N measurements and σ_i is the uncertainty in x_i.

Experimental uncertainties were propagated using [70]

$$\sigma_f(x, y, ..., n) = \sqrt{\left(\frac{\partial f}{\partial x}\sigma_x\right)^2 + \left(\frac{\partial f}{\partial y}\sigma_y\right)^2 + \cdots + \left(\frac{\partial f}{\partial n}\sigma_n\right)^2} \tag{3.3}$$

where $\sigma_f(x, y, ..., n)$ is the uncertainty in parameter f, which is a multivariate function of variables (x,y,..,n), each of which has an associated uncertainty (σ_x, σ_y,..,σ_n).

3.3.1 Uncertainty in Mass Caused by Diurnal Environmental Variations

During the testing of the balance inside the PES chamber at each experimental pressure, where the balance output was being recorded with only a constant test mass applied, a small variation in the mass measurements was observed. The variations were cyclical by approximately 24 hours, suggesting they were likely caused by diurnal temperature fluctuations. To quantify this variation at each experimental pressure used in this thesis, with a test mass on the balance, mass measurements were taken every minute for ∼one day. This was performed in triplicate for each experimental pressure (7 mb, 10 mb, 50 mb, 100 mb and 1000 mb). The difference in the maximum and minimum recorded mass values were calculated and halved to determine the uncertainty in mass measurements. The mean of the three triplicates was calculated to determine the mean uncertainty in the mass measurements due to daily variation in the balance readings. The results are presented in Table 3.1 and Figure 3.3.

3.3.2 Salt Content of Saturated Brines

The fractions of salt and water contained within a pure $MgSO_4$ brine and a mixed $FeSO_4$ & $MgSO_4$ brine were necessary for several calculations throughout this thesis. Three samples of ∼0.5 g of each brine in each relevant experimental environment were taken and dried in an oven at 120°C for 24 hours. The dried samples were weighed. The salt fraction of the brine, s, was calculated using

$$s = \frac{m_{after}}{m_{before}} \tag{3.4}$$

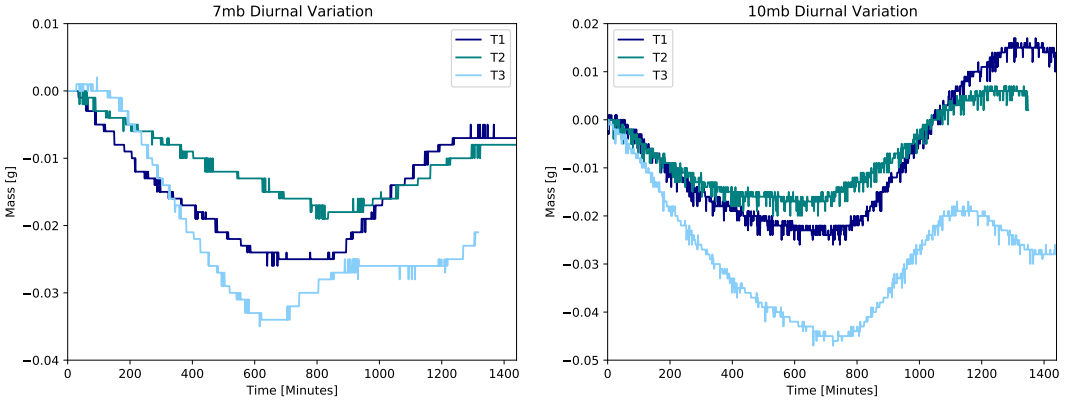

(a) 7 mb

(b) 10 mb

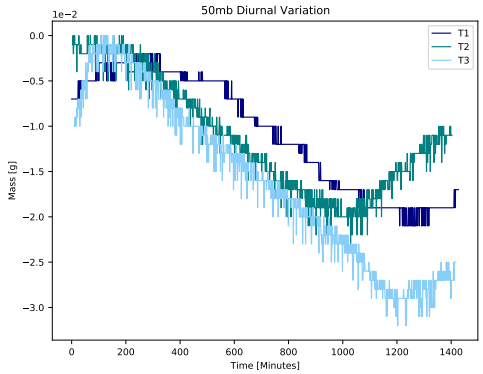

(c) 50 mb

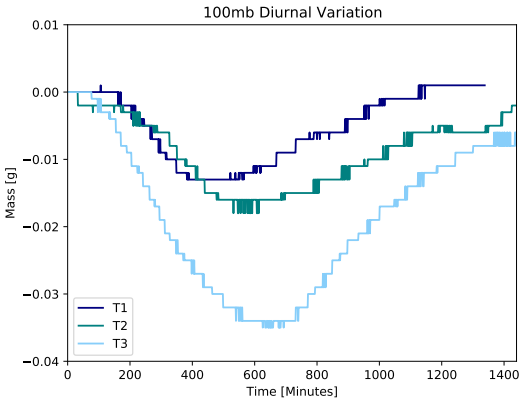

(d) 100 mb

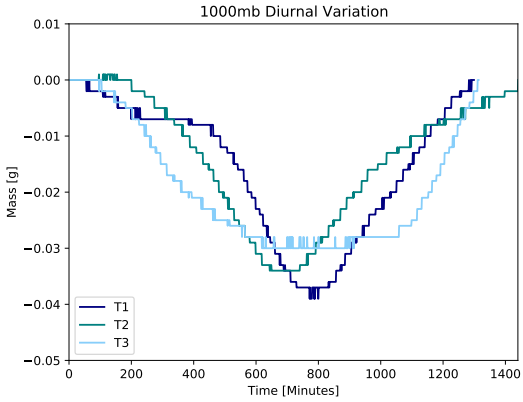

(e) 1000 mb

Figure 3.3: Diurnal Variation in Measurements of a Fixed Mass at Each Experimental Pressure. Measurements were taken with a fixed test mass on the balance to determine the maximum variation in mass measurement caused by diurnal environmental fluctuations. T1-T3 refers to each triplicate of the test experiment set.

Table 3.1: Diurnal Variation in Fixed Mass Measurement at Each Experimental Pressure. T1-T3 refers to each triplicate of the test experiment set. The mean variation at each pressure was used as the uncertainty in the mass measurement for uncertainty propagation.

Pressure [mb]	Triplicate	Mass variation [g]
7	T1	±0.013
	T2	±0.010
	T3	±0.019
	Mean	±0.014
10	T1	±0.024
	T2	±0.021
	T3	±0.014
	Mean	±0.020
50	T1	±0.011
	T2	±0.012
	T3	±0.016
	Mean	±0.013
100	T1	±0.007
	T2	±0.009
	T3	±0.018
	Mean	±0.011
1000	T1	±0.019
	T2	±0.018
	T3	±0.015
	Mean	±0.017

where m_{before} [g] is the mass of solution sample before drying and m_{after} [g] is the mass of solid salt remaining after drying has removed the water. The water fraction, w, of the brine was therefore calculated using

$$w = 1 - s \tag{3.5}$$

The mass of salt (m_{salt} [g]) and water (m_{water} [g]) in a fresh brine sample was calculated using

$$m_{salt} = s \cdot m_{brine} \tag{3.6}$$

$$m_{water} = w \cdot m_{brine} \tag{3.7}$$

respectively, where m_{brine} [g] is the mass of the brine sample. The salt and water fractions for each brine in each environment are presented in Table 3.2. Uncertainties were propagated using Equation 3.3. The mean values across triplicates and their associated uncertainties were calculated using Equation 3.1 and Equation 3.2 respectively.

Table 3.2: Brine Salt and Water Fractions The salt and water fractions of $MgSO_4$ and mixed $FeSO_4$ & $MgSO_4$ brines were measured from samples taken from each relevant environment. Samples of brine were dried to determine these fractions.

Environment	Brine	Triplicate	Sample Mass [g]	Dried Sample Mass [g]	Salt Fraction	Water Fraction
PES Chamber (ambient temperature, ≤20% RH)	$MgSO_4$	T1	0.500 ± 0.017	0.165 ± 0.017	0.33 ± 0.04	0.67 ± 0.04
		T2	0.555 ± 0.017	0.183 ± 0.017	0.34 ± 0.03	0.66 ± 0.03
		T3	0.508 ± 0.017	0.179 ± 0.017	0.35 ± 0.04	0.65 ± 0.04
		Mean	0.521 ± 0.010	0.176 ± 0.010	0.34 ± 0.02	0.66 ± 0.02
	$FeSO_4$ & $MgSO_4$	T1	0.504 ± 0.017	0.134 ± 0.017	0.27 ± 0.01	0.73 ± 0.10
		T2	0.501 ± 0.017	0.131 ± 0.017	0.26 ± 0.01	0.74 ± 0.10
		T3	0.502 ± 0.017	0.142 ± 0.017	0.28 ± 0.01	0.72 ± 0.09
		Mean	0.502 ± 0.010	0.136 ± 0.010	0.27 ± 0.01	0.73 ± 0.06
Climate Controlled Room (30°C, ≤25% RH)	$MgSO_4$	T1	0.500 ± 0.017	0.196 ± 0.017	0.39 ± 0.04	0.60 ± 0.04
		T2	0.502 ± 0.017	0.201 ± 0.017	0.40 ± 0.04	0.60 ± 0.04
		T3	0.504 ± 0.017	0.190 ± 0.017	0.38 ± 0.04	0.62 ± 0.04
		Mean	0.502 ± 0.010	0.196 ± 0.010	0.39 ± 0.02	0.61 ± 0.02

Chapter 4

The Astrobiological Potential of Brine Evaporites

4.1 Introduction

In 1976 the Viking landers touched down on the Martian surface at Utopia Planitia and Chryse Planitia where elemental analysis of the soil at the landing sites indicated the abundant presence of salts [71–74]. Since those early observations, manifold detections of salt deposits have been made globally on Mars including sulphates, chlorides, and perchlorates [32, 46, 75–78]. The observation of these salts implies the historical presence of water, which they usually require to form. One mode of formation is through the evaporation of liquid brine resulting in the precipitation of evaporites. Many of the deposits observed on Mars are thought to have formed this way.

Evaporites are populated by communities of microorganisms in polyextreme environments all over planet Earth including in Antarctica and hot deserts. The composition, processes, and structure of these communities have been studied in depth since they were first characterised in the 1960's, revealing the contribution of the salts that they inhabit to their survival [53, 79, 80]. Samples taken from ancient terrestrial evaporites contain fluid inclusions that reportedly harbour viable microorganisms [58, 81]. On Earth, life associated with evaporite crusts is mainly found in halite and gypsum deposits. However, on Mars, a wide variety of other salts have been identified and proposed as potential habitats.

Brine evaporite environments have been suggested as potential Martian habitats due a number of properties that buffer extreme environmental conditions including UV scattering, deliquescence, and freezing point depression [82]. These environments may therefore have served as the last vestiges of liquid water on the surface of Mars as the planet became more hostile. By understanding which brine compositions produce evaporites with properties that contribute to the formation and persistence of habitats, targets for current and future biosignature seeking missions can be identified.

The combination of the prevalence of salt deposits on the Martian surface, the ubiquity of habitation in polyextreme terrestrial evaporites, and the preservation of biosignatures over potentially geologic timescales make Martian evaporites an environment of particular astrobiological interest. This work aims to contribute to our understanding of the habitability of these environments by characterising the morphology of a range of Mars-relevant pure and mixed brine evaporites. We explore how the physical characteristics of the evaporites may influence their habitability and other potential astrobiological implications.

This chapter investigates saturated sulphate, chloride, and perchlorate salt solutions and binary mixtures of these salt solutions under Earth and low pressure conditions to understand the physical behaviour of their evaporites. In particular, the following questions are addressed:

- What evaporite morphologies do Mars-relevant brines typically form?
- How does exposure to low pressure affect the formation of these morphologies?
- Are brines that form interfacial crusts effective at inhibiting evaporation under Earth and low pressure conditions?
- Can creeping evaporites transport micron-scale objects?

4.2 Background

4.2.1 Terrestrial Hypersaline Habitats

Hypersaline environments on Earth are inhabited by diverse microbial communities with members from all three domains of life [83–91]. Even in polyextreme environments, where hypersalinity is combined with extremes of temperature, aridity and pH, microorganisms live and proliferate.

Many studies have looked at life in naturally occurring concentrated brine environments. A diverse range of microorganisms have been isolated from $MgSO_4$ saturated North American lakes considered potential analogues for ancient Martian lakes [83, 85, 92]. Organisms have also been isolated from the Antarctic $MgCl_2$ saturated Don Juan Pond and salt flat located in the dry valleys, one of the coldest and driest environments on Earth [52, 93, 94]. Inhabited gypsum ($CaSO_4 \cdot 2H_2O$) evaporites have also been observed in Antarctica [95], examples of which are shown in Figure 4.1. The Atacama desert is one of hottest and driest environments on the planet [96]. This, combined with the high soil salinity [97–99] and UV radiation flux [100, 101], makes it one of the closest Earth analogues to present-day Mars [102]. Samples of halite (NaCl) and gypsum salt crusts from salars (salt flats) in the Atacama revealed surprisingly diverse halophilic microbial communities even in the most arid region [103–105]. Examples of these communities are shown in Figure 4.2. Given that the soil in the hyperarid region of the Atacama has extremely low levels of culturable bacteria, these salt deposits provide an oasis where life can persist [102]. Recent work has shown that microorganisms can survive and possibly grow in some of the hydrothermal brine pools at the Dallol area, Ethiopia, another environment considered a terrestrial analogue to Mars due to its arid, hypersaline conditions [91, 106–108]. The pools are highly saline and of diverse chemical composition including sulphates and chlorides of Mg, Na, Ca and Fe [109, 110].

Evaporite environments are able to host diverse microbial communities in inhospitable environments due to several properties that allow them to buffer extreme conditions. Substantial evaporite crusts have been observed in desert environments [111], Canadian hypersaline lake systems [83], and in dry caves [112, 113]. Evaporite crusts have been noted to reduce evaporation, preserving liquid brine beneath the crust [111, 114–116]. Salt crusts form when evaporation

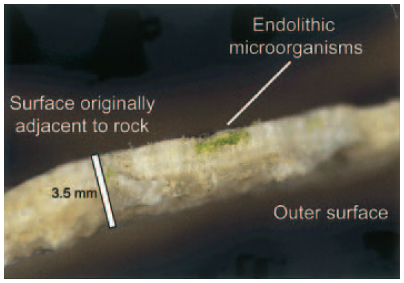

(a)

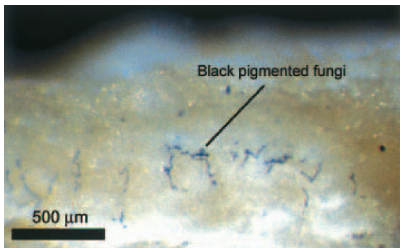

(b)

Figure 4.1: Communities of Microorganisms in Antarctic Gypsum Salt Crusts. (a) The green region is an phototrophic microbial community within a gypsum crust. (b) The black regions are fungi within a gypsum crust (both images from Hughes and Lawley (2003) [95]).

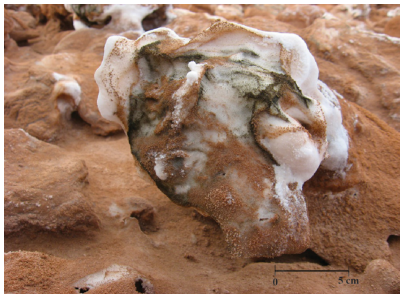

(a)



(b)

Figure 4.2: Communities of Microorganisms Living in Atacama Salt Crusts. (a) The dark green regions are microbial communities in a halite salt crust (from Finstad et al. (2017) [103]). (b) The green regions are endoevaporitic microbial communities within a gypsum salt crust (from Wierzchos et al. (2011) [105]).

from the liquid-gas interface increases local ion concentration, triggering crystal nucleation and growth on the liquid surface where the crystals are suspended due to surface tension. As more crystals form they adhere to each other, eventually forming a continuous crust. This process continues, forming a continuous layer of solid crystals at the liquid-gas interface (Figure 4.3). An example of a halite and gypsum salt crust with sub-crust liquid brine in a desert sabkha is shown in Figure 4.4. In the Atacama evaporites, the hygroscopic nature of halite allows it take on water from the atmosphere, providing sufficient moisture within the salt crust for life to persist [117]. Furthermore, halite crystals have been shown to scatter short wavelength UV radiation [118], while transmitting photosynthetically useful wavelengths, creating an oasis for microorganisms in otherwise hostile radiation environments [82, 119].

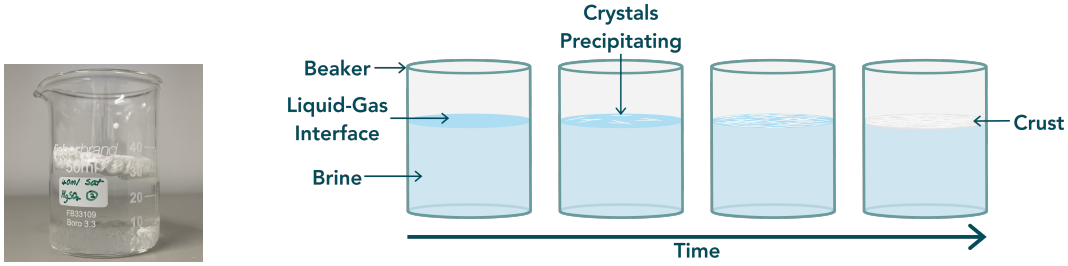

Figure 4.3: Salt Crust and Crust Formation Mechanism. (a) An example of a $MgSO_4$ interfacial salt crust. (b) The formation of an interfacial salt crust. Crystals precipitate at the liquid-gas interface and are suspended due to surface tension. This process continues, forming an interfacial crust.

As they precipitate, evaporite salt crystals can form intracrystalline fluid inclusions, trapping liquid and microscopic debris present at the time of their formation [120]. The inclusions can protect trapped fluid from the chemical environment outwith the salt crystals and if the deposit has not experienced post-depositional modification it can provide insight into the environmental conditions at the time of formation. There have been a number of reports of viable microorganisms being isolated from fluid inclusions in ancient halite evaporites up to 250 million years old [58, 81, 121–126]. An example of microorganisms trapped in a fluid inclusion from ancient halite is shown in Figure 4.5. It has also been shown that organic material can be trapped in intracrystalline inclusions in $MgSO_4$, a salt that is abundant on Mars [127]. The potential of salt crystals to trap microorganisms in intracrystalline inclusions, preserving biosignatures or extant life over geologic timescales and protecting them from the harsh conditions experienced on Mars contributes further to the astrobiological

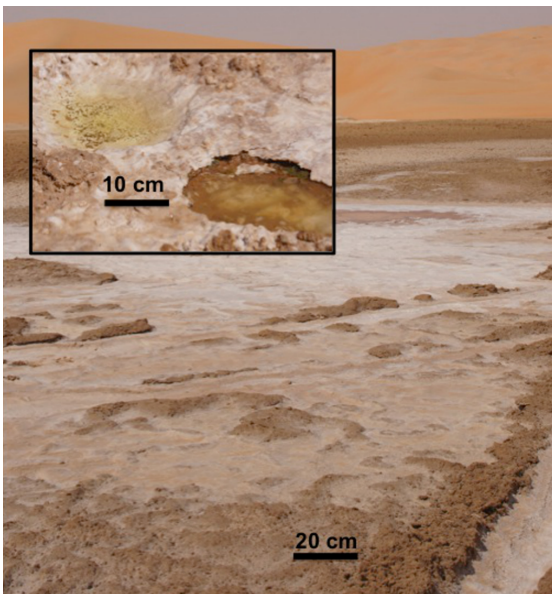

Figure 4.4: Halite Evaporite Crust in UAE Sabkha. The inset image shows liquid brine beneath the white salt crust (from McKay et al. 2016 [111]).

relevance of evaporite deposits.

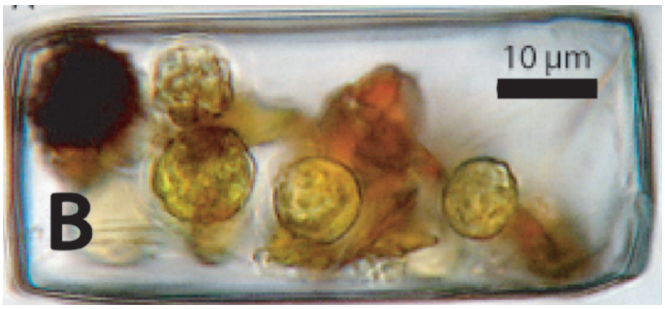

Figure 4.5: Microorganisms in a Fluid Inclusion in Ancient Halite The ancient halite sample was taken from deposits in Death Valley, California (from Lowenstein et al. (2011) [128]).

4.2.2 Creeping Evaporites as Habitats and Paleoenvironmental Indicators

Evaporite caves in the Atacama desert host rare and unique mineral assemblages with a variety of distinctive morphologies that form and are preserved in the caves due to the hyperarid and hypersaline conditions. These conditions make them a good analogue environment to understand mineral formation and preservation on Mars [113]. Dendritic mineral formations have been observed on the Martian surface at Gale Crater by Curiosity rover (Figure 4.6). Analysis of other dendritic

features at Gale crater show them to be enriched in Mg, interpreted as Mg-sulphates [129, 130]. Although these structures are thought to be early diagenetic concretions rather than post-diagenetic mineral assemblages like those observed in terrestrial dry caves, they are an example of distinctive mineral assemblages preserved on the Martian surface over geologic time scales. By understanding the conditions under which distinctive mineral morphologies form and persist it may be possible to use structures observed on Mars as environmental indicators.

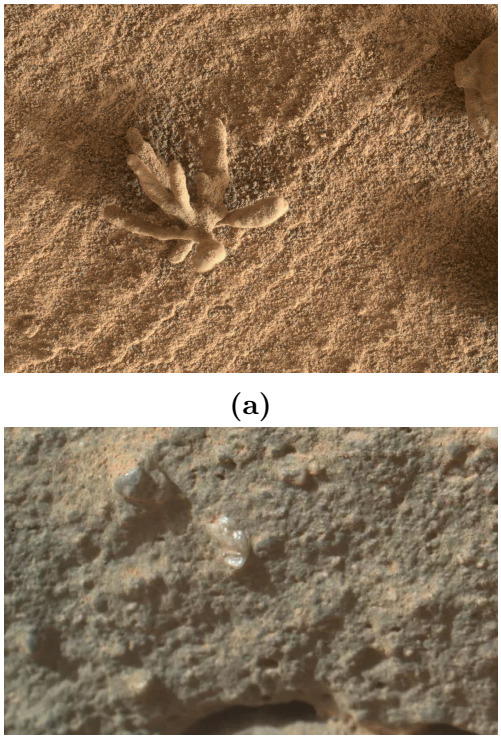

(a)

(b)

Figure 4.6: Dendritic Mineral Assemblages at Gale Crater, Mars. Similar structures nearby have been found to be enriched with magnesium, attributed to magnesium sulphate (NASA/JPL-Caltech/MSSS).

Dendritic salt assemblages have been shown to form through a self-amplifying creeping process. Crystals precipitate and become trapped in the liquid meniscus. Space between the crystals and the wall of the beaker, as well as pore spaces between crystals themselves, wick solution by capillary action, coating the crystal surface in a thin layer of solution, allowing further precipitation to occur. The solution then precipitates at the periphery of the crystal and the process repeats, forming distinctive creeping structures until the solution runs out or evaporation can no longer occur [131–133]. If the creeping occurs primarily on the substrate (e.g. a beaker wall) it is referred to as a primary or surface creep. Secondary creeping occurs when crystals precipitate onto other crystals, growing outwards,

away from the substrate, forming three-dimensional structures. An example of a secondary creeping structure and the formation mechanism is shown in Figure 4.7. It has been noted that some brines only form creeping structures under particular environmental conditions [131, 134]. Salt efflorescence is a related phenomena where salts precipitate at the surface of porous media when water is wicked by the material. These mechanisms have been studied with respect to being a nuisance during industrial crystallisation processes [135], corroding outdoor electronics [136] and degrading monuments, frescoes, and cave art [137]. Microbes have been isolated from these environments [137–139] raising the question of whether salt creeping phenomena represent a mechanism for habitat establishment and expansion. No work has been done to determine the potential of salt creeping mechanisms to transport material or expand habitat space. This chapter aims to address this as well as determine which Mars-relevant brines are likely to be able to form such environments under Earth and Mars pressure conditions.

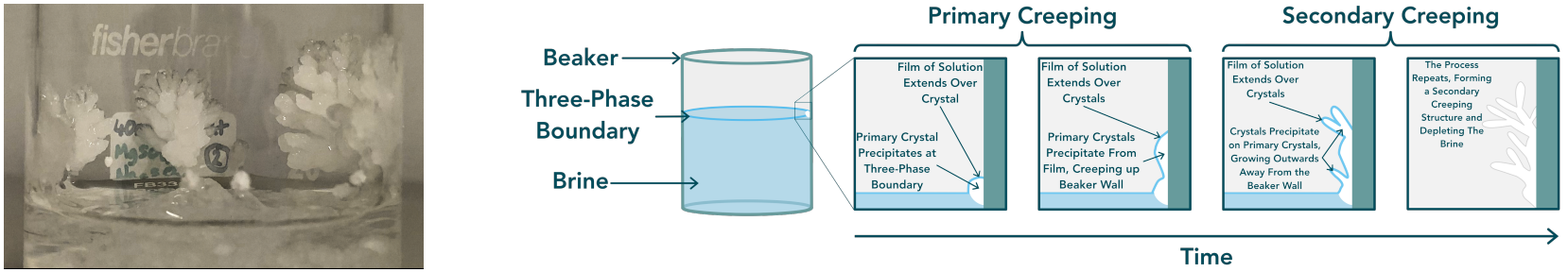

(a) **(b)**

Figure 4.7: Creeping Structure and Salt Creeping Formation Mechanism. (a) An example of a mixed $MgSO_4$ & Na_2SO_4 brine salt creep growing up a glass beaker. (b) The salt creeping mechanism. A thin film of solution extends over precipitated crystals. Evaporation occurs causing further precipitation of crystals that are subsequently coated with the advancing solution and the cycle repeats. Adapted from Qazi et al. (2019) [131] and van Enckevort & Los (2013) [134].

4.2.3 Limits to Life in Martian Brines

Organisms isolated from Canadian epsomic lakes have been shown to grow in saturated solutions of $MgSO_4$ and 3.5 M NaCl in laboratory experiments [85]. Many different microorganisms have been shown to live and grow in saturated NaCl in natural and laboratory settings [140]. Microbial growth has been observed in saturated $MgSO_4$ and saturated Na_2SO_4 as well as in less concentrated solutions of and Ca-, Mg- and Na- chloride [141]. Microorganisms have also been shown to grow Ca-, Mg- and Na- perchlorate brines despite the extreme stressors imposed by the highly deleterious salts. The current reported limit for microorganism growth in perchlorate brine is that of a halotolerant yeast in 2.4 M $NaClO_4$ [141–145]. It has been suggested that putative Martian microbes, which would have been exposed to high salt concentrations over long time frames, could have plausibly adapted to even higher concentrations than the currently observed limits [144]. The research conducted in this field shows that halotolerant and halophilic organisms on Earth are able to survive in some highly concentrated Martian brines, contributing further to the astrobiological potential of hypersaline environments and evaporite deposits on the surface of Mars.

4.2.4 Salt Deposits on Mars

Abundant salt deposits have been detected globally on the surface Mars by remote sensing and in situ measurements [146]. Orbital data from the Mars Reconnaissance, Mars Odyssey, and Mars Global Surveyor orbiters revealed abundant and widespread deposits of chlorides [77] and hydrated sulphates [32] in the southern highlands of Mars. Hecht et al. (2009) presented the detection of perchlorate, chloride, and possibly sulphate anions as well as Mg, Na, and Ca at the Phoenix lander site in the north polar region. Sulphate signatures attributed to hydrated calcium sulphate were also detected in north polar regions by Mars Express [46]. Mars Express also detected hydrated magnesium sulphate minerals and potentially Ca-, Fe- and Na- sulphates in the equatorial Valles Marineris region [34, 76]. In equatorial regions, numerous detections of abundant salt deposits have been made at various rover and lander sites. At Meridiani Planum, detection of Mg-, Fe-, and Ca- sulphate minerals and potentially some Mg- and Ca- chlorides have been made by instruments on the Opportunity rover [147–149]. At Gale Crater, instruments on the Curiosity rover have detected hydrated

Ca- and Mg- sulphates as well as chlorides interpreted as halite [78, 150–152]. Signatures that could indicate the presence of perchlorates have also been detected at Gale crater [153, 154]. Spirit, at Gusev crater, has detected Fe-, Mg-, and Ca-sulphate minerals in the regolith and rocks [155–158]. Recent results from the Perseverance rover indicate the presence of hydrated Ca- and Mg- sulphates and likely $NaClO_4$ [39, 40, 159] at Jezero Crater. Many of these deposits have been interpreted as evaporites, suggesting the presence of standing bodies of liquid brine in Mars' history, potentially similar to lacustrine and playa environments on Earth [43, 78, 146, 160–164]. Phillips et al. (2023) used remote sensing techniques to identify potential salt flats on the surface of Mars, identifying 16 sites with topographical features indicating the presence of salt constructs [43]. Some deposits have been suggested as potential habitats for past and present putative Martian microorganisms due to their hygroscopic characteristics causing deliquescence and freezing point depression, which can significantly extend the stable range of liquid water in dry, low pressure conditions [165, 166]. Additionally the ability of some minerals to block harmful UV radiation, an effect likely enhanced by the presence of the iron-bearing compounds present on Mars [148, 155], could serve to buffer the extreme radiation environment while allowing the transmission of photosynthetically useful wavelengths [82, 167–170].

4.2.5 The Astrobiological Potential of Brine Evaporites

Given the role of evaporite deposits as refugia for life in polyextreme terrestrial environments, it is possible that the abundant salt deposits observed on Mars could similarly represent locations of enhanced habitability. However, study of evaporative habitats on Earth has largely been focused on highly abundant halite and gypsum salts. We have little knowledge of the physical behaviour of the variety of other salts observed on Mars with respect to their suitability as habitats. Understanding the behaviour and properties of potential Martian brines contributes to our understanding of where traces of putative Martian life may have existed and thus where to look for biosignatures.

In this chapter, the habitability of evaporites was investigated by observing the formation and long-term behaviour of evaporite structures from pure and binary mixtures of saturated brines consisting of sulphate, chloride, and perchlorate salts comprising ions detected on Mars. We sought to investigate the bulk behaviour of the solids formed with respect to their biological potential, particularly their

ability to extend the lifetime of liquid water and expand the physical habitat space. Brines that produced evaporite structures of particular interest were also studied under low pressure conditions to further characterise their potential as habitats under Martian conditions.

Table 4.1: Parameters and Nomenclature

Parameter	Symbol	Units
Volume	V	mL
Mass	m	g
Time	t	Days or Minutes
Mass Loss Rate	$\dot{m}$	g day^{-1}
Pressure	P	mb
Diameter	$\varnothing$	mm
Microsphere Density	ρ	ms g^{-1}
Number of Microspheres	n_{sphere}	-
Microsphere Diameter	$\varnothing_{sphere}$	μm

4.3 Materials and Methods

4.3.1 Preliminary Experiment: The Morphology of Evaporites Formed From Martian Brines

Some brines have been observed to form substantial, long-lived interfacial crusts, preserving the sub-crust brine over periods of at least several months (A. Stevens, personal communication, 2018). This preliminary work was performed to establish which solutions of Mars-relevant ions typically form these crusts and how mixing brines affects the evaporite morphology formed. The solutions used in the preliminary study were composed of salts detected on the Martian surface or combinations of ions that have been observed on Mars and could plausibly form salts. Magnesium sulphate and sodium sulphate were initially of particular interest due to their being the dominant salts in the inhabited hypersaline Spotted Lakes of Canada, which exhibit salt crusts [83, 171]. Saturated solutions of $MgCl_2$, $Mg(ClO_4)_2$, $MgSO_4$, and Na_2SO_4 were prepared by gradually adding salt (Alfa Aesar, Acros Organics, and Fisher Scientific) to de-ionised (DI) water (Nanopure, Fisher) in a flask on a heated magnetic stirrer until dissolution ceased. In a climate-controlled room (30 $\pm$ 2)°C the prepared solutions were left overnight to come to equilibrium with the environment, after which 80 mL of each saturated solution was added to a 100 mL Pyrex beaker. It is likely that Martian brines would be composed of a mixture of salts in solution, so to explore the effect of combining brines on the macrostructure of evaporite formed, mixtures of the aforementioned brines were also studied. Binary mixtures were prepared by adding 40 mL of each solution to a 100 mL beaker and stirring.

The mixtures prepared were $MgCl_2$ & $Mg(ClO_4)_2$, $MgCl_2$ & $MgSO_4$, $MgCl_2$ & Na_2SO_4, $Mg(ClO_4)_2$ & $MgSO_4$, $Mg(ClO_4)_2$ & Na_2SO_4, and $MgSO_4$ & Na_2SO_4. The solutions and binary mixtures were left in the climate-controlled room for one year and the formation of evaporite structures was observed.

4.3.2 Main Experiment: The Morphology of Evaporites Formed From Martian Brines

After interesting results were observed from the preliminary study, the experiment was extended to explore the evaporite macro-structures of brines composing several more Mars-observed ions. Calcium chloride, perchlorate and sulphate, sodium chloride and perchlorate, and iron sulphate were added to the list of salts used in the preliminary work. Therefore, the brines studied in this experiment were saturated solutions of $CaCl_2$, $Ca(ClO_4)_2$, $CaSO_4$, $FeSO_4$, $MgCl_2$, $Mg(ClO_4)_2$, $MgSO_4$, NaCl, $NaClO_4$, Na_2SO_4, and each pairwise mixture of the ten saturated solutions. This experiment was performed, building on the results from the preliminary experiment, to identify potentially astrobiologically interesting evaporite morphologies of a wider range of brines. Each experiment was conducted in triplicate to improve rigour.

Saturated solutions of $CaCl_2$, $Ca(ClO_4)_2$, $CaSO_4$, $FeSO_4$, $MgCl_2$, $Mg(ClO_4)_2$, $MgSO_4$, NaCl, $NaClO_4$, and Na_2SO_4 were prepared by gradually adding salt (Manufacturers: Alfa Aesar, Acros Organics, and Fisher Scientific) to deionised (DI) water (Fisher, Nanopure) in a flask on a heated magnetic stirrer until dissolution ceased. In a climate-controlled room at which temperature was maintained at (30 ± 2)°C, 40 mL of each saturated solution was added to a 50 mL Pyrex beaker. Binary mixtures were prepared by adding 20 mL of each solution to a 50 mL beaker and stirring. Three beakers of 40 mL of DI water were prepared as a control. The solutions and binary mixtures were left in the climate-controlled room for 11 months and the formation of evaporite structures was observed. Measurements of the mass and bulk volume (volume of liquid brine and any solid precipitate within the brine) of the brine-evaporite systems were taken periodically. Mass measurements were taken using a precision balance (Entris, Sartorius) and volume measurements were taken using the graduated scale on the beakers.

Evaporation Rate From Brines

The overall mean mass $\bar{m}$ across the triplicate samples at each time point was calculated using Equation 3.1. The associated uncertainty in the mean was calculated using Equation 3.2. The rate of mass loss $\dot{m}$ [g day^{-1}] was calculated using

$$\dot{m} = \frac{\Delta \bar{m}}{\Delta t} \tag{4.1}$$

where $\Delta \bar{m}$ [g] is the change in overall mean mass and Δt [days] is the time interval over which the mass change took place. In the case that one of the triplicates deviated significantly from the others it was not included in the calculation. The uncertainty in the mass loss rate was propagated using Equation 3.3.

4.3.3 The Morphology of Evaporites at Low Pressure

In order to determine the effect of low atmospheric pressure on the formation of evaporite structures, the brines that produced the most distinct creep and crust were exposed to 50 mb pressure conditions. Using present-day Martian pressure (7 mb) caused low pressure boiling and sputtering, which we wished to avoid in order to observe more controlled evaporite formation behaviour. In preliminary experiments, sputtering was observed in some brines at pressures as high as 40 mb. An atmospheric pressure of 50 mb was therefore chosen for the experiment.

A saturated $MgSO_4$ solution, Na_2SO_4 solution, and a 1:1 mixture of $MgSO_4$ & Na_2SO_4 were prepared as described in section 4.3.2. Forty millilitres of prepared solution in a 100 mL beaker was placed in the Planetary Environment Simulation (PES) chamber at ambient temperature. The PES chamber was gradually depressurised to 50 mb over 5 minutes. A tray of silica beads in the base of the chamber was used to minimise humidity, maintaining the relative humidity at <20%. The experimental apparatus is shown in Figure 3.1. The mass of the brine was recorded every minute with a precision balance (KERN PCB 100-3) and the formation of evaporite structures observed over 4 days. These experiments were repeated in triplicate for each brine. The experiment was also repeated in triplicate using 40 mL of DI water.

Mass Loss Rate From Brines

Mass loss rates $\dot{m}$ [g minute^{-1}] from each of the brine samples (mass loss rate here refers to the rate of mass loss due to evaporation and splashing caused by outgassing) were calculated using

$$\dot{m} = \frac{\Delta m}{\Delta t} \tag{4.2}$$

where Δm [g] is the change in mass and Δt [minutes] is the time interval over which the mass change took place. The uncertainty in the mass loss rate was calculated using Equation 3.3. Mean rates across triplicate experiments and their associated uncertainties were calculated using Equation 3.1 and Equation 3.2 respectively.

4.3.4 The Effect of a $MgSO_4$ Crust on Evaporation at Ambient and Low Pressure

An experiment was performed to quantify the extent to which the interfacial surface crust evaporite formed by saturated $MgSO_4$ brine would inhibit evaporation under ambient and low pressure (50 mb) conditions.

Ambient Pressure

Saturated $MgSO_4$ solution was prepared as in section 4.3.2. Six beakers, each containing 40 mL of saturated $MgSO_4$ solution, were prepared. They were all allowed to form an interfacial surface crust over 24 hours. Each beaker was weighed. After one hour, they were weighed again to confirm that the crust was fully formed and no mass loss was occurring. Three of the samples then had their crust manually broken every hour for 5 hours. The beakers were weighed just before each time the crust was broken. The final mass measurement was taken 60 minutes after the 5th and final time the crust was broken. The three control beakers were also weighed every hour but otherwise undisturbed. The crusts were broken by applying pressure using a plastic rod, taking care not to allow the rod to contact the liquid or remove any crust it came into contact with to avoid affecting the mass readings. The mass was checked directly before and after the crust was broken to further ensure the crust breaking processes did not affect the mass loss rate calculation. The mass of three beakers of 40 mL of pure DI water were also measured over the same time intervals. The mass loss rate and associated uncertainty for each sample was calculated using Equation 4.2 and Equation 3.3 respectively. The rate was calculated between just before the first time the crust was broken and the end of the experiment (60-360 Minutes). Across the three triplicates, overall mean rates and their associated uncertainties were calculated using Equation 3.1 and Equation 3.2 respectively.

Low Pressure - 50 mb

Saturated $MgSO_4$ solution was prepared as in section 4.3.2. A beaker containing 40 mL of saturated $MgSO_4$ solution was put into the PES chamber. A depiction of the apparatus is shown in Figure 3.1. The chamber was depressurised to 50mb over $\sim$5 minutes. A crust was allowed to form until the mass readings became

constant for 60 minutes. The crust was then broken every hour for 5 hours. The mass of the beaker was measured every minute for the duration of the experiment. A manipulation arm with a pincer end allowed for interaction with samples in the chamber without disrupting the pressure conditions (Figure 3.1). The crusts were broken manually via the manipulation arm. Mechanical pressure was applied to the crusts using the arm until the entirety of the crust broke and sank into the solution. Any outlying mass data points obviously caused by the manipulation arm coming into contact with the beaker were discarded. This was performed in triplicate.

During the five periods of mass loss after the crust was broken, the mass loss rate was calculated using Equation 4.2. The mean and associated uncertainty across the five rates were calculated using Equation 3.1 and Equation 3.2 respectively. This calculation was performed for each of the three triplicates. The overall mass loss rate for the duration of the breakage (60-300 minutes) was calculated using Equation 4.2. The mass loss rate during intervals of crust breakage and intervals of crust reformation were also calculated using Equation 4.2. The overall mean mass loss across the triplicate experiments and associated uncertainty were then calculated using Equation 3.1 and Equation 3.2 respectively.

4.3.5 Creeping Evaporites as Environmental Indicators

Based on the results of the main evaporite morphology experiment in section 4.3.2 and the low pressure evaporite morphology in section 4.3.3, the following experiment was performed to explore the effect of porous media (vesicular basalt) on creeping brines at low pressure and to establish whether there is a link between atmospheric pressure and the maximum extent of creeping structures formed in the presence of porous media. A 1:1 mixture of $MgSO_4$ & Na_2SO_4 was chosen due to its propensity to form distinctive and robust creeping evaporite structures at ambient pressure.

Into three crystallising dishes ($\varnothing = 70$ mm), 40 mL of the mixed brine was added. A single porous rock (Icelandic vesicular basalt) was placed in each dish. The dish was placed in the PES chamber (Figure 3.1) which was depressurised to 50 mb over $\sim$5 minutes. The samples were exposed to 50 mb pressure for four days and the formation of evaporite structures observed. This was repeated at 7 mb and $\sim$1000 mb. The 1000 mb experiments were performed outwith the chamber in a sealed plastic box of similar volume to the PES chamber and with the same mass of silica beads present to maintain the relative humidity at $\leq$20%. The maximum extent of the structures that formed on the surface of the porous rock were measured using calipers. The individual structures were carefully detached from the rock and measurements were taken from the point of attachment to the rock to the greatest radial extent of each structure. This was repeated up to 9 times for each rock. The overall mean maximum structure extent across triplicates and associated uncertainty were calculated using Equation 3.1 and Equation 3.2 respectively.

4.3.6 Analogue Microorganism Transport in Creeping Evaporites

Some brines produce 'creeping' evaporites – structures that grow up and along the substrate and over previously precipitated crystals, forming extensive dendritic structures. To determine the capability of creeping evaporite structures to transport microorganisms, fluorescent microspheres, similar to the typical size of some prokaryotes (1 μm), were added to a binary mixture of $MgSO_4$ & Na_2SO_4, which produces a stable and distinct creeping structure.

A solution of $MgSO_4$ & Na_2SO_4 was prepared as described in section 4.3.1. Eighty millilitres of a 1:1 mixture of $MgSO_4$ & Na_2SO_4 was added to a 100 mL beaker. A volume of 176 μL (resulting in $\sim 10^8$ spheres per mL of brine) of fluorescent microsphere solution (sphere diameter $\varnothing_{sphere} = 1$ μm, FluoresBrite, Polysciences Inc) was added and the solution stirred.

The beakers were left in the climate-controlled room for four weeks to allow evaporite structures to form. Three samples of evaporite from each evaporite structure were prepared by breaking pieces of the evaporite off from different points on the structure. The mass of each sample was measured using an analytical balance (SI-64, Denver Instruments). Each sample was dissolved in a measured quantity of DI water, added gradually via pipette ((20-200 $\pm$ 2) μL, P200, Gilson). The resultant brine volume was measured. An aliquot of 10 μL was loaded into a hemocytometer (Neubauer Bright Line, Blau Brand) using a pipette ((2-20 $\pm$ 0.1) μL, P20, Gilson) and the fluorescent microspheres counted using the fluorescence microscope apparatus outlined in Chapter 3 and Figure 3.2. Counts were performed on each of the four 1x1 mm hemocytometer squares. This was repeated for two more aliquots. Before use and between each sample the hemocytometer and glass cover slip were cleaned using 70% ethanol and kimwipes to prevent contamination between samples. Each experiment was performed in triplicate and with a control to which no microspheres were added.

Icelandic basalt [172] was used to investigate the effect of the presence of porous rock on the formation of creeping evaporites and their ability to transport micron-sized objects. To a petri dish (diameter $\varnothing_{sphere} = 90$ mm), 40 mL of a 1:1 binary mixture of $MgSO_4$ & Na_2SO_4 was added. A volume of 88 μL (resulting in $\sim 10^8$ spheres per mL of brine) of fluorescent microsphere solution was added and the solution stirred. One rock was partially submerged in the mixture. The

petri dish was left in the climate controlled room and the formation of evaporite structures observed. Three samples of evaporite from each evaporite structure were prepared by breaking pieces off from different points on the structures that formed on the rock. Each sample was prepared as above and microsphere counts performed. Each experiment was repeated in triplicate and with a control to which no microspheres were added. The rocks were split open using a hammer and chisel. Samples of crystallised salt were scraped from the rock interior onto a glass slide and viewed under the fluorescence microscope to determine whether microspheres were present in the rock interior. Samples were taken from the central region of the newly exposed rock interior to minimise the potential for contamination from the splitting process. It was not possible to procure enough salt from within the rock to perform counts using the hemocytometer.

The number of microspheres per mass of salt sampled ρ [ms g^{-1}] was calculated using

$$\rho = \frac{n_{spheres}}{V_h} \frac{V_r}{m_s} \tag{4.3}$$

where $n_{spheres}$ is the number of spheres counted in one of the hemocytometer squares, V_h is the volume [mL] of one hemocytometer square (d = 0.1 mm, l = 1 mm, $V_h = 1 \times 10^{-4}$ mL), V_r [mL] is the resultant volume of the sample of salt and the water used to dissolve it, m_s [g] is the mass of the salt sample taken from a creeping structure. Each triplicate experiment had three samples of the creeping structure taken. Each sample had three hemocytometer counts performed, involving a count from each of the 4 hemocytometer squares. This resulted in 12 counts per sample and 36 counts per triplicate. The overall mean microsphere densities and associated uncertainties for each substrate were calculated using Equation 3.1 and Equation 3.2 respectively.

4.4 Results

4.4.1 Preliminary Experiment: The Morphology of Evaporites Formed From Martian Brines

The resultant evaporite morphologies broadly fell into three categories that we defined as: crusting, creeping, and a combination of both. Crusting evaporites form a solid crust at the liquid-gas interface. Creeping evaporites fell into two sub-categories; primary and secondary. Primary creeping occurs when crystals form directly on the receptacle surface and advance up the receptacle wall. Secondary creeping structures form when crystals precipitate on previously formed crystals causing growth away from the receptacle wall, creating cloud-like or dendritic structures. Table 4.2 summarises the most persistent evaporite structures for each pure and mixed brine.

Pure Brines

Crusts Crusts form when crystals precipitate at the liquid-gas interface. A full or partial crust can form. Saturated $MgSO_4$ brine formed a solid, translucent crust at the liquid-gas interface within a few hours of preparation. Figure 4.8a shows the crust on the day it formed - a few hours after the experiment initiated. This crust persisted, maintaining the liquid solution at approximately 80 mL for 2 months. Over the following 10 months, the crust thickened and the bulk solution reduced from ∼80 mL to ∼50 mL.

For Na_2SO_4, a thick but incomplete crust (Figure 4.8b) formed within three days of preparation, allowing evaporation to continue until only dry, friable evaporite remained.

Creeping Structures The $MgCl_2$ brine formed a distinctive cloud-like secondary creeping structure at ∼4 months after preparation. Figure 4.9 shows the structure, which persisted for the remaining experimental period except when some deliquescence occurred in the final month, slightly dissolving the structure. The formation of the structure completely depleted the bulk volume of the brine.

Crusts & Creeping Structures The $Mg(ClO_4)_2$ brine formed a primary creep up the beaker wall at ∼2 months after preparation. Over one night, the creep advanced over the top of the beaker and onto the bench-top and an interfacial crust formed as shown in Figure 4.10. The experiment was disposed of at this stage.

Binary Mixtures

The results from the preliminary binary mixtures suggest that in most cases, when two brines are mixed together, the resultant evaporite morphology is a combination of the evaporite morphologies that form from the constituent brines. The exception to this was sulphate-sulphate mixture of $MgSO_4$ & Na_2SO_4 which formed an extensive, dendritic secondary creeping structure.

Creeping Structures For the $MgSO_4$ & Na_2SO_4 mixture, within a week of preparation, evaporation and subsequent crystal precipitation took place in the solution and an extended, dendritic creep structure formed, advancing to the top of the beaker. Evaporation and creeping continued until 14 days after preparation when the solution was completely depleted and only the solid extended creep evaporite structure remained as shown in Figure 4.11. The structure was stable and did not alter during the remainder of 12-month experiment. This was the only evaporite that deviated significantly from the evaporites produced by its constituent brines. As pure brines, both $MgSO_4$ and Na_2SO_4 produced interfacial surface crust evaporites.

Crusts & Creeping Structures The $MgCl_2$ & $Mg(ClO_4)_2$ brine formed a crust and a creeping structure that advanced over the top of the beaker. The creeping structure continued to grow over the course of ∼4 months, completely depleting the sub-crust solution. Figure 4.12a shows the combined structure when the creeping structure was at its most extensive and the bulk solution was fully depleted. The creeping component is similar in morphology to that produced by pure $MgCl_2$.

For $MgCl_2$ & $MgSO_4$ a crust and creeping structure formed ∼3 months after preparation (Figure 4.12b). The structure continued to grow until the bulk solution beneath the crust was depleted. The creeping structure morphology

Table 4.2: Results of Preliminary Evaporite Experiment: Evaporite Structures Formed From Each Pure and Mixed Brine. The possible evaporite morphologies are Crust, Creep and Crust & Creep (CC). Gold cells highlight evaporite structures that did not reflect the structures formed by either of their constituent brines. Each result cell shows the most persistent evaporite morphology observed for that brine or mixture. For example cell [$MgCl_2$,$MgCl_2$] is the evaporite formed from pure $MgCl_2$ solution and cell [$MgCl_2$,$Mg(ClO_4)_2$] is the evaporite formed from a mixture of $MgCl_2$ & $Mg(ClO_4)_2$.

	$MgCl_2$	$Mg(ClO_4)_2$	$MgSO_4$	Na_2SO_4
$MgCl_2$	Creep			
$Mg(ClO_4)_2$	CC	CC		
$MgSO_4$	CC	CC	Crust	
Na_2SO_4	CC	CC	Creep	Crust

was cloudy and similar to the structures formed by pure $MgCl_2$ brine.

For $MgCl_2$ & Na_2SO_4, a thick crust formed rapidly at the liquid gas interface and persisted for three weeks, preventing evaporation. The crust deliquesced or broke, allowing evaporation to occur and primary creeping and some secondary creeping took place (Figure 4.12c shows the evaporite structures at 6 months after preparation). The crust reformed, preserving ∼30 mL of solution for several months until further secondary creeping occurred, depleting the sub-crust solution completely by the end of the 1 year experiment.

For $Mg(ClO_4)_2$ & $MgSO_4$, ∼2 weeks after preparation an interfacial crust and surface creep formed. Figure 4.12d shows the evaporite structures at ∼3 months after preparation. The crust maintained the bulk solution at ∼45 mL for the remaining 11 months of the experiment.

After ∼7 days of evaporation the $Mg(ClO_4)_2$ & Na_2SO_4 mixture began forming a primary creep. Creeping continued for another ∼14 days when a crust formed as shown in Figure 4.12e. Creeping continued until the solution was completely depleted, leaving a crust, surface creep and slightly extended secondary creep structures.

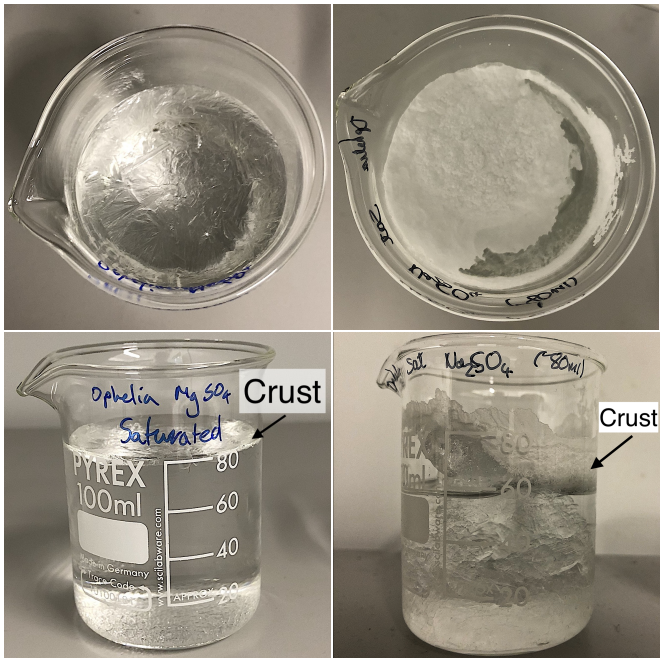

(a) $MgSO_4$ **(b)** Na_2SO_4

Figure 4.8: Results of Preliminary Evaporite Experiment: Photographs of Pure Brines That Formed Interfacial Crust Evaporites. Salt crystals precipitate on the liquid surface, forming a solid crust. The images were taken soon after the formation of their respective crusts (a few hours and ∼3 days after preparation for $MgSO_4$ and Na_2SO_4 respectively). Notably, both are sulphate brines.

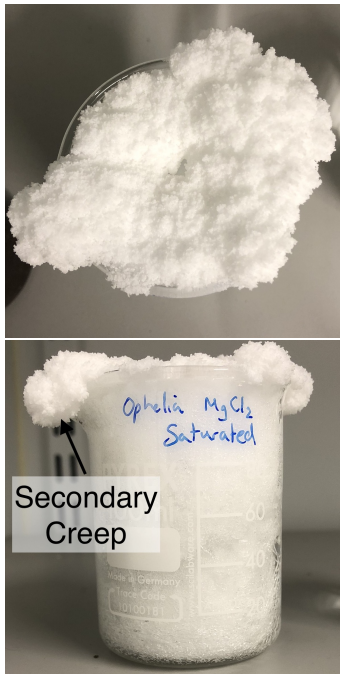

Figure 4.9: Results of Preliminary Evaporite Experiment: Photographs of a Pure Brine That Formed a Creeping Evaporite Structures. Saturated $MgCl_2$ brine formed an efflorescent secondary creeping structure. The image was taken soon after the structure formed (∼4 months after preparation).

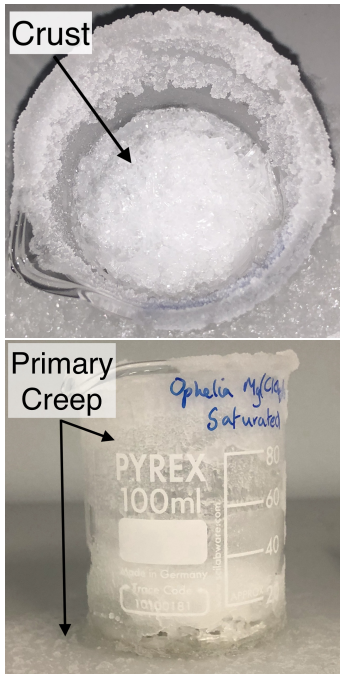

Figure 4.10: Results of Preliminary Evaporite Experiment: Photographs of a Pure Brine That Formed both a Crust and Creeping Evaporites. Saturated $Mg(ClO_4)_2$ brine formed both an interfacial crust and primary creeping evaporites. The image was taken within a day of the crust formation (∼2 months after preparation).

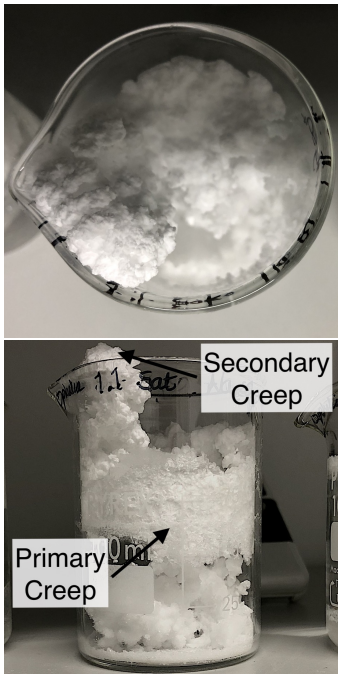

Figure 4.11: Results of Preliminary Evaporite Experiment: Photographs of a Mixed Brine That Formed Creeping Evaporites. $MgSO_4$ & Na_2SO_4 formed a distinctive secondary creeping evaporite. The images were taken soon after the formation of the structure (∼14 days after preparation).

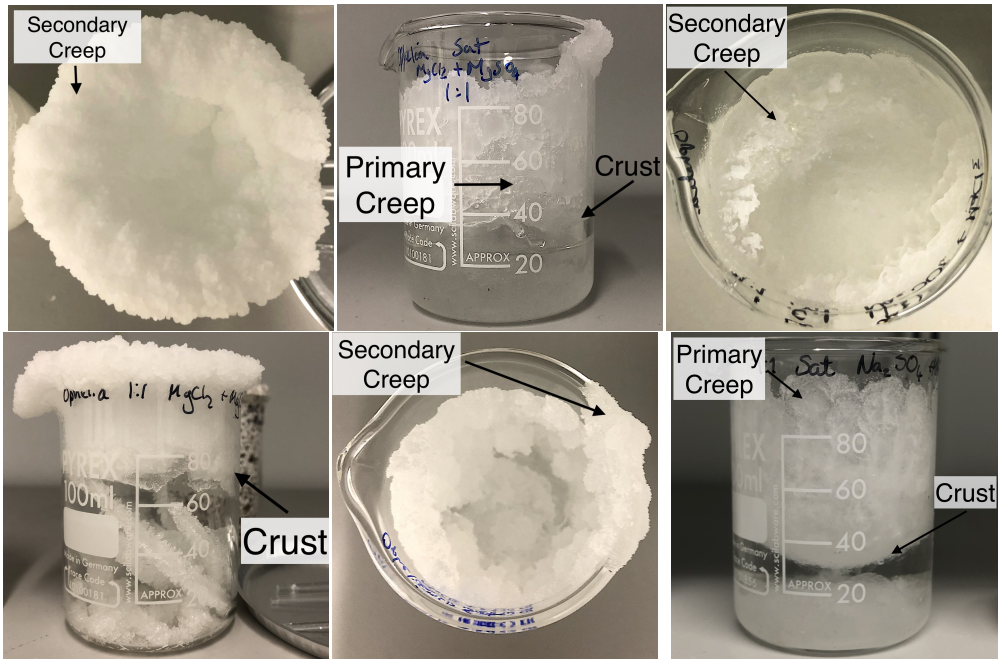

(a) $MgCl_2$ & $Mg(ClO_4)_2$ **(b)** $MgCl_2$ & $MgSO_4$ **(c)** $MgCl_2$ & Na_2SO_4

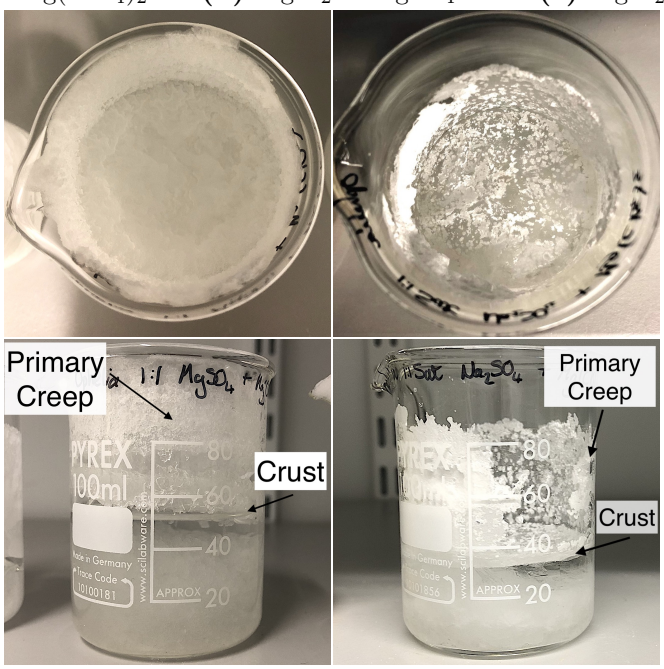

(d) $Mg(ClO_4)_2$ & $MgSO_4$ **(e)** $Mg(ClO_4)_2$ & Na_2SO_4

Figure 4.12: Results of Preliminary Evaporite Experiment: Photographs of Mixed Brines That Formed Both Crusts and Creeping Evaporites. Each mixture formed evaporites that reflected the evaporites formed by their constituent pure brines.

4.4.2 Main Experiment: The Morphology of Evaporites Formed From Martian Brines

As in the preliminary experiments, the resultant evaporite morphologies broadly fell into three categories that we defined as: crusting, creeping, and a combination of both. Table 4.3 summarises the most prevalent and persistent evaporite structures for each pure and mixed brine. Figure 4.13 compares the overall mean mass and bulk volume over time of brines that formed a particularly clear example of an evaporite structure from each category.

Overall mean refers to the the rate calculated by taking the mean mass across the samples at each time point then calculating the mass loss rate. This is usually calculated using all three triplicate samples. If the behaviour of one of the samples deviated significantly from the others, it was not included in the calculation of the mean mass loss rate.

Pure Brines - No Evaporite Macrostructure Formation

For three pure brines, no evaporite macrostructure formed. These were all Ca-brines. The two highly deliquescent Ca- brines - $CaCl_2$ and $Ca(ClO_4)_2$ - did not evaporate sufficiently for crystal precipitation to occur.

$CaCl_2$ The solution deliquesced and evaporated over time causing fluctuations in the mass and volume of the solution (Figure A.1a). The solution is so hygroscopic under the experimental conditions that it did not evaporate sufficiently to produce any evaporite structures (Figure A.2a).

$Ca(ClO_4)_2$ Similar to $CaCl_2$, the $Ca(ClO_4)_2$ solution deliquesced and evaporated over time causing fluctuations in the mass and volume of the solution (Figure A.1b). The solution is so hygroscopic under the experimental conditions that it did not evaporate sufficiently to produce any evaporite structures by the end of the 11 month experimental period (Figure A.2b).

$CaSO_4$ The three $CaSO_4$ brine samples evaporated at an overall mean rate of (1.85 ± 0.06) g day^{-1} over 21 days until no solution remained (Figure A.1c).

The resultant evaporites were granular crystals that had not organised into a macrostructure (Figure A.2c).

Pure Brines - Crusts

Of the three pure brines - all of which were sulphate brines - that formed only interfacial crusts, $FeSO_4$ and $MgSO_4$ crusts were effective at inhibiting evaporation. The $MgSO_4$ crust was the most effective, preserving ∼30 mL of the original 40 mL of brine over 11 months.

$FeSO_4$ Triplicates T1 and T2 evaporated at an overall mean rate of (1.06 ± 0.05) g day^{-1} forming partial crusts over 14 days (these crusts were delicate and were sometimes disrupted or broken in the process of taking volume and mass measurements, affecting the mass loss rate from the solution). Subsequently, the overall mean mass loss rate reduced to (5.39 ± 0.02)×10^{-2} g day^{-1} for the following 202 days until the solution evaporated completely and the evaporites dehydrated (Figure 4.14a and Figure A.3). Triplicate T3 formed a crust over 7 days, significantly reducing the mass loss rate from the sub-crust solution compared to the T1 and T2 with partial crusts. Figure 4.15a shows the crust of sample T3 at 7 days after preparation. The mass loss rate over the first 7 days was (0.76 ± 0.08) g day^{-1}, reducing to (8.14 ± 0.02)×10^{-2} g day^{-1} for the remaining 11 months. None of the samples had any solution remaining beneath the crust after 11 months.

$MgSO_4$ The three $MgSO_4$ brine samples evaporated at an overall mean rate of (2.09 ± 0.77) g day^{-1} until they formed a complete crust at the liquid-gas interface within one day, reducing the rate by 108 times to (1.94 ± 0.06)×10^{-2} g day^{-1} for the remaining 11 months. Figure 4.15b shows the crust of sample T2 1 day after preparation. This crusts persisted for the duration of the experiment, inhibiting evaporation from the solution. Over the 11 month experimental duration a mean mass of 10 g of water was lost from each solution, leaving ∼30 mL of solution beneath each crust at the experiment end (Figure 4.14b and Figure A.4).

Na_2SO_4 For each of the three Na_2SO_4 samples, a partial crust formed at the liquid-gas interface within 7-14 days (Figure 4.15c andA.5). In each case it was not a full, continuous crust and evaporation continued until all the water contained

in the solution had evaporated. Figure 4.14c shows the crust of sample T1 at 14 days after preparation. The water in the bulk solution evaporated within 14 days at an overall mean rate of (1.41 ± 0.08) g day^{-1}. The interstitial solution (solution held between crystals by capillary forces) evaporated and salts became dehydrated at an overall mean rate of (0.24 ± 0.01) g day^{-1} within the following 49 days. For T1, after 49 days, salt creep from adjacent beakers of $NaClO_4$ climbed up the beaker, affecting the mass readings.

Pure Brines - Creeping Structures

$MgCl_2$ Each of the three $MgCl_2$ samples bulk volume remained constant for 14 days after initially deliquescing for 7 days (Figure 4.16a). Evaporation then occurred at an overall mean rate of (0.39 ± 0.02) g day^{-1} for 28 days and an extensive efflorescent creeping structure formed. The mass loss rate reduced to (5.96 ± 0.15)×10^{-2} g day^{-1} for the following 60 days. The structure of this formation was efflorescent and cloud-like in appearance and extended from the walls of the beaker into the centre as well as creeping directly upwards from crystals formed in the body of the brine. Figure 4.17a shows the creeping structure soon after it formed, at 49 days after preparation. Some deliquescence occurred at 150-226 days after preparation, partially dissolving the creeping structure and replenishing bulk solution. Subsequent evaporation reformed the efflorescent creeping structure (Figure A.6).

NaCl For NaCl samples T1 and T2 the solution evaporated at an overall mean rate of (1.20 ± 0.04) g day^{-1} for 28 days until fully depleted. Creeping structures began forming within 1 day after preparation and growth continued until the solution was fully depleted (Figure 4.16b). Primary creeping occurred up the beaker wall and over the beaker lip. A small dendritic efflorescent creeping structure formed from the centre of the beaker base (Figure 4.17b). For T3, after 28 days, salt creep from adjacent beakers of $NaClO_4$ climbed up the beaker, affecting the mass readings.

Pure Brines - Crusts & Creeping Structures

$Mg(ClO_4)_2$ Initially, the $Mg(ClO_4)_2$ samples deliquesced before sufficient evaporation occurred at an overall mean rate of (0.18 ± 0.02) g day^{-1} over 21 days.

At around 21 days an interfacial crust and a primary creep formed simultaneously (Figure 4.19a). The solutions evaporated at an overall mean rate of (2.97 $\pm$ 0.32)$\times 10^{-2}$ g day^{-1} over the next 127 days. Subsequently, more creeping occurred, completely depleting the sub-crust solution (Figure 4.18a) and resulting in a more extensive, efflorescent secondary creeping structure forming (Figure A.8). The creeping structure incorporated ink particles from the label on the beaker, tinting sections of the structure red (Figure A.8).

$NaClO_4$ Over the first 7 days the mass and bulk volume of all three $NaClO_4$ samples solution did not change significantly. For samples T2 and T3 evaporation occurred at an overall mean rate of (0.36 $\pm$ 0.03) g day^{-1} for the following 21 days (Figure 4.18b) until an interfacial crust and primary creep formed simultaneously (Figure 4.19b and Figure A.9). The crust was not effective at preventing mass loss of water from the system and the evaporation continued at a rate of (0.33 $\pm$ 0.01) g day^{-1} for 56 days. After this the crust maintained a bulk volume of $\sim$10 mL beneath the crust. At the end of the experiment, investigating beneath the crust showed that most of the bulk volume was precipitated salt but there was some liquid solution remaining. Sample T1 behaved similarly, evaporating at a rate of (0.47 $\pm$ 0.03) g day^{-1} for 28 days until the crust and creeping structures began to form. However, the mass loss rate increased to (0.70 $\pm$ 0.02) g day^{-1} for the following 35 days until the bulk solution was completely depleted. The salt creep was very extensive for all three samples, creeping over the top of the beaker, down the side, over the bench surface and up and into adjacent beakers.

Water Control

The three samples of 40 mL of water evaporated at an overall mean rate of (3.09 $\pm$ 0.14) g day^{-1} over 13 days until fully evaporated.

Table 4.3: Main Evaporite Experiment Results: Evaporite Structures Formed From Each Pure and Mixed Brine. The possible evaporites are Crust, Creep and Crust & Creep (CC). Gold cells highlight evaporite structures formed from mixed brines that did not reflect the structures formed by either of their constituent brines. Each result cell shows the most persistent evaporite morphology observed for that brine or mixture. For example cell [$CaCl_2$,$CaCl_2$] is the evaporite formed from pure $CaCl_2$ solution and cell [$CaCl_2$,$Ca(ClO_4)_2$] is the evaporite formed from a mixture of $CaCl_2$ & $Ca(ClO_4)_2$.

	$CaCl_2$	$Ca(ClO_4)_2$	$CaSO_4$	$FeSO_4$	$MgCl_2$	$Mg(ClO_4)_2$	$MgSO_4$	NaCl	$NaClO_4$	Na_2SO_4
$CaCl_2$	-									
$Ca(ClO_4)_2$	-	-								
$CaSO_4$	-	-	-							
$FeSO_4$	Crust	Crust	Crust	Crust						
$MgCl_2$	-	-	Creep	Crust	Creep					
$Mg(ClO_4)_2$	-	-	CC	CC	CC	CC				
$MgSO_4$	Crust	CC	Crust	Crust	CC	CC	Crust			
NaCl	-	-	Creep	CC	Creep	CC	CC	Creep		
$NaClO_4$	-	-	CC	CC	CC	CC	CC	CC	CC	
Na_2SO_4	Crust	Crust	Crust	Creep	CC	CC	Creep	Creep	CC	Crust

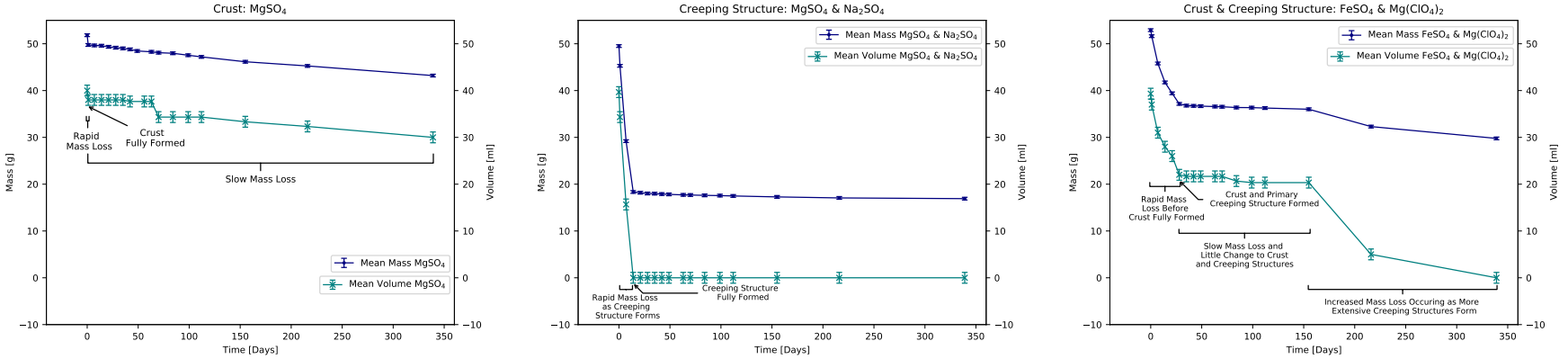

(a) Crust **(b)** Creeping Structure **(c)** Crust & Creeping Structure

Figure 4.13: Main Evaporite Experiment Results: Overall Mean Mass and Bulk Volume of Brines That Formed a Particularly Clear Example of an Evaporite Structure From Each Category. (a) The crusting brine, $MgSO_4$, briefly evaporated rapidly until a crust formed, after which evaporation occurred very slowly, preserving the sub-crust brine. (b) The creeping brine ($MgSO_4$ & Na_2SO_4) evaporated rapidly as the creeping structure formed until the brine was fully depleted. (c) The crusting and creeping brine ($FeSO_4$ & $Mg(ClO_4)_2$) evaporated relatively rapidly until a crust and primary creeping structure formed, after which evaporation occurred slowly, preserving the sub-crust brine. When the creeping structure began to form more extensively the mass loss rate increased, continuing until the brine was fully depleted.

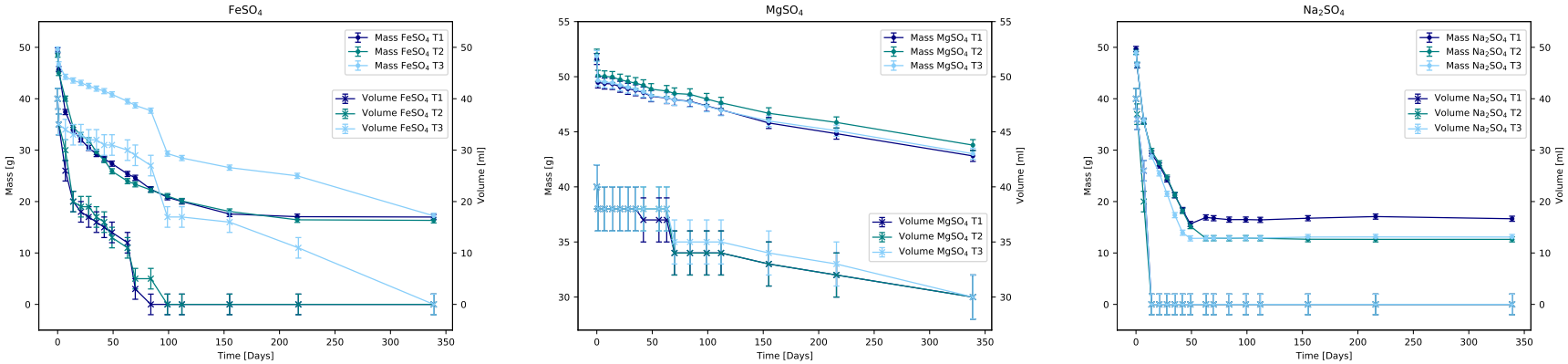

(a) $FeSO_4$ **(b)** $MgSO_4$ **(c)** Na_2SO_4

Figure 4.14: Main Evaporite Experiment Results: Mass and Bulk Volume of Pure Brines That Formed Interfacial Crusts. Bulk volume refers to the volume of liquid brine and any precipitated salt within the body of the brine. T1-T3 are the labels for each experiment in the set of triplicates.

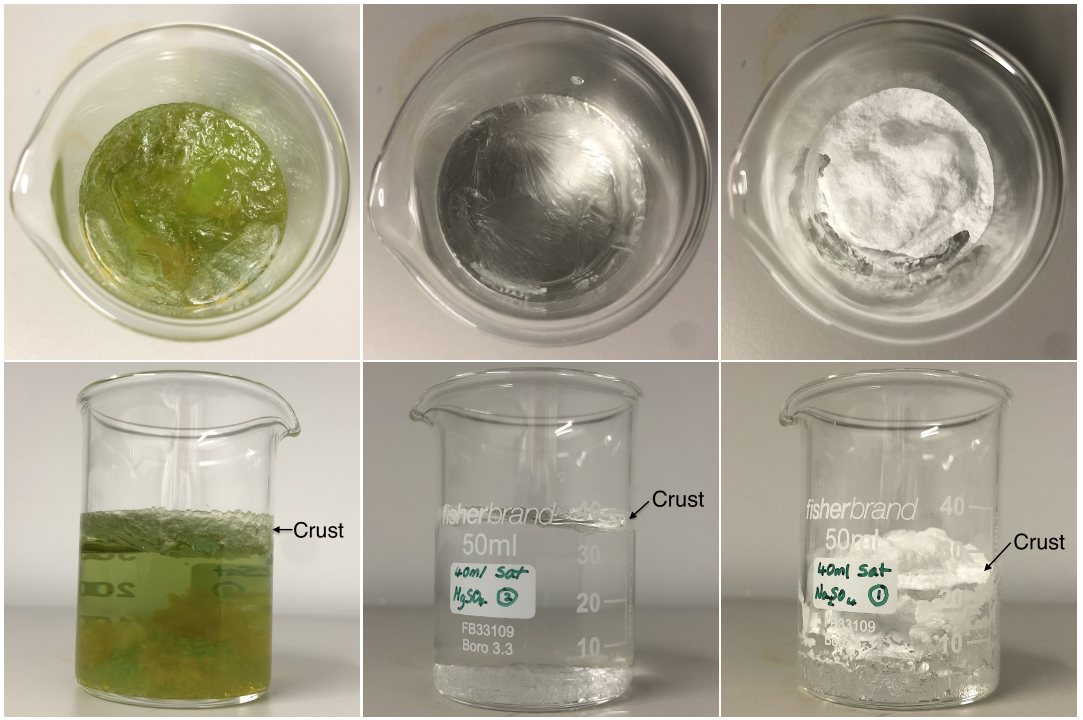

(a) $FeSO_4$ **(b)** $MgSO_4$ **(c)** Na_2SO_4

Figure 4.15: Main Evaporite Experiment Results: Photographs of Pure Brines That Formed Interfacial Crusts. The figures show one example of each brine soon after crust formation.

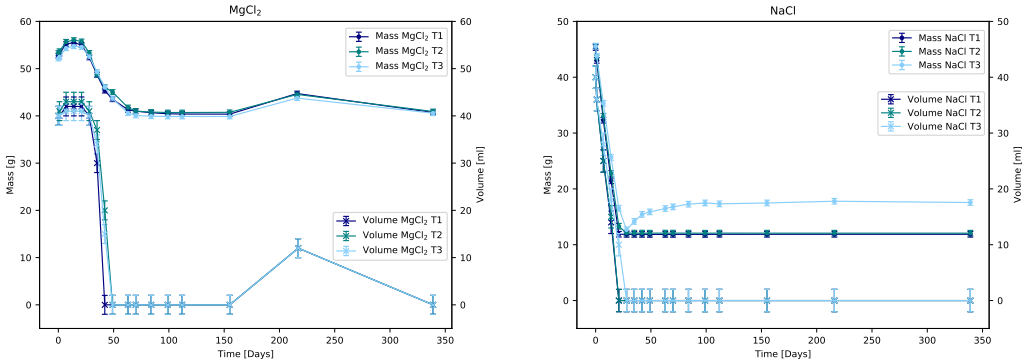

(a) $MgCl_2$ **(b)** NaCl

Figure 4.16: Main Evaporite Experiment Results: Mass and Bulk Volume of Pure Brines That Formed Creeping Evaporites. Bulk volume refers to the volume of liquid brine and any precipitated salt within the body of the brine. T1-T3 are the labels for each experiment in the set of triplicates.

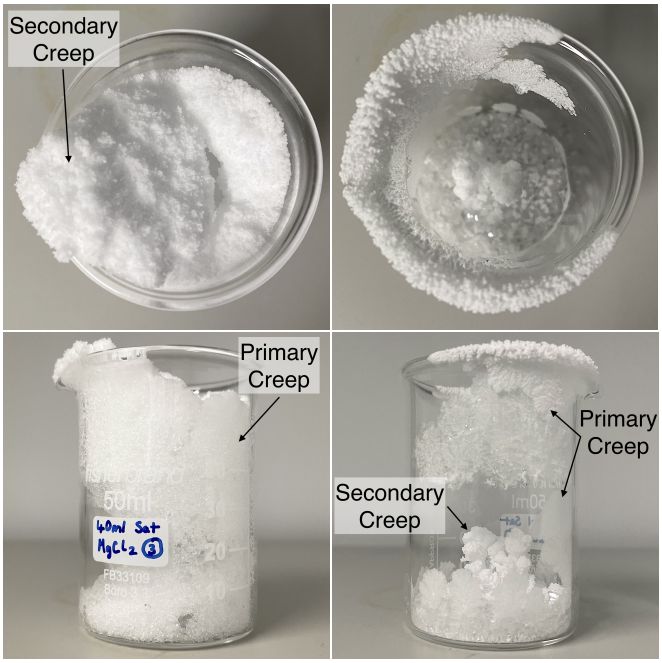

(a) $MgCl_2$ **(b)** NaCl

Figure 4.17: Main Evaporite Experiment Results: Photographs of Pure Brines That Formed Creeping Evaporites. The figures show one example of each brine soon after the creeping structure formed.

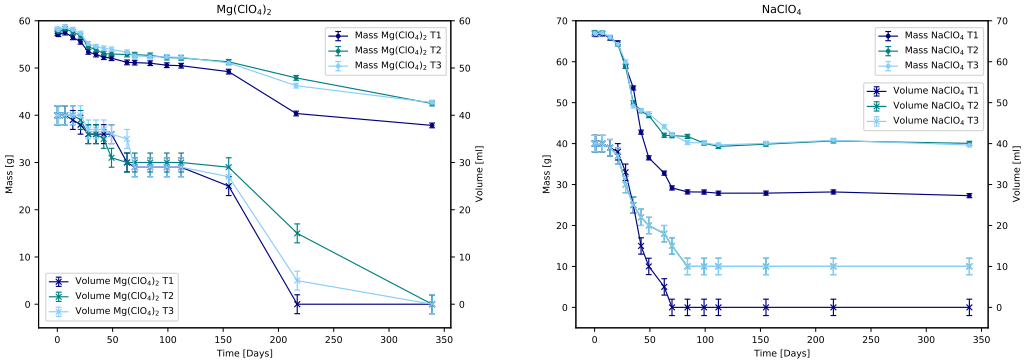

(a) $Mg(ClO_4)_2$ **(b)** $NaClO_4$

Figure 4.18: Main Evaporite Experiment Results: Mass and Bulk Volume of Pure Brines That Formed Both Crusts and Creeping Evaporites. Bulk volume refers to the volume of liquid brine and any precipitated salt within the body of the brine. T1-T3 are the labels for each experiment in the set of triplicates.

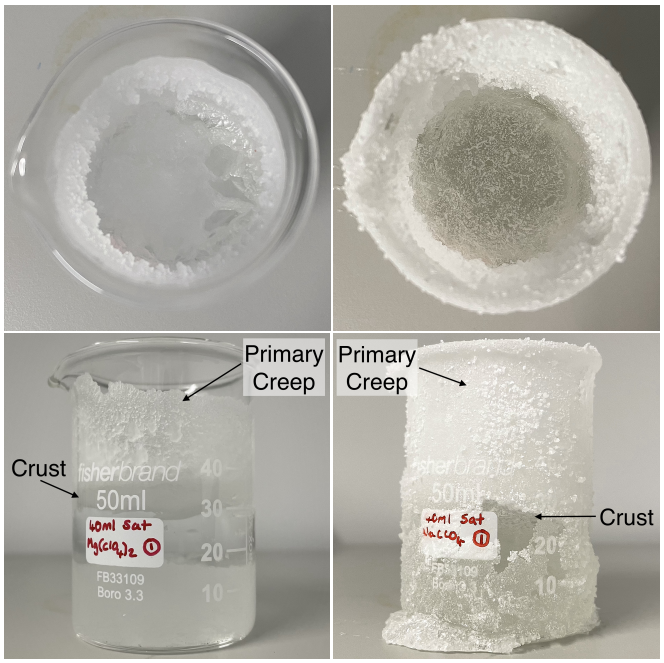

(a) $Mg(ClO_4)_2$ **(b)** $NaClO_4$

Figure 4.19: Main Evaporite Experiment Results: Photographs of Pure Brines That Formed Both Crusts and Creeping Evaporites. The figures show one example of each brine soon after the formation of the structures.

Binary Mixtures - No Evaporite Macrostructure Formation

Eleven of the binary mixtures did not form evaporite macrostructures. They did not evaporate sufficiently within the 11 month experimental period for precipitation to occur. They are summarised in Table 4.3, indicated with a dash. Each mixture contained $CaCl_2$, $Ca(ClO_4)_2$, or both. The only binary mixtures that contained either $CaCl_2$ or $Ca(ClO_4)_2$ that did form evaporites had a highly soluble sulphate brine as the second brine in the mixture. These are described in more detail in the proceeding sections.

Binary Mixtures - Crusts

Ten of the binary brines produced interfacial crust evaporite structures. Every one of the mixtures contained at least one highly soluble sulphate salt ($FeSO_4$, $MgSO_4$ or Na_2SO_4). When the mixture contained highly soluble calcium salts ($CaCl_2$ and $Ca(ClO_4)_2$), precipitates within the bulk volume of the solution formed immediately upon preparation and crusts formed later after sufficient evaporation occurred. When highly soluble sulphate brines were mixed with highly insoluble $CaSO_4$ brine, the crusts formed after approximately half of the solution evaporated, suggesting that the $CaSO_4$ does not interact with the other sulphate brines in any significant way with respect to the formation of evaporite macrostructures and that sufficient evaporation has to occur to bring the brines to saturation before the crusts form as they do for the pure highly-soluble sulphate brine. The evaporite formed by the $FeSO_4$ & $MgCl_2$ brine did not exhibit the distinctive efflorescent structures associated with pure $MgCl_2$ brine. Those mixtures containing hygroscopic salts displayed deliquescence, with liquid droplets forming on top of the crusts, likely caused by a weather-induced spike in humidity.

Overall mean refers to the the rate calculated by taking the mean mass across the samples at each time point then calculating the mass loss rate. This is usually calculated using all three triplicate samples. If the behaviour of one of the samples deviated significantly from the others, or its mass was affected by adjacent creeping evaporite formations, it was not included in the calculation of the mean mass loss rate.

$CaCl_2$ & $FeSO_4$ The three samples evaporated at an overall mean rate of (0.31 $\pm$ 0.01) g day^{-1} over 63 days during which time a filmy crust formed and gradually thickened. Figure 4.21a shows the filmy crust soon after it formed, at 28 days after preparation. The rate reduced the rate to (2.46 $\pm$ 0.09)$\times 10^2$ g day^{-1} for the following 49 days (Figure 4.20a). Subsequently, some deliquescence occurred, forming droplets on top of the crust. At the end of the experiment, $\sim$20 mL of bulk solution remained beneath the crust (Figure A.10). Investigation of the sub-crust revealed there was some aqueous solution still present, but much of the bulk was precipitated salt.

$CaCl_2$ & $MgSO_4$ The three samples evaporated at an overall mean rate of (0.47 $\pm$ 0.02) g day^{-1} for 21 days during which time an interfacial crust formed (Figure 4.21b). The was not effective at maintaining bulk solution, which evaporated within this time-frame (Figure 4.20b). Mass loss from the system continued, likely interstitial solution evaporating from between precipitated crystals and the salts themselves dehydrating. Some deliquescence subsequently occurred, replenishing the sub-crust solution. Mixing $MgSO_4$ - which as a pure solution forms a crust highly effective at inhibiting evaporation - with $CaCl_2$ appears to decrease this efficacy even though a crust does form.

$CaCl_2$ & Na_2SO_4 $CaCl_2$ & Na_2SO_4 samples T1 and T2 evaporated at a mean rate of (0.73 $\pm$ 0.04) g day^{-1} for 14 days (4.20c). A crust formed at $\sim$14 days after preparation after which the mass loss rate reduced by 79 times to (9.28 $\pm$ 0.25)$\times 10^{-3}$ g day^{-1} for the remaining 10 months. At the experiment end $\sim$27 mL of bulk solution remained beneath the crusts. Sample T3 evaporated at a rate of (0.70 $\pm$ 0.02) g day^{-1} for 21 days, reducing by 96 times to (7.28 $\pm$ 0.36)$\times 10^{-3}$ g day^{-1} for the remaining 10 months of the experiment. Sample T3 formed a crust (Figure 4.21c) at $\sim$14 days after preparation. At the experiment end $\sim$24 mL of bulk solution remained beneath the crust (Figure A.12). In all three cases, much of the volume of the bulk solution consisted of precipitate but there was some liquid brine present.

$Ca(ClO_4)_2$ & $FeSO_4$ Samples T1 and T3 evaporated at a mean rate of (0.36 $\pm$ 0.01) g day^{-1} for 35 days until an interfacial crust formed (Figure 4.21d). The rate then reduced by 38 times to (9.56 $\pm$ 0.17)$\times 10^{-3}$ g day^{-1} for the remaining 10 months (Figure 4.20d). Sample T2 behaved similarly but with some deliquescence

occurring after 155 days. Each sample contained ∼22 mL of bulk solution beneath the crust at the experiment end (Figure A.13), much of which was precipitate though after breaking the crust at the end of the experiment there was clearly some liquid brine present.

$Ca(ClO_4)_2$ & Na_2SO_4 The three samples evaporated at an overall mean rate of (0.38 ± 0.01) g day^{-1} for 49 days. An interfacial crust formed at ∼49 days (Figure 4.21e). The mass loss rate then reduced to $(8.20 \pm 0.66)\times10^{-3}$ g day^{-1} for the following 63 days (Figure 4.20e). Subsequently, some deliquescence occurred, increasing the volume of the bulk solution. At the end of the experiment, each sample had ∼20 mL of bulk solution beneath the crust (Figure A.14), much of which consisted of precipitate though there was some liquid brine visible.

$CaSO_4$ & $FeSO_4$ The three samples evaporated at an overall mean rate of (1.66 ± 0.08) g day^{-1} for 14 days (Figure 4.20f). An interfacial crust formed at ∼14 days after preparation (Figure 4.21f). The rate then reduced to $(3.46 \pm 0.02)\times10^{-2}$ g day^{-1} for the remaining 10.5 months. At the end of the experiment, samples T1 and T3 were dry with no bulk solution remaining. Sample T2 had a few millilitres of bulk solution remaining (Figure A.15).

$CaSO_4$ & $MgSO_4$ The three samples evaporated at a mean rate of (1.51 ± 0.08) g day^{-1} for 14 days until a full crust formed, after which the mass loss rate reduced by 88 times to $(2.06 \pm 0.02)\times10^{-2}$ g day^{-1} for the remaining 10.5 months (Figure 4.20g). Figure 4.21g is the crust formed by sample T1 soon after formation. At the end of the 11-month experiment, ∼8 mL of bulk solution remained beneath each crust (Figure A.16).

$CaSO_4$ & Na_2SO_4 For triplicate T2 and T3, evaporation occurred at an overall mean rate of (1.83 ± 0.06) g day^{-1} over 14 days, until a partial crust formed (Figure 4.20h) after which the mass loss rate reduced to (0.50 ± 0.05) g day^{-1} for 7 days until the bulk solution was completely depleted. Figure 4.21h shows the crust of sample T2 at 14 days after preparation, soon after formation. The mass loss continued for 42 days at a rate of (0.19 ± 0.01) g day^{-1} as the interstitial brine evaporated and evaporite crystals dehydrated. No change occurred from that time to the experiment end (Figure A.17). Triplicate T1 evaporated at (1.83

$\pm$ 0.06) g day^{-1} over 21 days with a primary creep forming, creeping up and over the top of the beaker. Some secondary creeping also occurred.

$FeSO_4$ & $MgCl_2$ In contrast to other solutions mixed with $MgCl_2$, an efflorescent secondary creep did not form. A crust formed after 28 days (Figure 4.21i). The crust was filmy and was not completely contiguous. The crust became thicker and more contiguous with evaporation reducing as this occurred (Figure 4.20i). The mean mass loss rate for the first 63 days was (0.32 $\pm$ 0.01) g day^{-1}, reducing to (8.88 $\pm$ 0.45)$\times 10^{-3}$ g day^{-1} after the crust became substantial until deliquescence occurred. After 155 days some deliquescence occurred, with droplets of brine forming on the crust surface (Figure A.18). After 11 months there was $\sim$16 mL of bulk solution remaining beneath each crust.

$FeSO_4$ & $MgSO_4$ For samples T2 and T3, evaporation occurred over 7 days at a mean rate of (0.96 $\pm$ 0.05) g day^{-1} until an interfacial crust formed, slowing the rate of mass loss to (3.75 $\pm$ 0.02)$\times 10^{-2}$ g day^{-1} (Figure 4.20j). For sample T1, the crust formed after 14 days of evaporation. Figure 4.21j shows the crust formed by T2 soon after formation. The crust inhibited evaporation effectively but in the case of T1 the bulk solution evaporated completely within 202 days after crust formation. T2 and T3 still had $\sim$15 mL of bulk solution beneath the crust at the end of the 11 month experiment (Figure A.19).

Binary Mixtures - Creeping Structures

Five of the binary brines produced only creeping structures. Those which had $CaSO_4$ as a constituent brine displayed their typical evaporite structure after sufficient evaporation occurred to bring the binary mixture to saturation. The sulphate-sulphate mixtures of $MgSO_4$ & Na_2SO_4 and $FeSO_4$ & Na_2SO_4 produced distinctive structures that were very different from the evaporite morphologies produced by their constituent brines.

$CaSO_4$ & $MgCl_2$ The three samples evaporated at an overall mean rate of (0.50 $\pm$ 0.01) g day^{-1} for 50 days during which time a cloudy, efflorescent secondary creeping structure formed, depleting the bulk solution (Figure 4.23a and Figure 4.22a). The morphology of the structure was visually similar to the one formed by

pure $MgCl_2$ brine. Some deliquescence took place after 155 days after preparation. The secondary creeping structures later reformed (Figure A.20).

$CaSO_4$ & NaCl The three samples evaporated at an overall mean rate of (1.32 ± 0.03) g day^{-1} for 28 days during which time primary creeping occurred, depleting the bulk solution completely (Figure 4.22b and Figure 4.23b). No further change occurred. The morphology of the structure was visually similar to the one formed by pure NaCl brine except that no almost secondary creeping occurred.

$FeSO_4$ & Na_2SO_4 The three samples evaporated at an overall mean rate of (1.54 ± 0.03) g day^{-1} for 21 days during which time small but distinctive dendritic secondary creeping structures formed (Figure 4.22c and Figure 4.23c). No further mass loss or evaporite growth subsequently occurred. The dendrites were coralloid in shape. Some primary creeping up the side of the beaker also occurred during this time.

$MgCl_2$ & NaCl The three samples evaporated at an overall mean rate of (0.51 ± 0.01) g day^{-1} for 34 days after which time an efflorescent secondary creeping structure formed, depleting the bulk solution (Figure 4.22d and Figure 4.23d). Some deliquescence took place after 155 days after preparation. The secondary creeping structures later reformed (Figure A.21). The morphology of the structure was visually similar to the one formed by pure $MgCl_2$ brine.

$MgSO_4$ & Na_2SO_4 One of the most distinctive morphologies observed in this chapter was the creeping evaporite structure produced by the $MgSO_4$ & Na_2SO_4 brine. Once sufficient evaporation occurred over ∼7 days, creeping initiated and the structure reached its final state within another 7 days (Figure 4.22e and Figure 4.23e). The overall mean mass loss rate during those 14 days was (2.23 ± 0.11) g day^{-1}. Creeping initiated at a few discrete points from which further self-sustaining growth occurred. This is in contrast to creeping perchlorates, which tend to creep over the entire surface of the substrate. The structures did not alter from that point to the end of the experiment.

NaCl & Na_2SO_4 The overall mean rate of mass loss across the three samples was (1.16 ± 0.06) g day^{-1} for the 21 days taken for the evaporites to form and

the bulk solutions to be completely depleted (Figure 4.22f). Primary creeping occurred up and over the beaker lip and down the side of the beaker (Figure 4.23f). The structures did not alter from that point to the end of the experiment. Pure Na_2SO_4 brine formed a partial crust which did not occur here.

Binary Mixtures - Crusts & Creeping Structures

The most common category of structure was the simultaneous appearance of crusts and creeping structures. In most cases the characteristics of the structures were reflections of the evaporite structures formed from the constituent pure brines. Most of the mixtures, despite forming crusts, eventually had all or most of their sub-crust solution depleted by the ongoing formation of creeping structures. This included those mixtures containing $MgSO_4$ which as a pure brine was able to preserve ∼30 mL of solution by the end of the experiment.

$Ca(ClO_4)_2$ & $MgSO_4$ The three samples evaporated at an overall mean rate of (1.34 ± 0.10) g day^{-1} over the first day during which time an interfacial crust formed (Figure 4.24a). The rate subsequently reduced to (3.41 ± 0.01)×10^{-2} g day^{-1} for the remaining 11 months. Some primary creeping occurred at ∼21 days (Figure 4.25a). At the end of the experiment each sample had ∼5 mL of bulk solution remaining beneath the crust (Figure A.23).

$CaSO_4$ & $Mg(ClO_4)_2$ The three samples evaporated at an overall mean rate of (0.76 ± 0.01) g day^{-1} for 28 days until a crust and primary creep formed (Figure 4.25b) after which the rate decreased to (1.93 ± 0.02)×10^{-2} g day^{-1} for 188 days (Figure 4.24b). For the remaining 123 days the mass loss rate was (1.75 ± 0.03)×10^{-2} g day^{-1}, with some secondary creeping occurring, depleting the sub-crust solution. At the end of the 11 month experiment, there was no bulk solution remaining beneath the crust of any of the three samples (Figure A.24).

$CaSO_4$ & $NaClO_4$ The three samples evaporated at an overall mean rate of (0.64 ± 0.01) g day^{-1} for 35 days (Figure 4.24c). A crust and primary creep formed at ∼35 days (Figure 4.25c). The rate subsequently reduced to (2.01 ± 0.03)×10^{-2} g day^{-1} for 120 days. Mass loss continued at an overall mean rate of (3.22 ± 0.69)×10^{-3} g day^{-1} for the following 60 days as more extensive primary creep formed until the sub-crust solution was completely depleted. At the end of

the 11 month experiment, there was no bulk solution remaining beneath any of the crusts (Figure A.25).

$FeSO_4$ & $Mg(ClO_4)_2$ The three samples evaporated at an overall mean rate of (0.56 ± 0.01) g day^{-1} (Figure 4.25d) for 28 days. At $\sim$ 28 days after preparation a crust and primary creep formed as shown in Figure 4.25d. Subsequently, the mass loss rate reduced by 62 times to $(8.98 \pm 0.32)\times10^{-3}$ g day^{-1} for 127 days. The rate then increased to $(3.39 \pm 0.02)\times10^{-2}$ g day^{-1} for the remaining 6 months as a more extensive, efflorescent secondary creep formed, depleting the sub-crust solution. At the end of the 11 month experiment, there was no bulk solution remaining beneath any of the crusts (Figure A.26).

$FeSO_4$ & NaCl A primary creep began forming at $\sim$14 days after preparation. The three samples evaporated at an overall mean rate of (1.13 ± 0.01) g day^{-1} for 28 days (Figure 4.24e) when a crust formed as shown in Figure 4.25e. Subsequently the rate reduced by 290 times to $(3.90 \pm 0.13)\times10^{-3}$ g day^{-1} for the remaining 10 months. At the end of the 11 month experiment, there was no bulk solution remaining beneath the crust of any of the three samples (Figure A.27).

$FeSO_4$ & $NaClO_4$ The three samples evaporated at an overall mean rate of (0.58 $\pm$ 0.01) g day^{-1} for 28 days until a crust formed (Figure 4.24f and Figure 4.25f) and reduced the rate to (0.12 ± 0.01) g day^{-1} for 14 days. The rate increased to (0.20 ± 0.01) g day^{-1} as both primary and secondary creeping occurred, depleting the solution beneath the crust. At the end of the 11 month experiment, there was no bulk solution remaining in any of the three samples (Figure A.28).

$MgCl_2$ & $Mg(ClO_4)_2$ For the first 7 days some deliquescence occurred. For the following 42 days, the solutions evaporated at an overall mean rate of (0.20 ± 0.01) g day^{-1} until an interfacial crust formed (Figure 4.24g and Figure 4.25g). The rate reduced to $(7.67 \pm 0.08)\times10^{-2}$ g day^{-1} for the following 63 days as both primary and some secondary, efflorescent creeping occurred. Subsequently deliquescence and evaporation took place and the evaporite structures dissolved then reformed respectively. At the end of the 11 month experiment, there was $\sim$30 mL of bulk solution beneath each crust (Figure A.29).

$MgCl_2$ & $MgSO_4$ The overall mean mass loss rate across the three samples was (0.35 ± 0.01) g day^{-1} for the first 35 days until a crust formed (Figure 4.24h). The rate subsequently reduced to (0.11 ± 0.01) g day^{-1} for 64 days as an efflorescent secondary creep formed (Figure 4.25h shows the crust and creeping structure at 63 days after preparation). Subsequently deliquescence and evaporation took place and the evaporite structures dissolved then more extensively reformed. At the end of the 11 month experiment, there were a few millilitres of bulk solution remaining beneath each crust (Figure A.30).

$MgCl_2$ & $NaClO_4$ The overall mean mass loss rate across the three samples was (0.21 ± 0.01) g day^{-1} for the first 35 days until a crust and primary creep formed (Figure 4.24i). The rate subsequently reduced to $(6.14 \pm 0.34)\times10^{-3}$ g day^{-1} for 120 days and primary creeping gradually continued (Figure 4.25i shows the crust and primary creep at 122 days after preparation). Subsequently deliquescence and evaporation took place and the evaporite structures dissolved then reformed respectively. At the end of the 11 month experiment there was $\sim$27 mL of bulk solution beneath each crust (Figure A.31).

$MgCl_2$ & Na_2SO_4 The overall mean mass loss rate across the three samples was (0.61 ± 0.01) g day^{-1} for the first 35 days until a crust formed (Figure 4.24j). Subsequently the rate reduced to $(5.01 \pm 0.01)\times10^{-2}$ g day^{-1} for 77 days and some secondary, efflorescent creeping occurred. Figure 4.25j shows the crust and secondary creep at 49 days after preparation. Subsequently deliquescence and evaporation took place and the evaporite structures dissolved then reformed. At the end of the 11 month experiment, there was no bulk solution remaining beneath each crust (Figure A.32).

$Mg(ClO_4)_2$ & $MgSO_4$ The overall mean mass loss rate across the samples T2 and T3 was (0.48 ± 0.01) g day^{-1} for 21 days until a crust formed (Figure 4.24k and Figure 4.25k). For the following 124 days the rate reduced to $(3.45 \pm 0.03)\times10^{-2}$ g day^{-1}. Then some secondary, efflorescent creeping occurred, increasing the mass loss rate slightly to $(3.51 \pm 0.03)\times10^{-2}$ g day^{-1} until the solution was completely depleted (Figure A.33). Sample T1 behaved similarly though its crust formed at $\sim$7 days after preparation.

$Mg(ClO_4)_2$ & NaCl For the first 42 days, the overall mean mass loss rate across the three samples was (0.48 ± 0.01 g day^{-1}) until a crust formed, reducing the rate to (1.06 ± 0.04)$\times 10^{-2}$ g day^{-1} for the following 113 days (Figure 4.24l) during which time some primary creeping took place. Figure 4.25l shows the crust and primary creep of sample T2 at 99 days after preparation. Subsequently deliquescence and evaporation took place and the evaporite structures dissolved then reformed respectively. At the end of the 11 month experiment, there was ∼15 mL bulk solution remaining beneath each crust (Figure A.34).

$Mg(ClO_4)_2$ & $NaClO_4$ The overall mean mass loss rate across the three samples was (0.18 ± 0.01) g day^{-1} for 35 days until a crust and primary creep formed (Figure 4.24m and Figure 4.25m). Subsequently the rate reduced to (3.31 ± 0.04)$\times 10^{-2}$ g day^{-1} for 120 days during which time a primary and secondary, efflorescent creep gradually formed. Subsequently deliquescence and evaporation took place and the evaporite structures dissolved then formed an even more extensive creep, completely depleting the bulk solution by the end of the experiment (Figure A.35). The creeping structure incorporated ink particles from the label on the beaker, tinting sections of the structure red (Figure A.35).

$Mg(ClO_4)_2$ & Na_2SO_4 The overall mean mass loss rate across the three samples was (0.80 ± 0.01) g day^{-1} for 28 days until a crust and primary creep formed (Figure 4.24n). Figure 4.25n shows the crust and primary creep of sample T1 at 35 days after preparation. The rate subsequently reduced to (5.89 ± 0.11)$\times 10^{-2}$ g day^{-1} for 42 days. During this time, some primary creeping and efflorescent secondary creeping occurred, depleting the solution completely (Figure A.36).

$MgSO_4$ & NaCl The overall mean mass loss rate across the three samples was (1.25 ± 0.02) g day^{-1} for 21 days until a crust formed (Figure 4.24o). Subsequently the mass loss rate was (0.13 ± 0.01) g day^{-1} for 14 days as some primary creeping occurred. Figure 4.25o shows the crust and primary creep of sample T1 at 35 days after preparation. No further change took place (Figure A.37).

$MgSO_4$ & $NaClO_4$ The overall mean mass loss rate across the three samples was (1.58 ± 0.07) g day^{-1} over the first day during which time a crust formed (Figure 4.24p). The rate reduced to (0.24 ± 0.01) g day^{-1} for the following 62

days during which time primary creeping began. Figure 4.25p shows the crust and primary creep of sample T1 at 35 days after preparation. The mass loss rate reduced further to $(9.22 \pm 0.11) \times 10^{-2}$ g day^{-1} for 49 days. Subsequently deliquescence and evaporation took place and the evaporite structures dissolved then formed an even more extensive secondary creep, completely depleting the bulk solution by the end of the experiment (Figure A.38).

NaCl & $NaClO_4$ The overall mean mass loss rate across the three samples was (0.87 ± 0.01) g day^{-1} over the first day until a crust formed. The rate reduced to (0.26 ± 0.01) g day^{-1} for the following 122 days while primary creeping occurred, completely depleting the bulk solution (Figure 4.24q). Figure 4.25q shows the crust and primary creep of sample T3 at 21 days after preparation. The creeps were extensive, growing up and over the beaker and down the side (Figure A.39).

$NaClO_4$ & Na_2SO_4 The overall mean mass loss rate across the three samples was (1.34 ± 0.03) g day^{-1} for 14 days until a partial crust and primary creep formed (Figure 4.24r). Figure 4.25r shows the crust and primary creep of sample T3 at 28 days after preparation. The rate reduced to $(5.92 \pm 0.03) \times 10^{-2}$ g day^{-1} for 141 days as creeping continued, completely depleting the sub crust solution. The creeps were extensive, growing up and over the beaker, then down the side of the beaker wall (Figure A.40).

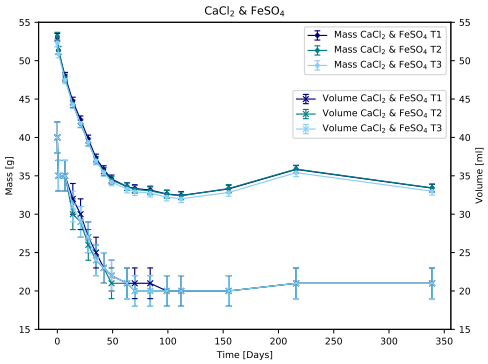

(a) $CaCl_2$ & $FeSO_4$

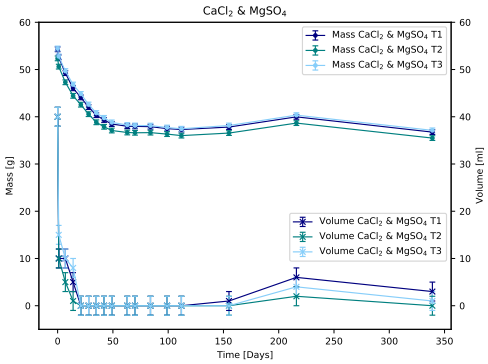

(b) $CaCl_2$ & $MgSO_4$

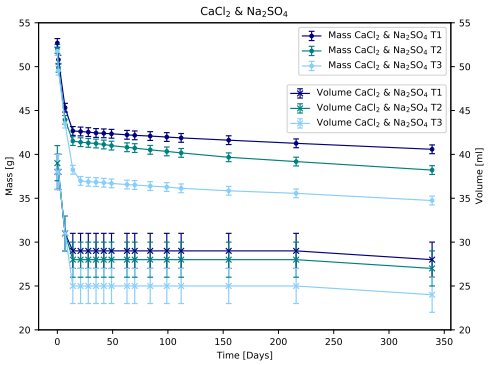

(c) $CaCl_2$ & Na_2SO_4

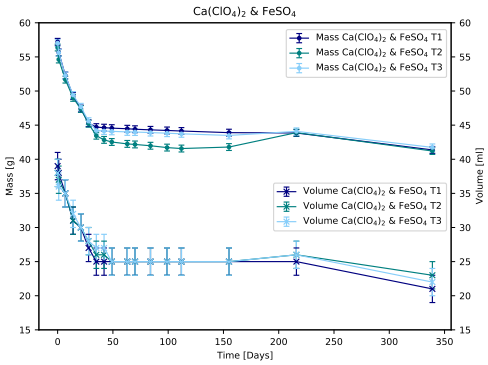

(d) $Ca(ClO_4)_2$ & $FeSO_4$

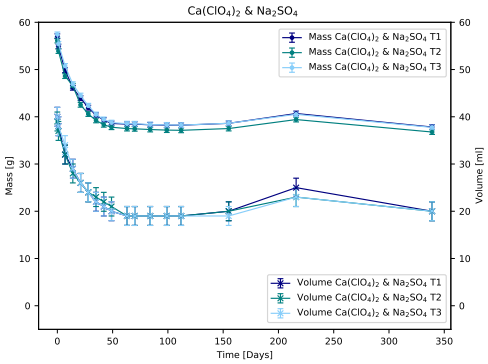

(e) $Ca(ClO_4)_2$ & Na_2SO_4

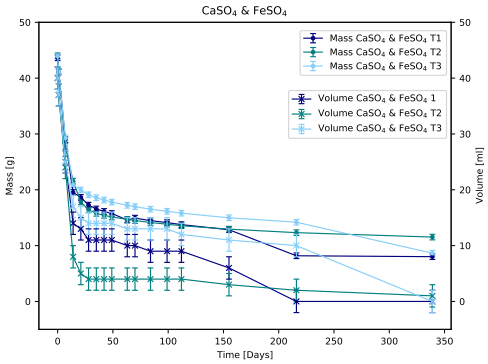

(f) $CaSO_4$ & $FeSO_4$

Figure 4.20: (Part 1/2)

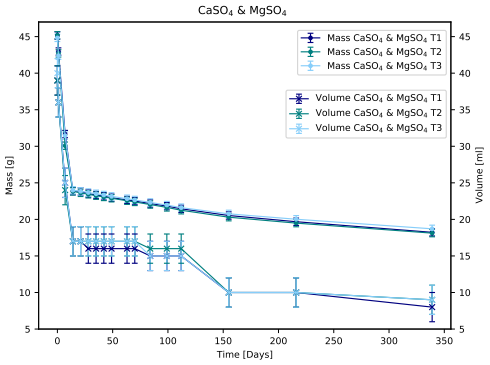

(g) $CaSO_4$ & $MgSO_4$

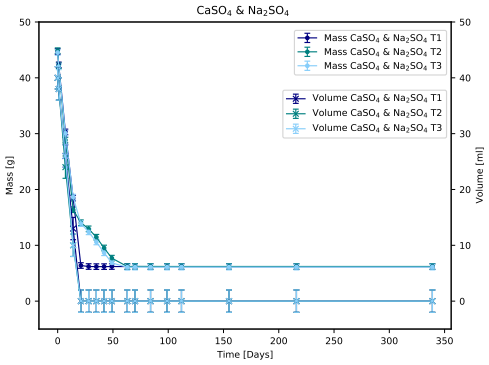

(h) $CaSO_4$ & Na_2SO_4

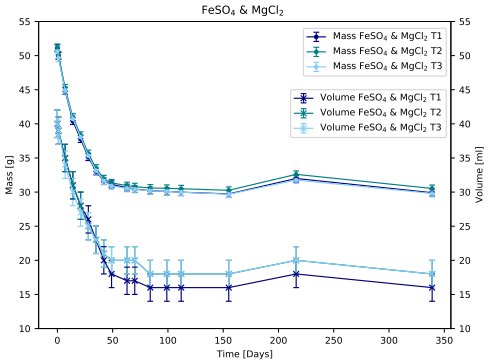

(i) $FeSO_4$ & $MgCl_2$

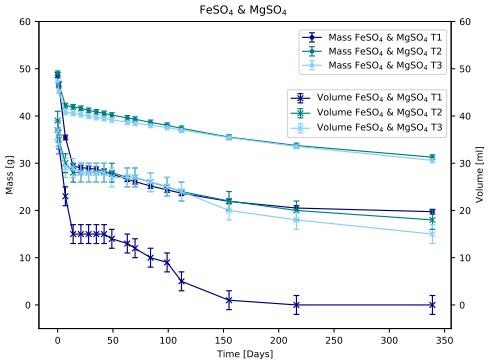

(j) $FeSO_4$ & $MgSO_4$

Figure 4.20: (Part 2/2) Results of Main Evaporite Experiment: Mass and Bulk Volume of Mixed Brines That Formed Interfacial Crusts. Bulk volume refers to the volume of liquid brine and any precipitated salt within the body of the brine. T1-T3 are the labels for each experiment in the set of triplicates.

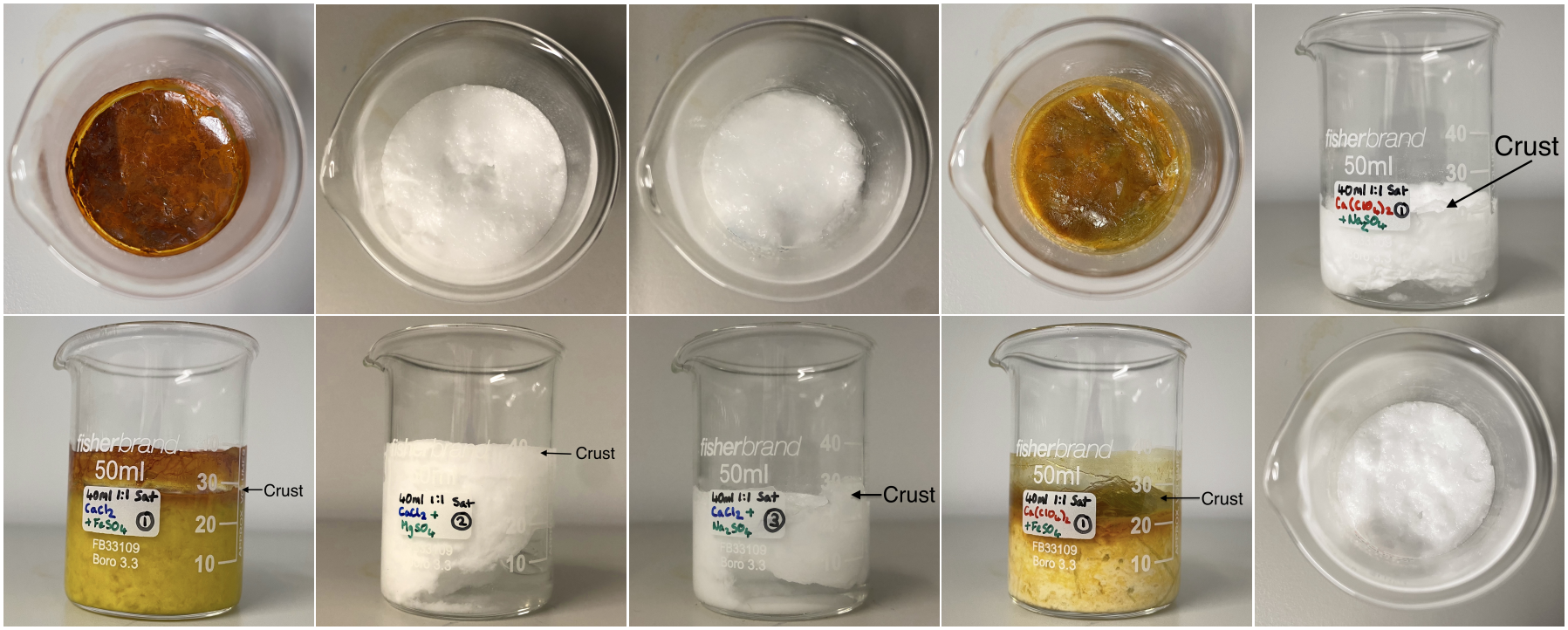

(a) $CaCl_2$ & $FeSO_4$ **(b)** $CaCl_2$ & $MgSO_4$ **(c)** $CaCl_2$ & Na_2SO_4 **(d)** $Ca(ClO_4)_2$ & $FeSO_4$ **(e)** $Ca(ClO_4)_2$ & Na_2SO_4

Figure 4.21: (Part 1/2)

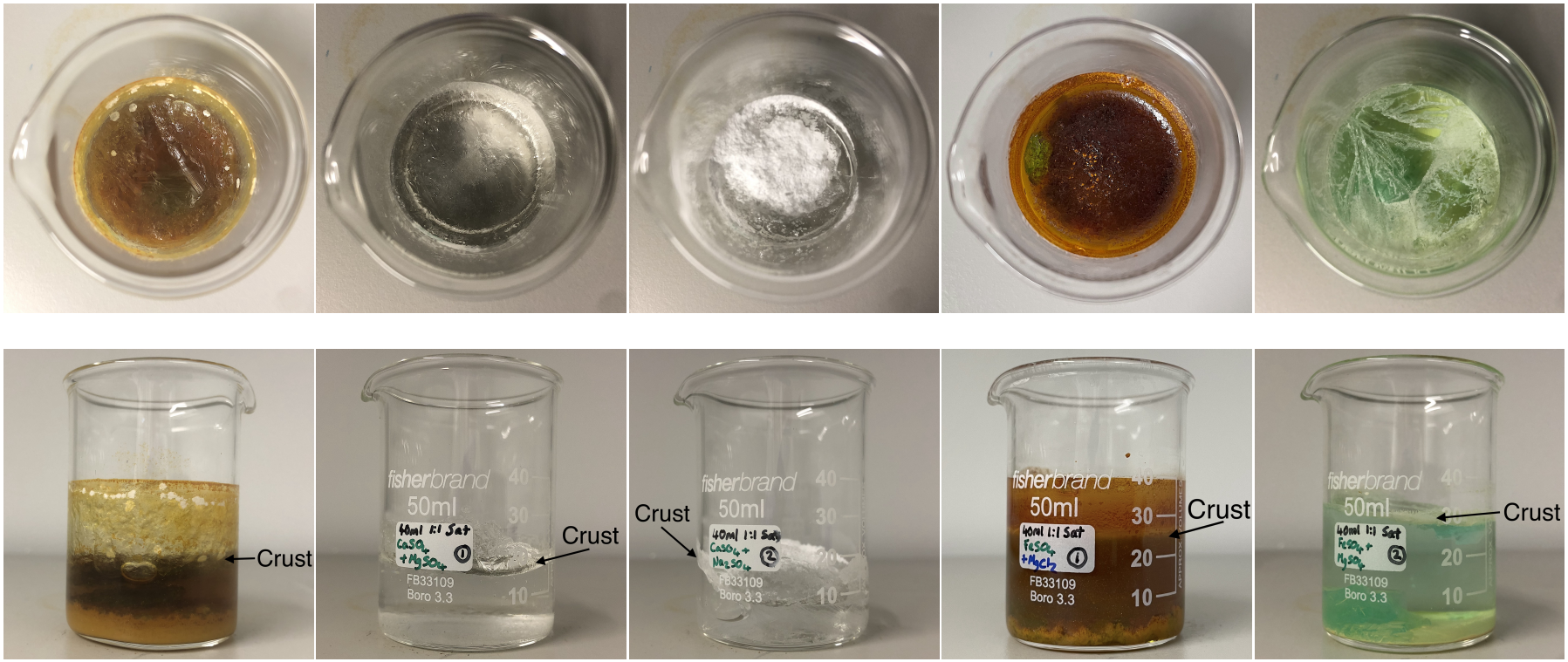

(f) $CaSO_4$ & $FeSO_4$ **(g)** $CaSO_4$ & $MgSO_4$ **(h)** $CaSO_4$ & Na_2SO_4 **(i)** $FeSO_4$ & $MgCl_2$ **(j)** $FeSO_4$ & $MgSO_4$

Figure 4.21: (Part 2/2) Results of Main Evaporite Experiment: Photographs of Mixed Brines That Formed Interfacial Crusts. The figures show one example of each brine soon after crust formation.

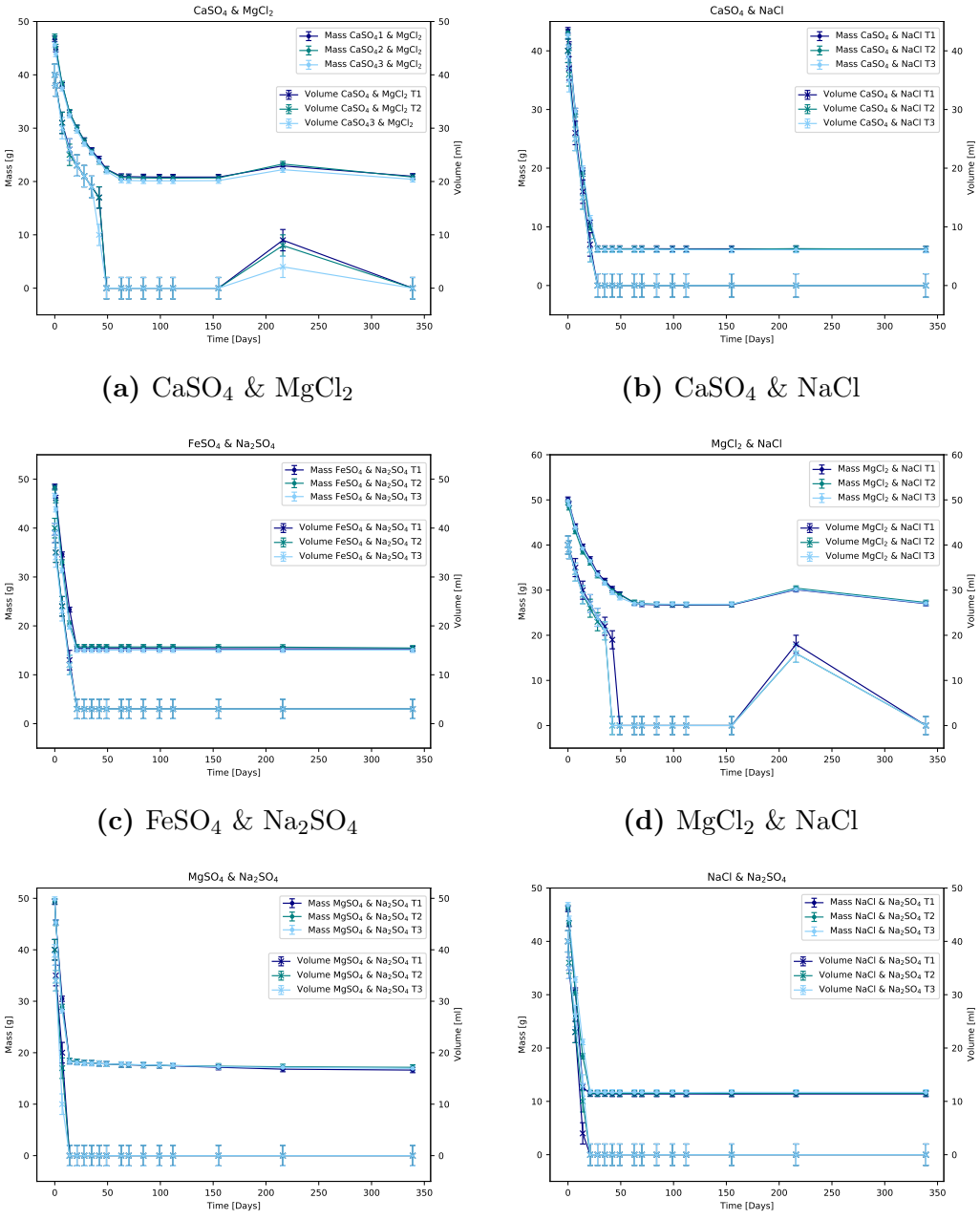

(a) $CaSO_4$ & $MgCl_2$ **(b)** $CaSO_4$ & NaCl

(c) $FeSO_4$ & Na_2SO_4 **(d)** $MgCl_2$ & NaCl

(e) $MgSO_4$& Na_2SO_4 **(f)** NaCl & Na_2SO_4

Figure 4.22: Results of Main Evaporite Experiment: Mass and Bulk Volume of Mixed Brines That Formed Creeping Evaporites. Bulk volume refers to the volume of liquid brine and any precipitated salt within the body of the brine. T1-T3 are the labels for each experiment in the set of triplicates.

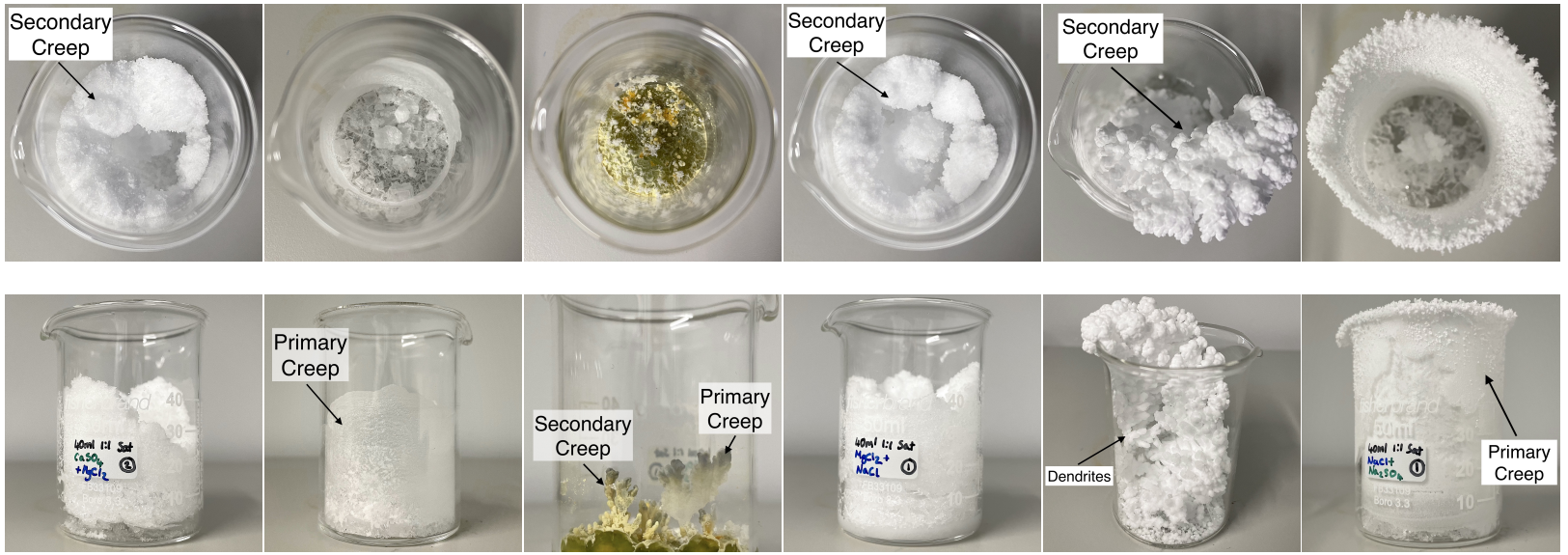

(a) $CaSO_4$ & $MgCl_2$ **(b)** $CaSO_4$ & NaCl **(c)** $FeSO_4$ & Na_2SO_4 **(d)** $MgCl_2$ & NaCl **(e)** $MgSO_4$ & Na_2SO_4 **(f)** NaCl & Na_2SO_4

Figure 4.23: Results of Main Evaporite Experiment: Photographs of Mixed Brines That Formed Creeping Evaporites. The figures show one example of each brine soon after the creeping structure formed.

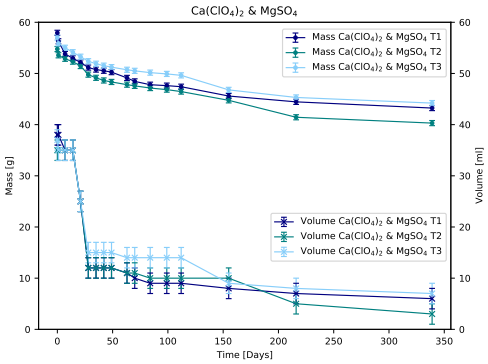

(a) $Ca(ClO_4)_2$ & $MgSO_4$

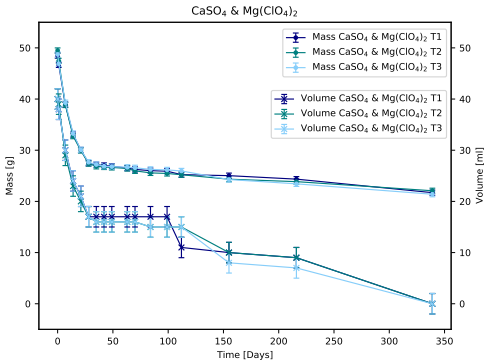

(b) $CaSO_4$ & $Mg(ClO_4)_2$

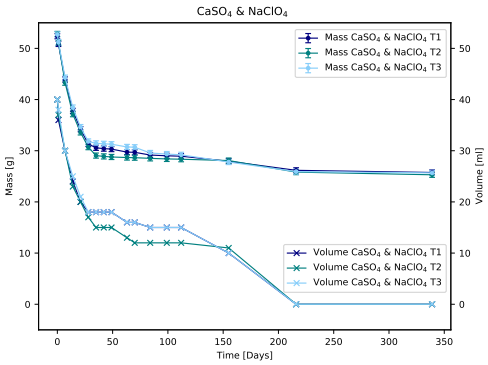

(c) $CaSO_4$ & $NaClO_4$

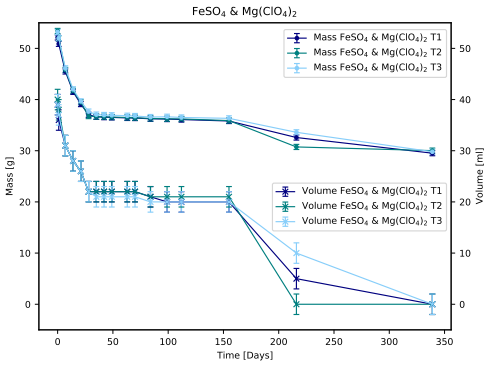

(d) $FeSO_4$& $Mg(ClO_4)_2$

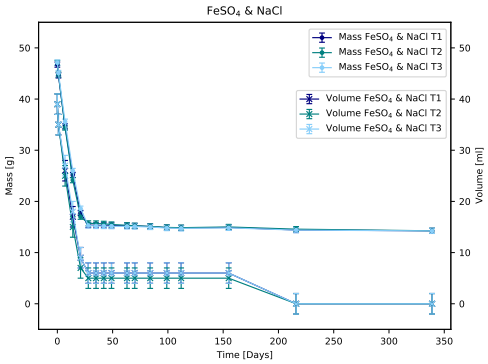

(e) $FeSO_4$ & $NaCl$

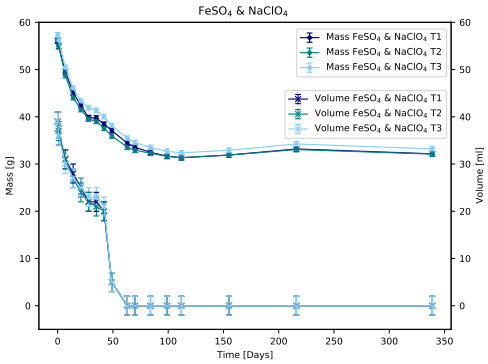

(f) $FeSO_4$ & $NaClO_4$

Figure 4.24: Part (1/3)

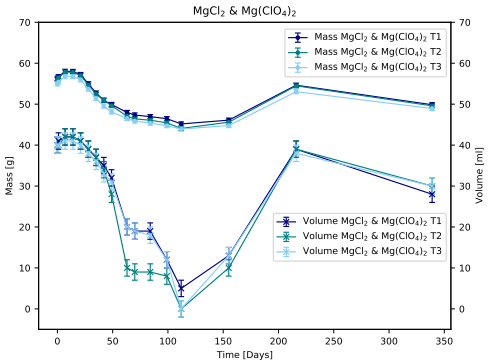

(g) $MgCl_2$ & $Mg(ClO_4)_2$

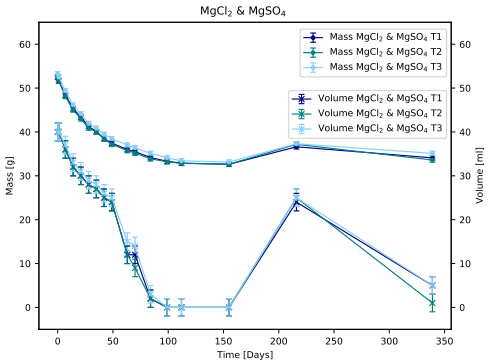

(h) $MgCl_2$ & $MgSO_4$

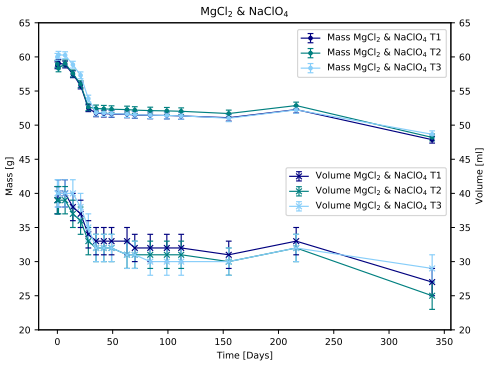

(i) $MgCl_2$ & $NaClO_4$

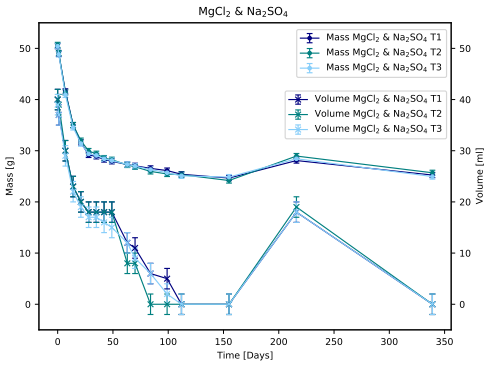

(j) $MgCl_2$ & Na_2SO_4

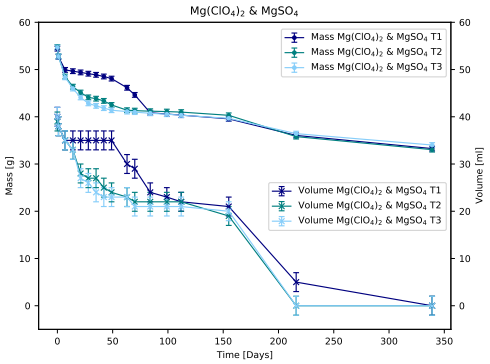

(k) $Mg(ClO_4)_2$ & $MgSO_4$

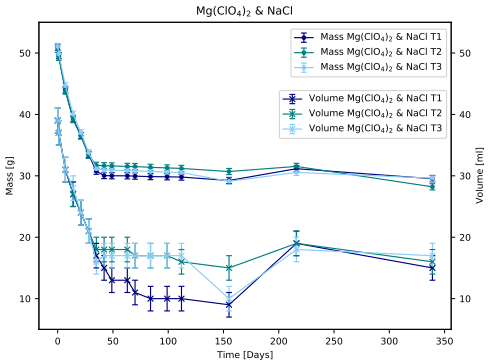

(l) $Mg(ClO_4)_2$ & $NaCl$

Figure 4.24: (Part 2/3)

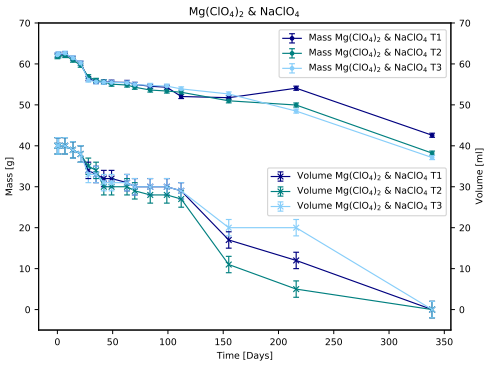

(m) $Mg(ClO_4)_2$ & $NaClO_4$

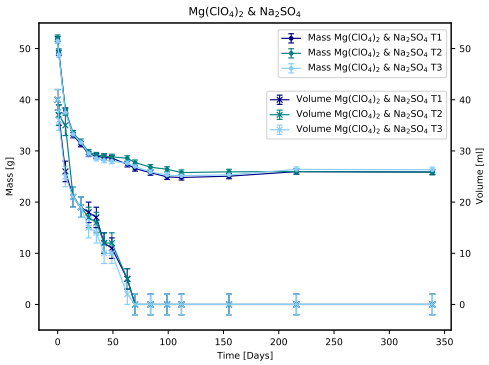

(n) $Mg(ClO_4)_2$ & Na_2SO_4

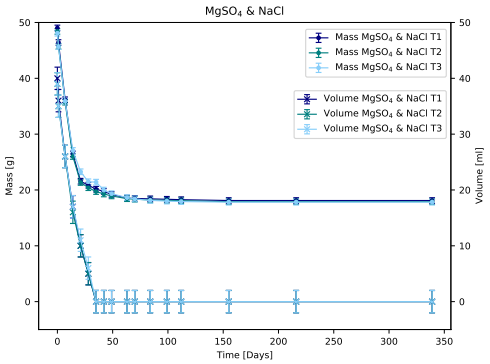

(o) $MgSO_4$ & NaCl

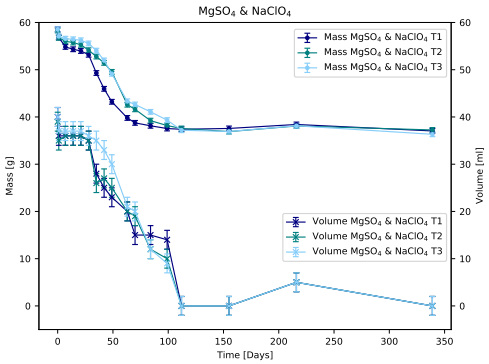

(p) $MgSO_4$ & $NaClO_4$

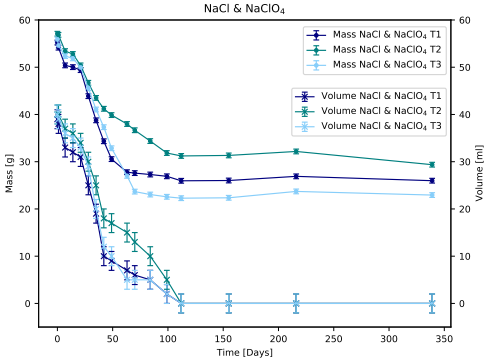

(q) NaCl & $NaClO_4$

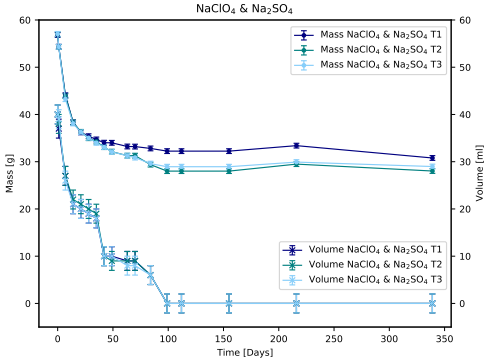

(r) $NaClO_4$ & Na_2SO_4

Figure 4.24: (Part 3/3) Results of Main Evaporite Experiment: Mass and Bulk Volume of Mixed Brines That Formed Interfacial Crusts and Creeping Evaporites. Bulk volume refers to the volume of liquid brine and any precipitated salt within the body of the brine. T1-T3 are the labels for each experiment in the set of triplicates.

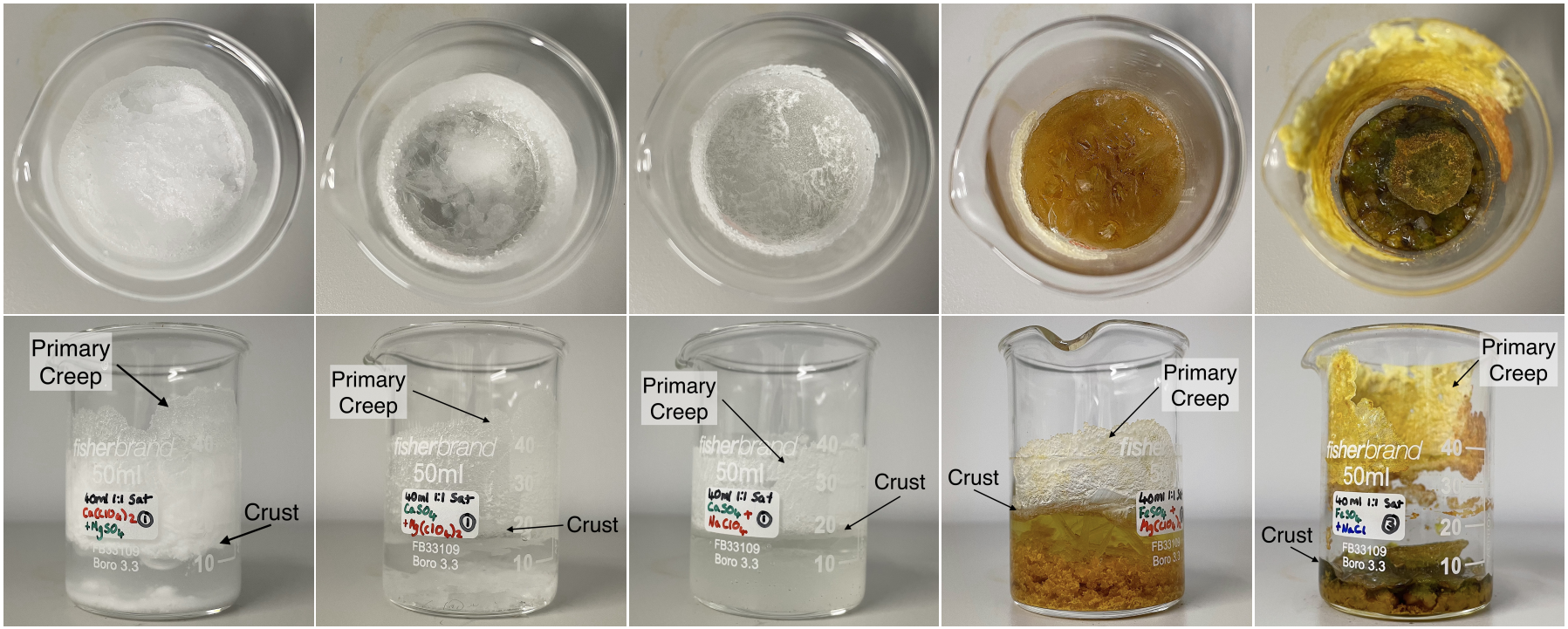

(a) $Ca(ClO_4)_2$ & $MgSO_4$ **(b)** $CaSO_4$ & $Mg(ClO_4)_2$ **(c)** $CaSO_4$ & $NaClO_4$ **(d)** $FeSO_4$ & $Mg(ClO_4)_2$ **(e)** $FeSO_4$ & NaCl

Figure 4.25: (Part 1/4)

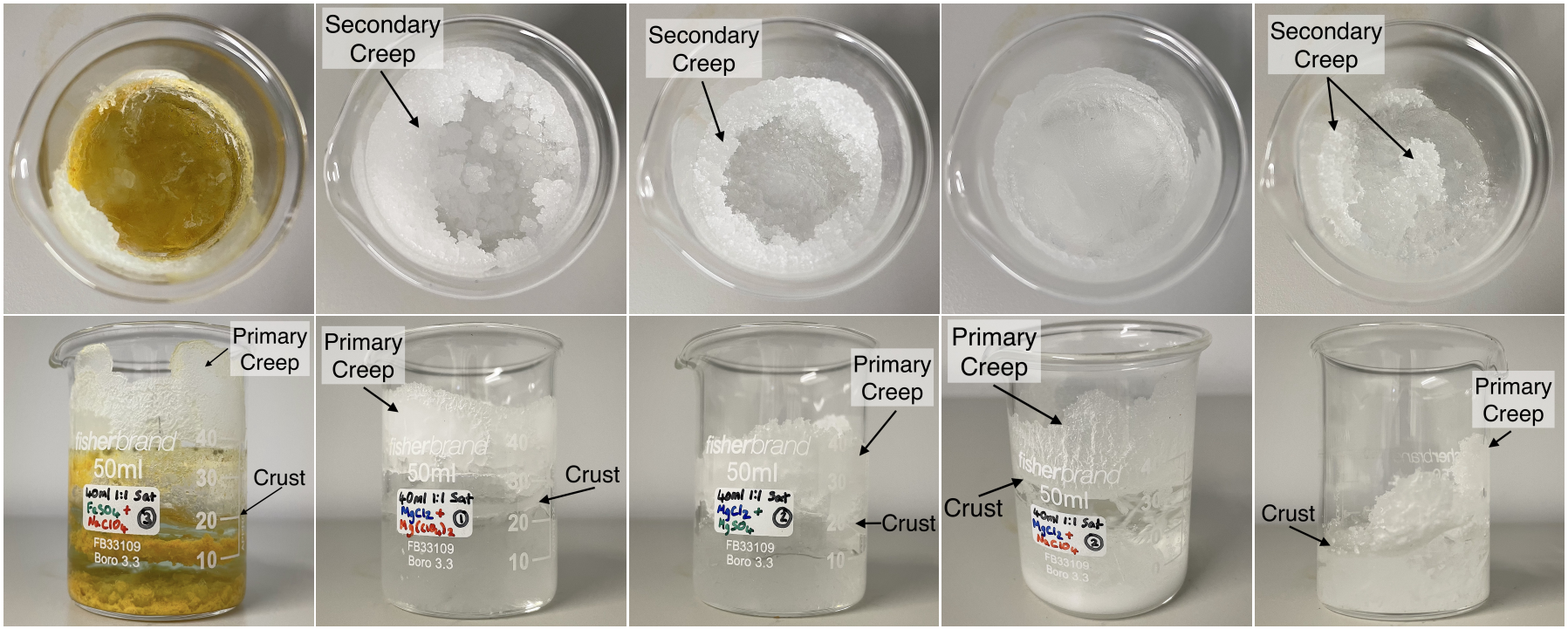

(f) $FeSO_4$ & $NaClO_4$ **(g)** $MgCl_2$ & $Mg(ClO_4)_2$ **(h)** $MgCl_2$ & $MgSO_4$ **(i)** $MgCl_2$ & $NaClO_4$ **(j)** $MgCl_2$ & Na_2SO_4

Figure 4.25: (Part 2/4)

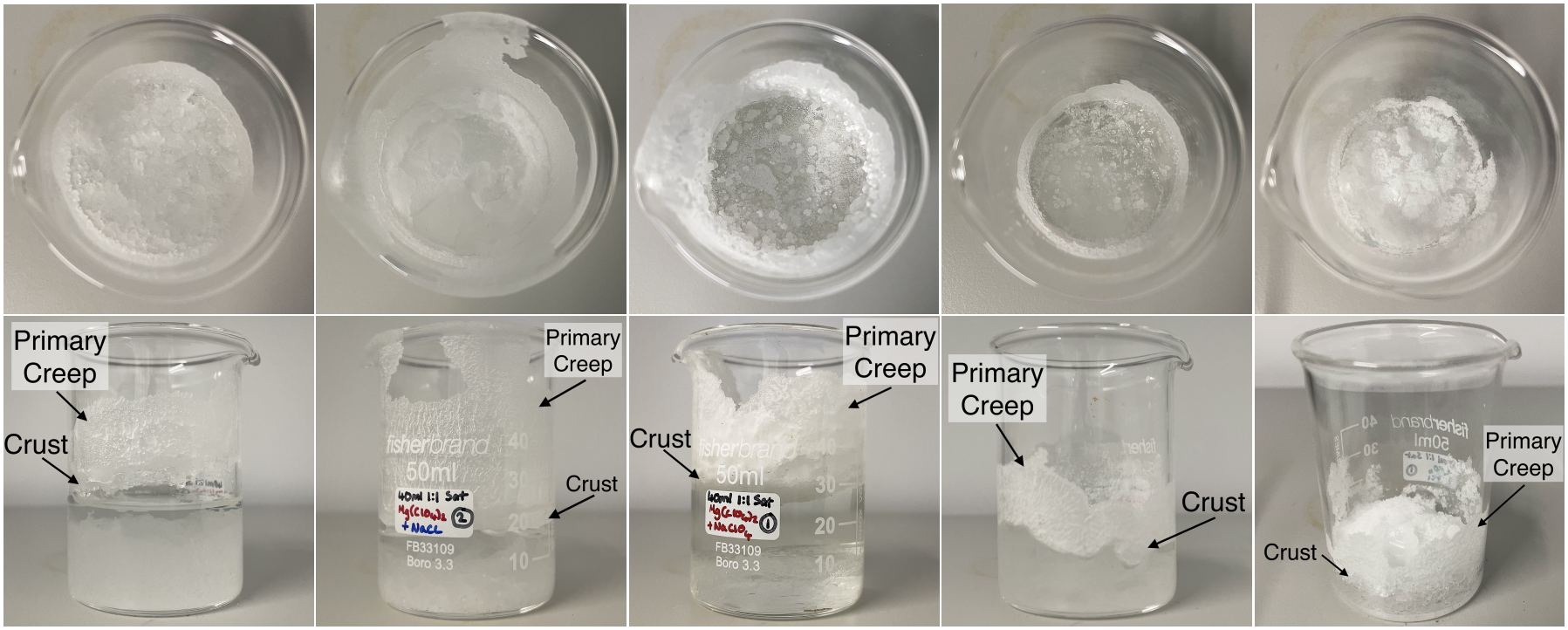

(k) $Mg(ClO_4)_2$ & $MgSO_4$ **(l)** $Mg(ClO_4)_2$ & $NaCl$ **(m)** $Mg(ClO_4)_2$ & $NaClO_4$ **(n)** $Mg(ClO_4)_2$ & Na_2SO_4 **(o)** $MgSO_4$ & $NaCl$

Figure 4.25: (Part 3/4)

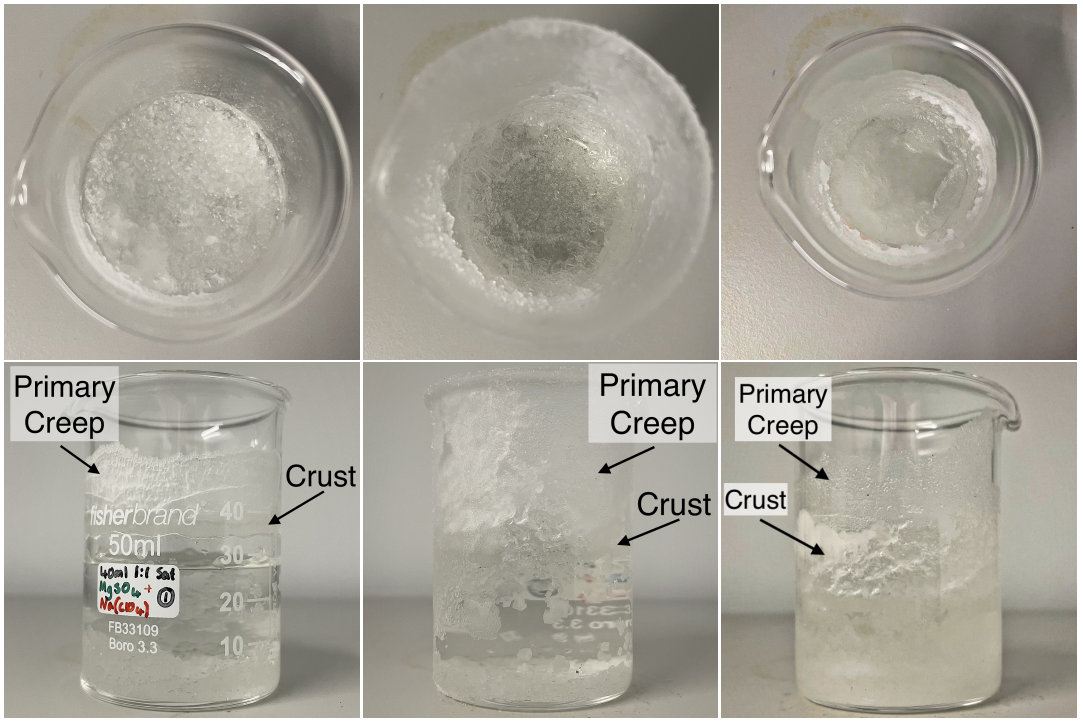

(p) $MgSO_4$ & $NaClO_4$ **(q)** NaCl & $NaClO_4$ **(r)** $NaClO_4$ & Na_2SO_4

Figure 4.25: (Part 4/4) Results of Main Evaporite Experiment: Photographs of Pure Brines That Formed Interfacial Crusts and Creeping Evaporites. The figures show one example of each brine.

4.4.3 The Morphology of Evaporites at Low Pressure

The mean mass loss rates for each triplicate and overall mean mass loss rates are presented in Table 4.4. For each brine where a crust significantly affected the mass loss rate, Table 4.5 presents a breakdown of the mass loss rates during different stages of evaporite formation. The mass of the solutions over time are plotted in Figure 4.26. An example of each resultant evaporite structure is shown in Figure 4.28.

$MgSO_4$

In all three triplicates, a crust formed rapidly. The crusts formed in experiments T2 and T3 were particularly efficacious at inhibiting evaporation from the solution. The overall mean mass loss rate over the entire duration of the experiments was $(4.86 \pm 0.03)\times10^{-4}$ g min^{-1} (Table 4.4). The masses of each $MgSO_4$ brine sample over time are plotted in Figure 4.26a.

The crust formed by sample T3 was the most efficacious at inhibiting evaporation from the brine. Over the first 12 minutes of experiment T3, the mass loss rate was $(1.20 \pm 0.18)\times10^{-2}$ g min^{-1} (Table 4.5). The complete formation of the crust at ∼250 minutes (Figure 4.27a) reduced the rate by 207 times to $(5.79 \pm 0.13)\times10^{-5}$ g min^{-1}. At ∼1838 minutes the crust partially broke due to the build up of bubbles (Figure 4.27b and 4.27c) increasing the mass loss rate to $(6.77 \pm 0.29)\times10^{-4}$ g min^{-1}. When the crust reformed fully at ∼4515 minutes (Figure 4.27e), the mass loss rate reduced to $(6.79 \pm 0.09)\times10^{-5}$ g min^{-1} for the remainder of the experiment. After 4 days at 50 mb, ∼38 mL of liquid brine remained beneath the crust as shown in Figure 4.28a.

Over the first 98 minutes of experiment T2, the mass loss rate was $(1.20 \pm 0.03)\times10^{-2}$ g min^{-1} (Table 4.5). The formation of the crust reduced this by 56 times to $(2.13 \pm 0.13)\times10^{-4}$ g min^{-1}. At 1500 minutes the crust partially broke due to the build up of bubbles increasing the mass loss rate to $(6.66 \pm 0.09)\times10^{-4}$ g min^{-1}. When the crust reformed fully at ∼2963 minutes, the mass loss rate reduced to $(1.66 \pm 0.09)\times10^{-4}$ g min^{-1} for the remainder of the experiment. After 4 days at 50 mb, ∼38 mL of liquid brine remained beneath the crust.

For experiment T1 the crust did not break and the mass loss rate was relatively constant at $(4.57 \pm 0.17)\times10^{-4}$ g min^{-1} after the crust formed (Table 4.5). The

crust formed by T1 was not as efficacious at preventing mass loss, which may be why the crust did not break - if diffusion through the crust was occurring, the gas bubbles which caused the breakages in T2 and T3 may have been able to escape. After 4 days at 50 mb, ∼38 mL of liquid brine remained beneath the crust.

Na_2SO_4

The three Na_2SO_4 brine samples evaporated at an overall mean rate of $(5.69 \pm 0.09)\times10^{-3}$ g min^{-1} over a mean of (6223 ± 97) minutes (Table 4.4) at which point all of the solution had evaporated leaving behind a friable evaporite deposit. An example of one of the samples after the experiment is shown in Figure 4.28b. Despite the formation of a partial crust (as shown in Figure 4.29), the mass decreased at a relatively constant rate throughout the duration of the experiment until the final few hundred minutes when the mass loss slowed.

$MgSO_4$ & Na_2SO_4

Each of the three samples of $MgSO_4$ & Na_2SO_4 formed an interfacial surface crust. The crust persisted for the remainder of the experiment, significantly limiting evaporation from the remaining sub-crust solution. Figure 4.26c shows how mass loss reduces significantly after the crust forms. This differs from the same binary solution at ambient pressure, which produced a distinct creeping structure. After the experiment, investigating beneath the crust showed that there was some liquid brine remaining though much of the volume was precipitated salt. Figure 4.28c shows sample T3 at the end of the experiment.

The overall mean mass loss rate across the triplicates was $(3.51 \pm 0.05)\times10^{-3}$ g min^{-1} (Table 4.4). For sample T1, the mass loss rate for the first ∼2300 minutes was $(8.69 \pm 0.02)\times10^{-3}$ g min^{-1}, reducing by 140 times to $(6.19 \pm 0.84)\times10^{-5}$ g min^{-1} for the remainder of the experiment (Table 4.5). Similarly for sample T3, the mass loss rate for the first ∼2900 minutes was $(7.49 \pm 0.01)\times10^{-3}$ g min^{-1}, reducing by 26 times to $(2.80 \pm 0.09)\times10^{-4}$ g min^{-1} for the remainder of the experiment. The change in mass loss rate due to crust formation was more gradual during experiment T2, starting at $(1.01 \pm 0.01)\times10^{-2}$ g min^{-1} for 680 minutes, reducing to $(2.11 \pm 0.01)\times10^{-3}$ g min^{-1} for the next 2820 minutes then reducing further to $(1.67 \pm 0.29)\times10^{-4}$ g min^{-1} for the remaining 2118 minutes of the experiment.

Table 4.4: Results of Evaporite Morphology at Low Pressure Experiment: Mass Loss Rates From Brines and Water at 50 mb. T1-T3 are the labels for each experiment in the set of triplicates.

Pressure	Triplicate	Time [mins]	Mass Loss Rate [g min^{-1}]
$MgSO_4$	T1	5735 ± 27	$(4.88 \pm 0.04)\times10^{-4}$
	T2	5748 ± 97	$(5.07 \pm 0.09)\times10^{-4}$
	T3	5753 ± 211	$(4.03 \pm 0.15)\times10^{-4}$
	Mean	-	$(4.86 \pm 0.03)\times10^{-4}$
Na_2SO_4	T1	6133 ± 456	$(5.56 \pm 0.41)\times10^{-3}$
	T2	5157 ± 243	$(6.86 \pm 0.32)\times10^{-3}$
	T3	6439 ± 109	$(5.59 \pm 0.09)\times10^{-3}$
	Mean	6223 ± 97	$(5.69 \pm 0.09)\times10^{-3}$
$MgSO_4$ & Na_2SO_4	T1	5759 ± 370	$(3.51 \pm 0.23)\times10^{-3}$
	T2	5618 ± 267	$(2.34 \pm 0.11)\times10^{-3}$
	T3	5759 ± 95	$(3.91 \pm 0.06)\times10^{-3}$
	Mean	-	$(3.51 \pm 0.05)\times10^{-3}$
Water	T1	4364 ± 2	$(9.17 \pm 0.01)\times10^{-3}$
	T2	4379 ± 2	$(9.14 \pm 0.01)\times10^{-3}$
	T3	4390 ± 2	$(9.11 \pm 0.01)\times10^{-3}$
	Mean	4378 ± 1	$(9.141 \pm 0.003)\times10^{-3}$

Water

The water evaporated at an overall mean rate of $(9.14 \pm 0.01)\times10^{-3}$ g min^{-1} within (4378 ± 1) minutes (Table 4.4 and Figure 4.26d).

Table 4.5: Results of Evaporite Morphology at Low Pressure Experiment: Breakdown of Mass Loss Rates During Different Stages of the Evaporite Formation Process For $MgSO_4$, the time intervals are split according to when crusts formed, broke and reformed. For $MgSO_4$ & Na_2SO_4, the time intervals are split according to when the crust formed or was forming.

Brine	Triplicate	Crust Behaviour	Time Interval [mins]	Mass Loss Rate [g min^{-1}]
$MgSO_4$	T1	No Crust	0-8	$(2.13 \pm 0.36)\times10^{-2}$
		Crust Formed	8-5735	$(4.57 \pm 0.17)\times10^{-4}$
	T2	No Crust	0-98	$(1.20 \pm 0.03)\times10^{-2}$
		Crust Formed	98-1500	$(2.13 \pm 0.13)\times10^{-4}$
		Crust Broken	1500-2963	$(6.66 \pm 0.19)\times10^{-4}$
		Crust Reformed	2963-5748	$(1.66 \pm 0.09)\times10^{-4}$
	T3	No Crust	0-12	$(1.20 \pm 0.18)\times10^{-2}$
		Crust Forming	12-250	$(7.86 \pm 1.81)\times10^{-4}$
		Crust Formed	250-1838	$(5.79 \pm 1.21)\times10^{-5}$
		Crust Broken	1838-4515	$(6.77 \pm 0.29)\times10^{-4}$
		Crust Reformed	4515-5753	$(6.79 \pm 1.80)\times10^{-5}$
$MgSO_4$ & Na_2SO_4	T1	No Crust	0-2302	$(8.69 \pm 0.02)\times10^{-3}$
		Crust Formed	2302-5759	$(6.19 \pm 0.84)\times10^{-5}$
	T2	No Crust	0-680	$(1.01 \pm 0.01)\times10^{-2}$
		Crust Forming	680-3500	$(2.11 \pm 0.01)\times10^{-3}$
		Crust Formed	3500-5618	$(1.67 \pm 0.29)\times10^{-4}$
	T3	No Crust	0-2900	$(7.49 \pm 0.01)\times10^{-3}$
		Crust Formed	2900-5759	$(2.80 \pm 0.09)\times10^{-4}$

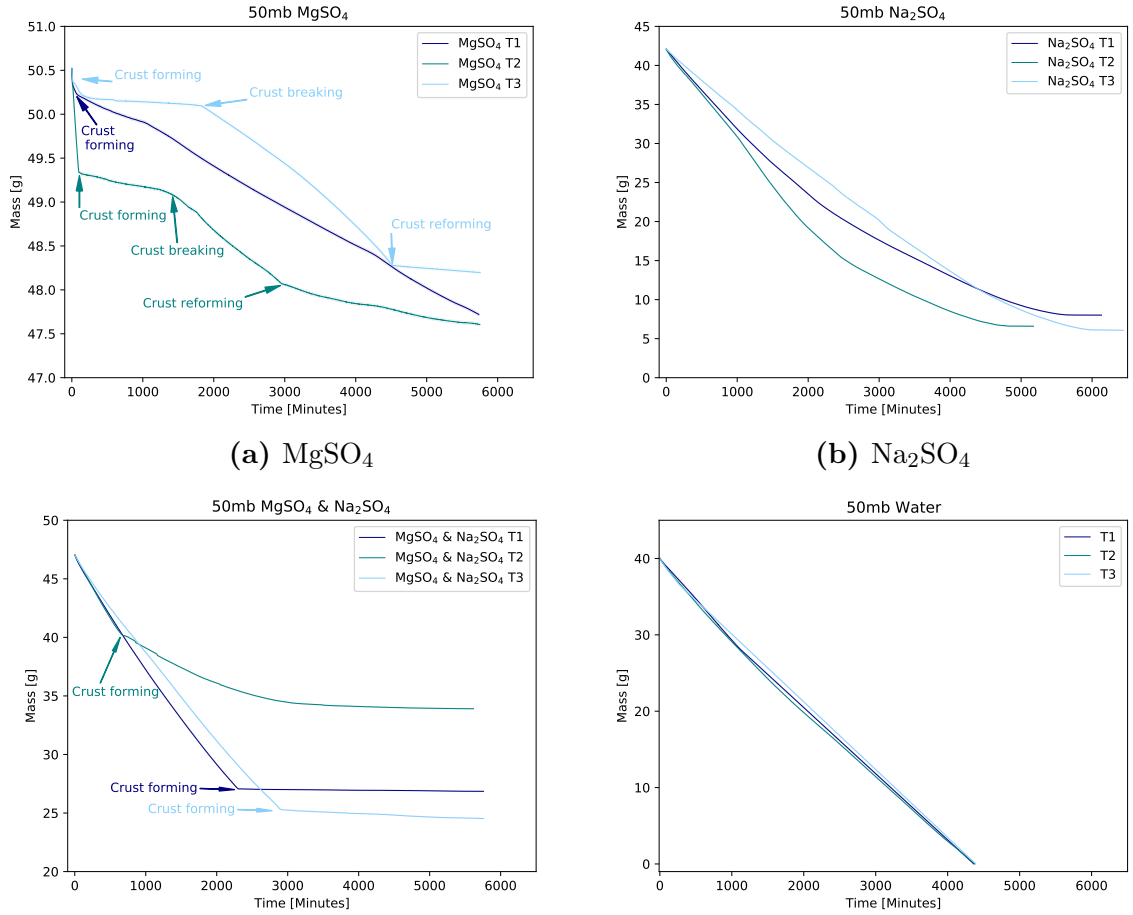

(a) $MgSO_4$ **(b)** Na_2SO_4

(c) $MgSO_4$ & Na_2SO_4 **(d)** Water

Figure 4.26: Results of Evaporite Morphology at Low Pressure Experiment: Plots of Brine and Water Mass Over ∼4 Days at 50 mb Pressure. The volume of each solution was 40 mL at the experiment start. T1-T3 are the labels for each experiment in each set of triplicates.

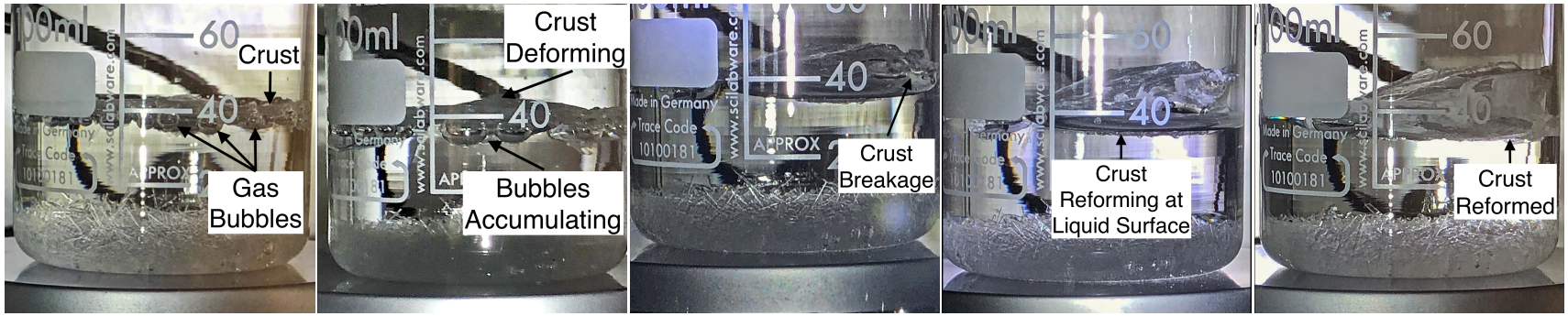

(a) 250 Minutes **(b)** 1300 Minutes **(c)** 2000 Minutes **(d)** 3000 Minutes **(e)** 4600 Minutes

Figure 4.27: Results of Evaporite Morphology at Low Pressure Experiment: Example of $MgSO_4$ Crust Forming and Changing over 4 Days at 50 mb Pressure. The crust formed then a gas bubble accumulated beneath it leading to a partial breakage of the crust. The crust reformed fully over ∼1 day. The images are of triplicate experiment T3.

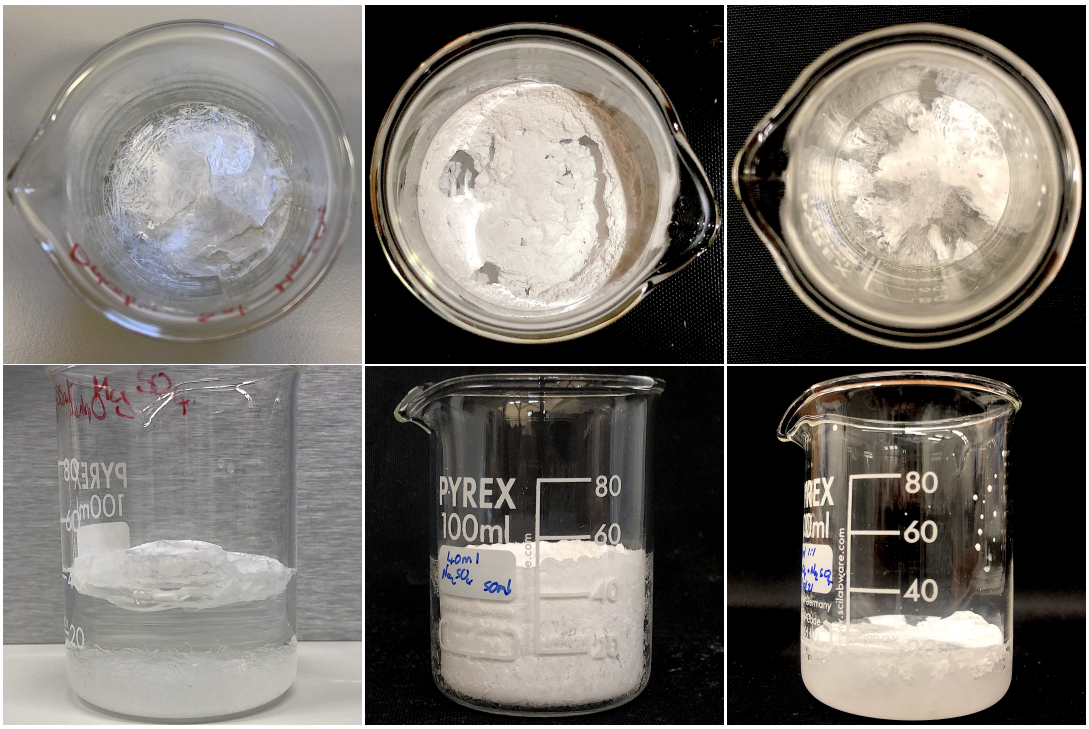

(a) $MgSO_4$ **(b)** Na_2SO_4 **(c)** $MgSO_4$ & Na_2SO_4

Figure 4.28: Results of Evaporite Morphology at Low Pressure Experiment: Examples of Each Evaporite Structure After 4 Days at 50 mb Pressure. (a) The $MgSO_4$ formed a crust that preserved most of the sub-crust solution. (b) The Na_2SO_4 evaporated completely, leaving behind a friable evaporite deposit. (c) The $MgSO_4$ & Na_2SO_4 also formed a crust, preserving some sub-crust solution.



(a) 1400 Minutes **(b)** 2800 Minutes **(c)** 4300 Minutes **(d)** 6439 Minutes

Figure 4.29: Results of Evaporite Morphology at Low Pressure Experiment: Example of Na_2SO_4 Crust Forming over 4 Days at 50 mb Pressure. A partial crust formed but did not prevent the evaporation of the sub-crust solution. The images are of triplicate experiment T1.

4.4.4 The Effect of a $MgSO_4$ Crust on Evaporation at Ambient and Low Pressure

Under both ambient pressure and 50 mb pressure conditions the $MgSO_4$ crust inhibited evaporation from the brine significantly.

Ambient Pressure

The samples of $MgSO_4$ solution that did not have their interfacial crusts broken (C1-C3) exhibited no mass loss over the experimental period (Figure 4.30). The overall mean mass loss rate across the three samples that had their crusts broken 5 times within 6 hours was $(3.38 \pm 0.14)\times10^{-3}$ g min^{-1}, losing a mean mass of (1.13 $\pm$ 0.04) g (Table 4.6). At this rate 40 mL of $MgSO_4$ (52 g of solution consisting of $\sim$32 g water and $\sim$20 g salt, calculated using the salt fractions from Table 3.2) would evaporate fully within $\sim$6.6 days. Compared to the $MgSO_4$ samples in the main evaporite experiment - section 4.4.2 - which maintained most of the original sub-crust brine over 11 months, the presence of a crust significantly reduces evaporation from the brine.

Low Pressure - 50 mb

During periods when the crust was fully formed, no mass loss took place (Table 4.8 and Figure 4.31). The overall mean mass loss rate across the three samples that had their crusts broken 5 times within 6 hours was $(1.97 \pm 0.01)\times10^{-3}$ g min^{-1}, losing a mean of (0.59 $\pm$ 0.01) g. The rates for the unbroken crust were calculated by splitting the experiment into time intervals where the crust was broken and when the crust was fully formed (Table 4.8). The overall mean mass loss rate when the crust was broken was (0.013 $\pm$ 0.001) g min^{-1} compared to 0 g min^{-1} mass loss when the crust was reformed. At the mass loss rate during the periods of broken crust 40 mL of $MgSO_4$ ($\sim$50 g of solution consisting of $\sim$33 g water and $\sim$17 g salt, calculated using the salt fractions from Table 3.2) would evaporate fully within $\sim$1.8 days. Compared to the $MgSO_4$ samples in the low pressure experiment - section 4.4.3 - which contained $\sim$38 mL of liquid brine after 4 days at 50 mb, the presence of a crust significantly reduces evaporation from the brine.

Table 4.6: Results of Effect of $MgSO_4$ Crust on Evaporation at Ambient Pressure Experiment: Mass Loss Rates From 40 mL of Solution at 1000 mb Over 300 Minutes. T1-T3 refer to each experiment in the set of triplicates. C1-C3 refer to each control experiment in the set of triplicates.

Experiment	Triplicate	Mass Loss Rate [g min^{-1}]
Crust Broken Hourly	T1	$(3.67 \pm 0.24)\times10^{-3}$
	T2	$(4.33 \pm 0.24)\times10^{-3}$
	T3	$(3.33 \pm 0.24)\times10^{-3}$
	Mean	$(3.38 \pm 0.14)\times10^{-3}$
Crust Unbroken	C1	0
	C2	0
	C3	0
	Mean	0
DI Water	T1	$(6.57 \pm 0.24)\times10^{-3}$
	T2	$(6.53 \pm 0.24)\times10^{-3}$
	T3	$(6.57 \pm 0.24)\times10^{-3}$
	Mean	$(6.56 \pm 0.14)\times10^{-3}$

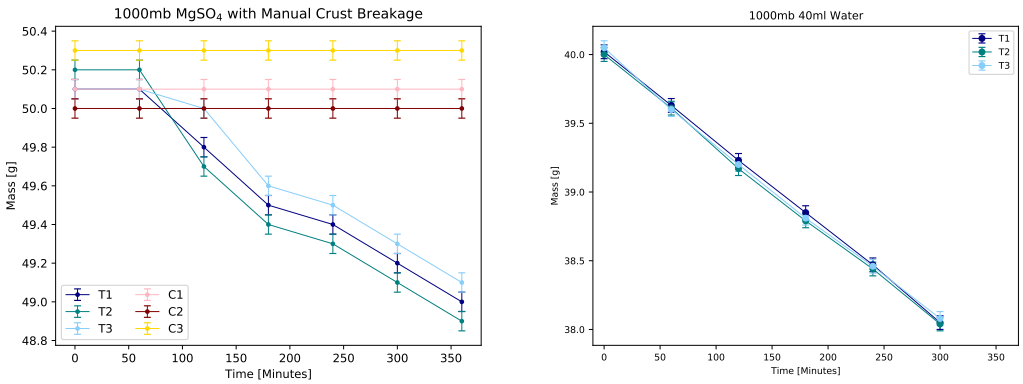

(a) $MgSO_4$ **(b)** Water

Figure 4.30: Results of Effect of $MgSO_4$ Crust on Evaporation at Ambient Pressure Experiment: Plots of Mass of Solution over 300 Minutes at 1000 mb. The experimental $MgSO_4$ crusts were broken hourly starting at 60 minutes. The control $MgSO_4$ crusts were undisturbed. T1-T3 and C1-C3 are labels for each experiment and control in the set of triplicates respectively. The first 60 minutes of the $MgSO_4$ experiment were to ensure the crust had formed fully and were not included in the mass loss rate calculations.

Table 4.7: Results of Effect of $MgSO_4$ Crust on Evaporation at Low Pressure Experiment: Mass Loss Rates From 40 mL of Solution at 50 mb over 300 Minutes. The total period refers to the 300 minutes subsequent to the first crust breakage at 60 minutes. Crust broken refers to the mean mass loss rate over the 5 periods when the crust was broken. Crust reformed refers to mean mass loss rate over the five periods when the crust had reformed. A breakdown of the mass loss rates during these periods is presented in Table 4.8. T1-T3 refer to each experiment in the set of triplicates.

Solution	Period	Triplicate	Mass Loss Rate [g min^{-1}]
$MgSO_4$	Total	T1	$(2.33 \pm 0.06)\times10^{-3}$
		T2	$(1.66 \pm 0.06)\times10^{-3}$
		T3	$(1.92 \pm 0.06)\times10^{-3}$
		Mean	$(1.97 \pm 0.03)\times10^{-3}$
	Crust Broken	T1	0.013 ± 0.001
		T2	0.011 ± 0.002
		T3	0.020 ± 0.003
		Mean	0.013 ± 0.001
	Crust Reformed	T1	0
		T2	0
		T3	0
		Mean	0
Water	Total	T1	$(9.16 \pm 0.01)\times10^{-3}$
		T2	$(9.14 \pm 0.01)\times10^{-3}$
		T3	$(1.24 \pm 0.01)\times10^{-2}$
		Mean	$(9.16 \pm 0.01)\times10^{-3}$

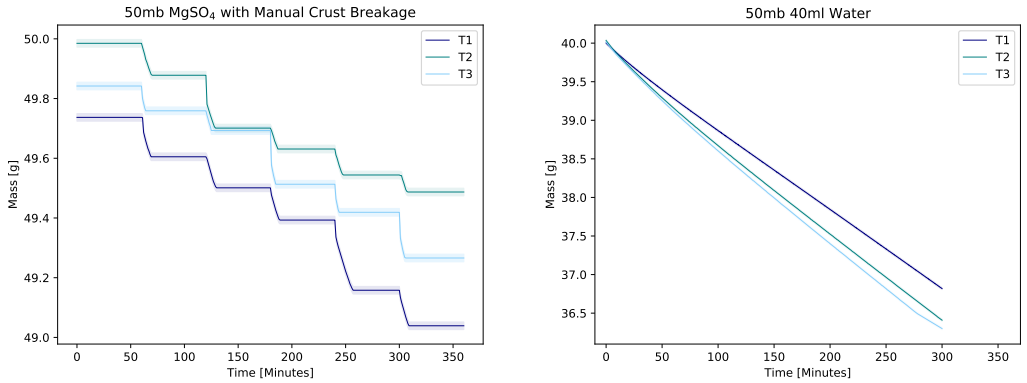

Figure 4.31: Results of Effect of $MgSO_4$ Crusts on Evaporation at Low Pressure Experiment: Plots of Mass of Solution over 300 Minutes at 50 mb. The $MgSO_4$ crusts were broken hourly starting at 60 minutes. T1-T3 are labels for each experiment in the set of triplicates. The first 60 minutes of the $MgSO_4$ experiment were to ensure the crust had formed fully and were not included in the mass loss rate calculations.

Table 4.8: Results of Effect of $MgSO_4$ Crusts on Evaporation at Low Pressure Experiment: Breakdown of Mass Loss Rate of $MgSO_4$ over 300 Minutes at 50 mb. The time intervals are split into groups of when the crust was broken and mass loss was taking place and intervals when the crust had reformed. T1-T3 refer to each experiment in the set of triplicates. C1-C3 refer to each control experiment in the set of control triplicates.

Crust State	Triplicate	Measurement	Time (Time Interval) [mins]	Mass Loss Rate [g min^{-1}]
Crust Broken	T1	1	9 ± 2 (60-69)	(0.015 ± 0.004)
		2	10 ± 2 (120-130)	(0.010 ± 0.003)
		3	9 ± 2 (180-189)	(0.012 ± 0.003)
		4	17 ± 2 (240-257)	(0.014 ± 0.002)
		5	9 ± 2 (300-309)	(0.013 ± 0.003)
		Mean	11 ± 1	(0.013 ± 0.001)
	T2	1	10 ± 2 (60-70)	(0.011 ± 0.003)
		2	9 ± 2 (120-129)	(0.020 ± 0.005)
		3	7 ± 2 (180-187)	(0.010 ± 0.004)
		4	8 ± 2 (240-248)	(0.011 ± 0.004)
		5	8 ± 3 (300-308)	(0.007 ± 0.003)
		Mean	8 ± 1	(0.011 ± 0.002)
	T3	1	4 ± 2 (60-64)	(0.021 ± 0.011)
		2	5 ± 1 (120-125)	(0.013 ± 0.004)
		3	5 ± 1 (180-185)	(0.036 ± 0.008)
		4	4 ± 3 (240-244)	(0.024 ± 0.018)
		5	6 ± 2 (300-306)	(0.025 ± 0.009)
		Mean	5 ± 1	(0.020 ± 0.003)
	Overall Mean		7 ± 1	(0.013 ± 0.001)
Reformed Crust	T1	1	51 ± 2 (69-120)	0
		2	50 ± 2 (130-180)	0
		3	51 ± 2 (189-240)	0
		4	43 ± 2 (257-300)	0
		5	51 ± 2 (309-360)	0
		Mean	49 ± 1	0
	T2	1	50 ± 2 (69-120)	0
		2	51 ± 2 (130-180)	0
		3	53 ± 2 (189-240)	0
		4	52 ± 2 (257-300)	0
		5	52 ± 2 (309-360)	0
		Mean	52 ± 1	0
	T3	1	56 ± 2 (64-120)	0
		2	55 ± 1 (125-180)	0
		3	55 ± 1 (185-240)	0
		4	56 ± 3 (244-300)	0
		5	54 ± 2 (306-360)	0
		Mean	55 ± 1	0
	Overall Mean		53 ± 1	0

4.4.5 Creeping Evaporites as Environmental Indicators

In section 4.4.3, the results showed that at 50 mb pressure, the $MgSO_4$ & Na_2SO_4 brine did not form creeping evaporites, despite forming a distinctive creeping structure at ambient pressure. To investigate whether the presence of porous media may promote the formation of creeping structures at low pressure by initiating creeping through capillary action, porous rocks were added to the brine.

The addition of the rock to the brine pool allowed some creeping structures to form at low pressure. The maximum vertical extent of the creeping structures decreases with reducing atmospheric pressure. They were (1.06 ± 0.01) mm, (2.28 ± 0.01) mm and (10.09 ± 0.01) mm for 7 mb, 50 mb and 1000 mb respectively (Table 4.9).

A single-factor ANOVA was performed on the maximum extent measurements across the three pressures, to test the null hypothesis that the mean maximum extent of the evaporite structures were the same at each pressure. The p-value was less than 0.0005 (Table 4.10) so the null hypothesis of the ANOVA can be rejected with 99.95% confidence. This suggests there is a statistically significant difference between the means of the maximum extent of evaporite structures formed in the presence of porous media at different pressures. This result suggests there is potential for evaporite structures that formed in the presence of porous media to tell us about the pressure conditions under which they formed. Dendritic mineral assemblages have been observed on the surface of Mars. Some dendritic creeping structures formed from $MgSO_4$ & Na_2SO_4 brine and $FeSO_4$ & Na_2SO_4 brine at ambient pressure were dusted with JSC Mars-1 regolith for a visual comparison to the Martian assemblages (Figure 4.35).

7 mb Pressure

The tendency of the mixture to form a crust at 50 mb, as seen in section 4.4.3, was also apparent at 7 mb despite the sputtering that occurred. However, the crust did not inhibit evaporation sufficiently for any liquid brine to remain beneath the crust by the experiment end. Most of the evaporite material was incorporated into the interfacial crust and the deposits beneath the crust. Figure 4.32 shows each of the triplicates after 4 days at 7 mb. Few secondary creeping structures formed on the rock surface and those that did were very small. The mean maximum extent across the triplicates was (1.06 ± 0.01) mm.

50 mb Pressure

The addition of the rock to the brine pool allowed some creeping structures to form over the rock at 50 mb, similar to those observed at ambient pressure with no rock present, though they were very small (Figure 4.33). The mean maximum structure extent over the triplicates was (2.28 ± 0.01) mm. The tendency of the mixture to form a crust at 50 mb, as seen in section 4.4.3 was still very apparent. Most of the evaporite material was incorporated into the interfacial crust and the deposits beneath the crust as shown in Figure 4.33. The mean maximum extent across the triplicates was (2.28 ± 0.01) mm.

1000 mb Pressure

At 1000 mb many extensive structures formed, using up most of the solution and leaving comparatively little evaporite material in the base of the dish as shown in Figure 4.34. The mean maximum extent across the triplicates was (10.09 ± 0.01) mm.

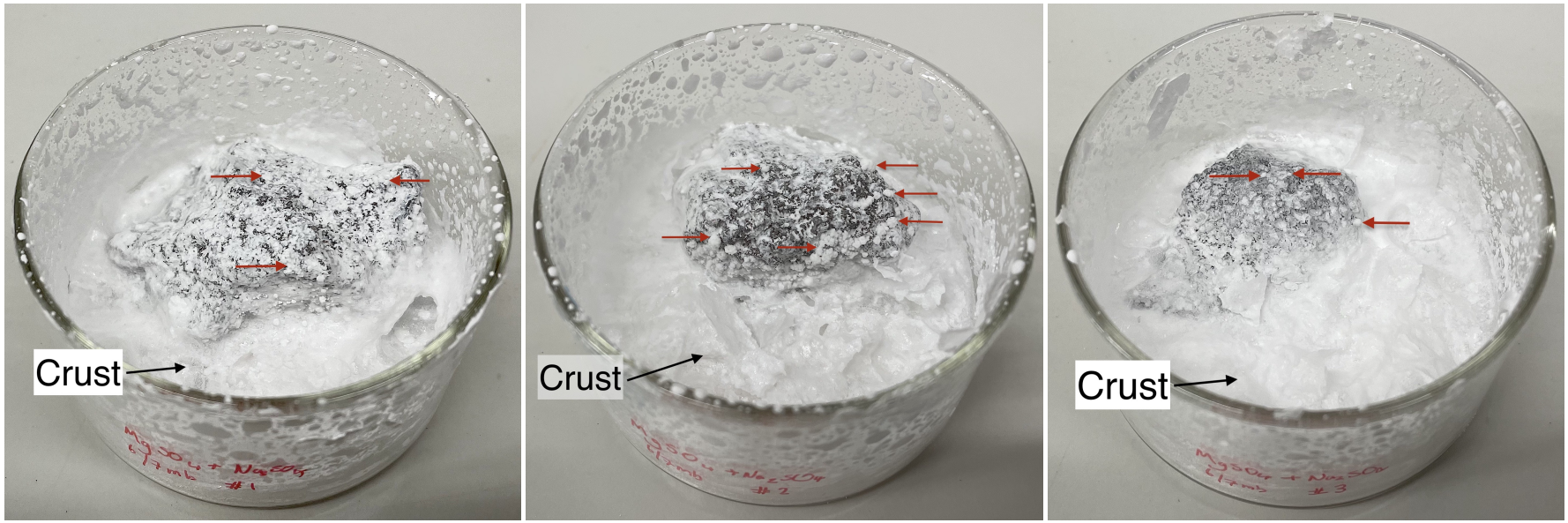

(a) T1 **(b)** T2 **(c)** T3

Figure 4.32: Results of Creeping Evaporites as Environmental Indicators Experiment: Photographs of Secondary Creep Structures Formed on Porous Rock During 4 Days at 7 mb. The red arrows indicate examples of creeping structures. The resultant structures were few and ∼1 mm in extent. T1-T3 are labels for each experiment in the set of triplicates.

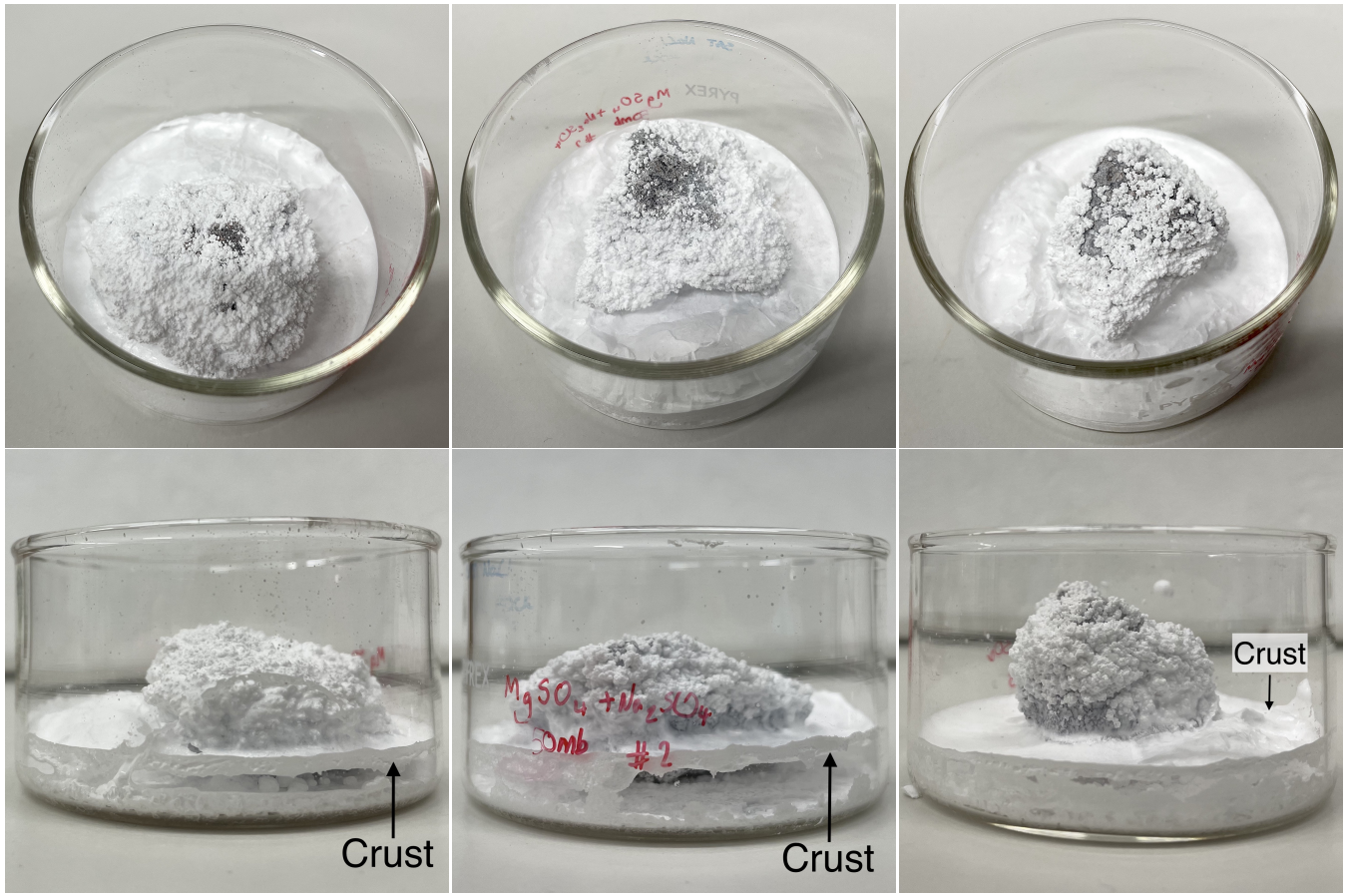

(a) T1 **(b)** T2 **(c)** T3

Figure 4.33: Results of Creeping Evaporites as Environmental Indicators Experiment: Photographs of Secondary Creep Structures Formed on Porous Rock at 50 mb. The red arrows indicate examples of creeping structures. The resultant structures were ∼2 mm in extent. T1-T3 are labels for each experiment in the set of triplicates.

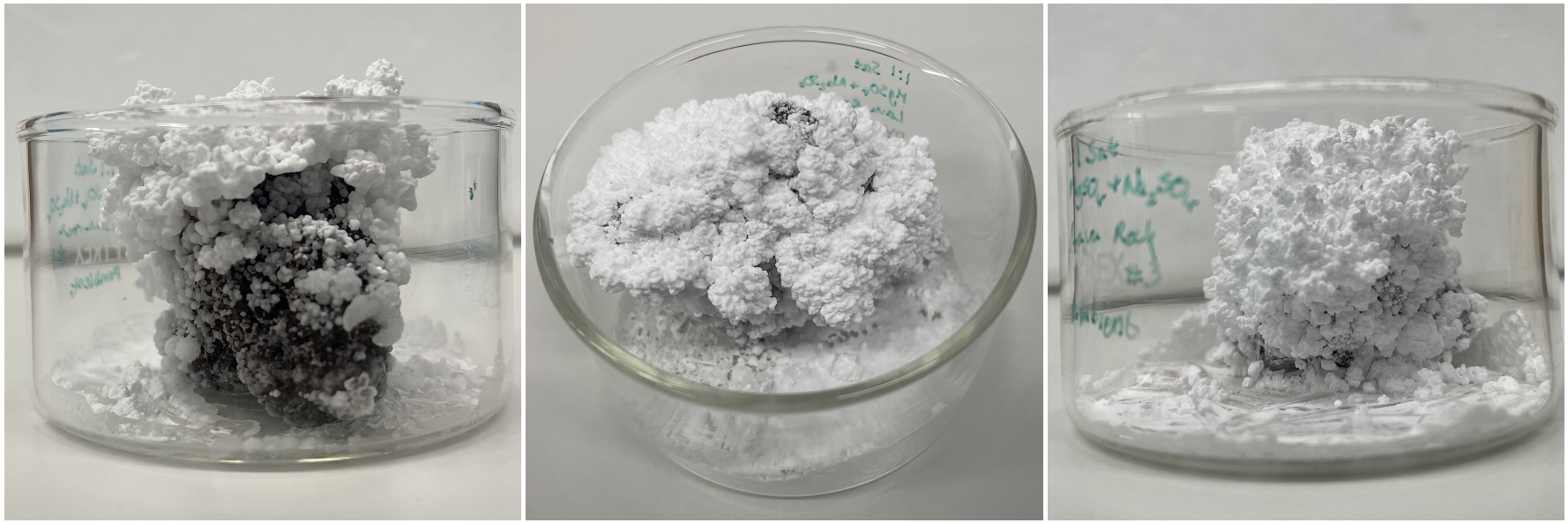

(a) T1 **(b)** T2 **(c)** T3

Figure 4.34: Results of Creeping Evaporites as Environmental Indicators Experiment: Secondary Creep Structures Formed on Porous Rock at 1000 mb. The red arrows indicate examples of creeping structures. The structures were ∼10 mm in extent. T1-T3 are labels for each experiment in the set of triplicates.

Table 4.9: Results of Creeping Evaporites as Environmental Indicators Experiment: Maximum Vertical Extent of Secondary Creep Evaporite Structures Formed in the Presence of Porous Rock at Different Pressures. T1-T3 are labels for each experiment in the set of triplicates.

Pressure [mb]	Triplicate	Maximum Extent [mm]
7	T1	1.01 ± 0.02
	T2	1.14 ± 0.02
	T3	1.00 ± 0.02
	Mean	1.06 ± 0.01
50	T1	2.28 ± 0.02
	T2	2.42 ± 0.02
	T3	2.15 ± 0.02
	Mean	2.28 ± 0.01
1000	T1	10.69 ± 0.02
	T2	9.64 ± 0.02
	T3	9.94 ± 0.02
	Mean	10.09 ± 0.01

Table 4.10: Results of Creeping Evaporites as Environmental Indicators Experiment: ANOVA Test Results for Maximum Structure Extent at Different Pressures.

Source of Variance	F-Critical	F-value	P-value
Pressure	3.12	434	1.31×10^{-41}

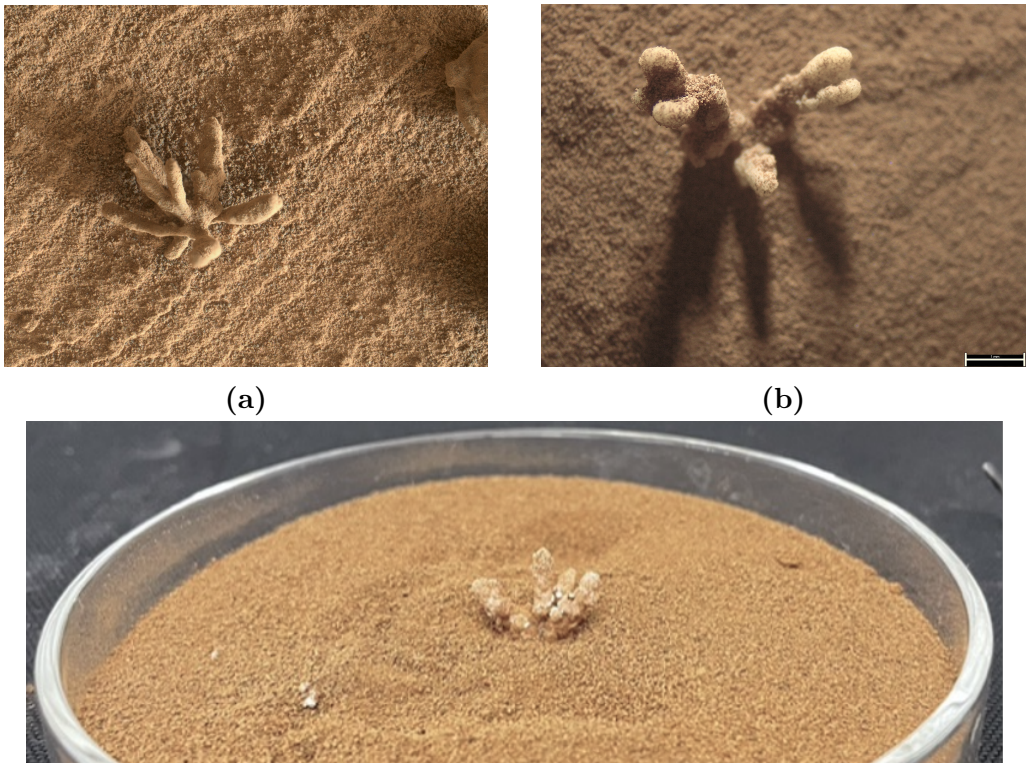

Figure 4.35: Dendritic Martian Mineral Assemblage Compared to Secondary Creeping Structures. (a) Photograph taken by NASA's Curiosity Rover of a dendritic mineral assemblage at Gale Crater(Credit: NASA/JPL-Caltech/MSSS). (b) Photograph of an evaporite structure formed from a $FeSO_4$ & Na_2SO_4 mixture and (c) formed from a $MgSO_4$ & Na_2SO_4 mixture. The structures in (b) and (c) were dusted with and set into a bed of JSC Mars-1 regolith for visual comparison to the Martian assemblage. If distinctive evaporite structures can be preserved on the Martian surface, such features could be used to indicate the pressure conditions under which they formed.

4.4.6 Analogue Microorganism Transport in Creeping Evaporites

For the beaker substrate experiment, the creeping structures that formed were similar in morphology to those previously presented for $MgSO_4$ & Na_2SO_4 evaporites in section 4.4.2, though slightly less dendritic and more cloudy in appearance. Sample T3 formed creeping structures but they did not creep up the beaker wall beyond the level at which the brine surface started at. Secondary creeping upward from the beaker base did occur so samples were taken from those structures. Figure 4.36 shows that the microspheres accumulated primarily at the level that the brine surface began at, forming a yellow band around the beaker. For the rock substrate experiment, the extensive and dendritic creeping structures that formed were very similar to those previously presented for $MgSO_4$ & Na_2SO_4 evaporites in section 4.4.2. Figure 4.37 shows yellow regions in the base and edge of the dish where microspheres have accumulated.

All of the samples taken from creeping evaporite structures that formed from brines containing microspheres had fluorescent microspheres present within them. The mean number of microspheres per gram of salt sample was $(3.29 \pm 0.02)\times10^5$ ms g^{-1} and $(9.54 \pm 0.02)\times10^7$ ms g^{-1} across the triplicates for the beaker and rock experiments respectively (Table 4.11). The control samples contained no microspheres. This implies that microbes could be incorporated into and transported via creeping evaporite structures. The samples taken from the rock interiors also contained microspheres though not enough crystallised salt was able to be collected to perform counts using the hemocytometer. Fluorescence micrographs of the samples taken from each rock interior are shown in Figure 4.38.



(a) T1 **(b)** T2 **(c)** T3

Figure 4.36: Results of Analogue Microorganism Transport in Creeping Evaporites Experiment: Photographs of $MgSO_4$ & Na_2SO_4 Evaporite Structures. Samples were taken from the creeping structures to determine if the microspheres were transported via capillary action during the formation of creeping structures. T1-T3 are labels for each experiment in the set of triplicates.

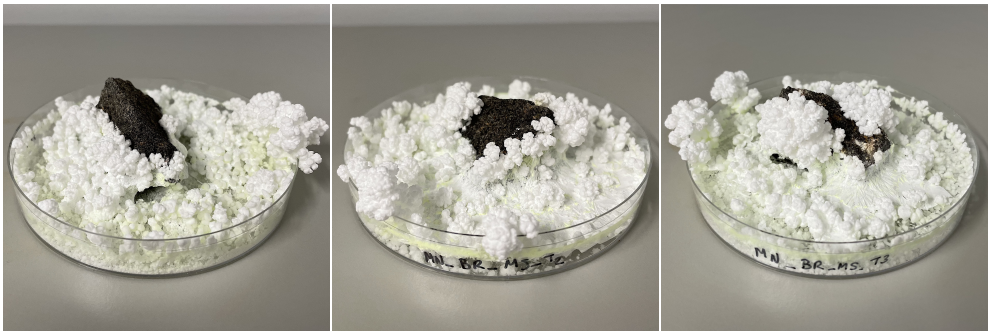

(a) T1 **(b)** T2 **(c)** T3

Figure 4.37: Results of Analogue Microorganism Transport in Creeping Evaporites Experiment: Photographs of $MgSO_4$ & Na_2SO_4 Evaporite Structures on Porous Rock. Samples were taken from the creeping structures to determine if the microspheres were transported via capillary action during the formation of creeping structures. T1-T3 are labels for each experiment in the set of triplicates.

Table 4.11: Results of Analogue Microorganism Transport in Creeping Evaporites Experiment: Mean Microsphere Counts. Mean microsphere counts are presented as number Density - the number of microspheres per gram of solid sample of $MgSO_4$ & Na_2SO_4 evaporite structure [ms g^{-1}]. T1-T3 are labels for each experiment in the set of triplicates. C1-C3 are labels for each control in the set of triplicates.

Substrate	Triplicate	Mean Number Density [ms g^{-1}]
Beaker	T1	$(3.71 \pm 0.04)\times10^5$
	T2	$(1.17 \pm 0.03)\times10^5$
	T3	$(5.00 \pm 0.04)\times10^5$
	Mean	$(3.29 \pm 0.02)\times10^5$
	C1	0
	C2	0
	C3	0
	Mean	0
Basalt Rock	T1	$(1.31 \pm 0.01)\times10^8$
	T2	$(8.04 \pm 0.03)\times10^7$
	T3	$(7.46 \pm 0.04)\times10^7$
	Mean	$(9.54 \pm 0.02)\times10^7$
	C1	0
	C2	0
	C3	0
	Mean	0

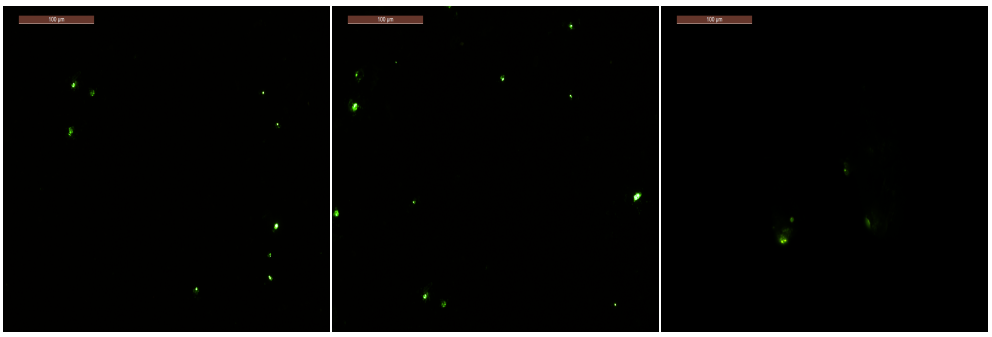

(a) T1 **(b)** T2 **(c)** T3

Figure 4.38: Results of Analogue Microorganism Transport in Creeping Evaporites Experiment: Fluorescent Micrograph of Salt Samples Taken From Rock Interior. The green fluorescent spots are microspheres that have been transported into the rock interior pore spaces, through which brine transport and salt creeping occurred. T1-T3 are labels for each experiment in the set of triplicates.

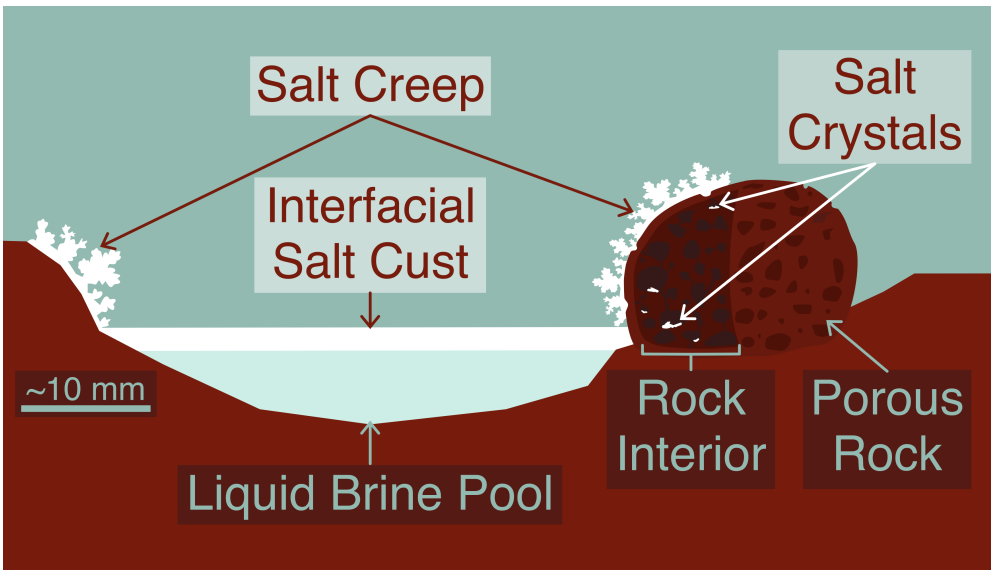

Figure 4.39: Summary Representation of Potential Evaporite Environments on the Surface of Mars. The evaporite structures and putative environments discussed in this chapter are represented together in this diagram. An interfacial salt crust on a shallow brine pool extends the lifetime of an aqueous environment. A rock contains salt crystals within its interior pores, providing a protected environment where biosignatures could be preserved. Habitat-expanding salt creeping structures emerge from the brine pool and from the rock surface.

4.5 Discussion

Brine evaporite environments have been proposed as potential habitats for putative Martian microorganisms. Mars is known to host a variety of salt solids whose bulk behaviour as potential habitats is poorly understood compared to the halite and gypsum crusts widely investigated on Earth. The work presented in this chapter contributes to our understanding of Mars-relevant brine evaporites and their properties of astrobiological interest. We investigated the physical behaviour of salt structures formed via evaporation from saturated brines and their binary mixtures and studied how this behaviour alters the persistence of liquid water and the extent of potential habitats under ambient and low pressure conditions. This work allowed us to develop a systematic and generalised understanding of the major types of habitats formed in salts beyond the more familiar halite and gypsum-based terrestrial evaporites. This was achieved by observing the formation of evaporite structures from ten brines and their pairwise binary mixtures, and determining how their morphology may contribute to the facilitation or expansion of a habitable environment. Brines that formed

particularly distinctive and stable evaporite structures were also studied under low pressure conditions to determine the effect this parameter had on their formation and astrobiologically-relevant properties.

In the main evaporite experiment, the structures that formed fell broadly into three categories: crusts, creeping structures, and a combination of both. The properties of interest in a habitability context were the preservation of liquid water and the ability to form new habitat space for crusts and creeping structures respectively. Another property of interest was the potential for distinctive creeping structures to act as environmental indicators. A representation of potential Martian evaporite environments exhibiting these properties is presented in Figure 4.39.

For the pure brines that formed evaporite macrostructures, the following observations were made, suggesting that anions broadly control the morphology of evaporite structure formed

- Sulphate brines form interfacial crusts
- Chloride brines form creeping structures
- Perchlorate brines form both crusts and creeping structures.

It was observed that binary mixtures of saturated salt solutions generally exhibited evaporite morphologies that were a combination of the evaporite morphologies of their constituent brines. There were two cases of mixed brines that formed an evaporite structure that reflected neither of the evaporites formed from the constituent brines. When Na_2SO_4 brine was mixed with another highly soluble sulphate salt solution ($FeSO_4$ or $MgSO_4$), dendritic secondary creeping structures formed, despite their constituent brines all forming crusts.

4.5.1 Crusts

One of the primary morphological categories of evaporites observed was the interfacial salt crust. Many of the crusts that formed were effective at inhibiting evaporation from the sub-crust brine as can be seen by the reduction in mass loss rate after crust formation. When compared to evaporation from the water control, which evaporated completely within ∼13 days, the presence of these salts

in solution can be seen to significantly extend the lifetime of liquid water. The presence of a salt crust further extends the liquid water lifetime. The $MgSO_4$ crust was particularly effective, reducing the mass loss rate from the brine by 108 times after the crust formed and preserving ∼30 mL of solution beneath the crust after 11 months. The crust was very stable and did not deliquesce at any point. $MgSO_4$ was the only pure crusting brine to retain sub-crust solution at the end of the experiment. The $FeSO_4$ crust retained some solution for at least 216 days. The Na_2SO_4 crust was not effective at preventing evaporation and the solution evaporated within 14 days. All of the mixed brines that formed only crusts retained some sub-crust liquid at the end of the 11 month experiment with the exception of of $CaSO_4$ & $FeSO_4$ and $CaSO_4$ & Na_2SO_4. However, most of the those mixtures contained either $CaCl_2$ or $Ca(ClO_4)_2$, whose pure brines did not form evaporites due to their highly hygroscopic nature preventing sufficient evaporation taking place. It is unclear whether the solution beneath the crusts for these mixtures was preserved as a consequence of the formation of a crust or due to their hygroscopicity. Further experiments would be required to determine this. Crusting binary mixtures that retained solution and did not contain either $CaCl_2$ or $Ca(ClO_4)_2$ were $CaSO_4$ & $MgSO_4$ and $FeSO_4$ & $MgSO_4$ - both mixtures containing $MgSO_4$. This highlights the ability of the $MgSO_4$ crusts to inhibit evaporation under ambient pressure conditions.

Due to the observed efficacy of the $MgSO_4$ crust in inhibiting evaporation, its formation was investigated under low pressure (50 mb) conditions. The brine readily formed a salt crust under these conditions though outgassing from the solution caused partial breakages of the crust, during which time the mass loss rate from the solution increased significantly. The experiment where the crust was manually broken highlighted this evaporation-inhibiting effect under both ambient and low pressure conditions. There was however a notable difference between the time taken for the crust to reform between the manual breakage and outgassing breakage low pressure experiments. For the experiments investigating the formation of the $MgSO_4$ crust at 50 mb, after the crust was partially broken due to outgassing it took more than a day to reform. In the experiments where the crust was broken manually at 50 mb, it typically reformed within ten minutes, subsequently preventing mass loss from the brine until the crust was broken again the following hour. A possible explanation for this difference is that in the experiments where the crust is manually broken, the whole crust is broken and falls into the body of the solution. This exposes the entire liquid surface to the dry atmosphere inside the chamber allowing evaporation to occur rapidly,

consequently causing precipitation to occur rapidly and a contiguous crust to reform. In the experiments where the brine is undisturbed only a partial crust breakage occurs. Here the breakage was located where the solution was no longer in contact with the brine due to a gas bubble exerting pressure on the crust, which eventually caused the puncture. The broken region was small and humidity may have built up between the brine interface and the remaining crust. This would result in a slow evaporation rate and therefore take longer for the crust to reform in that region.

These results show that brines that form crusts can preserve liquid water over extended periods of time. This is consistent with naturally-occurring terrestrial examples, where halite and gypsum crusts preserve brine and briney soil in hot, arid environments [111, 114–116]. This is also consistent with work examining brines under current Mars temperature and pressure conditions. Hudson et al. (2008) found that heavily $MgSO_4$-encrusted soils inhibited water diffusion [173]. When investigating the evaporation rate of brines under Martian surface conditions, Altheide et al. (2009) noted that the formation of salt crusts correlated with reduced evaporation rates from sulphate brines [165].

Implications for Habitability

Our data show that on present and early Mars interfacial salt crusts can act as an evaporation barrier, maintaining liquid brine under conditions where water would otherwise rapidly evaporate. Though many of the pure and mixed brines exhibited interfacial crusts, the most efficacious at inhibiting evaporation and preserving substantial volumes of sub-crust solution was $MgSO_4$. Observations of the Martian surface show that Mg^{2+} and $SO_4{}^{2-}$ ions are widespread and abundant ions and direct detections of $MgSO_4$ associated with historic aqueous processes have been made [32, 34, 35, 76, 147]. There are several terrestrial examples of natural $MgSO_4$ saturated lakes subject to freezing temperatures that are inhabited by diverse and abundant microorganisms [83, 85]. Furthermore, several organisms, including non-halophiles have been shown to grow in saturated $MgSO_4$ [85, 141].

Locations with a particularly high relative abundance of $MgSO_4$ could be sites where the lifetime of the last vestiges of liquid water was extended by salt crusts (an example of such a putative environment is depicted in Figure 4.39), providing a habitable refugia as Mars transitioned from Earth-like to the

inhospitable environment of the present day. This, combined with the existence of inhabited terrestrial $MgSO_4$ saturated lakes and the ability of salts to preserve biosignatures, makes $MgSO_4$ deposits on the surface of Mars regions of particular astrobiological interest.

4.5.2 Creeping Structures

The second primary morphological evaporite category observed was the creeping structure. The binary mixtures of saturated $FeSO_4$ & Na_2SO_4 and $MgSO_4$ & Na_2SO_4 produced particularly stable and pronounced dendritic creeping structures. Perchlorate brines produced more spatially extensive creeping structures that crept over the top of the beaker, down the side, over the bench-top and into adjacent beakers.

This self-amplifying creeping mechanism was able to transport microbial analogue microspheres over at least centimetre scales. Samples of the evaporite structure that formed on a porous rock from the binary mixture of $MgSO_4$ & Na_2SO_4 doped with microspheres contained an average of 9.54×10^7 ms g^{-1} and microspheres were present in the rock interior. This demonstrates that micron-sized objects can be transported by the creeping mechanism. This process could transport microorganisms, liquid water and nutrients to environments more conducive to survival and proliferation. For example, microbes in a brine pool could be transported via the creeping mechanism into the interior porespace of a rock where they would be protected from UV radiation and where liquid water may persist within the pore space. On Earth, there are examples of refugia where centimetre-scale environmental variations can be the difference between life and death for microorganisms in environments with hostile conditions [43, 104]. For example levels of culturable bacteria in soil samples from the most arid locations in the Atacama desert are extremely low [102, 174] compared to microbial oasis environments within rock interiors where abundant and diverse communities of microorganisms persist [175]. The solutions that display creeping evaporite behaviours demonstrate a mechanism for habitat expansion and transportation between microenvironments in hypersaline environments.

The incorporation of micron-sized objects into the structure of the evaporite of the binary mixture of $MgSO_4$ & Na_2SO_4 demonstrated here also has implications for the search for preserved biosignatures on Mars. The relative stability of the structure, compared to many of the other creeping structures that deliquesced

readily, make it interesting from a preservation perspective. There are examples of possible fossilised microbes in terrestrial sedimentary salt deposits [176, 177] and even purported example of cells cultured from ancient salt fluid inclusions sampled from a range of terrestrial evaporite deposits [58, 121–126]. The results presented here are an example of analogue microorganisms becoming incorporated into the structure of evaporites formed from brine composed of ions that have been observed on Mars. However, further research is required to ascertain the long-term stability and biosignature preservation potential of the $MgSO_4$ & Na_2SO_4 evaporite under Martian conditions.

At at ambient pressure, the binary mixture of $MgSO_4$ & Na_2SO_4 produced a distinctive and extensive creeping structure with dendritic morphology. The same mixture under 50 mb atmospheric pressure conditions produced no such structure, instead forming an interfacial crust. A potential explanation for this is that creeping may not have been able to initiate due to the rapid rate of evaporation that occurs under low pressure conditions. Qazi et al. (2019) studied the mechanism that initiates salt creeping. They observed that initially, when crystals form at the interface near the meniscus, they fall into the body of the solution due to their mass. As evaporation occurs, the contact angle of the meniscus decreases due to the meniscus being pinned to the substrate. Eventually, sufficient evaporation occurs such that a critical angle is reached and precipitating salt crystals become trapped between the meniscus and the substrate, initiating creeping. At low pressure, higher evaporation rates could lead to evaporative cooling of the brine. The surface tension of water[178, 179] and brines [180, 181] increases with decreasing temperature, leading to a greater meniscus contact angle. This could prevent the trapping of crystals between the meniscus and the glass and hence prevent the initiation of creeping. Rapid evaporation increases the concentration of ions at the surface, which can also increase surface tension and consequently increase the contact angle [181, 182]. Additionally, higher evaporation rate and evaporative cooling can induce supersaturation, increasing crystal nucleation rate and leading to the precipitation of more, smaller crystals at the liquid-gas interface compared to a low evaporation rate [183, 184]. These smaller crystals would be less likely to fall into the body of solution and thus are more likely to be able to form a crust. The formation of a crust may then cut off the solution from the three-phase boundary and prevent creeping from occurring, an effect that has been observed in evaporating brine droplets [134]. This hypothesis could be confirmed by the photography and measurement of contact angles similar to the work done by Qazi et al. (2019) but in a low-

pressure environment.

To further understand the physical behaviour of creeping under low pressure conditions, we added porous media to the mixture of $MgSO_4$ & Na_2SO_4 and exposed it to 7 mb, 50 mb and 1000 mb pressure conditions. The roughness of the rock created a more wettable surface and the porosity allows for capillary action to occur, both allowing for the formation of primary crystals that can initiate creeping. This allowed creeping structures to form on the porous rock surface. However their maximum extent was limited by pressure. The maximum extent of the structures decreased with decreasing atmospheric pressure, suggesting that it is possible for creeping to initiate and structures to form at low pressure but there is some factor limiting their growth. A possible explanation for this is the rapid evaporation rate at low pressure may cause precipitation to occur before solution can be wicked up over previously formed salt crystals, resulting in the small structures observed. If the film of solution cannot extend up the primary crystal growth, then further crystal growth cannot take place, limiting the extent to which creeping structures can grow. It is possible the structure extent was limited by the volume of solution available. A large proportion of the precipitated salt was deposited in the base of the dish however, suggesting that most of the brine evaporated from the dish rather than the rock or creeping structure surfaces. Future experiments should be performed with a larger reservoir of solution available to determine how the availability of brine affects creeping structure extent.

This work has shown that atmospheric pressure can affect the maximum extent of evaporite structures formed in the case of $MgSO_4$ & Na_2SO_4 producing a distinctive dendritic creep structure at ambient pressure and a crust at 50 mb. Dendritic mineral assemblages, like the examples in Figure 4.6 have been observed on Mars at Gale crater. Other dendritic structures in that region have been analysed and are enriched in Mg, interpreted as $MgSO_4$ [129, 130]. Dendritic evaporite structures with a similar morphology to the Gale crater structures formed from the binary mixtures of $FeSO_4$ & Na_2SO_4 and $MgSO_4$ & Na_2SO_4 (Figure 4.35). This work showed that under low pressure (50 mb) conditions, the creeping structures of $MgSO_4$ & Na_2SO_4 did not form unless a porous rock was present to facilitate creeping. Creeping then occurred under 50 mb and even 7 mb pressure conditions, but the structures that formed were very small and not very dendritic, exhibiting a more cloudy or cauliflower-like appearance. The maximum extent of the creeping structures decreased with

decreasing pressure. Structures like those observed at Gale crater suggest that - potentially $MgSO_4$ - mineral assemblages can be preserved or uncovered at the Martian surface. The preservation of evaporite structures would be highly dependent on their physical properties such as hardness and solubility as well as the environmental conditions experienced post formation. Preserved creeping evaporite assemblages that are well characterised could be used as environmental indicators, providing insight into the pressure environment at the time of their formation and the environmental conditions post formation. The preservation potential of the structures could be established by quantifying their physical properties and understanding their resilience to various Martian environmental conditions. Further study is also required to determine the extent to which other environmental factors such as temperature and relative humidity affect the formation of these mineral structures in order to rigorously establish their potential as environmental indicators.

4.5.3 Crusts and Creeping Structures

In the brines where both crusting and creeping structure formed, many of the creeping structures continued to grow gradually despite the formation of a crust. In most cases, this creeping occurred very gradually over the course of the experiment, suggesting that the crusts do contribute to the preservation of the brine but the creeping structures eventually win out and deplete the sub-crust solution fully. As discussed previously these creeping structures are also likely to be able to transport micron-scale objects. These brine therefore have both the ability to extend the lifetime of liquid water beneath their crusts and expand habitats through their creeping structure formation.

4.5.4 Deliquescence of Evaporite Structures

Some of the evaporite structures that formed from $MgCl_2$, $Mg(ClO_4)_2$, and $NaClO_4$ and binary mixtures containing one or more of them, partially dissolved due to a period of weather-induced elevated humidity and the highly deliquescent nature of chloride and perchlorate salts [27, 185]. Despite the instability of these evaporites limiting their potential to preserve biosignatures, their deliquescent nature could allow the formation of transient liquid water habitats under Martian surface temperature conditions as their eutectic temperatures are very

low [28, 166]. During periods of suitable temperature and humidity, chloride and perchlorate-containing evaporites on the Martian surface could deliquesce, producing transient liquid brine, potentially providing an ephemeral habitable environment. Then, when evaporation occurs, putative microbes entombed in crystals or protected under crusts could survive in a dormant state until the next period of elevated humidity. These deliquescent brines formed creeping or crusting & creeping evaporites, even when in binary mixtures, with the exception of $FeSO_4$ & $MgCl_2$. The mixture $MgSO_4$ & Na_2SO_4 was able to transport micron-sized objects throughout its creeping structure as it formed. It is likely that the creeping structures formed from these more hygroscopic brines would also be able to do so. This is supported by the observation of the $Mg(ClO_4)_2$ creep which, as it crept over the beaker label, incorporated red ink particles into the creep and transported them throughout the structure, turning sections pink. Ink pigment particles are typically an order of magnitude smaller than the microspheres used so the applicability to putative microorganisms would need to be confirmed in a similar microsphere experiment. These deliquescent creeping structures could allow for the transfer of putative resident microorganisms to new nutrient sources or more protected environments, encouraging their survival and proliferation, and providing them with transient liquid water under clement environmental conditions.

4.5.5 Limitations and Further Work

This work focused on developing a systematic and generalised understanding of the major types of habitats formed in Mars-relevant salts beyond the more familiar halite and gypsum-based terrestrial evaporites. Select brines were also studied under low pressure conditions to determine how this factor affected the formation and properties of their evaporite structures. The effect of pressure was found to be dependent on the individual brine, with $MgSO_4$ and Na_2SO_4 forming crusts similar to their ambient counterparts but the mixture of $MgSO_4$ & Na_2SO_4 forming a crust instead of a creeping structure like it's ambient counterpart. It is therefore important to test each individual brine to establish the behaviour of its evaporites under low pressure conditions. Now that the typical evaporite structures have been established for a range of pure and mixed Mars-relevant brines under ambient pressure conditions, this work could be built upon by studying the formation and properties of evaporites formed from these brines under low pressure conditions, in addition to those studied in this thesis. This

would further our understanding of the habitability of potential Martian brines and reveal if the suppression of creeping and promotion of crust formation is a universal effect of low pressure conditions across creeping brines.

Environmental Conditions

The climate controlled room could maintain a constant temperature and the relative humidity was usually $\leq$25%. However, dramatic variations in weather affected the humidity, causing the very hygroscopic evaporites to deliquesce. The experiment would be improved through the use of a climate chamber that can accurately control both temperature and relative humidity.

The PES chamber was not capable of temperature control, accurate humidity control, or atmospheric composition control. In future if these controls could be implemented, the individual and coupled effects of temperature, humidity, and atmospheric composition on morphology and physical behaviour of evaporites should be investigated to contribute further to our understanding of the habitability of these environments under past and present Martian conditions.

Liquid Water Longevity in Mixed Deliquescent Brines

Many of the mixed brines produced evaporites that had an interfacial crust element. Some of these mixtures were composed partially of highly hygroscopic $CaCl_2$ and $Ca(ClO_4)_2$ solutions. As pure brines, $CaCl_2$ and $Ca(ClO_4)_2$ did not form evaporites. Under the experimental conditions and time-frame they were unable to evaporate sufficiently for precipitation to occur. In mixed brines containing these salts, the longevity of liquid brine could be attributed to this hygroscopicity, rather than the effect of an interfacial crust. To determine the contributions of the hygroscopicity of the brine and the crust to the longevity of the sub crust brine, experiments similar to those presented in section 4.3.3, where the crust is regularly broken could be performed. In particular the mixtures of $CaCl_2$ & $FeSO_4$, $CaCl_2$ & $MgSO_4$, $CaCl_2$ & Na_2SO_4, $Ca(ClO_4)_2$ & $FeSO_4$, $Ca(ClO_4)_2$ & Na_2SO_4, and $Ca(ClO_4)_2$ & $MgSO_4$ should be investigated as these all had liquid brine preserved beneath their crusts at the end of the 11 month experimental period.

The Physical Behaviour of Creeping Evaporites

Several of the more hygroscopic brines studied ($Mg(ClO)_4$ and $NaClO_4$ and some mixtures containing one or both of them) readily formed surface creeps that were evenly distributed across the glass beaker walls. The creeping evaporite of $MgSO_4$ & Na_2SO_4 only initiated creeping from a few discrete points on the beaker wall. Brines that creep evenly across the substrate could also be studied at low pressure to determine whether atmospheric pressure affects their ability to initiate creeping. This would contribute to our understanding of the physical behaviour of brines which creep very readily and their astrobiological potential. Building on this, it would be useful to determine the spacial limit of surface creeping brines. Experiments should be performed with a greater reservoir of solution available. This would allow for the investigation of whether more extensive structures could form if a greater supply of solution was available or if the limitation of structure extent was due primarily to atmospheric pressure. This would also contribute to our understanding of the potential for these brines to expand habitat space.

The Effect of a $MgSO_4$ Crust on Evaporation at Ambient Pressure

The $MgSO_4$ crust breakage experiment performed under ambient pressure conditions had mass measurements taken hourly. This experiment would benefit from being repeated using continuous mass measurement as was the case with the 50 mb experiment. This would give a more accurate picture of how quickly crust formation occurs under ambient pressure conditions and how this correlates with mass loss rate.

Creeping Evaporite Transport Mechanism

The microsphere transport through evaporite creeping media experiment should be repeated at low pressure to quantify the effect of atmospheric pressure on the ability of creeping structures to transport micron-scale objects. Additionally the experiment could be repeated under ambient and low pressure conditions using other creeping brines such as $Mg(ClO_4)_2$ and $NaClO_4$ to establish whether the transport mechanism is universal across creeping brines. This would contribute further to our understanding of the potential of salt creeps to expand putative habitats under Mars surface conditions.

Microspheres in Salt Crystals Salt Within Rock Pores

Microspheres were observed in salt crystals within the porous rock used in the salt creep transport experiments. This has implications for the preservation of biosignatures on the surface of Mars. Microscopy could be performed with carefully harvested and prepared samples to determine whether these microspheres were incorporated into inclusions in the crystal structure, or if they resided in interstitial spaces. This would be useful in determining the potential of salt crystals within rock pores for preserving biosignatures like the terrestrial examples previously discussed. Furthermore, if there are intracrystalline inclusions containing fluid, this could have implications for using such crystals as environmental indicators.

Creeping Evaporites as Environmental Indicators

Future experiments investigating the potential for creeping structures to be used as environmental indicators could include the use of other substrates and other brines. In particular, the formation of evaporites from a mixture of $FeSO_4$ & Na_2SO_4 should be investigated under low pressure conditions given their strong resemblance to the coralloid structures observed on Mars. Here the effect of porous rock on the formation of creeping structures was studied under ambient and low pressure conditions. The effect of other types of porous media such as regolith and rocks of varying porosity and pore-size distribution on the formation and extent of creeping structures should also be investigated.

4.6 Conclusions

Saturated solutions of salts comprising ions observed on Mars' surface, and binary mixtures of such solutions, produce distinct evaporite structures with different astrobiological implications.

The systematic study of the pure and mixed brines revealed that generally the anion of the salt dictates the morphology of the evaporite structure formed and that mixed brines form evaporites that are a combination of the structures formed by their constituent brines, with a few notable exceptions.

The results presented here demonstrate that brine evaporite crusts that could have existed in the past on Mars have the ability to inhibit evaporation and extend the lifetime of liquid water. The crust formed by the $MgSO_4$ brine could extend liquid water lifetime significantly, even under low pressures, suggesting that as the surface of Mars transitioned to its present desiccated state, salts could have preserved the last remnants of surface water and created an encrusted aqueous refugia.

These results also show the intriguing potential for certain salts to expand habitats through the formation of creeping structures that can transport analogue microorganisms to potentially new microhabitats with more favourable local conditions for growth and/or preservation.

Furthermore, distinctive dendritic creeping evaporites have the potential to be used as environmental indicators due to their maximum extent being limited at low pressure.

In summary, this chapter shows that diverse salts that are uncommon on Earth but more prevalent on Mars have bulk evaporative properties that can improve the conditions for habitability at small scales. These results have implications for the habitability potential of briny environments on Mars as evaporite environments may have been locations of the last vestiges of liquid water as the planet's surface became more hostile.

Chapter 5

The Lifetime of Liquid Water in Porous Media at Low Pressure

5.1 Introduction

In the early 20th century the desolate landscape of the McMurdo dry valleys in Antarctica was thought to be devoid of life. Robert Scott, the explorer who led the pioneering expedition there, dubbed the region 'a valley of the dead' [186]. Well into the latter half of the century, the soils there were still considered virtually sterile [187]. However in the late 1970's, surprisingly complex communities of microorganisms were discovered taking refuge from the inhospitable conditions in the pores of rocks [53]. Further investigation revealed the rocks could retain moisture despite the extremely arid exterior conditions, providing the water imperative to the survival of these communities [79, 188].

The presence of these complex communities in such an extreme environment, which has been compared to the surface of Mars due to their common freezing, arid, and high UV conditions, raises the question of whether similar environments could have provided a refuge to putative Martian life during the planet's history.

Many of the rocks that have been investigated by the rovers of Mars bear indications of interaction with liquid water in their interiors, with some of these interactions considered to have taken place relatively recently [38]. Some of those rocks, spotted by Opportunity rover at Endeavour Crater, had a bright white coating found to be an encrustation of sulphate salts [189]. In the

previous chapter, we observed that some sulphate salts are effective at preventing evaporation by the formation of crusts. These factors indicate that the effect of dissolved salts on the longevity of liquid brine inside porous rock environments should be considered.

By understanding the limits of the conditions under which liquid water can persist in these environments, this work aims to contribute to the identification of sites of high habitability potential on the surface of Mars. If identified to have good habitability potential, porous rocks with signs of recent interaction with water on the Martian surface could constitute appealing targets for life and biosignature seeking missions as they are relatively easy to access and sample.

This chapter will investigate the habitability of porous rocks on the Martian surface and shallow subsurface by determining the extent to which porous media can extend the lifetime of liquid water under ambient and low pressure conditions. In particular, the following questions will be addressed:

- How does the presence of porous media affect the lifetime of liquid water under ambient pressure conditions?
- How does the presence of porous media affect the lifetime of liquid water under low pressure conditions?
- How does the presence of sulphate salts in solution affect the lifetime of liquid water in porous media at 7 mb pressure?

5.2 Background

5.2.1 Terrestrial Endolithic Habitats

Endoliths are rock inhabiting microorganisms [190]. They include epiliths that inhabit exterior rock surfaces, chasmoendoliths that inhabit cracks and fissures in rocks, hypoliths that inhabit the underside of rocks, and cryptoendoliths that inhabit the interior pore spaces and vesicles of rocks (Figure 5.1). Communities of endolithic microorganisms are found in manifold extreme environments across the world. They were first noted in hot deserts by Friedmann et al. (1967), who described cyanobacterial communities populating sandstone, limestone, and chalk rocks in the Negev desert (Figure 5.2a) [79]. Subsequently, endolthic communities have been observed in hot desert environments worldwide [191, 192] including in the Mojave desert [50, 80, 193] and the hyper-arid Chilean Atacama desert [194]. Communities of endolithic microorganisms have also been studied in the polyextreme environment of the McMurdo Dry Valleys, Antarctica, where life must contend with frigid temperatures, xericity, high UV irradiation and high winds. Here, endoliths inhabit sandstone, granite and marble rocks (Figure 5.2b) [53, 195–198]. Endolithic communities have also been found in porous shocked gneiss in the high Arctic [199, 200] and vesicular basalt glasses in Iceland [201] (Figure 5.2d) . The communities of the Arctic, Antarctic and hot deserts are typically dominated by photosynthetic cyanobacteria and lichens. However, communities consisting predominantly of non-photosynthetic organisms have been sampled from surface vesicular basalt rocks in Iceland and the Arctic [202, 203] as well as continental subsurface [204, 205] and sub-ocean crustal vesicular basalt environments [206, 207].

Cryptoendolithic communities can persist in polyextreme environments due to the protection from environmental stressors provided by the rocks they inhabit. The rock can provide protection from harsh exterior conditions, including UV irradiation, aridity, high winds, and extremes of temperature. The Atacama desert, one of the most extreme and Mars-like environments on planet Earth, hosts endolithic communities in the hyper-arid region, where soils are virtually abiotic [102, 208]. Vesicular ignimbrite rocks inhabited by microorganisms (Figure 5.2c) have been shown to retain moisture after wetting events [175]. Measurements taken of the relative humidity within semi-desert sandstones and the exterior air showed the humidity to be consistently higher within the rocks

[56, 209]. Similarly, rocks in Antarctica have been shown to retain moisture for days after the air humidity has dropped significantly [52, 188, 191, 200, 210]. Rocks also provide a shield from the high levels of UV radiation received in the dry valleys, with only a millimetre of rock needed to attenuate UV sufficiently to protect resident endoliths [211–214]. In the dry valleys, temperatures at the surface of inhabited rocks have been found to be up to ∼20°C higher than the exterior air due to solar-heating, buffering the endoliths from the extreme cold temperatures of the Antarctic desert [215, 216].

Endolithic environments have the additional benefit of potentially preserving evidence of the organisms that colonised them over periods of hundreds of millions years [62, 217, 218] or possibly even billions of years [219]. There are many examples of vesicular basalts hosting fossil endoliths, typically from oceanic crusts [62, 217, 218, 220–222], but also in continental crusts [63]. However, the validity of some reported fossils has been challenged due to the abiotic cultivation of morphologically similar structures - biomorphs - in 'chemical gardens' in a laboratory setting [64, 65].

Vesicular basalts have been discussed as potential sites of astrobiological interest on Mars [223, 224] as they exhibit several properties that could contribute to habitability in surface and subsurface environments throughout Mars' history. Their high porosity and permeability allows liquid water to enter and distribute within the rock interior [225, 226]. Components of the rocks themselves can act as abundant nutrient sources for microbial metabolisms [227, 228]. The high internal surface area caused by the presence of vesicles acts as a good substrate for microbial colonisation [223]. These properties, combined with presence of inhabited vesicular rocks in extreme environments on Earth, make vesicular rocks in Martian surface environments where long-lasting or transient liquid water was present interesting as potential habitats or sites of biosignature preservation.

5.2.2 Martian Vesicular Rock Environments

Orbital observations and in-situ analysis have shown that Mars' crust is largely basaltic in composition [146, 229–235]. Furthermore, observations of highly porous, vesicular basalt rocks have been made at several locations on the planet's surface. Highly pitted rocks, likely to be vesicular basalt, were first observed at the Viking 2 lander site (Figure 5.3) [74, 236]. At Gusev crater the Spirit rover observed many highly vesicular rocks, examples of which are presented

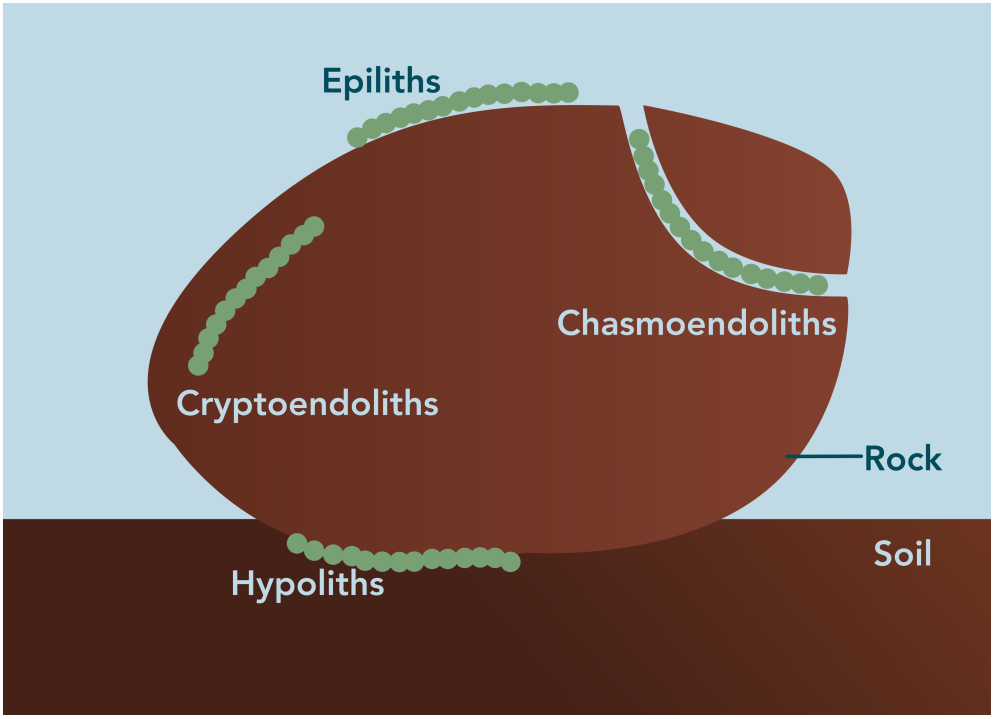

Figure 5.1: Endolithic habitats. The green filaments represent microbial communities inhabiting a rock. Epiliths populate the rock surface. Chasmoendoliths inhabit rock fractures and fissures. Hypoliths populate the rock underside. Cryptoendoliths inhabit rock pores and vesicles. Diagram is not to scale. Adapted from Ramond & Cowan (2022) [192] and Wierzchos et al. (2018) [208].

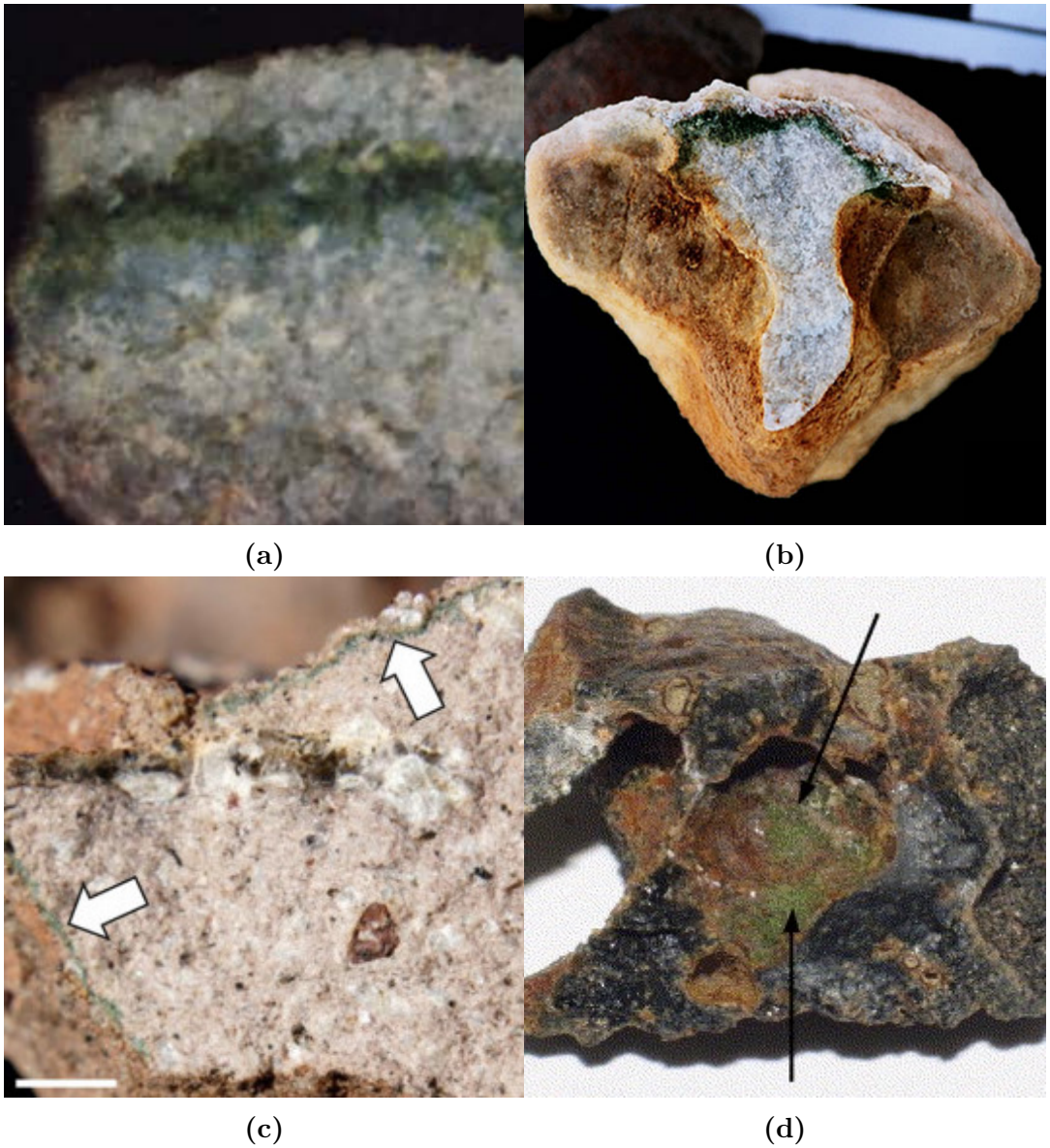

Figure 5.2: Endolithic Microorganisms in Various Lithic Environments. (a) Sandstone from the Negev desert, Israel. The green band is a community of cyanobacteria (from Friedmann et al. (1967) [79]). (b) Sandstone from the dry valleys of Antarctica. The green band is an endolithic colony (adapted from Archer et al. (2017) [198]). (c) Ignimbrite from the Atacama desert, Chile. The green cyanobacteria colonies are indicated by the arrows (adapted from Meslier et al. (2018) [194]). (d) Vesicular rock from Svalbard. The arrows indicate the endolithic colonies (from Jorge Villar et al. (2006) [203]).

in Figure 5.3 [237–239]. Rocks in the region that had their interiors sampled exhibited evidence of alteration by interactions with water [158]. Analysis of nearby regolith suggested the presence of up to 22% wt of hydrated Mg-, Fe- and Ca- sulphates salts in the regolith [158]. Vesicular float rocks have been observed at Murray Ridge on the edge of Endeavour Crater, Meridiani Planum, in a region where aqueous alteration has taken place and sulphate salts are present [240]. Pinnacle Island, a basaltic rock accidentally uncovered by the wheels of the Opportunity rover at Murray ridge, was encrusted with a bright white coating (Figure 5.4) interpreted as $MgSO_4$ and other sulphate and chloride salts thought to be precipitated from aqueous solutions [189]. At Perseverance Valley, Endeavour crater, there is an outcrop of pitted rock that may be vesicular [241]. Furthermore, analysis of the composition differences between the exterior and interior of rocks at Perseverance Valley suggest repeated and recent emplacement of salts by ephemeral liquid water [38]. Recent photographs taken at Jezero crater by the Perseverance rover show rocks with holes and pits that may be vesicles [40, 159, 242, 243]. There is evidence of perchlorate and sulphate salts including $MgSO_4$ within rock pores suggesting that alteration of the rocks by aqueous brines has occurred [39, 40]. Vesicular float rocks have also been observed at Gale crater by the Curiosity rover [244–246]. The observation of vesicular rocks on the Martian surface at locations where historic and possibly recent interactions with liquid water resulting in the deposition of salts has occurred, combined with observations from the Chapter 4 that some brine evaporites are effective at inhibiting water loss, even under low pressure conditions, highlights the astrobiological potential of these environments.

5.2.3 Water and Brines in Porous Media

One of the properties that contribute to the habitability of endolithic environments is the retention of liquid water and humid air within the pore space. Rocks colonised by endoliths in hot and cold deserts have been shown to shown to absorb moisture from humid air [57] and retain moisture after wetting events, even when the exterior air is very dry [52, 56, 188, 191, 200, 209, 210]. The retention of moisture in porous media is a phenomenon that has been noted and studied in the construction industry and cultural heritage conservation due to the effect internal water can have on the efficacy and degradation of building materials [247, 248]. Liquid water has been shown to persist for many days in small samples of various stone building materials under ambient environmental

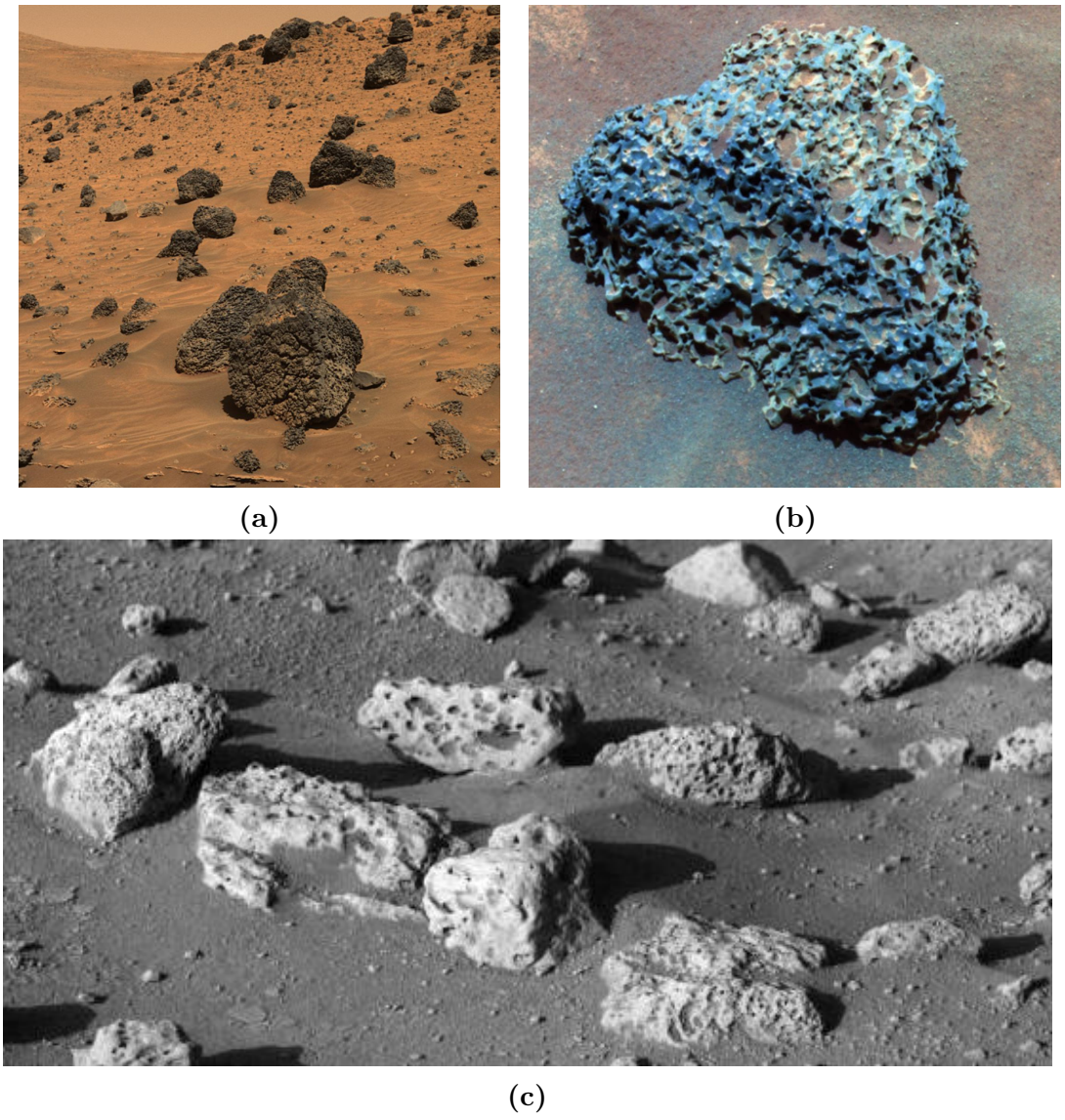

(a) **(b)**

(c)

Figure 5.3: Vesicular Basalt on the Surface of Mars (a) Vesicular basalt boulder landscape and (b) an individual vesicular basalt rock at Gusev crater (Spirit rover Pancam, NASA/JPL/Cornell). (c) Rocks at the Viking 2 lander site that appear to be vesicular (Viking, NASA/JPL).

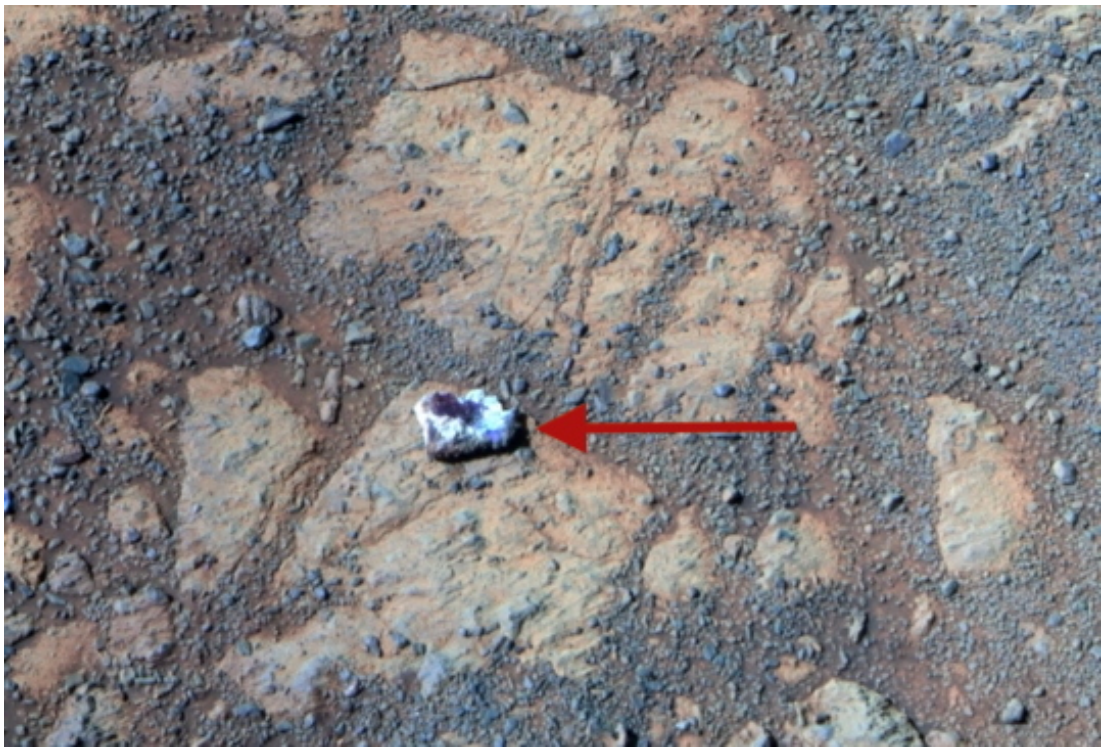

Figure 5.4: Pinnacle Island - A Salt Encrusted Rock at Endeavour Crater, Mars. The rock was unearthed by the wheels of the Opportunity rover at Endeavour crater. The rock surface is encrusted with salts dominated by $MgSO_4$ [189]. The red arrow scale bar is ∼10 cm (NASA/JPL-Caltech/Cornell Univ./Arizona State Univ.).

conditions in a laboratory setting. Several samples - including a highly porous volcanic rock - did not fully dry within the 100 hour experimental period [249]. The dynamics of water mass loss from stone materials is heavily dependent on the environmental temperature and humidity conditions [248]. Previous work (personal communications, Benjamin Bowring (2018)) has shown that liquid water in a bundle of capillary tubes simulating porous rock can have its lifetime significantly extended compared to the same volume of free water when dried under ambient pressure and high-temperature (40-90°C) conditions.

The introduction of dissolved salts into liquid water can impede the rate of evaporation from the solution [250, 251]. The evaporation rate of concentrated sulphate brines under Martian temperature and pressure conditions has been shown to be significantly lower than for pure water [165, 252]. This, combined with the propensity of some brines to rapidly crystallise at the liquid-gas interface, makes dissolved salts of interest when investigating liquid water lifetime on the surface of Mars. Furthermore, the phenomenon of salts dissolved in water precipitating within porous media and obstructing pore-openings has been studied in the construction industry. The pore-clogging effect can cause internal water retention and inter-granular stress, contributing to the degradation of building materials. For example, Todorovic & Janssen (2018) found that gypsum ($CaSO_4$) crystallising in the pores of ceramic bricks caused the average pore radius to decrease, thus reducing the liquid diffusivity [253]. NaCl precipitating in capillary tubes has been shown to effectively obstruct the pore entrance while Na_2SO_4 precipitated within the solution body and did not obstruct the pore openings (Figure 5.5)[254]. Gupta et al. (2014) found that at low relative humidity, NaCl precipitating in clay bricks blocked pores and reduced the drying rate of the bricks significantly. However, they also observed that at high relative humidity, the evaporation rate from the brick was increased due to the salt efflorescing (the solution migrated to the surface of the medium, precipitating salt there rather than within the pore space) rather than clogging pores [255]. Espinosa-Marzal et al. (2013) found the drying rates of limestones were reduced significantly when $MgSO_4$, NaCl, and Na_2SO_4 salts were dissolved in water due to precipitated salts obstructing the pore openings. The stones impregnated with $MgSO_4$ and NaCl brines did not dry within the experimental time frame of 80 days despite the control stones drying within $\sim$14 days. The $MgSO_4$ precipitates were the most effective at retaining liquid water within the rock pores [256]. Work focusing on the drying behaviour of porous media impregnated with water and salt solutions highlights the dependency of this behaviour on salt type and

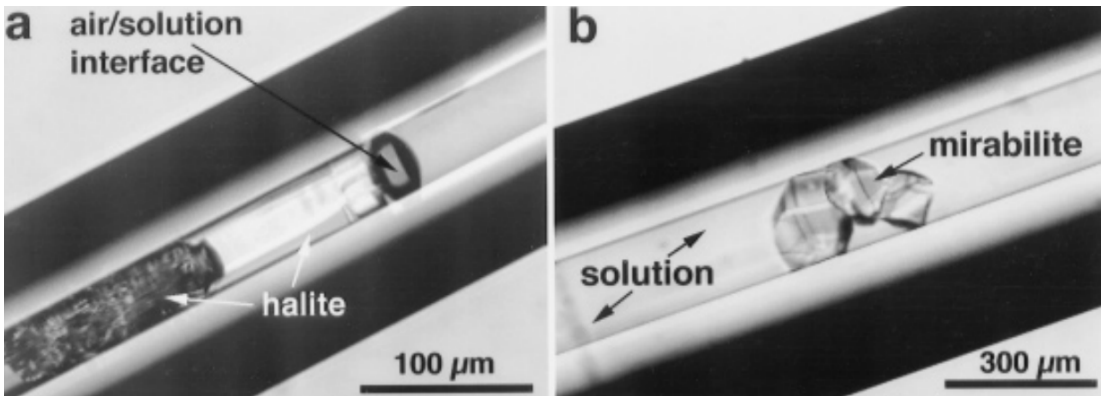

Figure 5.5: Salt Crystals Precipitating From Brine in Capillary Tubes. (a) Halite (NaCl) crystals form at the liquid-gas interface, plugging the tube. (b) Mirabilite ($Na_2SO_4 \cdot 7H_2O$) crystals form within the solution and did not plug the tube (from Rodriguez-Navarro & Doehne (1999)) [254].

environmental conditions, such as relative humidity and temperature. The effect of low pressure on these mechanisms is unexplored.

Though the phenomena of rocks retaining moisture has been studied regarding terrestrial endolthic habitats and porous building materials, the power of porous media and precipitating salts in extending the lifetime of liquid water under the low pressure conditions experienced by the surface of Mars has not been explored or quantified. This chapter aims to address this gap and contribute to establishing the habitability potential of porous rock on Mars. Understanding the habitability of such environments could contribute to the determination of sites of astrobiological interest on the relatively accessible Martian surface and shallow subsurface, with the aim of maximising the potential of life and biosignature-seeking missions.

Table 5.1: Parameters and Nomenclature.

Parameter	Symbol	Units
Radius	r	[mm]
Length	l	[mm]
Number of Tubes	N_{tubes}	-
Volume	V	[mm^3]
Porosity	ϕ	-
Mass	m	g
Time	t	Minutes
Mass Loss Rate	$\dot{m}$	g min^{-1}
Mass Flux	f	g $min^{-1}mm^{-2}$
Surface area	A_s	mm^2
Salt Fraction in Brine	s	-
Water Fraction in Brine	w	-
Number of Experiment Duplicates	N	-

Table 5.2: Free Water Glass Dish Parameters.

Parameter	Symbol	Units	Measurement
Dish Radius	r_{dish}	[mm]	27.8 ± 0.05
Flux Surface Area	$A_{s,dish}$	[mm^2]	2428 ± 9

5.3 Materials and Methods

5.3.1 Parameters and Materials

Experimental Media

Free Water - Dish To provide a comparison to the mass loss rate and mass flux from porous media, a glass dish of radius r_{dish} = (27.8 ± 0.05) mm was used as the free water scenario - water not contained within porous media - examples of which could be puddles, ponds and lakes (Table 5.2).

Porous Media - Capillary Tubes Bundles of capillary tubes that are open at both ends have been used previously as analogues to rock in experiments simulating the flow of fluid through rock and as models for porous media [257, 258]. Here, bundles of glass capillary tubes (with each tube open at both ends), of radius r_{tube} = (0.595 ± 0.005) mm were used as an analogue for porous rock.

Table 5.3: Capillary Tube and Tube Bundle Parameters. Each bundle consisted of N_t tubes open at both ends.

Parameter	Symbol	Units	Measurements	
			75 mm Tubes	20 mm Tubes
Number of Tubes	N_t	-	22	80
Tube Radius	r_{tube}	[mm]	0.595 ± 0.005	0.595 ± 0.005
Cross-Sectional Area of a Tube Opening	A_{tube}	[mm^2]	1.11 ± 0.01	1.11 ± 0.01
Flux Surface Area of Tube Bundle	$A_{s,tubes}$	[mm^2]	48.9 ± 0.8	178 ± 3

Table 5.4: Rock Cube Parameters

Parameter	Symbol	Units	Measurement
Rock mass	m_{cube}	[g]	20.240 ± 0.017
Cube length	l_{cube}	[mm]	20 ± 0.5
Cube Volume	V_{cube}	[mm^3]	8000 ± 600
Pore Volume	V_{pore}	[mm^3]	1816 ± 24
Porosity	ϕ	-	0.23 ± 0.02
Cube Face Area	A_{face}	[mm^2]	400 ± 20
Flux Area	$A_{s,rock}$	[mm^2]	545 ± 27

Two lengths of tube were used; 75 mm and 20 mm. The tube bundles consisted of $N_t = 22$ and $N_t = 80$ tubes for the 75 mm and 20 mm lengths respectively (Table.5.3). Each bundle consequently contained 1.75 g of water when saturated - the same volume of water that the saturated rock cube held.

Porous Media - Rock The porosity of rocks on Earth varies greatly, with vesicular volcanic rocks ranging from 0.02 to over 0.8 [225, 259]. Samples of Martian meteorites have been found to have a porosity of up to 0.11 [260] and estimates of the porosity of Mars' crust at shallow depths are up to 0.35 [261]. Images taken at various locations on the Martian surface (Figure.5.3) depict rocks which appear highly vesicular suggesting the potential for even higher porosities. For this work a cube (l_{cube} = (20 ± 0.5) mm, V_{cube} = (8000 ± 600) mm^3) of basalt with porosity ϕ = (0.23 ± 0.02) was used (Table.5.4). The rock was cut into a cube to allow an estimate of the surface area through which evaporated water exits the rock to be made. In the preliminary work involving brine soaked rock, basalt rocks of undetermined porosity and porous surface area were used.

Brines

The brines investigated were saturated $MgSO_4$ and a binary mixture of saturated $FeSO_4$ & $MgSO_4$. These brines were chosen due to their propensity to form substantial salt crusts at the liquid-gas interface that inhibit evaporation from the sub-crust solution, as shown in Chapter 4. Additionally, the ions present in these brines have been observed at several locations on the surface of Mars [34, 76, 155–158]. The $FeSO_4$ & $MgSO_4$ brine was used in only the preliminary test rock experiment and not in the 7 mb capillary tube experiments due to $FeSO_4$ supply issues.

Pressure

The experiments were performed under four pressure conditions; 7 mb, 10 mb, 100 mb and 1000 mb. The mean atmospheric pressure on the surface of Mars is $\sim$7 mb, which is the triple point of water. Consequently, in some of the 7 mb experiments presented here the water froze and sublimated. By performing the experiments at 10 mb the mass loss rate at pressures close to typical Martian atmospheric pressure could be investigated while preventing the water from freezing. In addition to 7 mb and 10 mb, the experiments were performed at 100 mb and 1000 mb to investigate the effect that pressure has on water mass loss rate from different media, providing insights into liquid water lifetime on Mars in the past and present. The brine experiments were performed at 7 mb only due to time constraints.

5.3.2 Protocol Development

Testing the Precision Balance at Low Pressure

A precision balance was used to measure the mass of the sample at regular intervals over the experimental period. To test the accuracy and ensure the efficacy of the mass balance at low pressure, test experiments were performed. A test mass was placed on the balance and the PES chamber depressurised to the experimental pressure. Mass measurements were taken before and after depressurisation and the difference calculated. This shift was corrected for during data analysis. Once at the test pressure, mass readings were taken every minute for 24 hours. The mass output of the balance became stable once the test pressure was reached until load cell creep (a small, gradual drift in the output of the balance load cell that occurs when the load is constant for an extended period of time) and diurnal environmental fluctuations caused small fluctuations in mass output. The diurnal variations in mass measurement were measured and accounted for during uncertainty propagation (see Chapter 3).

Determining the Experiment Conclusion Time

The point at which the water evaporation or sublimation was complete was determined through a combination of indicators. Firstly, in the case of the dish and the 75 mm tubes, it was possible to visually ascertain whether liquid water was still present in the medium. Additionally, by observing the mass measurements, it was clear when the mass became constant over an extended period of time. Furthermore an effect called load cell creep begins to occur once the mass on the balance is no longer changing, causing the balance to record the mass as gradually creeping upwards by a small amount. The load cell is a transducer that converts the force applied by the mass on the balance to an electrical signal proportional to that force. Load cell creep, a drift in the output of the load cell, can be caused by the gradual deformation of materials within the load cell under a constant load. If load cell creep is occurring, it is an indication that the water has fully evaporated or sublimated and exited the substrate. For the first triplicate of each set of experimental variables, the experiment was allowed to continue beyond the time that these factors suggested the water had fully evaporated, to ensure no further mass loss occurred.

Saturating Capillary Tubes With Water

Initially an attempt was made to fill the capillary tubes by submerging one end of the tubes into a reservoir of degassed, deionised (DI) water and allowing the tubes to saturate via capillary action. This method had the benefit of minimising the introduction of bubbles and dissolved gas into the degassed water during the tube filling process. However, to achieve saturation, a significant portion of the external tube surface was in contact with the water reservoir. The water on the outside of the tubes would significantly affect the mass loss rate data so another method of tube filling was developed. A syringe was filled with degassed DI water and a long needle used to fill the tubes individually. This was performed carefully to minimise the introduction of bubbles and dissolved gas. This method was effective at fully saturating the tubes without wetting the outer surface of the tubes.

Capillary Tubes Filled With Water at 1000 mb

The measurement of the mass of the water evaporating from 75 mm capillary tube bundle at 1000 mb had to be performed outwith the PES chamber due to the length of time taken for the volume of water to evaporate from this medium. As the experiment was to take place at ambient pressure, the low pressure chamber was not necessary. A plastic box with a volume similar to the internal volume of the PES chamber was used, and mass measurements taken at regular intervals. A tray of silica beads was placed in the base of the box to maintain the relative humidity within the box such that it was comparable with the relative humidity within the PES chamber (<20% RH). This apparatus was also used for the solution position within porous media experiment.

Saturating Rock With Water

In preliminary work rocks were soaked in a beaker of DI water overnight to saturate them. However, it was clear that the rocks were not filling sufficiently - when the beaker containing the rocks was agitated, air bubbles would emanate from the rock interior. The rocks were then soaked by placing the beaker onto a shaker for 24 hours to agitate any air bubbles from the rock, displacing them with water. This was more effective but still insufficient at fully saturating the

rock. Exposing the rock in a beaker of DI water to low pressure (10 mb) for two hours was found to be the most efficient and effective method of saturating the rock with water. Increasing the exposure to low pressure time from 2 hours to 24 hours did not result in measurable further saturation so 2 hours was deemed sufficient.

Saturating Rock With Brine

It was first attempted to fill the porous rocks with brine as above; by filling a beaker containing the rock with the brine and then exposing the system to low pressure allowing the brine to displace the gas expelled from the pore space. This rapidly resulted in the precipitation of crystals, which would significantly affect the salt concentration of the solution inside the rock. Porous rocks were therefore soaked in saturated brine over 24 hours on a shaker under ambient pressure conditions to allow the solution to penetrate as much as possible through the rock. The beakers in which the rocks soaked were covered to prevent evaporation and crystal precipitation.

Brine Saturated Porous Media At Low Pressure

Brine filled tubes and rocks were exposed to low pressure to measure the mass loss from porous media. This was initially done immediately after saturation. However, likely due to the introduction of dissolved gas during the saturation process, violent outgassing occurred from within the porous media, causing the liquid brine to be rapidly and violently expelled. This meant there was little chance for crystallisation to occur and clog the pore openings. Subsequently, after saturating the rocks and tubes with brine, the porous media was allowed to dry at atmospheric pressure for three days in order for crystallisation to occur on the outer surface of the rock. To ensure that liquid brine was present within the rock before exposure to low pressure, its mass was measured directly after soaking and directly before exposure to low pressure. Additionally, for each experiment one rock was split into two pieces before saturation. Both rocks were soaked in brine and a crust allowed to form. Before the experiment under low pressure conditions was started, one piece of the rock was broken open to confirm the presence of solution. The other, unbroken, piece was used in the low pressure experiment. The presence of pore-clogging salt crystals and internal liquid brine

was easy to ascertain by sight in the glass capillary tubes.

Photographing Brine Within Rocks

To visually demonstrate the presence of liquid brine within porous rocks exposed to low pressure conditions, the rocks were split open after the experiment to ascertain the presence of liquid brine. The presence significant quantities of liquid could be determined visually due to small pools of liquid brine settled into the rock vesicles and darkening of wet areas. Furthermore, the areas identified as containing liquid were tapped using a gloved finger, transferring brine droplets to the glove surface. It was however, very challenging to obtain photographs which effectively showed the liquid within the rock. Once the rock was split open, the brine would rapidly crystallise due to evaporation when a large surface area of wet rock was exposed to the atmosphere, making it difficult to take images demonstrating the presence of liquid. It was attempted to take pictures under a microscope, which more effectively showed the presence of liquid but caused accelerated crystal precipitation due to the heat of the microscope light. The most efficient method was to take photographs using a magnifying glass. The pictures presented here best convey the wet regions of the rock when compared with dry regions within the same piece of rock.

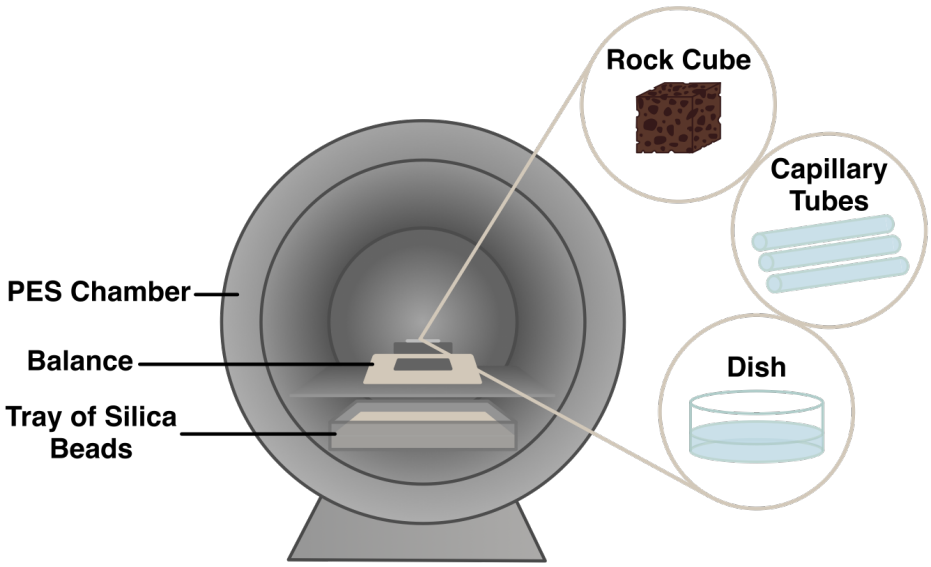

Figure 5.6: The Lifetime of Liquid Water in Porous Media Experimental Apparatus. Inside the PES chamber, a precision balance measures the mass of the water in the substrate over the experimental period. A tray of silica beads minimises the relative humidity within the chamber.

5.3.3 Experimental Methods

Mass Loss of Water From Porous Media at Low Pressure

To probe the effect of porous media on the mass loss rate of liquid water under low pressure conditions, the following experiment was performed. For each combination of experimental variables, a sample of 1.75 g of water was evaporated or sublimated. To minimise the formation of gas bubbles during the low pressure experiments, deionised water was degassed by exposing it to 10 mb pressure for 2 hours before use in the experiment. For each experiment, the water-saturated substrate was placed on a precision balance within the Planetary Environment Simulation (PES) chamber (Figure 5.6). The PES chamber contained a tray of 2 kg of silica beads to minimise the relative humidity within the chamber to $<20\%$. All experiments took place at ambient temperature ($(20 \pm 2)^{\circ}$C).The chamber was depressurised over a few minutes. Once the experimental pressure was reached the mass of the sample was recorded every minute until the water had fully evaporated/sublimated.

Free Water - Dish To compare the evaporation rate from porous media to that from 'free' surface water, 1.75 g of water was evaporated or sublimated from a glass dish of radius r_{dish} = (27.8 ± 0.05) mm. This was performed in triplicate at 7 mb, 10 mb, 100 mb and 1000 mb pressure.

Porous Rock Cube The experiment was also performed using a cube (l_{cube} = (20 ± 0.5) mm, V_{cube} = (8000 ± 600) mm^2) basalt rock of porosity ϕ = (0.23 ± 0.02). The rock cube was prepared by baking for 24 hours at 120°C to remove any water from the pore-space. The mass of the rock was recorded. The rock was then submerged fully in a beaker of DI water. The beaker was exposed to 10 mb pressure for two hours in order to saturate the rock with water. The low pressure expels gas from the rock pores which is consequently replaced by DI water, maximising the filling of the rock pores. The rock was then extracted from the water using tweezers and immediately exposed to the experimental pressure until all water had evaporated or sublimated away. This experiment was repeated in triplicate at 7 mb, 10 mb, 100 mb, and 1000 mb pressure.

75 mm Capillary Tubes Twenty-two glass capillary tubes (l_{tube} = 75 mm, r_{tube} = (0.595 ± 0.005) mm) were filled with DI water via syringe (this method was found to be the most effective at filling the tubes without introducing air bubbles and minimising water on the outside of the tubes that would affect the mass loss data). The bundle of tubes was exposed to the experimental pressure until the water had fully evaporated. These experiments were repeated in triplicate at 7 mb, 10 mb, 100 mb and 1000 mb pressure.

20 mm Capillary Tubes For the 20 mm tubes, a bundle of 80 tubes (l_{tube} = 20 mm, r_{tube} = (0.595 ± 0.005) mm) was used. The tubes were filled with DI water via syringe. The bundle of tubes was exposed to the experimental pressure until the water had fully evaporated. These experiments were repeated in triplicate at 10 mb, 100 mb and 1000 mb.

The Effect of Solution Position Within Porous Media on the Mass Loss of Water

To explore the effect of the position of the solution within porous media on mass loss rate, a bundle of 22 capillary tubes (l_{tube} = 75 mm, r_{tube} = (0.595 ± 0.005)

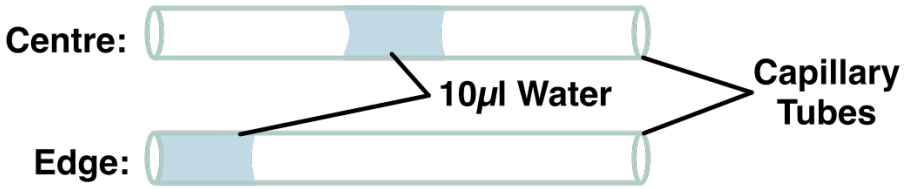

Figure 5.7: Solution Position Within Porous Media Experimental Apparatus. The position of 10 μL of water within 75 mm capillary tubes for the 'centre' and 'edge' experiments.

mm) was used. Capillary tubes were chosen as they could easily be filled with a precise volume of solution and that volume of solution could be deposited at a set position within the tube. For each experiment, 22 capillary tubes had 10 μL of DI water deposited at the centre of the tube. Another 22 tubes had the 10 μL of DI water deposited at one of the openings of the tube (Figure 5.7). The mass of the system was measured each day until the water had fully evaporated. The experiment was performed concurrently in triplicate under ambient temperature and pressure conditions.

Table 5.5: Flux Surface Area of Dishes and Single Capillary Tubes. The capillary tubes were open at both ends.

Substrate	Radius [mm]	Surface Area [mm^2]
Dish 1	27.8 ± 0.05	2428 ± 9
Dish 2	17.6 ± 0.05	970 ± 6
Dish 3	5.6 ± 0.05	98 ± 2
Single 75 mm Tube	0.595 ± 0.005	2.22 ± 0.02
Single 20 mm Tube	0.595 ± 0.005	2.22 ± 0.02

The Effect of Flux Surface Area on the Mass Loss of Water

To investigate the effect of the flux surface area of the medium (the surface area through which mass-loss can occur) on the mass loss rate of water at low pressure, the following experiment was performed. One gram of degassed, DI water was added to Dish 1, a circular dish of radius $r_{dish,1}$ = (27.8 ± 0.05) mm. The water was exposed to a pressure of 7 mb in the PES chamber and the mass of the water measured by a precision balance until the water had completely evaporated or sublimated (Figure.5.6). This was repeated for 1 g of water in circular dishes of radii $r_{dish,2}$ = (17.6 ± 0.0) mm (dish 2), and $r_{dish,3}$ = (5.6 ± 0.05) mm (dish 3) (Table 5.5). Each experiment was also performed at 10 mb, 100 mb and 1000 mb. Due to a technical issue, the mass readings for Dish 2 and Dish 3 were taken manually for the experiments at 7 mb, 100 mb and 1000 mb, resulting in the mass readings being taken at greater time intervals and only during working hours. The additional uncertainty introduced by this was accounted for in the propagation of uncertainty calculations.

The Effect of Crusting Brines on the Mass Loss of Water From Porous Media

The saturated brines were prepared by adding salt to DI water on a heated magnetic stirrer until dissolution ceased. The binary mixtures were prepared by measuring out equal volumes of each brine, adding them to a bottle and stirring. The brines were then allowed to come to equilibrium with the laboratory temperature environment overnight before use. Samples of 0.5 g of each brine were taken and dried in an oven at 120°C for 24 hours to determine the ratio of salt to water under the laboratory environmental conditions (see Chapter 3).

75 mm Capillary Tubes Twenty-two capillary tubes (l_{tube} = 75 mm, r_{tube} = (0.595 ± 0.005) mm) were filled with 1.75 mL (2.1 g) of saturated $MgSO_4$ solution using a syringe. The tubes were left under ambient pressure conditions for three days (the ambient crystallisation period) in order for crystallisation to occur at the tube openings, forming salt plugs. The tubes were then exposed to 7 mb atmospheric pressure for four days and the mass of the tube-brine system measured every minute. After the experiment, each tube was visually examined for the presence of liquid brine. The number of tubes still containing liquid brine was counted. This experiment was repeated in triplicate.

Rocks - Preliminary Experiments The rocks used in these preliminary experiments were not cut into cubes and will be referred to as preliminary test rocks. Each preliminary test rock was split in half before preparation such that a pair of rocks could be used to confirm that brine was present within the rock before exposure to low pressure conditions. The rock pair was prepared by baking both for 24 hours at $120°C$ to remove any water, then weighing them. The rocks were then soaked in saturated $MgSO_4$ brine for 24 hours on a shaker. The rocks were removed from the solution and the mass of each rock-brine system measured. Salt crusts were allowed to form over the surface of each rock over three days under ambient atmospheric pressure conditions (the ambient crystallisation period). One of the rocks from the pair was then split open to confirm liquid brine was present. The second rock was then exposed to pressure conditions of 7 mb for four days and the mass was measured every minute over the course of the experiment. At the end of the experiment, the rock was removed from the chamber and split open to examine for the presence of liquid brine. This was repeated using a

second test rock pair. This experiment was also performed using an $FeSO_4$ & $MgSO_4$ mixed brine.

5.3.4 Data Processing and Calculations

For each experiment, the mass data recorded by the precision balance in the PES chamber was processed using the following steps:

1. Mass measurements taken as the chamber depressurised were discarded.
2. The shift in mass measurement caused by the chamber depressurisation was subtracted from each mass measurement.
3. For experiments where mass loss was being measured from porous media (tubes or rock), the mass of the medium was subtracted from the gross mass to procure the net mass of solution.

For experiments performed outwith the PES chamber, only the final step was applied to the data.

Flux Surface Area of Each Medium

The surface area through which the mass flow of water vapour occurs (the flux surface area) was calculated for each medium. The mass loss was measured using a mass balance so the loss of water vapour is only measured once it has exited the porous medium through its surface. The flux surface area of each medium is depicted in Figure 5.8.

Rock Cubes The surface area through which water vapour exits the rock cube was calculated using

$$A_{s,rock} = 6A_{face}\phi = 6l_{cube}^2\phi \tag{5.1}$$

where A_{face} [mm^2] is the surface area of one face of the cube and l_{cube} [mm] is the length of the edge of the cube. The factor of 6 accounts for the six faces of a cube. The porosity ϕ was determined by measuring the mass of the rock cube when dry and when saturated with water to determine the volume of water within the saturated rock cube [262, 263]. The porosity was then calculated using

$$\phi = \frac{V_{pore}}{V_{cube}} = \frac{V_{water}}{V_{cube}} \tag{5.2}$$

V_{pore} [mm^3] is the pore volume, V_{cube} [mm^3] is the bulk volume of the rock cube and V_{water} [mm^3] is the volume of water contained within the saturated rock.

Capillary Tubes The surface area through which water vapour exists a bundle of capillary tubes, $A_{s,tubes}$ [mm^2] was calculated using

$$A_{s,tubes} = 2N_t A_{tube} \tag{5.3}$$

where N_t is the number of tubes, the factor of 2 accounts for the tubes being open at both ends and A_{tube} [mm^2] the cross-sectional surface area of the capillary tube opening was calculated using

$$A_{tube} = \pi r_{tube}^2 \tag{5.4}$$

where r_{tube} [mm] is the mean internal radius of the capillary tubes.

Dish The surface area through which water vapour exists the dish was calculated using

$$A_{s,dish} = \pi r_{dish}^2 \tag{5.5}$$

where r_{dish} [mm] is the radius of the dish.

Mass Loss Rate and Mass Flux

The mass loss rate is the rate at which evaporated or sublimated water exits the medium. For each of the experiments, the mean mass loss rate $\dot{m}$ [g min^{-1}] over the experimental period was calculated using

$$\dot{m} = \frac{m_{start} - m_{end}}{t} \tag{5.6}$$

where m_{start} [g] is the mass of the solution at the start of the experiment, m_{end} [g] is the mass of solution at the end of the experiment and t [minutes] is time over which the mass loss took place. The mass flux is the rate at which mass exits the medium per unit area. The mass flux f [g min^{-1} mm^{-2}] was calculated using

$$f = \frac{\dot{m}}{A_s} \tag{5.7}$$

where A_s [mm^2] is the flux surface area (the surface area through which evaporated water exits the medium).

For each set of triplicate experiments, the weighted mean across the triplicates and associated uncertainty was calculated using Equation 3.1 and Equation 3.2 respectively. Uncertainties were propagated using Equation 3.3.

The Effect of Flux Surface Area on the Mass Loss Rate of Water From Porous Media

For the experiment where the mass loss of 1 g of water was measured from dishes of different radii, the mass loss rate from each dish was was calculated using Equation 5.6. The mass flux was calculated using Equation 5.7, where A_s is the flux surface area of the dish (Table.5.5). The values calculated for the single 75 mm and 20 mm long tubes were extrapolated from the flux calculated from the experiments described in section 5.3.3. The mass loss rate from a single tube was approximated by rearranging Equation 5.7 to

$$\dot{m}_{tube} = 2A_{tube}f_{tube} \tag{5.8}$$

where A_{tube} [mm^2] is the internal cross sectional surface area of a tube opening and f_{tube} [g min^{-1} m^{-2}] is the mass flux from the bundle of tubes. The factor of 2 accounts for the capillary tube being open at both ends.

The Effect of Crusting Brines on the Mass Loss Rate of Water from Porous Media

To calculate the mass of water contained within brine within a medium at the initiation of the low pressure experiment, the water lost during the crystallisation period under ambient conditions, Δm_w [g] had to be accounted for. This was calculated using

$$\Delta m_w = m_{gross,i} - m_{gross,a} \tag{5.9}$$

where $m_{gross,i}$ [g] and $m_{gross,a}$ [g] are the gross masses of the substrate-brine system before and after the ambient crystallisation period. The mass of the brine and

precipitated salt $m_{brine,i}$ [g] contained within the medium directly before the start of the ambient crystallisation period was calculated using

$$m_{brine,i} = m_{gross,i} - m_m \tag{5.10}$$

where $m_{gross,i}$ [g] is the gross mass of the medium-brine system directly post soaking (directly before the ambient crystallisation period) and m_m [g] is the mass of the medium. The mass of water contained within the brine within the substrate after the ambient crystallisation period (i.e. at the start of the low pressure experiment), $m_{water,a}$ [g], was therefore calculated using

$$\begin{aligned} m_{water,a} &= m_{water,i} - \Delta m_{water} \\ &= w \cdot m_{brine,i} - \Delta m_{water} \\ &= w \cdot (m_{gross,i} - m_m) - m_{gross,i} + m_{gross,a}. \end{aligned} \tag{5.11}$$

where $m_{water,i}$ [g] is the mass of water contained within the brine before the ambient crystallisation period, w is the water fraction (see Chapter 3) and Equation 5.10 and Equation 5.9 are substituted in.

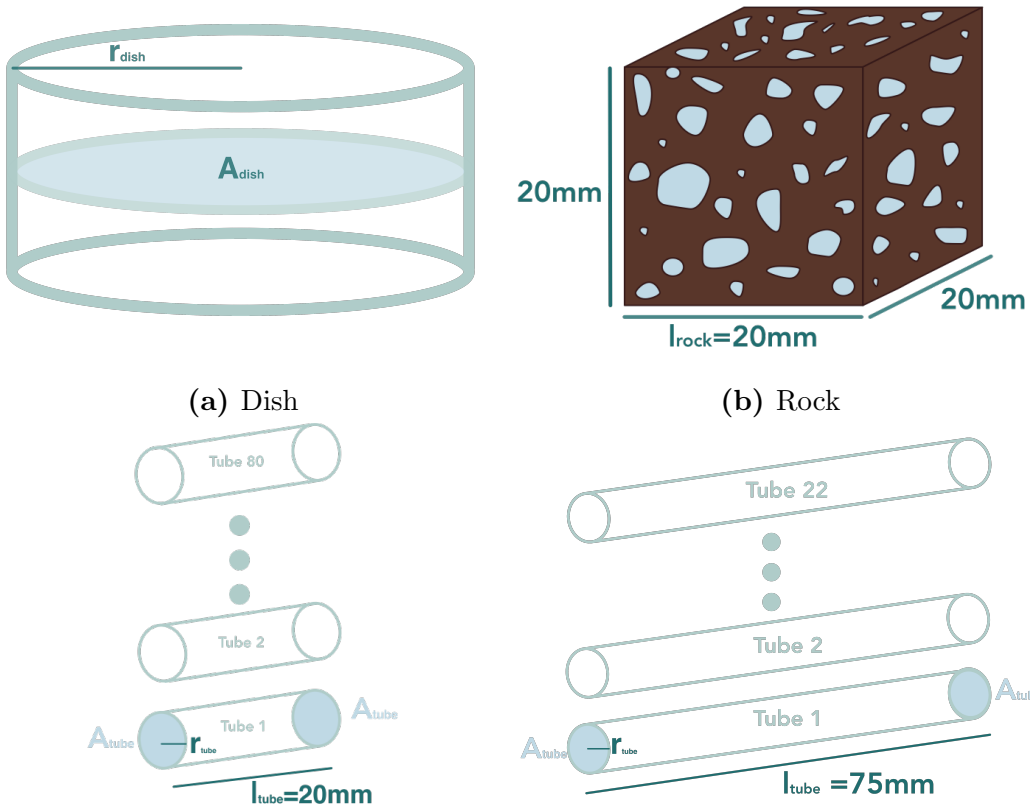

(a) Dish **(b)** Rock

(c) 20 mm Tubes Bundle **(d)** 75 mm Tube Bundle

Figure 5.8: Parameters and Flux Area of Each Substrate. The surface areas are highlighted in pale blue. This is the area through which mass loss can occur during evaporation or sublimation of the water contained in the substrate.

5.4 Results

5.4.1 Mass Loss of Water From Porous Media at Low Pressure

At each of the pressures the experiment was performed at, the water in the glass dish - the free water - evaporated most rapidly. The proportionate difference in the mass loss rate between the free water in the dish and the water in the porous media was most extensive at ambient atmospheric pressure and decreased with decreasing pressure. The results of the experiment duration, mass loss rate and mass flux for each experiment triplicate are presented for each medium - the dish, rock cube, 20 mm tube bundle and 75 mm tube bundle in Tables 5.6, 5.7, 5.8 and 5.9 respectively. Mass loss rate refers to the absolute rate of mass loss from each substrate [g min^{-1}]. Mass flux refers to the mass loss rate per unit area [g min^{-1} mm^{-2}] (the area through which mass can leave the substrate). The overall mean duration, mean mass loss rate and mean flux are summarised in Tables 5.10, 5.11 and 5.12 respectively.

1000 mb

Free Water The mean mass loss rate and mean mass flux of the 1.75 g of free water evaporating from the dish were (1.72 $\pm$ 0.04)$\times 10^{-3}$ g min^{-1} and (7.03 $\pm$ 0.17)$\times 10^{-7}$ g min^{-1} mm^{-2} over (1010 $\pm$ 22) minutes (Table 5.6). The mass loss rate was relatively constant at 1.97×10^{-3} g min^{-1} for the majority of the evaporation period, only changing markedly - by a factor of 2.77 - to 7.10×10^{-4} g min^{-1} for the final 200 minutes (Figure 5.9a and Figure 5.10a).

Rock Cube The mean mass loss rate and mean mass flux of 1.75 g of water from the rock cube were (1.59 $\pm$ 0.18)$\times 10^{-3}$ g min^{-1} and (2.91 $\pm$ 0.34)$\times 10^{-6}$ g $min^{-1}mm^{-2}$ over (1079 $\pm$ 119) minutes (Table 5.7). Figure 5.10b shows that there is an initial rapid rate of mass loss of 4.01×10^{-3} g min^{-1} for the first 400 minutes. The rate subsequently reduced by a factor of 18.4 to 2.11×10^{-4} g min^{-1} for the for the remaining 679 minutes, until the water had fully evaporated.

20 mm Tube Bundle The mean mass loss rate and mean mass flux of 1.75 g of water from the 20 mm tube bundle (80 tubes open at both ends) were (6.29 $\pm$ 0.15)$\times 10^{-4}$ g min^{-1} and (3.53 $\pm$ 0.09)$\times 10^{-6}$ g min^{-1}mm^{-2} over (2754 $\pm$ 62) minutes (Table 5.8). To a lesser extent than the rock cube, the mass loss rate from the bundle of 20 mm tubes also exhibited the trend of the mass loss rate reducing with time (Figure 5.10c. The rate over the first 700 minutes was 1.11×10^{-3} g min^{-1}, reducing to 5.64×10^{-4} g min^{-1} for the following 1500 minutes. For the remaining 554 minutes, the mean mass loss was 2.00×10^{-4} g min^{-1}, a factor of 5.6 less than the rate in the first 700 minutes.

75 mm Tube Bundle The mean mass loss rate and mean mass flux of 1.75 g of water from the 75 mm tube bundle (22 tubes open at both ends) were (3.56 $\pm$ 0.20)$\times 10^{-5}$ g min^{-1} and (7.27 $\pm$ 0.42)$\times 10^{-7}$ g min^{-1}mm^{-2} over (48252 $\pm$ 2657) minutes (Table 5.9). Similar to the rock cube the mass loss rate decreased significantly with time (Figure 5.10d. The mean mass loss rate for the first 8000 minutes was 1.34×10^{-4} g min^{-1} and 1.87×10^{-5} g min^{-1} for the following 36000 minutes. For the final 5760 minutes, the mass loss rate was 2.89×10^{-6} g min^{-1}, a decrease of a factor of 46 compared to the initial 8000 minutes.

Summary Out of the four media types investigated, the 1.75 g of liquid water in the bundle of 75 mm capillary tubes took the longest to fully evaporate, with a mean complete mass loss time of 48252 minutes ($\sim$33.5 days). The same mass of liquid water in the other substrates, evaporated within 1-2 days (Figure 5.9 and Figure 5.17). The mass loss rate from the bundle of 75 mm tubes (3.56×10^{-5} g min^{-1}) was 45 times lower than that of the free water (1.72×10^{-3} g min^{-1}), which evaporated most rapidly - within 1010 minutes. The rock cube and bundle of 20 mm tubes were much less effective at retaining liquid water than the 75 mm tubes, exhibiting liquid water mass loss rates that were 2.7 and 1.1 times lower than the free water respectively.

The mean mass fluxes from the dish and the 75 mm tube bundle were similar at 7.03×10^{-7} g min^{-1}mm^{-2} and 7.27×10^{-7} g min^{-1}mm^{-2} respectively. The mass fluxes from the 20 mm tubes and the rock cube were also similar at 3.53×10^{-6} g min^{-1}mm^{-2} and 2.91×10^{-6} g min^{-1}mm^{-2} respectively. The greatest discrepancy in mass flux was between the free water and the 20 mm tube bundle, with the latter exhibiting a mass flux 5 times greater than the free water. This shows that, at 1000 mb, although the absolute time taken for the same mass of water

to evaporate from porous media is greater than from the dish, the mass loss per unit surface area is smallest from the non-porous medium.

100 mb

Free Water At 100 mb the mean mass loss rate and mean mass flux of 1.75 g of water from the dish were $(8.16 \pm 0.10)\times10^{-3}$ g min^{-1} and $(3.37 \pm 0.04)\times10^{-6}$ g min^{-1}mm^{-2} over (216 ± 2) minutes (Table 5.6). For the first 180 minutes the mass loss rate was relatively constant at 8.66×10^{-3} g min^{-1}, reducing by 1.59 times to 5.44×10^{-3} g min^{-1} for the final 36 minutes (Figure 5.11a and Figure 5.12a).

Rock Cube The mean mass loss rate and mean mass flux of 1.75 g of water from the rock cube at 100 mb were $(2.34 \pm 0.35)\times10^{-3}$ g min^{-1} and $(4.31 \pm 0.66)\times10^{-6}$ g min^{-1}mm^{-2} over (731 ± 110) minutes (Table 5.7). The mass loss rate was high for the first 200 minutes at 7.92×10^{-3} g min^{-1} after which it reduced by 24.8 times to 3.20×10^{-4} g min^{-1} for the remaining 531 minutes (Figure 5.11b and Figure 5.12b).

20 mm Tube Bundle The mean mass loss rate and mean mass flux of 1.75 g of water from the bundle of 20 mm tubes were $(4.90 \pm 0.07)\times10^{-3}$ g min^{-1} and $(2.72 \pm 0.05)\times10^{-5}$ g min^{-1}mm^{-2} over (355 ± 4) minutes (Table 5.8). In the first 280 minutes the mass loss rate was 5.62×10^{-3} g min^{-1}, reducing by 2.63 times to 2.14×10^{-3} g min^{-1} for the final 75 minutes (Figure 5.11c and Figure 5.12c).

75 mm Tube Bundle The mean mass loss rate and mean mass flux of 1.75 g of water from the bundle of 75 mm tubes were $(7.92 \pm 0.15)\times10^{-4}$ g min^{-1} and $(1.60 \pm 0.03)\times10^{-5}$ g min^{-1}mm^{-2} over (2129 ± 37) minutes (Table 5.9). For the first 850 minutes, the mean mass loss rate was 1.37×10^{-3} g min^{-1}, reducing by 3.21 times to 4.27×10^{-4} g min^{-1} for the remaining period of 1279 minutes (Figure 5.11d and Figure 5.12d).

Summary At 100 mb pressure, the free water evaporated fully in an average of 216 minutes at a mean rate of 8.16×10^{-3} g min^{-1}. The 75 mm tubes took 2128

minutes at a mean rate of 7.92×10^{-4} g min^{-1} to evaporate the same mass of water - a factor of 10.3 lower than the free water. The rock cube and 20 mm tubes had mass loss rates 3.49 and 1.67 times lower than the free water (Table 5.11). The proportionate difference between the mass loss rate from the dish and from the 75 mm tube bundle is smaller at 100 mb than at 1000 mb. By contrast, the proportionate difference between the mass loss rate from the dish and from both the rock cube and the 20 mm tube bundle is greater at 100 mb than 1000 mb (5.18a).

At 100 mb the mean mass flux from the rock cube (4.31×10^{-6} g min^{-1}mm^{-2}) was more comparable to the free water (3.37×10^{-6} g min^{-1}mm^{-2}) than either of the bundles of tubes (Table 5.12 and Figure 5.18b). The tube bundles had mass fluxes that were similar at 1.60×10^{-5} g min^{-1}mm^{-2} and 2.72×10^{-5} g min^{-1}mm^{-2} for 75 mm and 20 mm tube bundles respectively (Table 5.12 Figure 5.18b).

10 mb

Free Water The mean mass loss rate and mean mass flux of 1.75 g of free water from the dish were (0.027 ± 0.001) g min^{-1} and $(1.13 \pm 0.04) \times 10^{-5}$ g min^{-1}mm^{-2} over (64 ± 2) minutes (Table 5.6). For the first 56 minutes the mean mass loss rate was 0.0291 g min^{-1}, reducing by 1.97 times to 0.0148 g min^{-1} for the final 8 minutes (Figure 5.13a and Figure 5.14a).

Rock Cube At 10 mb pressure the mean mass loss rate and mean mass flux of 1.75 g of water from the rock cube were $(9.42 \pm 0.75) \times 10^{-3}$ g min^{-1} and $(1.73 \pm 0.15) \times 10^{-5}$ g min^{-1}mm^{-2} over (188 ± 15) minutes (Table 5.7). For the first 25 minutes the mass loss rate was 0.0294 g min^{-1}. This reduced to 9.25×10^{-3} g min^{-1} for the following 100 minutes and further reduced to 1.85×10^{-3} g min^{-1} for the final 63 minutes - reductions of 3.18 and 15.9 times respectively from the mean mass loss rate over the first 25 minutes (Figure 5.13b and Figure 5.14b).

20 mm Tube Bundle The mean mass loss rate and mean mass flux of 1.75 g of water from the bundle of 20 mm tubes were (0.0133 ± 0.0003) g min^{-1} and $(7.49 \pm 0.16) \times 10^{-5}$ g min^{-1}mm^{-2} over (132 ± 2) minutes (Table 5.8). For the first 80 minutes, the mean mass loss rate was 0.0163 g min^{-1}. This reduced to 9.51×10^{-3}

g min^{-1} for the following 40 minutes and further reduced to 5.71×10^{-3} g min^{-1} for the final 12 minutes - reductions by a factor of 1.71 and 2.85 respectively compared to the first 80 minutes (Figure 5.13c and Figure 5.14c).

75 mm Tube Bundle The mean mass loss rate and mean mass flux of 1.75 g of water from the bundle of 75 mm tubes were $(9.14 \pm 0.28) \times 10^{-3}$ g min^{-1} and $(1.86 \pm 0.06) \times 10^{-4}$ g $min^{-1}mm^{-2}$ over (189 ± 5) minutes (Table 5.9). Over the first 50 minutes, the mass loss rate was 0.0137 g min^{-1}, reducing to 8.63×10^{-3} g min^{-1} for the following 100 minutes and reducing further to 4.72×10^{-3} g min^{-1} for the final 39 minutes, reductions of 1.59 and 2.90 times respectively compared to the first 50 minutes (Figure 5.13d and Figure 5.14d).

Summary At 10 mb pressure, the free water evaporated most rapidly, within a mean time of 64 minutes at a mean mass loss rate of 0.027 g min^{-1}. The water in the 75 mm tubes evaporated most slowly, closely followed by the water in the rock cube at mean mass loss rates of 9.14×10^{-3} g min^{-1} over 189 minutes and 9.42×10^{-3} g min^{-1} over 188 minutes respectively (Table 5.11). The greatest proportionate difference in mean mass loss rate was between the free water and the 75 mm tube bundle, with the former being 2.95 times greater than the latter (Figure 5.18a). At 10 mb the greatest disparity in mass flux was between the free water and the 75 mm tube bundle (Figure 5.18b), with the mass flux from the 75 mm tube bundle (1.86×10^{-4} g $min^{-1}mm^{-2}$) being 16.5 times greater than the free water (1.13×10^{-5} g $min^{-1}mm^{-2}$).

7 mb

Free Water The mean mass loss rate and mean flux of 1.75 g of water from the dish were (0.018 ± 0.001) g min^{-1} and $(7.12 \pm 0.37) \times 10^{-6}$ g $min^{-1}mm^{-2}$ over (100 ± 5) minutes (Table 5.6). For the first 10 minutes, the mean mass loss rate was 0.0505 g min^{-1}. This decreased to 0.0249 g min^{-1} for the following 40 minutes then decreased further to 5.13×10^{-3} g min^{-1} for the final 50 minutes - 2.03 and 9.84 times lower than the mass loss rate in the first ten minutes respectively (Figure 5.15a and Figure 5.16a). The dish of liquid water rapidly froze at this pressure, so although the mass loss rate was initially due to evaporation, for the majority of the experiment it was due to sublimation.

Rock Cube At 7 mb the mean mass loss rate and mean flux of 1.75 g of water from the rock cube was (8.69 ± 0.62) × 10^{-3} g min^{-1} and (1.59 ± 0.13)×10^{-5} g $min^{-1}mm^{-2}$ over (201 ± 14) minutes. For the first 15 minutes the mean mass loss rate was 0.0388 g min^{-1} (Table 5.7). The rate reduced to 7.40×10^{-3} g min^{-1} for the following 155 minutes then reduced further to 5.91×10^{-4} g min^{-1} over the final 31 minutes - 5.24 and 65.7 times less than the mass loss rate in the first 15 minutes respectively (Figure 5.15b and Figure 5.16b).

75 mm Tube Bundle The mean mass loss rate and mean mass flux of 1.75 g of water from the bundle of 75 mm tubes was (0.0122 ± 0.0004) g min^{-1} and (2.51 ± 0.09)×10^{-4} g $min^{-1}mm^{-2}$ over (143 ± 5) minutes (Table 5.9). For the first 40 minutes, the mean mass loss rate was 0.0215 g min^{-1}, reducing to 9.96×10^{-3} g min^{-1} for the following 80 minutes then reducing further to 4.39×10^{-3} g min^{-1} for the final 23 minutes - 2.16 and 4.90 times lower than the initial 40 minutes respectively (Figure 5.15c and Figure 5.16c). The water was visible in the tubes and did not appear to freeze during the experimental period.

Summary The mass loss rate of the free water was 0.018 g min^{-1} over 100 minutes. By comparison the mass loss rate from the 75 mm tubes was 0.0122 g min^{-1} over 143 minutes (Table 5.11). The mass loss rate from the dish was therefore only 1.5 times greater than from the 75 mm tubes and thus the proportionate difference in mass loss rates across the media tested was smallest at 7 mb (Figure 5.18a). At 7 mb the greatest difference in mass flux was between the free water and the 75 mm tube bundle (Figure 5.18b), with the mass flux from the 75 mm tube bundle (2.51×10^{-4} g $min^{-1}mm^{-2}$) being 35.3 times greater than the free water (7.12×10^{-6} g $min^{-1}mm^{-2}$)(Table 5.12).

Summary

1. The mean mass loss rate from porous media is lower than the free water scenario at all pressures tested.

2. The mean mass loss rate of liquid water (10 mb, 100 mb and 1000 mb) from each medium has a power law relationship with pressure (Figure 5.18a).

3. The proportionate difference between the maximum and minimum mass loss rates across the media tested typically decreases with decreasing pressure.

4. The mass loss rate of liquid water from porous media at 100 mb and 1000 mb reduced significantly with time, while the mass loss rate from the dish was relatively constant until it reduced a small amount towards the end of the evaporation period.

5. The mean mass flux is smallest from the free water scenario at all pressures tested.

6. The mean mass flux of liquid water (10 mb, 100 mb and 1000 mb) from each medium has a power law relationship with pressure (Figure 5.18b).

Table 5.6: Results of the Lifetime of Liquid Water in Porous Media at Low Pressure Experiment: Mass Loss Rate and Mass Flux of Free Water at Different Pressures.

Pressure [mb]	Triplicate	Time [mins]	Mass Loss Rate [g min^{-1}]	Mass Flux [g $min^{-1}mm^{-2}$]
7	T1	85 ± 13	0.021 ± 0.003	$(8.55 \pm 1.31)\times10^{-6}$
	T2	110 ± 9	0.016 ± 0.001	$(6.55 \pm 0.54)\times10^{-6}$
	T3	98 ± 7	0.018 ± 0.001	$(7.45 \pm 0.54)\times10^{-6}$
	Mean	100 ± 5	0.018 ± 0.001	$(7.12 \pm 0.37)\times10^{-6}$
10	T1	64 ± 4	0.027 ± 0.002	$(1.12 \pm 0.07)\times10^{-5}$
	T2	64 ± 3	0.027 ± 0.001	$(1.13 \pm 0.05)\times10^{-5}$
	T3	64 ± 4	0.027 ± 0.002	$(1.13 \pm 0.07)\times10^{-5}$
	Mean	64 ± 2	0.027 ± 0.001	$(1.13 \pm 0.04)\times10^{-5}$
100	T1	225 ± 4	$(7.84 \pm 0.16)\times10^{-3}$	$(3.23 \pm 0.07)\times10^{-6}$
	T2	212 ± 4	$(8.32 \pm 0.17)\times10^{-3}$	$(3.43 \pm 0.07)\times10^{-6}$
	T3	210 ± 4	$(8.41 \pm 0.18)\times10^{-3}$	$(3.46 \pm 0.07)\times10^{-6}$
	Mean	216 ± 2	$(8.16 \pm 0.10)\times10^{-3}$	$(3.37 \pm 0.04)\times10^{-6}$
1000	T1	939 ± 42	$(1.87 \pm 0.09)\times10^{-3}$	$(7.69 \pm 0.36)\times10^{-7}$
	T2	1123 ± 40	$(1.56 \pm 0.06)\times10^{-3}$	$(6.42 \pm 0.25)\times10^{-7}$
	T3	972 ± 35	$(1.80 \pm 0.07)\times10^{-3}$	$(7.43 \pm 0.29)\times10^{-7}$
	Mean	1010 ± 22	$(1.72 \pm 0.04)\times10^{-3}$	$(7.03 \pm 0.17)\times10^{-7}$

Table 5.7: Results of the Lifetime of Liquid Water in Porous Media at Low Pressure Experiment: Mass Loss Rate and Mass Flux of Water From Rock Cube at Different Pressures

Pressure [mb]	Triplicate	Time [mins]	Mass Loss Rate [g min^{-1}]	Mass Flux [g $min^{-1}mm^{-2}$]
7	T1	210 ± 33	$(8.18 \pm 1.29)\times10^{-3}$	$(1.50 \pm 0.25)\times10^{-5}$
	T2	191 ± 45	$(9.26 \pm 2.18)\times10^{-3}$	$(1.70 \pm 0.41)\times10^{-5}$
	T3	200 ± 17	$(8.80 \pm 0.75)\times10^{-3}$	$(1.61 \pm 0.16)\times10^{-5}$
	Mean	201 ± 14	$(8.69 \pm 0.62) \times 10^{-3}$	$(1.59 \pm 0.13)\times10^{-5}$
10	T1	187 ± 28	$(9.52 \pm 1.43)\times10^{-3}$	$(1.75 \pm 0.28)\times10^{-5}$
	T2	182 ± 31	$(9.81 \pm 1.68)\times10^{-3}$	$(1.80 \pm 0.32)\times10^{-5}$
	T3	191 ± 21	$(9.23 \pm 1.02)\times10^{-3}$	$(1.69 \pm 0.21)\times10^{-5}$
	Mean	188 ± 15	$(9.42 \pm 0.75)\times10^{-3}$	$(1.73 \pm 0.15)\times10^{-5}$
100	T1	789 ± 157	$(2.23 \pm 0.44)\times10^{-3}$	$(4.09 \pm 0.84)\times10^{-6}$
	T2	639 ± 181	$(2.75 \pm 0.78)\times10^{-3}$	$(5.05 \pm 1.45)\times10^{-6}$
	T3	767 ± 287	$(2.28 \pm 0.85)\times10^{-3}$	$(4.19 \pm 1.58)\times10^{-6}$
	Mean	731 ± 110	$(2.34 \pm 0.35)\times10^{-3}$	$(4.31 \pm 0.66)\times10^{-6}$
1000	T1	1184 ± 217	$(1.47 \pm 0.27)\times10^{-3}$	$(2.70 \pm 0.51)\times10^{-6}$
	T2	1205 ± 470	$(1.46 \pm 0.57)\times10^{-3}$	$(2.67 \pm 1.05)\times10^{-6}$
	T3	1017 ± 149	$(1.72 \pm 0.25)\times10^{-3}$	$(3.16 \pm 0.49)\times10^{-6}$
	Mean	1079 ± 119	$(1.59 \pm 0.18)\times10^{-3}$	$(2.91 \pm 0.34)\times10^{-6}$

Table 5.8: Results of the Lifetime of Liquid Water in Porous Media at Low Pressure Experiment: Mass Loss Rate and Mass Flux of Water From 20 mm Capillary Tube Bundle at Different Pressures.

Pressure [mb]	Triplicate	Time [mins]	Mass Loss Rate [g min^{-1}]	Mass Flux [g $min^{-1}mm^{-2}$]
10	T1	133 ± 3	0.0134 ± 0.0004	$(7.51 \pm 0.24)\times10^{-5}$
	T2	130 ± 4	0.0136 ± 0.0005	$(7.62 \pm 0.29)\times10^{-5}$
	T3	135 ± 5	0.0130 ± 0.0005	$(7.28 \pm 0.32)\times10^{-5}$
	Mean	132 ± 2	0.0133 ± 0.0003	$(7.49 \pm 0.16)\times10^{-5}$
100	T1	353 ± 4	$(4.97 \pm 0.07)\times10^{-3}$	$(2.79 \pm 0.06)\times10^{-5}$
	T2	415 ± 23	$(4.22 \pm 0.24)\times10^{-3}$	$(2.37 \pm 0.14)\times10^{-5}$
	T3	365 ± 19	$(4.85 \pm 0.26)\times10^{-3}$	$(2.72 \pm 0.15)\times10^{-5}$
	Mean	355 ± 4	$(4.90 \pm 0.07)\times10^{-3}$	$(2.72 \pm 0.05)\times10^{-5}$
1000	T1	2660 ± 186	$(6.58 \pm 0.47)\times10^{-4}$	$(3.69 \pm 0.27)\times10^{-6}$
	T2	2668 ± 79	$(6.56 \pm 0.21)\times10^{-4}$	$(3.68 \pm 0.14)\times10^{-6}$
	T3	2975 ± 116	$(5.88 \pm 0.24)\times10^{-4}$	$(3.31 \pm 0.15)\times10^{-6}$
	Mean	2754 ± 62	$(6.29 \pm 0.15)\times10^{-4}$	$(3.53 \pm 0.09)\times10^{-6}$

Table 5.9: Results of the Lifetime of Liquid Water in Porous Media at Low Pressure Experiment: Mass Loss Rate and Mass Flux of Water From 75 mm Capillary Tube Bundle at Different Pressures.

Pressure [mb]	Triplicate	Time [mins]	Mass Loss Rate [g min^{-1}]	Mass Flux [g $min^{-1}mm^{-2}$]
7	T1	148 ± 12	0.0118 ± 0.0010	$(2.41 \pm 0.20)\times10^{-4}$
	T2	141 ± 7	0.0126 ± 0.0006	$(2.57 \pm 0.14)\times10^{-4}$
	T3	144 ± 8	0.0122 ± 0.0007	$(2.49 \pm 0.15)\times10^{-4}$
	Mean	143 ± 5	0.0122 ± 0.0004	$(2.51 \pm 0.09)\times10^{-4}$
10	T1	184 ± 6	$(9.58 \pm 0.35)\times10^{-3}$	$(1.96 \pm 0.08)\times10^{-4}$
	T2	201 ± 17	$(8.73 \pm 0.75)\times10^{-3}$	$(1.78 \pm 0.16)\times10^{-4}$
	T3	220 ± 17	$(7.97 \pm 0.63)\times10^{-3}$	$(1.63 \pm 0.13)\times10^{-4}$
	Mean	189 ± 5	$(9.14 \pm 0.28)\times10^{-3}$	$(1.86 \pm 0.06)\times10^{-4}$
100	T1	2304 ± 86	$(7.61 \pm 0.29)\times10^{-4}$	$(1.55 \pm 0.06)\times10^{-5}$
	T2	2004 ± 44	$(8.75 \pm 0.21)\times10^{-4}$	$(1.79 \pm 0.05)\times10^{-5}$
	T3	2649 ± 114	$(6.61 \pm 0.29)\times10^{-4}$	$(1.35 \pm 0.06)\times10^{-5}$
	Mean	2129 ± 37	$(7.92 \pm 0.15)\times10^{-4}$	$(1.60 \pm 0.03)\times10^{-5}$
1000	T1	31740 ± 9415	$(5.48 \pm 1.63)\times10^{-5}$	$(1.12 \pm 0.33)\times10^{-6}$
	T2	49680 ± 4992	$(3.54 \pm 0.36)\times10^{-5}$	$(7.24 \pm 0.74)\times10^{-7}$
	T3	49680 ± 3328	$(3.52 \pm 0.24)\times10^{-5}$	$(7.20 \pm 0.51)\times10^{-7}$
	Mean	48252 ± 2657	$(3.56 \pm 0.20)\times10^{-5}$	$(7.27 \pm 0.42)\times10^{-7}$

Table 5.10: Results of the Lifetime of Liquid Water in Porous Media at Low Pressure Experiment: Summary of Time Taken For Mass Loss to Complete

	Mean Time for 1.75 g Water to Evaporate/Sublimate [Minutes]			
	Free Water	Porous Media		
Pressure [mb]	Dish	Rock Cube	20 mm Tubes	75 mm Tubes
7	100	201	-	143
10	64	188	132	189
100	216	731	355	2129
1000	1010	1079	2754	48252

Table 5.11: Results of the Lifetime of Liquid Water in Porous Media at Low Pressure Experiment: Summary of Mean Mass Loss Rates

	Mean Mass Loss Rate [g min^{-1}]			
	Free Water	Porous Media		
Pressure [mb]	Dish	Rock Cube	20 mm Tubes	75 mm Tubes
7	0.018	8.69×10^{-3}	-	0.0122
10	0.027	9.42×10^{-3}	0.0133	9.14×10^{-3}
100	8.16×10^{-3}	2.34×10^{-3}	4.90×10^{-3}	7.92×10^{-4}
1000	1.72×10^{-3}	1.59×10^{-3}	6.29×10^{-4}	3.56×10^{-5}

Table 5.12: Results of the Lifetime of Liquid Water in Porous Media at Low Pressure Experiment: Summary of Mean Mass Flux

	Mean Mass Flux [g $min^{-1}mm^{-2}$]			
	Free Water	Porous Media		
Pressure [mb]	Dish	Rock Cube	20 mm Tubes	75 mm Tubes
7	7.12×10^{-6}	1.59×10^{-5}	-	2.51×10^{-4}
10	1.13×10^{-5}	1.73×10^{-5}	7.49×10^{-5}	1.86×10^{-4}
100	3.37×10^{-6}	4.31×10^{-6}	2.72×10^{-5}	1.60×10^{-5}
1000	7.03×10^{-7}	2.91×10^{-6}	3.53×10^{-6}	7.27×10^{-7}

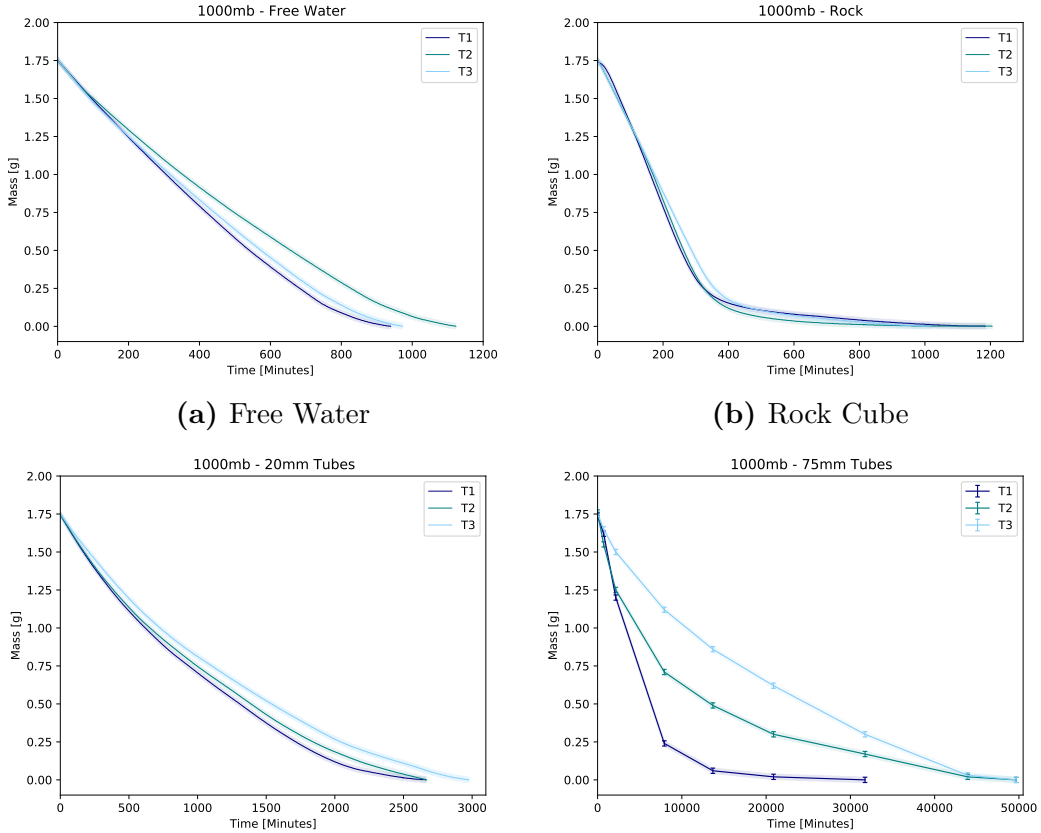

(a) Free Water

(b) Rock Cube

(c) 20 mm Tube Bundle

(d) 75 mm Tube Bundle

Figure 5.9: Results of the Lifetime of Liquid Water in Porous Media at Low Pressure Experiment: Mass of Water Over Time at 1000 mb. T1-T3 are labels for each experiment in the set of triplicates.

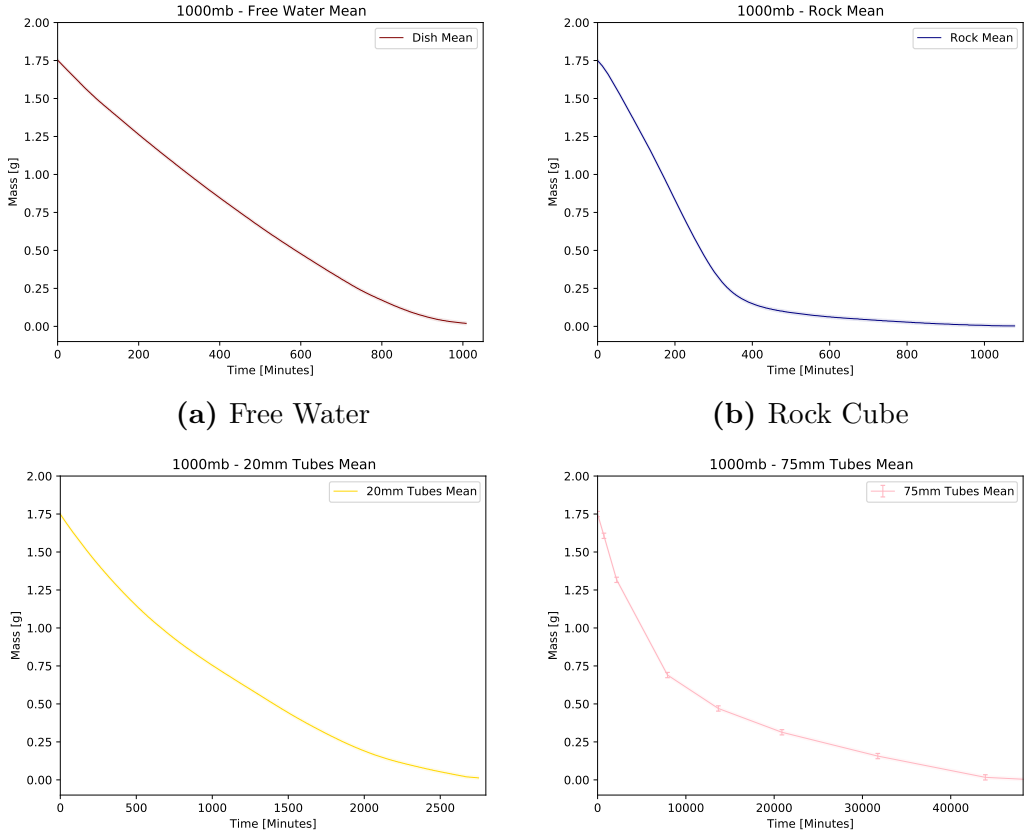

(a) Free Water

(b) Rock Cube

(c) 20 mm Tube Bundle

(d) 75 mm Tube Bundle

Figure 5.10: Results of The Lifetime of Liquid Water in Porous Media Experiment: Overall Mean Mass of Water Across Triplicate Experiments Over Time at 1000 mb.

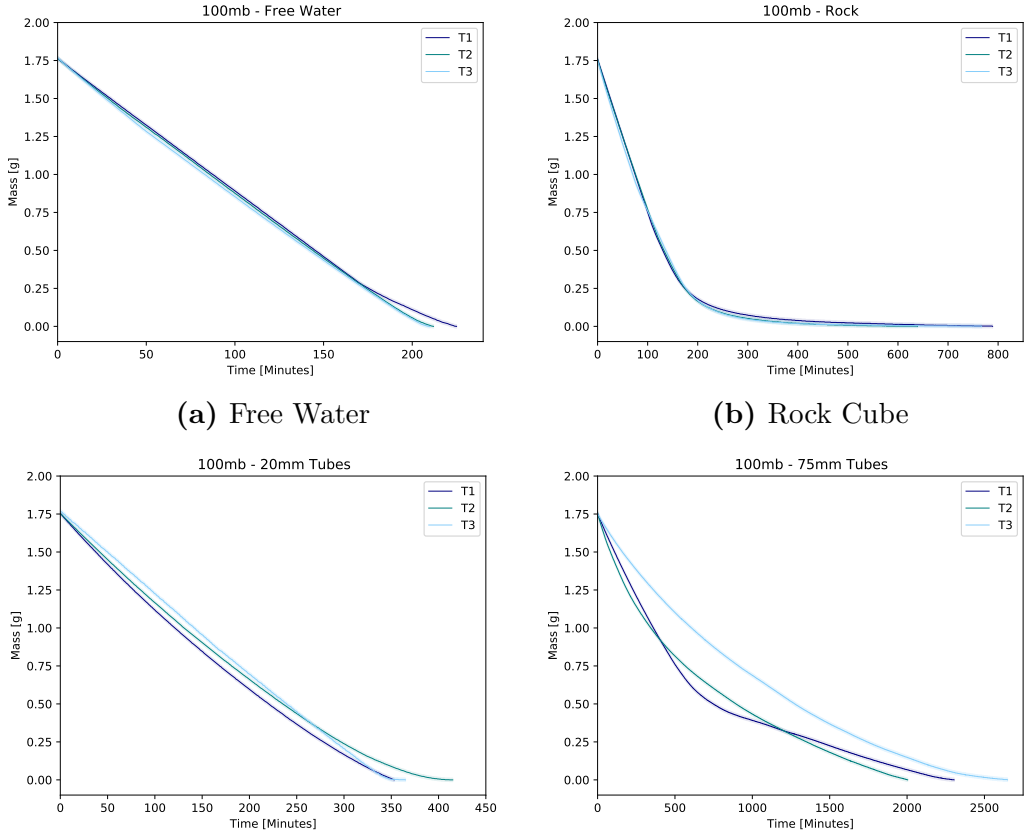

(a) Free Water

(b) Rock Cube

(c) 20 mm Tube Bundle

(d) 75 mm Tube Bundle

Figure 5.11: Results of The Lifetime of Liquid Water in Porous Media Experiment: Mass of Water Over Time at 100 mb. T1-T3 are labels for each experiment in the set of triplicates.

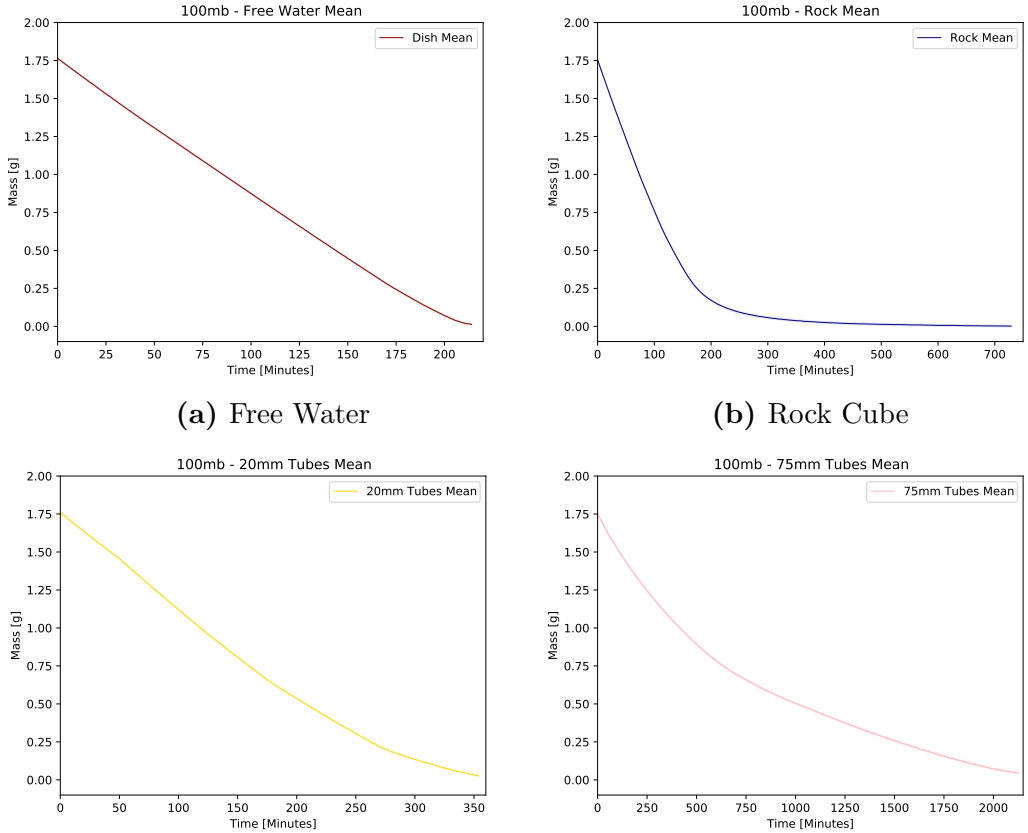

(a) Free Water

(b) Rock Cube

(c) 20 mm Tube Bundle

(d) 75 mm Tube Bundle

Figure 5.12: Results of The Lifetime of Liquid Water in Porous Media Experiment: Overall Mean Mass of Water Across Triplicate Experiments Over Time at 100 mb.

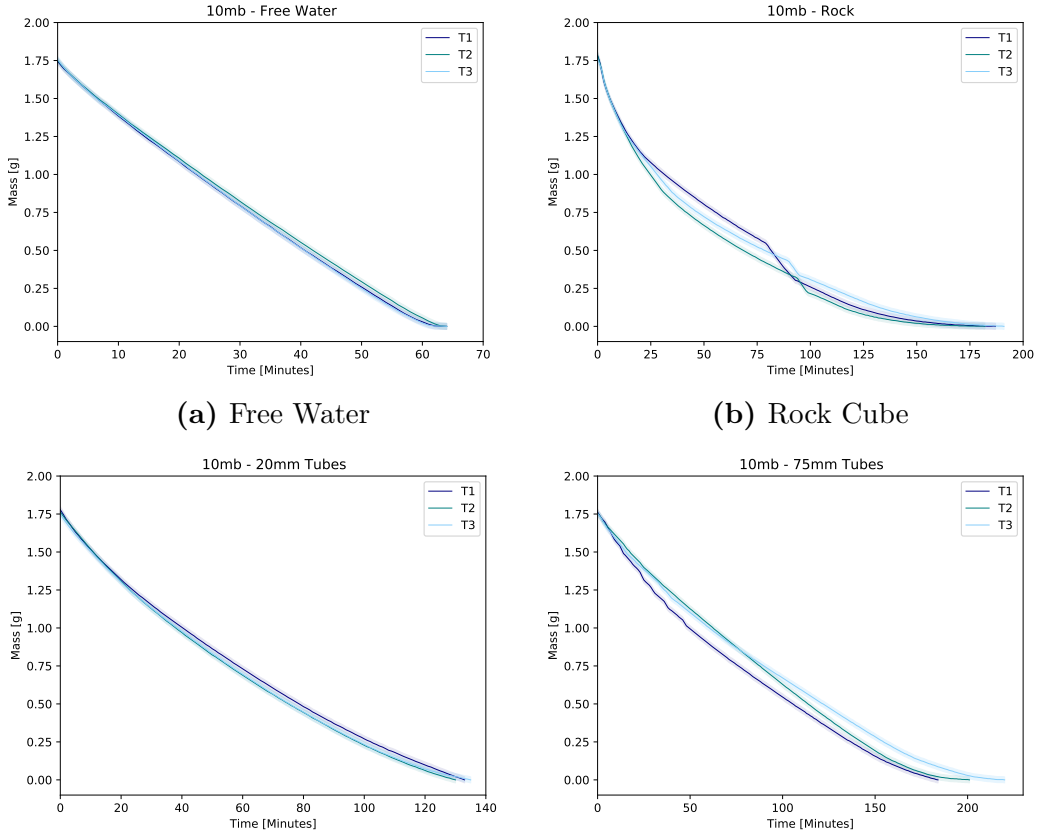

(a) Free Water

(b) Rock Cube

(c) 20 mm Tube Bundle

(d) 75 mm Tube Bundle

Figure 5.13: Results of the Lifetime of Liquid Water in Porous Media Experiment: Mass of Water Over Time at 10 mb. T1-T3 are labels for each experiment in the set of triplicates.

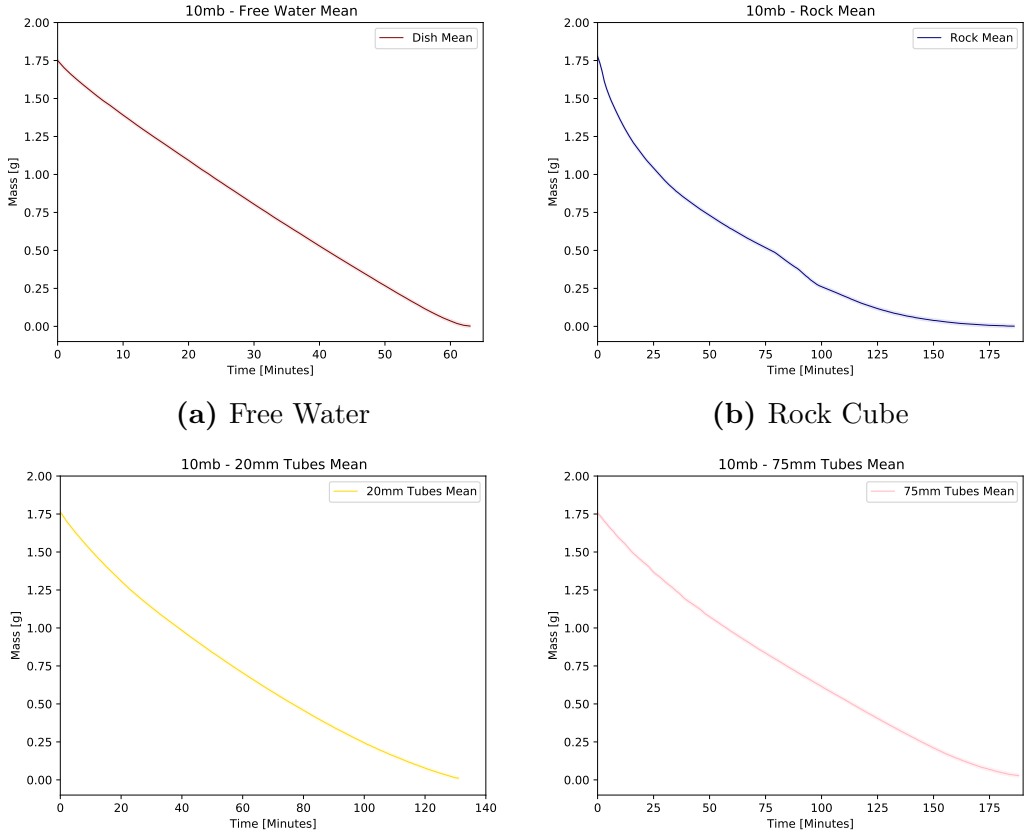

(a) Free Water

(b) Rock Cube

(c) 20 mm Tube Bundle

(d) 75 mm Tube Bundle

Figure 5.14: Results of the Lifetime of Liquid Water in Porous Media Experiment: Overall Mean Mass of Water Across Triplicate Experiments Over Time at 10 mb.

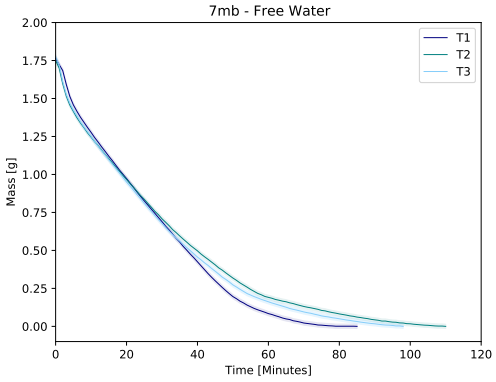

(a) Free Water

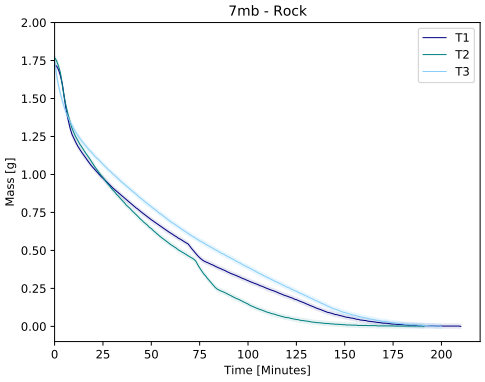

(b) Rock Cube

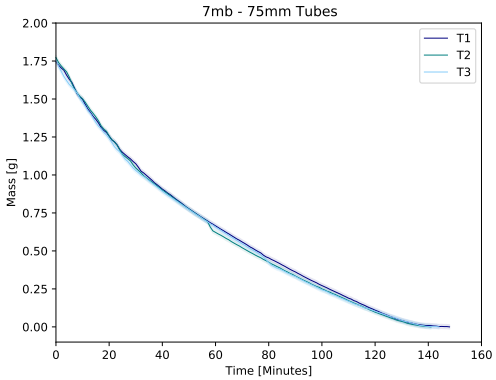

(c) 75 mm Tube Bundle

Figure 5.15: Results of the Lifetime of Liquid Water in Porous Media Experiment: Mass of Water Over Time at 7 mb. T1-T3 are labels for each experiment in the set of triplicates.

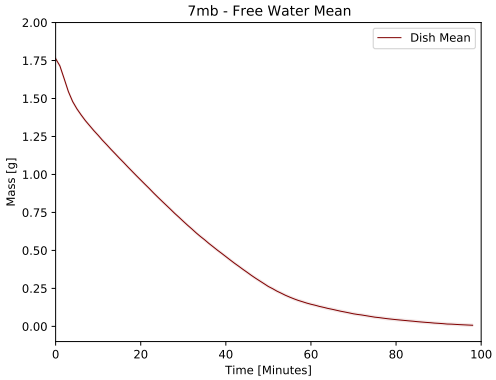

(a) Free Water

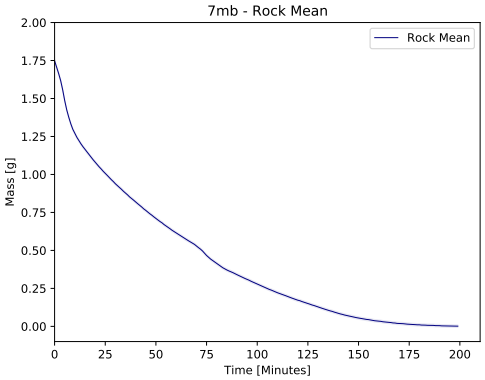

(b) Rock Cube

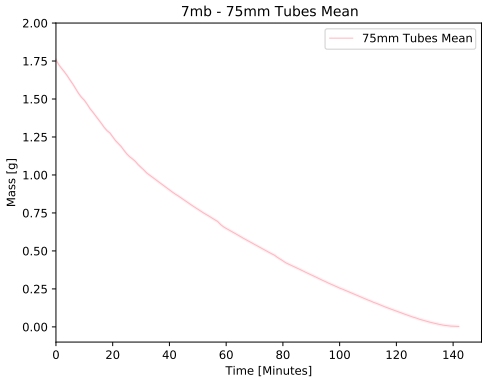

(c) 75 mm Tube Bundle

Figure 5.16: Results of the Lifetime of Liquid Water in Porous Media Experiment: Overall Mean Mass of Water Across Triplicate Experiments Over Time at 7 mb.

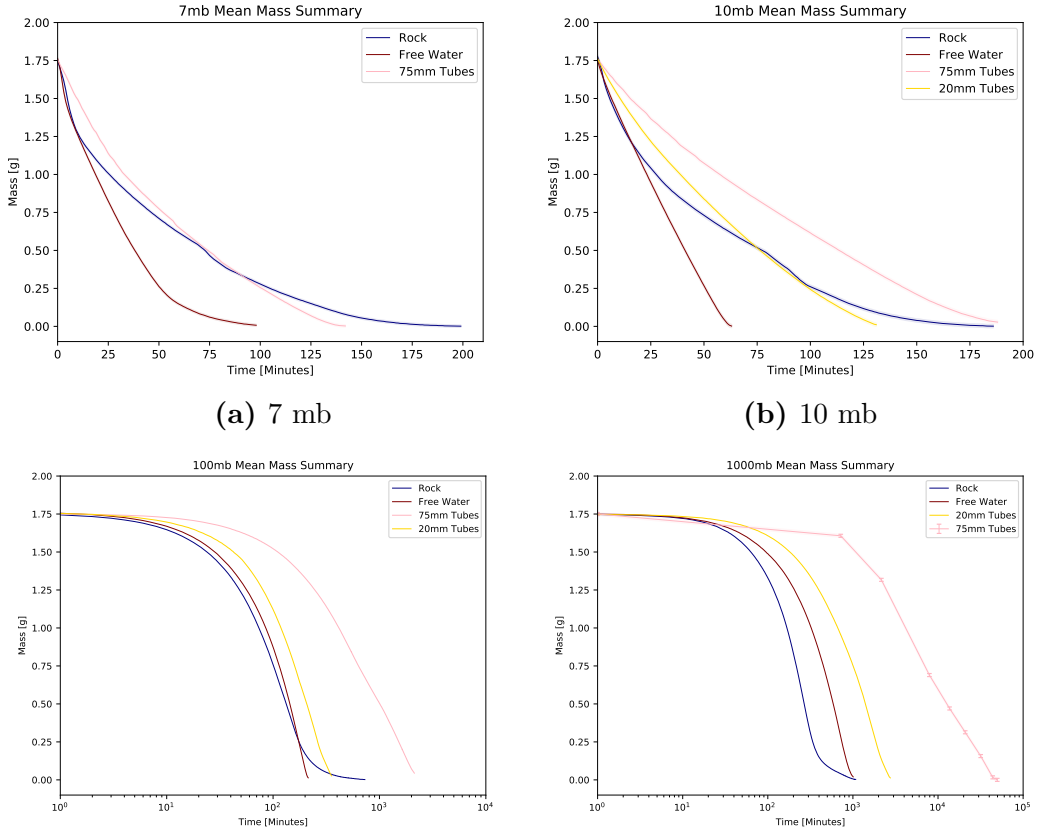

(a) 7 mb **(b)** 10 mb

(c) 100 mb **(d)** 1000 mb

Figure 5.17: Results of the Lifetime of Liquid Water in Porous Media Experiment: Summary of Overall Mean Mass of Water in Each Substrate Over Time at Each Pressure

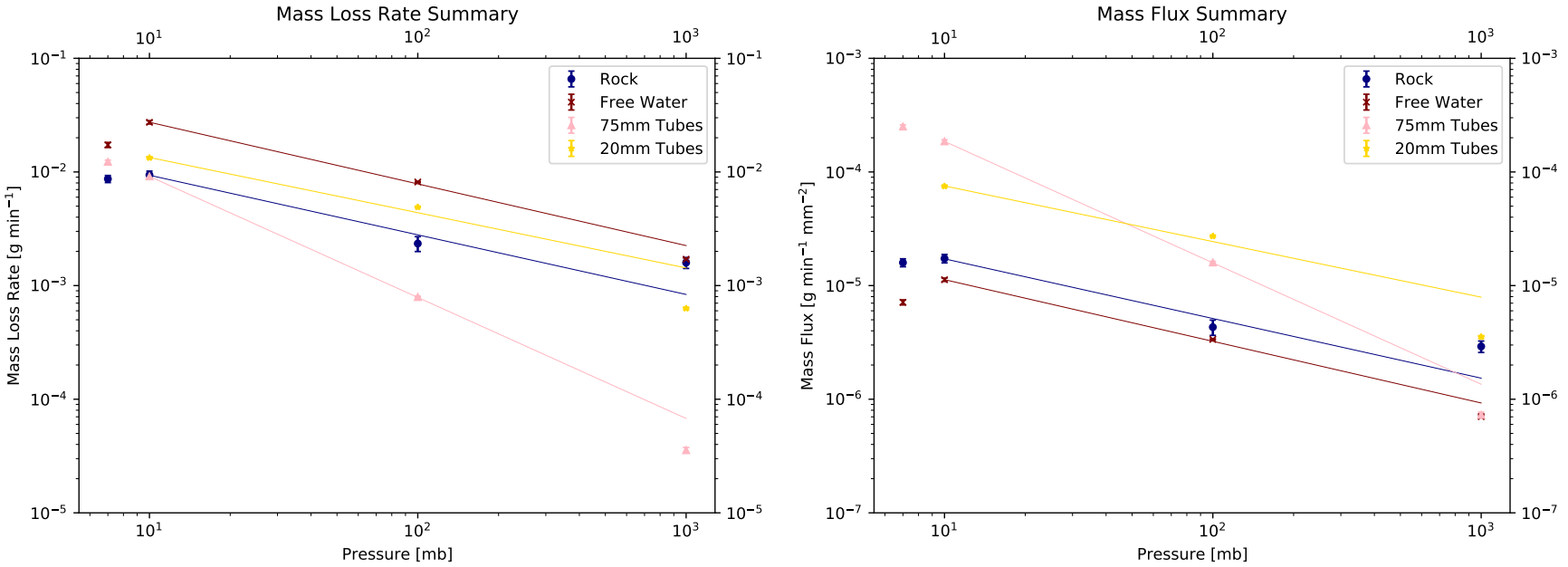

(a) Mass Loss Rate

(b) Mass Flux

Figure 5.18: Results of the Lifetime of Liquid Water in Porous Media Experiment: Summary of Mean Mass Loss Rate and Mean Mass Flux From Each Substrate at Each Experimental Pressure. The trend lines are fitted to the 10 mb, 100 mb and 1000 mb data points only due to the water freezing at 7 mb. The fitted lines show that the mass loss rate and the mass flux have a power law relationship with pressure.

Table 5.13: Results of the Effect of Solution Position Within Porous Media Experiment: Mass Loss Rate and Mass Flux From Capillary Tubes Bundles Containing Water at Different Positions Within the Tubes. Edge refers the bundle of tubes that had the 10 μL of water positioned at one opening of each tube. Centre refers to the bundle of tubes that had the 10 μL of water positioned in the centre of each tube. T1-T3 are labels for each experiment in the set of triplicates.

		Time [mins]	Mass Loss Rate [g min^{-1}]	Mass Flux [g min^{-1} mm^{-2}]
Edge	T1	1440 ± 354	$(1.53 \pm 0.24)\times10^{-4}$	$(2.76 \pm 0.43)\times10^{-7}$
	T2	1440 ± 354	$(1.53 \pm 0.24)\times10^{-4}$	$(2.76 \pm 0.43)\times10^{-7}$
	T3	1440 ± 354	$(1.53 \pm 0.24)\times10^{-4}$	$(2.76 \pm 0.43)\times10^{-7}$
	Mean	1440 ± 204	$(1.53 \pm 0.14)\times10^{-4}$	$(2.76 \pm 0.25)\times10^{-7}$
Centre	T1	4320 ± 467	$(5.09 \pm 0.65)\times10^{-5}$	$(9.21 \pm 1.18)\times10^{-8}$
	T2	4320 ± 467	$(5.09 \pm 0.65)\times10^{-5}$	$(9.21 \pm 1.18)\times10^{-8}$
	T3	4320 ± 467	$(5.09 \pm 0.65)\times10^{-5}$	$(9.21 \pm 1.18)\times10^{-8}$
	Mean	4320 ± 270	$(5.09 \pm 0.38)\times10^{-5}$	$(9.21 \pm 0.69)\times10^{-8}$

5.4.2 The Effect of Solution Position Within Porous Media on the Mass Loss of Water

The 10 μL of water situated at the capillary tube openings (bundle of 22 75 mm tubes, open at both ends) evaporated within (1440 ± 204) minutes at an overall mean rate of $(1.53 \pm 0.14)\times10^{-4}$ g min^{-1} compared with (4320 ± 270) minutes at a rate of $(5.09 \pm 0.38)\times10^{-5}$ g min^{-1} for the same volume of water situated at the centre of the tubes (Table 5.13 and Figure 5.19). The water in the centre of the tubes evaporated at a rate three times smaller than the water at the tubes edge demonstrating the inhibiting effect of the depth of water within porous media on mass loss rate at ambient atmospheric pressure.

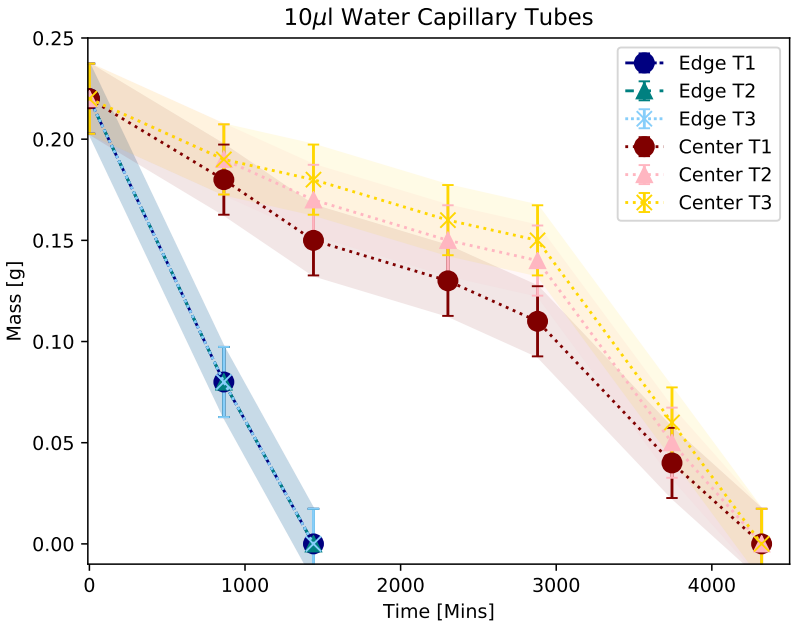

Figure 5.19: Results of the Effect of Solution Position Within Porous Media Experiment: Plot of Mass of Water in Capillary Tubes Containing Water at Different Positions Within the Tube. In one bundle of tubes, the position of the water within the tubes was at the tube opening (edge) and in another bundle, the position of the water was at the tube centre (centre). T1-T3 are labels for each experiment in the set of triplicates.

5.4.3 The Effect of Flux Surface Area on the Mass Loss of Water

The time taken for 1 g of water to completely evaporate or sublimate and the mass loss rate and the mass flux from each dish are summarised in Tables 5.14, 5.15, 5.16 and 5.17 for the experiments performed at 1000 mb, 100 mb, 10 mb and 7 mb respectively. The plots of mass loss rate against the flux surface area (the surface area through which mass loss can occur) of the dishes shows there is a linear relationship between mass loss rate and flux surface area at each pressure.

The mass loss rates from a single tube of 75 mm and a single tube of 20 mm length calculated from the mass flux from the tube bundles (Table 5.12) were situated on or very close to the line fit, with the exception of the 75 mm tube at 7 mb (Figure 5.20). This result shows that, at each experimental pressure, the relationship between mass loss rate and flux surface area of the regular circular media is linear. Figure 5.20 shows that the mass loss rate from the rock cube does not coincide with the fitted to the mass loss rate from the dishes, consistently displaying a mass loss rate greater than the line predicts given the porous surface area of the rock.

The mass loss rate and mass flux from all media had an approximately power law relationship with atmospheric pressure from 10 mb to 1000 mb (Figure 5.18b and Figure 5.21). At 7 mb the mass loss rate and mass flux from the dishes and the rock decreases relative to 10 mb. The power law relationship continues to 7 mb in the 75 mm tube bundle. The mass flux from the porous media is consistently greater from the porous media than from the dishes with the exception of the 75 mm tube bundle at 1000 mb which is very consistent with the dishes (Figure 5.21).

Summary

1. In regular circular media (dishes and single tubes) the mass loss rate of water is linearly dependent on the flux surface area of the medium.
2. The mean mass loss rate from the rock cube is higher than the line fit predicts for its flux surface area at every pressure.
3. The mean mass flux decreases with increasing flux surface area except for

the 75 mm tube bundle at 1000 mb.

4. The mean mass flux from porous media is typically higher than from the free water scenarios (dishes 1-3).

Table 5.14: Results of the Effect of Flux Surface Area on the Mass Loss of Water Experiment: Mass Loss Rate and Mass Flux From Each Substrate at 1000mb.

Substrate	Surface Area [mm^2]	Time [mins]	Mass Loss Rate [g min^{-1}]	Mass Flux [g min^{-1} mm^{-2}]
Dish 1	2428 ± 9	797 ± 47	(1.39 ± 0.03)×10^{-3}	(5.74 ± 0.14)×10^{-7}
Dish 2	970 ± 6	1800 ± 30	(5.56 ± 0.14)×10^{-4}	(5.73 ± 0.14)×10^{-7}
Dish 3	98 ± 2	15840 ± 624	(6.31 ± 0.15)×10^{-5}	(6.47 ± 0.20)×10^{-7}
Single 75 mm Tube	2.2 ± 0.02	-	(1.62 ± 0.09)×10^{-6}	(7.27 ± 0.42)×10^{-7}
Single 20 mm Tube	2.2 ± 0.02	-	(7.86 ± 0.22)×10^{-6}	(3.53 ± 0.09)×10^{-6}

Table 5.15: Results of the Effect of Flux Surface Area on the Mass Loss of Water Experiment: Mass Loss Rate and Mass Flux From Each Substrate at 100mb.

Substrate	Surface Area [mm^2]	Time [mins]	Mass Loss Rate [g min^{-1}]	Mass Flux [g min^{-1} mm^{-2}]
Dish 1	2428 ± 9	132 ± 6	(7.59 ± 0.12)×10^{-3}	(3.13 ± 0.05)×10^{-6}
Dish 2	970 ± 6	330 ± 8	(3.03 ± 0.05)×10^{-3}	(3.12 ± 0.05)×10^{-6}
Dish 3	98 ± 2	3290 ± 119	(3.04 ± 0.05)×10^{-4}	(3.11 ± 0.07)×10^{-6}
Single 75 mm Tube	2.2 ± 0.02	-	(3.55 ± 0.08) × 10^{-5}	(1.60 ± 0.03)×10^{-5}
Single 20 mm Tube	2.2 ± 0.02	-	(6.06 ± 0.13) × 10^{-5}	(2.72 ± 0.05)×10^{-5}

Table 5.16: Results of the Effect of Flux Surface Area on the Mass Loss of Water Experiment: Mass Loss Rate and Mass Flux From Each Substrate at 10mb.

Substrate	Surface Area [mm^2]	Time [mins]	Mass Loss Rate [g min^{-1}]	Mass Flux [g min^{-1} mm^{-2}]
Dish 1	2428 ± 9	41 ± 3	0.025 ± 0.001	(1.01 ± 0.03)×10^{-5}
Dish 2	970 ± 6	92 ± 4	0.0108 ± 0.0003	(1.12 ± 0.03)×10^{-5}
Dish 3	98 ± 2	813 ± 22	(1.23 ± 0.03)×10^{-3}	(1.26 ± 0.04)×10^{-5}
Single 75 mm Tube	2.2 ± 0.02	-	(4.13 ± 0.14)×10^{-4}	(1.86 ± 0.06)×10^{-4}
Single 20 mm Tube	2.2 ± 0.02	-	(1.67 ± 0.04)×10^{-4}	(7.49 ± 0.16)×10^{-5}

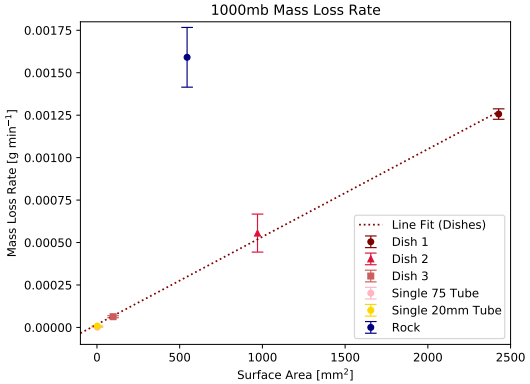

(a) 1000 mb

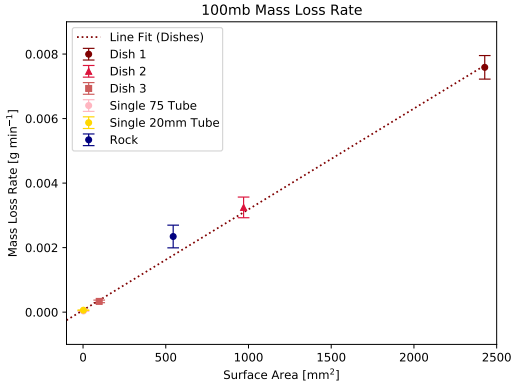

(b) 100 mb

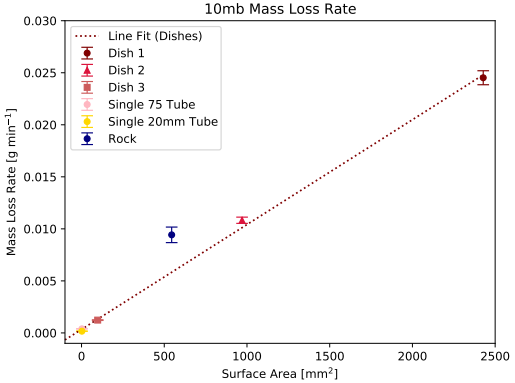

(c) 10 mb

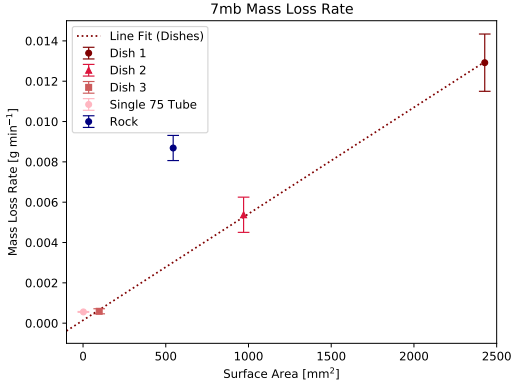

(d) 7 mb

Figure 5.20: Results of the Effect of Flux Surface Area on the Mass Loss of Water Experiment: Plots of Mass Loss Rate From Each Substrate at Each Pressure. The mass loss rate from each substrate is plotted against the surface area through which mass loss can occur (the flux surface area). The dashed line is the line of best fit to the mass loss rates from the dishes of varying surface area. The mass loss rates from the tubes and the rock are overlaid.

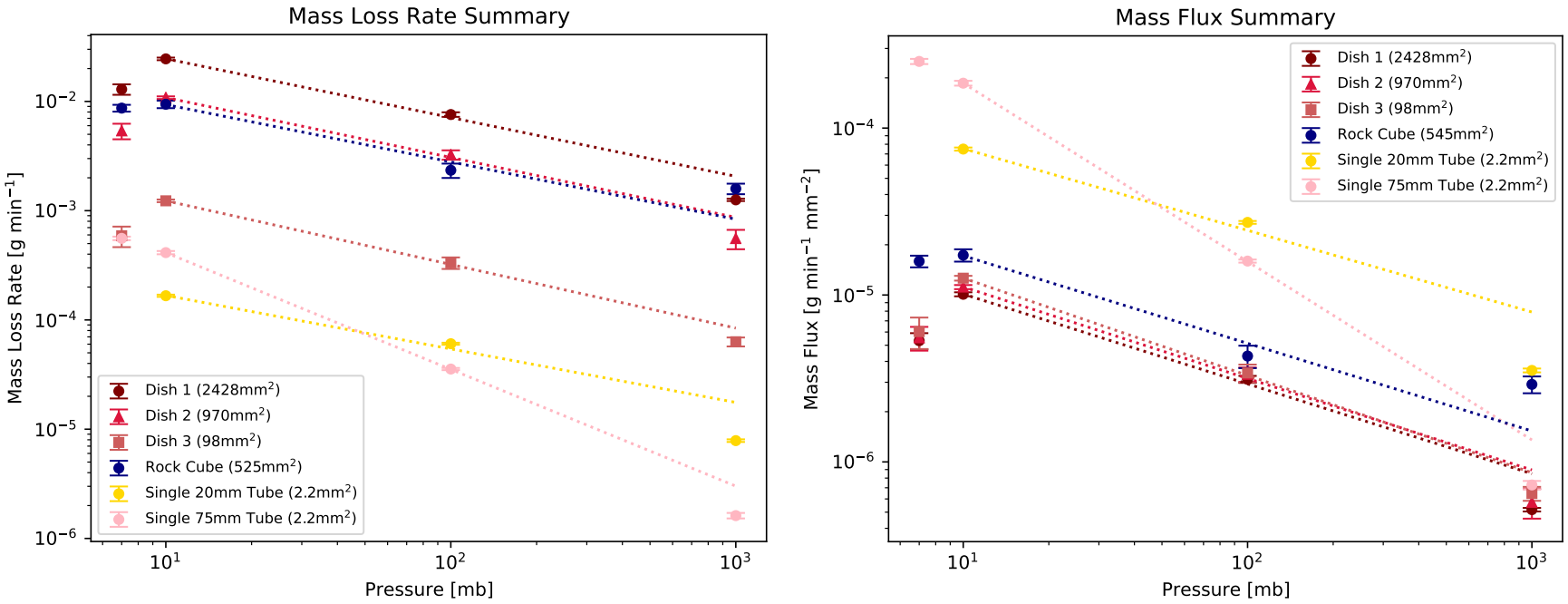

(a) Mass Loss Rate

(b) Mass Flux

Figure 5.21: Results of the Effect of Flux Surface Area on the Mass Loss of Water Experiment: Plots of Mass Loss Rate and Mass Flux From Each Substrate Vs Pressure. The dashed trend lines are fitted to the 10 mb, 100 mb and 1000 mb data points only due to the water freezing at 7 mb. The fitted lines show that the mass loss rate and the mass flux have a power law relationship with pressure.

Table 5.17: Results of the Effect of Flux Surface Area on the Mass Loss of Water Experiment: Mass Loss Rate and Mass Flux From Each Substrate at 7mb.

Substrate	Surface Area [mm^2]	Time [mins]	Mass Loss Rate [g min^{-1}]	Mass Flux [g min^{-1} mm^{-2}]
Dish 1	2428 ± 9	83 ± 9	0.0129 ± 0.0014	$(5.32 \pm 0.59)\times10^{-6}$
Dish 2	970 ± 6	200 ± 10	$(5.38 \pm 0.87)^{-3}$	$(5.54 \pm 0.90)\times10^{-6}$
Dish 3	98 ± 2	1980 ± 174	$(5.89 \pm 1.26)\times10^{-4}$	$(6.04 \pm 1.29)\times10^{-6}$
Single 75 mm Tube	2.2 ± 0.02	-	$(5.58 \pm 0.21)\times10^{-4}$	$(2.51 \pm 0.09)\times10^{-4}$

5.4.4 The Effect of Crusting Brines on the Mass Loss of Water From Porous Media

Salt Fractions

The mean salt and water fractions of the $MgSO_4$ solution were 0.34 and 0.66 respectively (Table 3.2). The mean salt and water fractions of the $FeSO_4$ & $MgSO_4$ solution were 0.27 and 0.73 respectively (Table 3.2).

$MgSO_4$

Capillary Tubes Each tube bundle (22 capillary tubes, open at both ends) contained a mean mass of (2.78 ± 0.01) g (1.75 mL) of $MgSO_4$ solution directly after they were filled. This mass of brine contains (1.83 ± 0.03) g of water. The mean mass of $MgSO_4$ solution and precipitated salt in the tube bundles after the ambient crystallisation period (ACP) was (2.67 ± 0.01) g, meaning (0.12 ± 0.02) g of water was lost (Table 5.18). This left a mean mass of (1.72 ± 0.04) g of water contained within the solution within the tubes at the start of the low pressure experiment.

At the end of the low pressure (7 mb) experiment, there was a mean of (1.33 ± 0.01) g of solution and precipitated salt within the each bundle of tubes. This brine mass corresponds to (0.39 ± 0.03) g of water remaining of the (1.72 ± 0.04) g of water at the start of the low pressure experiment. Therefore, after 4 days at 7 mb pressure, ∼23% of the water contained within the tubes at the start of the low pressure experiment remained. Of the 22 tubes in each bundle, a mean of 12 still contained visible liquid solution at the experiment conclusion. All of these tubes had solid salt formations plugging the tube openings with some having multiple salt plugs within the tube (Figure 5.22). Several of the tubes that did not contain solution were empty due to outgassing causing the solution to be violently expelled from the tube, despite the salt plug formations. The mean mass loss rate from the $MgSO_4$ solution in the bundle of 75 mm capillary tubes at 7 mb pressure was $(2.40 \pm 0.09) \times 10^{-4}$ g min^{-1} (Table 5.19). At this rate, the 1.72 g of water contained within each tube bundle would fully evaporate within ∼5 days (7167 minutes).

The mass loss rate of 1.72 g of pure water from the same bundle of 22 75 mm

tubes and from the dish were calculated using the data presented in section 5.4.1 and a rearranged Equation 5.6. The mean mass loss rate of water from the 75mm tube bundle at 7 mb was (0.0122 ± 0.0004) g min^{-1}. A mass of 1.72 g of water would have evaporated within 140 minutes. From the dish, the mass loss rate of water at 7 mb was (0.018 ± 0.001) g min^{-1}. A mass of 1.72 g of water would have sublimated within 95.5 minutes. Comparing the mean mass loss rate from the $MgSO_4$ solution in the 75 mm tube bundle to that of the same mass of pure water from the bundle of 75 mm tube bundle and the dish, there is a decrease in mass loss rate by a factor 51 and 75 times respectively.

Additionally, looking at the shape of the mass plot, after an initial period of relatively rapid mass loss - some of which was caused by violent expulsion due to outgassing - the curve flattens considerably (Figure 5.23). This effect is most prevalent in experiment T1, where the mean mass loss rate over the first 1500 minutes was 5.59×10^{-4} g min^{-1}, reducing by a factor of 10.4 to 5.37×10^{-5} g min^{-1} for the remaining 4042 minutes. If the mass loss continued at that rate, it would take ∼11.5 days (16480 minutes) for the mass of water contained within the tubes at 1500 minutes to evaporate completely. Adding the first 1500 minutes of water loss, this would result in an overall time of 12.5 days for the 1.72 g of water to evaporate completely (17980 minutes). This extends the lifetime of water by 128 and 188 times compared to 1.72 g of pure water in the 75 mm tube bundle and dish respectively.

Porous Rocks Rock P1-M contained (10.75 ± 0.02) g of $MgSO_4$ solution directly after soaking (Table 5.18). During the ambient crust-formation period (0.67 ± 0.03) g of water evaporated, resulting in brine within the rock containing (6.43 ± 0.22) g of water at the start of the low pressure experiment. After 4 days at 7 mb pressure, rock P1-M contained (3.89 ± 0.02) g of solution and crystallised salt, corresponding to (0.24 ± 0.02) g of water. By comparison, in the free water case, (6.43 ± 0.22) g of water would be fully evaporated/sublimated within 357 minutes (calculated using the mass loss rate of water from the dish at 7mb ((0.018 ± 0.001) g min^{-1}) determined in section 5.4.1 and Equation 5.6). The mean mass loss rate from rock P1-M was (1.09 ± 0.04) $\times 10^{-3}$ g min^{-1} (Table 5.19). At this rate, the (6.43 ± 0.22) g of water contained within the rock at the start of the experiment would evaporate within 4.1 days (5899 minutes), extending the lifetime of water by 16.5 times compared to the free water scenario.

The mean mass loss rate over the experimental period of (5699 ± 218) minutes

was (1.09 ± 0.04) $\times 10^{-3}$ g min^{-1} (Table 5.19 and Figure 5.24). For the first 500 minutes, the mean mass loss rate was 5.43×10^{-3} g min^{-1} reducing to 8.78×10^{-4} g min^{-1} for the following 3800 minutes then further reducing to 9.79×10^{-5} g min^{-1} - reductions by a factor of 6.18 and 55.5 compared to the mean mass loss rate of the first 500 minutes. Towards the end of the experiment, the mass of brine within rock P1-M was approaching the salt fraction meaning there was only a very small amount of liquid brine remaining. The mass broached the upper limit of the uncertainty in the salt fraction so within the bounds of uncertainty it is possible that no liquid water remained at all. When rock P1-M was split open, no liquid was visible.

Rock P2-M contained (6.16 ± 0.02) g of $MgSO_4$ solution directly after soaking (Table 5.18). During the ambient crystallisation period (0.38 ± 0.03) g of water evaporated, resulting in the brine within the rock containing (3.69 ± 0.13) g of water at the start of the low pressure experiment. After 4 days at 7 mb pressure, rock P2-M contained (4.01 ± 0.02) g of solution and crystallised salt, corresponding to (1.92 ± 0.02) g of water (Table 5.19). By comparison, in the free water case, 3.69 g of water would be fully evaporated/sublimated within 205 minutes (calculated using the mass loss rate of water from the dish at 7mb ((0.018 ± 0.001) g min^{-1}) determined in section 5.4.1 and Equation 5.6). The mean mass loss rate from rock P2-M was (3.18 ± 0.08) $\times 10^{-4}$ g min^{-1}. At this rate, the (3.69 ± 0.13) g of water contained within the rock at the start of the experiment would evaporate within 8 days (11603 minutes), extending the lifetime of water by 57 times compared to the free water scenario.

The mean mass loss rate over the experimental period of (5561 ± 126) minutes was (3.18 ± 0.08)$\times 10^{-4}$ g min^{-1} (Table 5.19 and Figure 5.24). For the first 100 minutes, the mean mass loss rate was 4.12×10^{-3} g min^{-1}, decreasing to 3.01×10^{-4} g min^{-1} for the following 3900 minutes then decreasing further to 1.17×10^{-4} g min^{-1} for the remaining 1561 minutes. These are reductions in mass loss rate by factors of 13.7 and 35.2 respectively compared to the first 100 minutes. Rock P2-M, despite initially containing a smaller volume of solution than P1-M, contained (4.01 ± 0.02) g of brine and precipitated salt after 4 days at 7 mb. A salt crust had formed over the surface of the rock, covering much of the pore surface area (Figure 5.25a) and when split open directly after the low pressure experiment, liquid solution was visible (Figure 5.25b). There was also evidence of some expulsion of solution from the rock occurring (Figure 5.25a) which suggests that even with some pores exposed, liquid water can be preserved

within the rock over a 4 day period at 7 mb. This may be due to the evaporation of water in the unclogged pores causing rapid salt crystallisation, re-plugging the exposed pores.

Table 5.18: Results of the Effect of Crusting Brines on the Mass Loss of Water From Porous Media Experiment: Summary of $MgSO_4$ Salt Crusted Porous Media Preparation. Initial brine mass is the mass of brine contained within the medium directly after soaking. Initial water mass is the mass of water contained within the initial brine mass. Brine mass after ACP (ambient crystallisation period) is the mass of brine contained within the porous medium after three days of crust formation has taken place under ambient conditions. ACP water loss is the mass of water lost during that period. Water mass after ACP is the water contained within the brine within the porous medium after the ambient crystallisation period. T1-T3 are labels for each experiment in the set of triplicates. P1-M and P2-M refer to each preliminary rock experiment.

Porous Medium	Triplicate	Initial Brine Mass ($m_{b,i}$ [g])	Initial Water Mass ($m_{w,i}$ [g])	Brine Mass After ACP ($m_{b,a}$ [g])	ACP Water Loss (Δm_w [g])	Water Mass After ACP (m_w [g])
Tubes	T1	2.78 ± 0.02	1.83 ± 0.06	2.67 ± 0.02	0.11 ± 0.03	1.72 ± 0.07
	T2	2.80 ± 0.02	1.85 ± 0.06	2.68 ± 0.02	0.12 ± 0.03	1.73 ± 0.07
	T3	2.76 ± 0.02	1.82 ± 0.05	2.64 ± 0.02	0.12 ± 0.03	1.70 ± 0.06
	Mean	2.78 ± 0.01	1.83 ± 0.03	2.67 ± 0.01	0.12 ± 0.02	1.72 ± 0.04
Rock	P1-M	10.75 ± 0.02	7.09 ± 0.22	10.08 ± 0.02	0.67 ± 0.03	6.43 ± 0.22
	P2-M	6.16 ± 0.02	4.07 ± 0.12	5.78 ± 0.02	0.38 ± 0.03	3.69 ± 0.13

Table 5.19: Results of the Effect of Crusting Brines on the Mass Loss of Water From Porous Media Experiment: Mass Loss Rate and Mass Flux of $MgSO_4$ Brine From Porous Media at 7 mb. N_{end} is the number of tubes (out of 22) that have liquid brine remaining in them after 4 days at 7 mb. The brine mass and water refer to the mass of brine and mass of water contained in that brine remaining within the porous medium after 4 days at 7 mb. T1-T3 are labels for each experiment in the set of triplicates. P1-M and P2-M refer to each preliminary rock experiment.

Pressure	Triplicate	Time [mins]	Mass Loss Rate [g min^{-1}]	Mass Flux [g $min^{-1}mm^{-2}$]	N_{end}	Brine Mass [g]	Water Mass [g]
Tubes	T1	5542 ± 482	$(1.91 \pm 0.17)\times10^{-4}$	$(3.89 \pm 0.35)\times10^{-6}$	16	1.61 ± 0.02	0.667 ± 0.019
	T2	5594 ± 443	$(2.66 \pm 0.21)\times10^{-4}$	$(5.43 \pm 0.45)\times10^{-6}$	11	1.19 ± 0.02	0.242 ± 0.019
	T3	5561 ± 273	$(2.60 \pm 0.13)\times10^{-4}$	$(5.31 \pm 0.28)\times10^{-6}$	8	1.19 ± 0.02	0.26 ± 0.02
	Mean	-	$(2.40 \pm 0.09)\times10^{-4}$	$(4.88 \pm 0.20)\times10^{-6}$	12	1.33 ± 0.01	0.39 ± 0.03
Preliminary Rocks	P1-M	5699 ± 218	$(1.09 \pm 0.04)\times10^{-3}$	-	-	3.89 ± 0.02	0.24 ± 0.02
	P2-M	5561 ± 126	$(3.18 \pm 0.08)\times10^{-4}$	-	-	4.01 ± 0.02	1.92 ± 0.02

$FeSO_4$ & $MgSO_4$

The brine composed of a 1:1 mixture of saturated $FeSO_4$ & $MgSO_4$ was effective at inhibiting water mass loss from test rocks.

Rock P1-F contained (7.87 ± 0.02) g of solution directly after soaking (Table 5.20). During the ambient crust-formation period (1.20 ± 0.03) g of water evaporated. The mass of water contained within the rock at the beginning of the 7 mb experiment was (4.54 ± 0.18) g. After 4 days at 7 mb pressure, rock P1-F contained (4.94 ± 0.02) g of solution and crystallised salt, corresponding to (2.81 ± 0.13) g of water (Table 5.21). By comparison, in the free water case, 4.54 g of water would be fully evaporated/sublimated within 252 minutes (calculated using the mass loss rate of water from the dish at 7mb ((0.018 ± 0.001) g min^{-1}) determined in section 5.4.1 and Equation 5.6). The mean mass loss rate over the experimental period was 3.00×10^{-4} g min^{-1}. At this rate, the (4.54 ± 0.18) g of water contained within the rock at the start of the low pressure experiment would evaporate within ∼10.5 days (15133 minutes), extending the lifetime of liquid water by 60 times compared to the free water scenario.

The mean mass loss rate over the experimental period was 3.00×10^{-4} g min^{-1} (Table 5.21 and Figure 5.26). For the first 250 minutes the rate was 2.20×10^{-3} g min^{-1}, decreasing by a factor of 10.3 to 2.14×10^{-4} g min^{-1} for the remaining 5509 minutes, during which time it was relatively constant. The mass of salt contained within the solution saturating the rock directly after soaking was 2.125 g. Figure 5.26 shows that the mass does not come close to reaching the salt fraction, suggesting there is still a substantial volume of liquid contained within the rock pore-space. When the rock was split open after the low pressure experiment it contained visible liquid solution within the vesicles and sections of the rock interior were darkened suggesting they were soaked with liquid (Figure 5.27b and Figure 5.27c).

Rock P2-F contained (6.65 ± 0.02) g of solution directly after soaking (Table 5.21). During the ambient crystallisation period (1.07 ± 0.03) g of water evaporated. The mass of water contained within the rock at the start of the low pressure experiment was therefore (4.51 ± 0.15) g. After 4 days at 7 mb, rock P2-F contained (3.98 ± 0.02) g of solution and crystallised salt, corresponding to (2.19 ± 0.11) g of water (Table 5.21). In the free water scenario, 4.51 g of water at 7 mb would evaporate/sublimate within 251 minutes (calculated using the mass loss rate of water from the dish at 7mb ((0.018 ± 0.001) g min^{-1}) determined

in section 5.4.1 and Equation 5.6). In this experiment, more than half the mass of water contained within the brine contained within the rock at the start of the low pressure experiment was preserved after 4 days at 7 mb. The mean mass loss rate from the rock was 2.98×10^{-4} g min^{-1}. At this rate, the (4.51 $\pm$ 0.15) g of water contained within the rock at the start of the low pressure experiment would evaporate within days ∼10.5 days (15134 minutes), extending the lifetime of liquid water by 60 times compared to the free water scenario.

The mean mass loss rate from the rock was 2.98×10^{-4} g min^{-1} (Table 5.21 and Figure 5.26). For the first 1300 minutes, the mean mass loss rate was 9.76×10^{-4} g min^{-1}, reducing by a factor of 12.1 to 8.07×10^{-5} g min^{-1} for the remaining 4063 minutes, during which time the rate was relatively constant. Figure 5.26 shows that the mass of the solution and crystallised salt within the rock at 7 mb does not approach the salt fraction, and the mass is almost constant from ∼2500 minutes onward.

Summary

1. $MgSO_4$ solution in salt-plugged 75 mm tube bundles had a mean mass loss rate of 2.40×10^{-4} g min^{-1}, a reduction by factors of 51 and 75 compared to the mass loss rate of pure water from the 75 mm tube bundle and the free water dish respectively.

2. The mass loss rate of water from the $MgSO_4$ solution in salt-plugged 75 mm tube bundles decreased with time. When this was accounted for, the lifetime of liquid water could be extended by up to 128 and 188 times compared to the corresponding mass of pure water from the 75 mm tube bundle and the free water dish respectively.

3. The tubes were plugged at each end with salt crystal formations that were in some cases sufficient to prevent the total evaporation of water from the brine within the experimental period, leaving a mean of 12 out of 22 tubes containing visible liquid brine after 4 days at 7 mb pressure.

4. At 7 mb pressure $MgSO_4$ crusted rocks could extend the lifetime of water by up to 57 times when compared to the same mass of free water.

5. One of the two $MgSO_4$ crusted rocks contained visible liquid brine after 4 days at 7 mb pressure.

6. At 7 mb pressure $FeSO_4$ & $MgSO_4$ crusted rocks could extend the lifetime of water by up to 60 times when compared to the same mass of free water.

7. Visible liquid brine was present within both of the $FeSO_4$ & $MgSO_4$ salt crusted rocks after 4 days at 7 mb pressure.

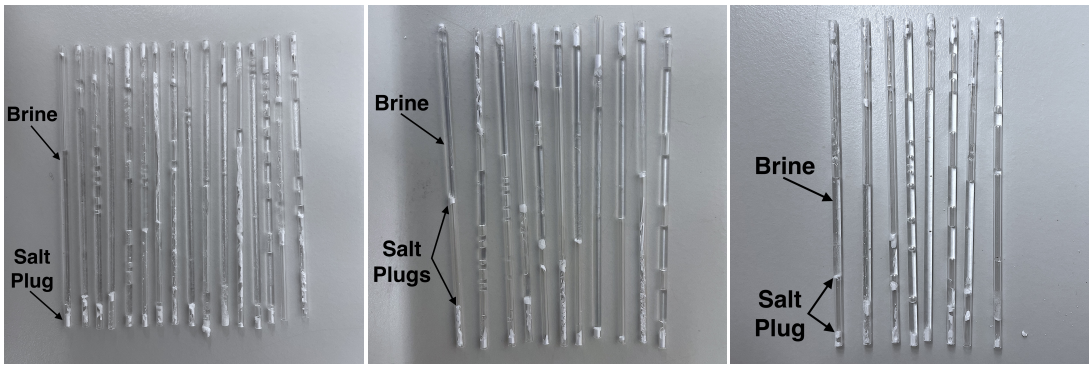

(a) T1 **(b)** T2 **(c)** T3

Figure 5.22: Results of the Effect of Crusting Brines on the Mass Loss of Water From Porous Media Experiment: Capillary Tubes That Contained Liquid $MgSO_4$ Solution After 4 Days at 7 mb. Crystallised salt has plugged the tube openings, preserving the liquid brine within. T1-T3 are labels for each experiment in the set of triplicates.

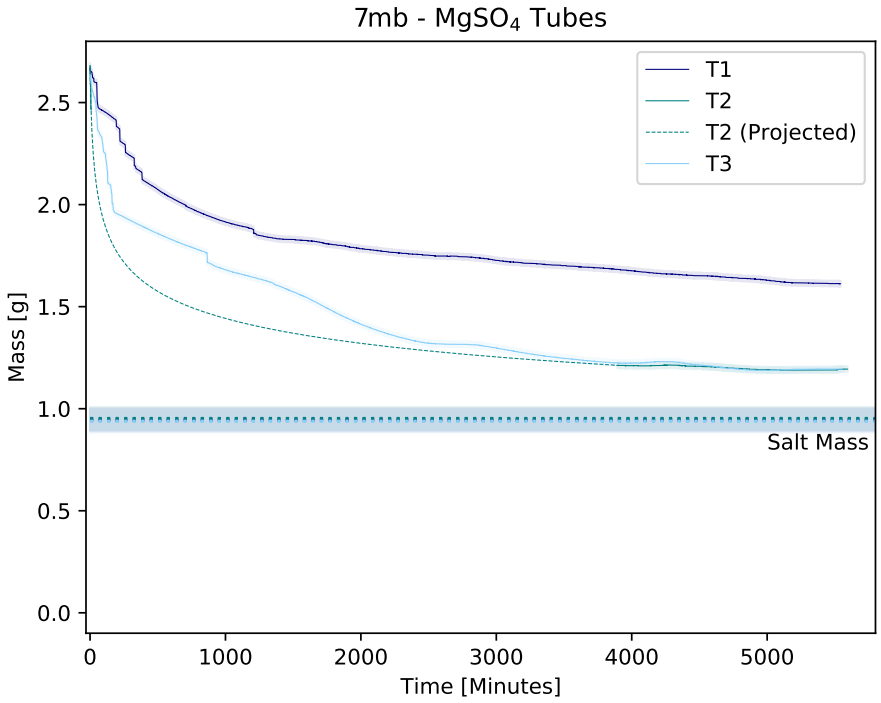

Figure 5.23: Results of the Effect of Crusting Brines on the Mass Loss of Water From Porous Media Experiment: Plot of Mass of $MgSO_4$ Brine and Precipitated Salt in 75 mm Tube Bundle Over 4 days at 7 mb. The mass data for T2 was not recorded from 10-3896 minutes due to a technical failure. The dotted line is an approximate projection of the mass over time. The horizontal dashed lines are the mass of the salt contained within the initial mass of brine saturating the tube bundles. T1-T3 are labels for each experiment in the set of triplicates. P1-M and P2-M refer to each preliminary rock experiment

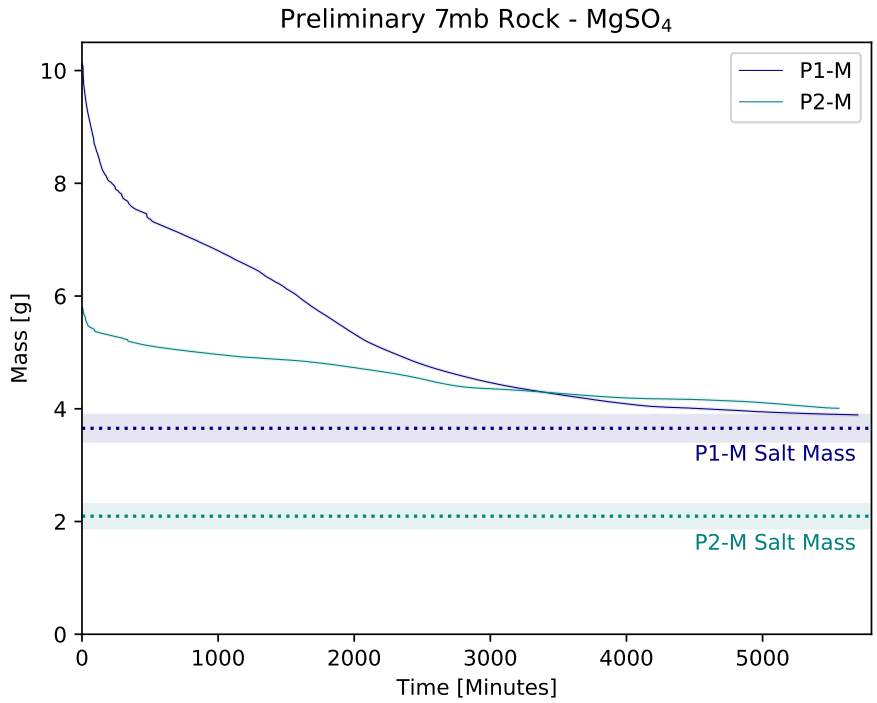

Figure 5.24: Results of the Effect of Crusting Brines on the Mass Loss of Water From Porous Media Experiment: Mass of $MgSO_4$ Brine and Precipitated Salt in Porous Rock Over 4 Days at 7 mb. The horizontal dashed lines are the mass of the salt contained within the initial mass of brine saturating the rocks. P1-M and P2-M refer to each preliminary rock experiment

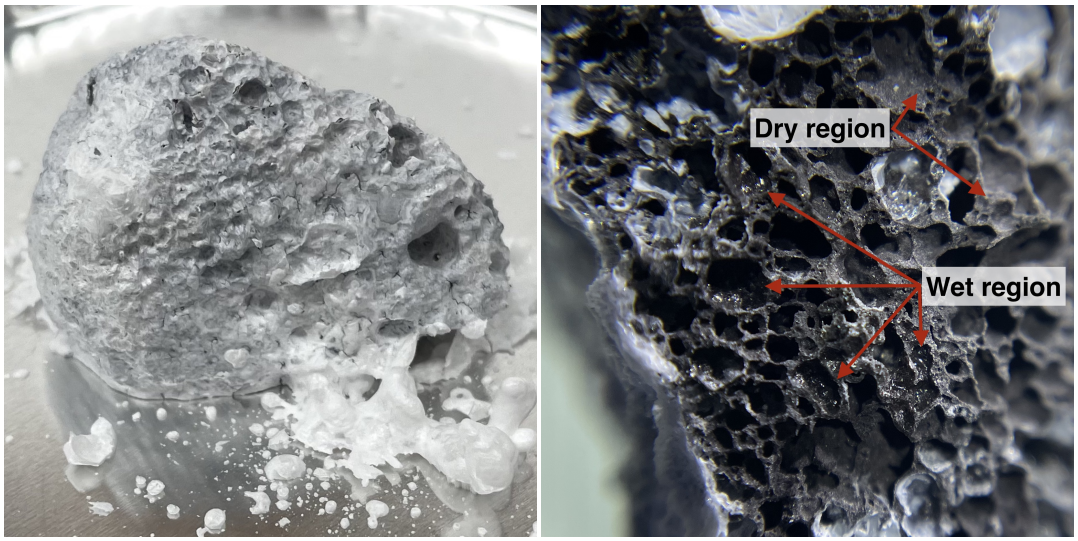

(a) Rock Exterior **(b)** Rock Interior

Figure 5.25: Results of the Effect of Crusting Brines on the Mass Loss of Water From Porous Media Experiment: Porous Rock PM-2 Interior Containing Liquid $MgSO_4$ Solution After 4 Days at 7 mb. (a) Salt crust covering rock exterior. The scattered salt formations are indicative of violent expulsion of solution from some of the rock pores. (b) Liquid $MgSO_4$ solution and $MgSO_4$ crystals are present in the rock interior.

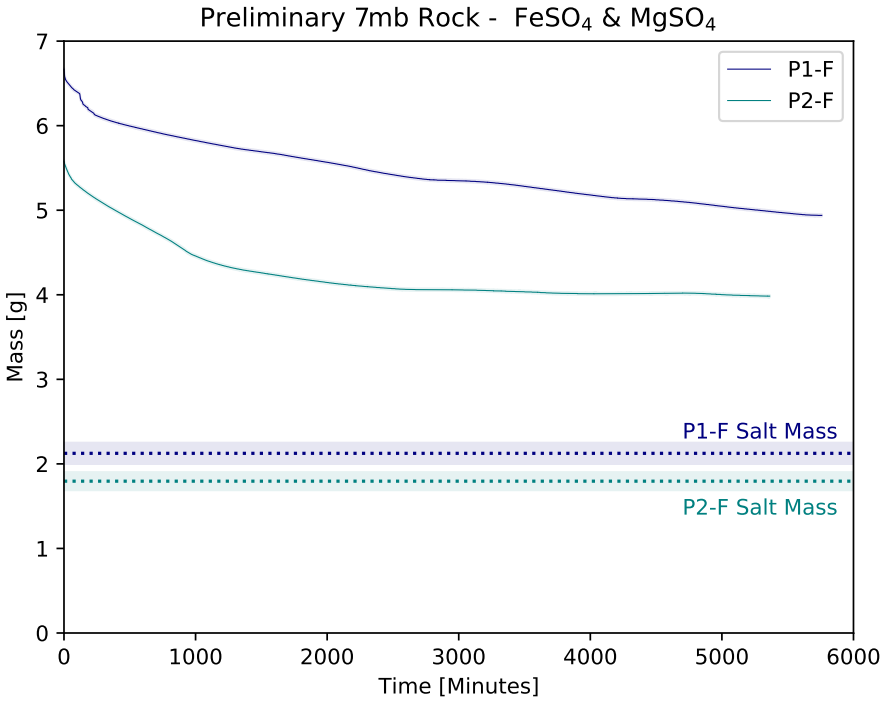

Figure 5.26: Results of the Effect of Crusting Brines on the Mass Loss of Water From Porous Media Experiment: Mass of $FeSO_4$ & $MgSO_4$ Brine and precipitated salt contained within porous rock over 4 days at 7 mb. The horizontal dashed lines are the mass of the salt contained within the initial mass of brine saturating the rocks. P1-F and P2-F refer to each preliminary rock experiment

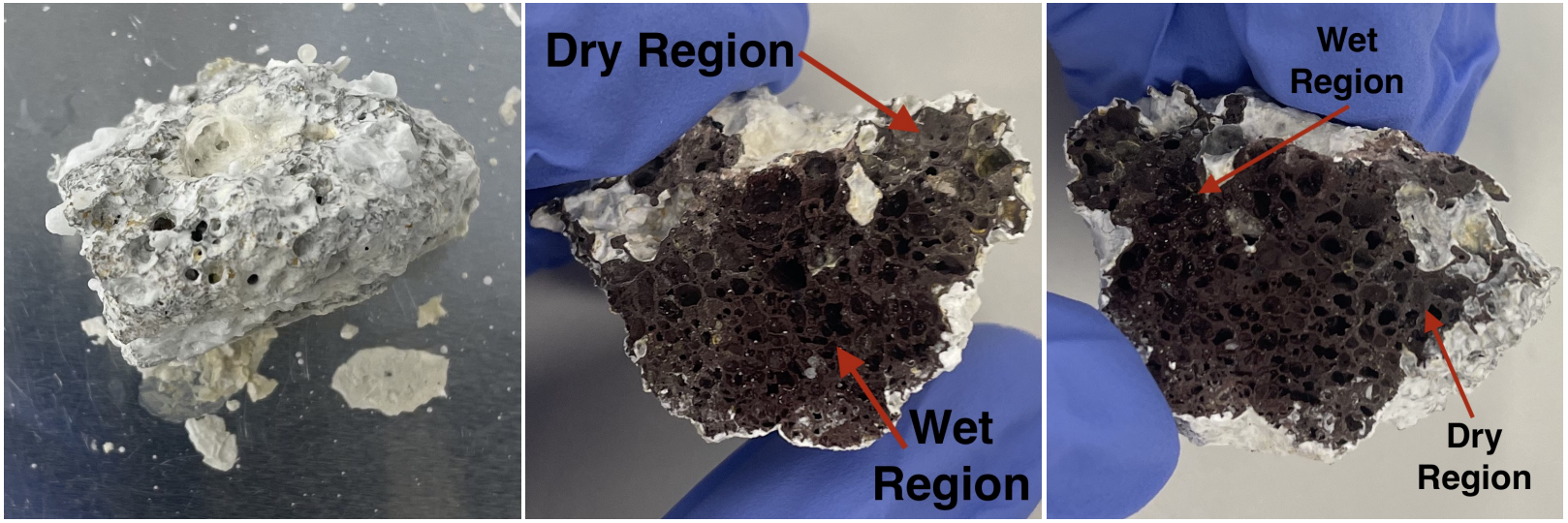

(a) Salt Crusted Rock Exterior **(b)** Rock interior 1 **(c)** Rock interior 2

Figure 5.27: Results of the Effect of Crusting Brines on the Mass Loss of Water From Porous Media Experiment: Porous Rock PF-1 Interior Containing Liquid $FeSO_4$ & $MgSO_4$ Solution After 4 days at 7 mb. (a) Salt crust covering rock exterior. (b) and (c) Liquid $FeSO_4$ & $MgSO_4$ solution and salt crystals are present in the rock interior.

Table 5.20: Results of the Effect of Crusting Brines on the Mass Loss of Water From Porous Media Experiment: Summary of $FeSO_4$ & $MgSO_4$ Salt Crusted Rock Preparation. Initial brine mass is the mass of brine contained within the medium directly after soaking. Initial water mass is the mass of water contained within the initial brine mass. Brine mass after ACP (ambient crystallisation period) is the mass of brine contained within the rock after three days of crust formation has taken place under ambient conditions. ACP water loss is the mass of water lost during that period. Water mass after ACP is the water contained within the brine within the rock after the ambient crystallisation period. P1-F and P2-F refer to each preliminary rock experiment.

Porous Medium	Experiment	Initial Brine Mass ($m_{b,i}$ [g])	Initial Water Mass ($m_{w,i}$ [g])	Brine Mass After ACP ($m_{b,a}$ [g])	ACP Water Loss (Δm_w [g])	Water Mass After ACP (m_w [g])
Rock	P1-F	7.87 ± 0.02	5.75 ± 0.18	6.67 ± 0.02	1.20 ± 0.03	4.54 ± 0.18
	P2-F	6.65 ± 0.02	4.86 ± 0.15	5.58 ± 0.02	1.07 ± 0.03	4.51 ± 0.15

Table 5.21: Results of the Effect of Crusting Brines on the Mass Loss of Water From Porous Media Experiment: Summary of $FeSO_4$ & $MgSO_4$ Mass Loss Rate From Porous Rock at 7 mb. The brine mass and water mass refer to the mass of brine (and precipitated face) and mass of water contained in that brine remaining within the porous medium after 4 days at 7 mb . P1-F and P2-F refer to each preliminary rock experiment

Pressure	Experiment	Time [mins]	Mass Loss Rate [g min^{-1}]	Brine/Salt Mass [g]	Water Mass [g]
Preliminary	P1-F	5759 ± 188	$(3.00 \pm 0.10)\times10^{-4}$	4.94 ± 0.02	2.81 ± 0.13
Rocks	P2-F	5363 ± 311	$(2.98 \pm 0.18)\times10^{-4}$	3.98 ± 0.02	2.19 ± 0.11

5.5 Discussion

Terrestrial endolithic habitats are populated by complex communities of microorganisms in many extreme environments, protected by the properties of their rocky homes that buffer the hostile exterior conditions. One of those properties is the ability to retain moisture in arid environments, providing the liquid water essential to their survival. By exploring the lifetime of liquid water and brine in porous media under low pressure conditions, the work presented in this chapter contributes to our understanding of the habitability of endolithic environments on the surface of Mars.

These results show that porous media decreases the mass loss rate of water by reducing the surface area through which evaporation or sublimation can occur. The proportionate difference in mass loss rate from porous media and the free water scenario diminishes with decreasing pressure. Under ambient atmospheric conditions, the effect of reducing evaporative surface area by introducing water to a porous substrate can be significant - the mass loss rate from the 75 mm capillary tube bundle was 48 times lower than free water case. At 10 mb, the proportionate difference of the mass loss rate between the same substrates reduced to a factor of 3. However, the introduction of saturated $MgSO_4$ to porous media can decrease the mass loss rate of water under 7 mb pressure conditions by up to 180 times due to the formation of pore-obstructing salt plugs.

5.5.1 Diminishing Efficacy at Low Pressure

As pressure decreases, the proportionate difference between the mass loss rate from the tube bundles and the mass loss rate from free water decreases. At 1000 mb the greatest difference was between the bundle of 22 75 mm capillary tubes and the free water. The mass loss rate from the tube bundle was a factor of 48 lower than from the free water. At 10mb this reduced to a factor of 3. A similar, though less pronounced effect was observed for the 20 mm tube bundle. A possible explanation for this is that at lower pressures it is easier for the evaporated water molecules to diffuse out of the porous media, resulting in less humidity build-up within the porespace compared to at higher pressures where there are more air molecules within the pores, reducing the mean-free-path of the escaping water vapour molecules and consequently causing them to take longer to exit the

porous medium. However, this was not the case for the porous rock cube. The proportionate difference between the mass loss rate from the rock cube and the free water was 1.1 and 2.9 at 1000 mb and 10 mb respectively. At 10 mb the mean mass loss rate from the rock was comparable to the 75 mm capillary tube bundle. At 1000 mb the mean mass loss rate from the rock was comparable to the free water.

5.5.2 Water Position Within Porous Media and and Mass Loss Rate Evolution

The mass loss rate from the 75 mm tube bundle and rock cube was often greatest for a period at the start of each experiment. This is consistent with previous literature that suggests that humidity buildup in pore spaces caused by evaporating water within the pores can slow down further evaporation by increasing the local concentration of water vapour [264]. This effect, combined with capillary forces, leads to a three-stage drying process where each stage is controlled by distinct physical processes [247, 249]. First, rapid mass loss occurs from the water close to the surface and flow of water from porespaces well connected to the rock surfaces, particularly to the lower face of the rock cube under gravity. Previous work studying the drying rate of stone suggests that this stage - the constant-rate stage - is controlled by external conditions and the supply of water flow to the rock surface. At this stage the mass loss is approximately linear [249]. The mass loss rate then rapidly decreases (falling-rate stage), followed by a long period of almost constant, low mass loss rate. This final stage is controlled by diffusion of the water through the porous medium as the water remaining in the rock is in poorly connected pores or is bound in the pores as capillary water (water retained in the rock pores against the force of gravity) [247]. This has interesting ramifications for the type of rock which may be most effective at retaining water. Rocks that hold a high proportion of water as capillary water may be more effective at extending the life of liquid water within the rock. It would be interesting to repeat the rock cube experiment with various, Mars-relevant rock types to explore this parameter. The stages of drying become increasingly less distinct at lower pressures, with the final stage shortening. A possible explanation for this is that at lower pressures, the density of air molecules decreases. This will increase the mean free path of evaporated water molecules, allowing them to diffuse more rapidly out of the porous medium.

This would result in a lower relative humidity inside the tubes compared to at higher pressures, allowing capillary water to evaporate more rapidly.

The bundle of 22 75 mm capillary tubes with 10 μL of water at each tube's opening had a higher evaporation rate than those with the same mass of water in the middle of the tubes. The water in the centre of the tubes has to diffuse its way out of the tube, building up humidity within the tube as it does so and consequently decreasing the evaporation rate of the remaining water. This demonstrates that liquid deep within porous media has a lower evaporation rate than liquid close to the media boundary, implying that larger rocks could retain liquid water in their interiors for longer than smaller ones. This is further corroborated by mass loss rate from the saturated tubes and rock cube decreasing with time, as the evaporation front moves inwards into the porespace. This is supported by previous work that found the time taken for samples of rock to dry is proportional to the square of their thickness [263].

These results suggest that the lifetime of water could be extended much further when contained in larger rocks. However, at low pressure the final stage of drying is shortened, so this ability of larger rocks to extend the lifetime of liquid water may be significantly limited under low pressure conditions. Future work could explore this factor using larger samples of rock.

5.5.3 Comparing Capillary Tube Lengths

At 1000 mb and 100 mb, the mass flux from the 20 mm tubes is greater than from the 75 mm tubes, suggesting there is some evaporation inhibiting factor causing a lower mass flux from the longer tubes. This may be due to vapour from the evaporation front not immediately exiting the tube as it takes time to diffuse out. This would result in a build-up of water vapour within the tube, increasing the local humidity and inhibiting evaporation from the liquid-gas interface. This effect would be greater in longer tubes due to the longer time taken for water vapour to diffuse out of the tube. This is an important result as it suggests that, when surface area is accounted for, there is a relationship between the length of the porous media and the time taken for the same volume of water to evaporate fully. Although in this study, for experimental purposes, small volumes of water were evaporated from small samples of porous media, the results can be extrapolated to larger porous environments like large rocks or boulders.

However, at 10 mb, the mass flux from the 20 mm tube bundle is less than from the 75 mm tube bundle. A possible explanation for this is the formation of gas bubbles due to low pressure outgassing (an effect that occurs at low pressures but not at 100 mb and 1000 mb). Although the water was degassed before the experiment, some gas may have re-dissolved into the water during the tube filling process. When a gas bubble forms within a capillary tube, it can force water to be expelled through one of the tube openings. More water is held in each 75 mm tube than in each 20 mm tube and there is therefore a higher likelihood of a bubble forming within a single 75 mm tube than a single 20 mm tube. A bubble forming within a 75 mm tube could therefore have a greater effect on the mass flux than one in a 20 mm tube as a single bubble has the potential to expel a larger volume of water. Once the water is ejected from the tubes it would evaporate very rapidly under 10 mb conditions. This contribution of bubbles causing expulsion of water may be sufficient to account for the higher mass flux from the 75 mm tubes at 10 mb. This may also explain why generally the mass flux from the porous media is greater than from free-water. If bubbles form in the free water scenario, they exit the water surface without causing expulsion of water from the dish. To more accurately determine the effect of pore length on liquid water lifetime at Mars-relevant pressures, this experiment could be repeated with a more rigorous water degassing process, eliminating the formation of gas bubbles during the experiment.

5.5.4 Mass Loss Rate From the Rock Cube

At pressures of 10 mb, 100 mb and 1000 mb, the reduction in mass loss rate experienced by liquid water in both the 20 mm and 75 mm tube bundles is consistent with the reduction in flux surface area through which mass loss can occur. The mass loss rate from the rock cube was higher than predicted given its estimated porous surface area. A possible explanation for this is that the estimation of the porous surface area was not sufficiently accurate. However, if this were the case, the data would likely show a consistent deviation from the line fit across the four pressures under which the experiments were performed, which is not the case. Another possible explanation is that, due to the irregular shape of the pores within the rock, the evaporative surface area of the water may be significantly increased and water may be pumped to the pore openings. This effect has been observed in rectangular capillary tubes. The adhesion of the water to the corners of the tubes results in a large meniscus surface area. This adhesion

also pumps the water towards the pore opening where evaporation takes place more readily [264]. Additionally, the rock cube has pores on all 6 faces, meaning that some water may have migrated through the porespaces under the influence of gravity, bringing liquid water to the lower surface where it can evaporate readily. These factors combined could explain the higher than expected mass loss rate of water from the rock cube given its porous surface area, particularly as these factors would not affect the capillary tube bundles or the free water scenario.

5.5.5 Prevention of Freezing in 75 mm Tubes at 7 mb

At 7 mb, water is at it's triple point and is unstable as a liquid. At this pressure, the water in the dish froze after a short initial period of evaporation and the mass loss rate reduced. This resulted in a lower free water mass loss rate at 7 mb than at 10 mb. Similarly, the mass loss rate from the rock cube was smaller at 7 mb than 10 mb. This is likely also due to the water within the rock freezing, however, the water within the rock was not observable so this could not be confirmed. In contrast, the mass loss rate from the bundle of 75 mm tubes increased from 10 mb to 7 mb, suggesting that the water did not freeze. Visual observation of the tubes throughout the experiment also indicated the water remained in liquid form. This could be caused by the low evaporative surface area within each tube preventing sufficient evaporative cooling to occur to allow freezing to take place. This result suggests that the introduction of porous media not only increases water lifetime, but can also prevent the freezing of water under Mars surface pressure conditions.

5.5.6 Salt Crusts in Porous Media

The mass loss rate of water from porous media was minimised most effectively by the introduction of dissolved salts. Crystallisation occurring at the evaporation front, causing pore openings to become clogged, significantly impeded evaporation. In three out of four preliminary rock experiments there was liquid solution present within the rock after 4 days at 7 mb pressure. Additionally, of the 22 capillary tubes containing $MgSO_4$ solution, a mean of 12 contained liquid $MgSO_4$ within them after 4 days at 7 mb pressure. Compared to the same mass of free water and water in a bundle of 22 75 mm tubes, which would sublimate/evaporate away in 95.5 minutes and 140 minutes respectively, this is a very significant increase in liquid water lifetime. When considering the

growth time of microorganisms, an increase of liquid water lifetime could allow a significant population to proliferate. The maximum projected lifetime of liquid water contained in $MgSO_4$ brine within the bundle of 22 75 mm capillary tubes under present-day Martian pressure conditions ($\sim$7 mb) was 12.5 days. The doubling time of organisms growing in saturated $MgSO_4$ at 25°C has been shown to be as low as 9.6 hours [265]. The presence of liquid water over a period of $\sim$12.5 days could therefore allow for the proliferation of a significant population of microorganisms.

A Potential Transient Liquid Water Environment

The results presented here could have implications for the production of transient habitable environments on the Martian surface in the present day. Evidence points to the presence of large volumes of water sequestered in minerals within rocks in the top 10 km of the Martian subsurface [36, 37]. The subsurface has been proposed as a potential habitat for putative Martian life in the present day with environments potentially hospitable to microbial life at depths as shallow as a few kilometres [266]. The relative inaccessibility of the deep subsurface means it can usually only be explored with remote sensing techniques. Impact events represent a mechanism for bringing subsurface material from as deep as 6 km to the surface where it can be accessed for analysis [267]. Though impacts are destructive, high energy events, studies have shown that biosignatures, fossils and microorganisms can withstand the induced temperatures and pressure conditions [268–272] and some material is left relatively intact [266, 267]. Impact events have also been suggested as possible mechanisms for the liberation of water sequestered by minerals in the crust [36, 37, 273]. An impact event that excavated some of these mineral bearing rocks could cause the formation of a transient liquid water environment by the liberation of water from the minerals. Under Mars surface pressure conditions, the water would typically freeze or evaporate rapidly. This work has shown that the presence of $MgSO_4$ in water in porous media can extend its lifetime by up to 180 times compared to pure free water under Martian surface pressure conditions. If an impact event occurred that ejected some of these mineral-bearing rocks onto the surface, the heating caused by the impact could release the mineral-bound water within the rock which may not immediately evaporate away if the pores were to become clogged by precipitating salts. This could make rocks containing precipitated salts, ejected due to impact events areas of potential interest with respect to the search for habitats and biosignatures.

In this scenario, low temperature conditions would also be a factor limiting the lifetime of liquid water. Salts dissolved in water can suppress the freezing point to temperatures as low as ∼-75°C [29]. $MgSO_4$ can only suppress the freezing point of water to as low as -3.6°C [274] but in combination with other ions may be able to precipitate pore-obstructing crystals while remaining liquid under simultaneous low pressure and low temperature conditions. Further work using mixed brines under low temperature and pressure conditions would need to be performed to determine this.

5.5.7 Implications For Habitability

The reduction in mass loss rate from the liquid brine contained within porous media was caused by salts crystallising within the pores. Salt crystals were also present within the rock interiors at the end of the experiment. Biosignatures and reportedly viable microorganisms have been extracted from fluid inclusions in ancient terrestrial salt deposits as old as 250 million years [58, 81, 122–126]. These deposits are typically halite (NaCl) but it is also possible to extract biosignatures from intracrystalline inclusions in $MgSO_4$ [127]. The precipitation of $MgSO_4$ crystals within rock pores could provide another layer of protection from the biosignature degrading, ionising conditions of the Martian surface.

Rocks at several locations on the surface of Mars exhibit signs of aqueous alteration [38–40, 158, 189]. Some of these interactions may have occurred repeatedly and relatively recently [38]. Salt-crusted rocks have been observed and rocks with salts deposited in their interiors have been sampled [38–40, 189]. The results of this chapter show that salt crusts can significantly inhibit the mass loss of water from porous media under present day Martian pressure conditions. Porous rocks on the Martian surface exhibiting signs of aqueous alteration and containing precipitated salts with a propensity for clogging pores could therefore be promising sites to search for biosignatures.

5.5.8 Limitations and Future Work

Presence of Dissolved Gas in Solution

Some of the mass loss rate results presented in this chapter are likely to have been affected by expulsion of water from the porous media due to low pressure outgassing. Attempts were made to mitigate this by degassing the water during preparation, but observations suggest that this was not completely effective. A more rigorous outgassing procedure and protocol for saturating the porous media without reintroducing dissolved gas would allow for the more accurate determination of mass loss rates.

The porous media in the brine experiments had to be dried for three days after saturation to allow salt crusts to form in the pore openings such that the mass loss rate from salt-crusted porous media could be measured. In future this protocol should be built upon such that the experiment can be performed directly after saturating the porous media. This would require the brine to be degassed so that violent outgassing does not cause the rapid expulsion of brine from the porous media. The data presented here is still useful as it demonstrates the ability of brines that have formed pore-obstructing salt crusts to impede evaporation from porous media at low pressure. Work presented in Chapter 4 shows that $MgSO_4$ brine does form evaporation impeding salt crusts under low pressure (50 mb). This process may also occur in porous media, if explosive outgassing can be prevented.

Exploring Pore Size

These results highlight the dependency of mass loss rate on pore parameters and environmental conditions. For example, the bundle of 75 mm tubes reduced the mass loss rate of liquid water significantly at 1000 mb while the mass loss rate from the rock cube was comparable to that of the free water. At 10 mb pressure, the 75 mm tube bundle and the rock cube had comparable mass loss rates, a factor of $\sim$3 less than the mass loss rate from the free water. This work focused on porous media in the form of capillary tubes of a single radius and generic vesicular basalt of undetermined average pore radius. The work would benefit from being repeated using tubes of varying radii and different Mars-relevant rock types to systematically quantify the effect of pore size and distribution on mass

loss rate.

Environmental Conditions

The experiments presented here were performed at room temperature as the PES chamber is not currently capable of refrigeration. It would be highly beneficial to repeat the work involving brines presented here under simultaneous low temperature and low pressure conditions to further constrain the mass loss rate of brines from porous media under Martian surface conditions.

Brine in Porous Media

The brine in rock experiments were preliminary and ideally would be performed in rocks of known porosity and estimatable surface area. This could be achieved, as in the preceding experiments, by cutting the rocks to a set size, measuring the porosity and estimating the porous surface area. Before saturating the rock with brine the experiment should first be performed with water, using the same rock, to serve as a comparison rate for the brine mass loss rate.

5.6 Conclusions

The work presented in this chapter shows that the reduction in evaporative surface area by the introduction of porous media leads to a reduction in the mass loss rate of a test volume of water compared to the same volume of free water. This effect becomes less pronounced as pressure decreases, likely due to a combination of factors including increased water vapour diffusion and low pressure outgassing.

The most significant reduction in mass loss rate of water was via the introduction of dissolved $MgSO_4$ salt causing salt plugs to form at the pore openings, effectively inhibiting evaporation. After 4 days at 7 mb, a mean of 12 capillary tubes out of 22 still contained liquid brine.

These results contribute to our understanding of the habitability of porous rock environments on the Martian surface by establishing the stability and lifetime of liquid water in porous media under low pressure conditions applicable to the surface of Mars.

These results suggest that porous rocks that have interacted with crust-forming brines could be promising locations for habitat and biosignature-seeking missions on the surface of Mars.

Chapter 6

A Potential Aqueous Environment on the Martian North Polar Residual Cap

6.1 Introduction

To date, the Phoenix lander is the only probe to successfully complete a mission in the Martian north polar region. One of its mission objectives was to investigate the habitability of the region, which was an area of interest due to Mars Odyssey observations indicating the presence of water ice close to the surface [275]. Sending a lander to Martian polar regions and ice caps poses immense challenges from a design, planetary protection, and mission longevity perspective [276]. This was highlighted by the Phoenix lander, which operated for 5 months before losing power due to lack of sunlight caused by dust storms and winter setting in. It is therefore imperative to thoroughly interrogate the habitability potential of the Martian north pole via the available avenues on Earth - one of which is analogue environment simulations.

With typical peak summer surface temperatures of ∼200 K [277–280], the frigid Martian north polar ice cap seems an unlikely place to find evidence of life. However, it harbours an essential component for life that much of the Martian surface lacks: an abundance of water [281, 282]. At present Martian temperatures, the water is permanently frozen. However, there is some evidence that liquid

water formed on the Martian north polar ice cap in the relatively recent past as a result of the solar-heating of low-albedo material [44].

Aqueous habitats on Mars' ice covered regions are of interest as on Earth there are many examples of complex communities of microorganisms establishing and proliferating in ice environments with ephemeral melt-water formed by the solar-heating of low-albedo material [51, 283–287].

This presents an interesting question that has not yet been thoroughly addressed or tested experimentally: could liquid water habitats form or have previously formed on the Martian north polar residual cap and, if so, under what environmental conditions?

This chapter will explore the potential for liquid water habitats to form under extreme Martian polar temperature conditions using physical simulations of irradiated ice environments. In particular the following questions are addressed:

- Can bulk melt occur via solar-heating of low albedo material superjacent to ice at Mars polar temperatures?
- Can bulk melt occur via solar-heating of low albedo material embedded within ice at Mars polar temperatures?
- Does the presence of $Mg(ClO_4)_2$ salt in analogue regolith material facilitate melt at Mars polar temperatures?

6.2 Background

6.2.1 Terrestrial Ice Habitats

There are several examples from the terrestrial cryosphere of dark material contributing to ice-melt, ranging from small fluid inclusions in lake ice to the potentially global environmental effects of increased glacial melt-water runoff. These materials can be abiotic, biotic, or some combination of both. The low albedo of the material causes it to absorb sufficient solar radiation to melt subjacent or surrounding ice, producing aqueous habitats in extreme environments.

Fluid Inclusions in Perennial Ice

The McMurdo Dry Valleys (MDV) of Antarctica are among the driest and coldest places on planet Earth [288–290] and have long been considered one of the closest terrestrial analogues to Mars [187, 195, 290, 291]. Life is scarce under these polyextreme conditions and the landscape initially appears completely barren. However, in this polar desert there are microenvironments which allow complex communities of microorganisms to establish and proliferate [51, 292, 293]. Within the 3-6 m thick perennial ice covering [294] of the lakes in the MDV, liquid water inclusions provide the elevated temperatures and available aqueous water necessary to support such communities [51, 295]. These environments form when material of aeolian origin is deposited on the surface of lake ice [296]. During the summer, when the sun shines for months at a time, the relatively low-albedo sediment is heated by solar radiation, subsequently melting subjacent ice causing downward migration of the sediment. When winter comes and the sun does not breach the horizon for months the melt-water freezes, incorporating the material into the ice matrix [297] (Figure 6.1). During the successive austral summers, solar-heated sediment within the ice matrix melts surrounding ice causing further downward migration and the formation of liquid water pockets that persist for around 150 days [298]. During this time, the elevated temperature and presence of liquid water allow microorganisms associated with the sediment, which itself acts as a nutrient source, to multiply and produce a cooperative consortium [51, 297, 299]. This process repeats until a dynamic equilibrium depth of $\sim$2 m is reached [51, 298]. The sediment and associated microbial communities can persist

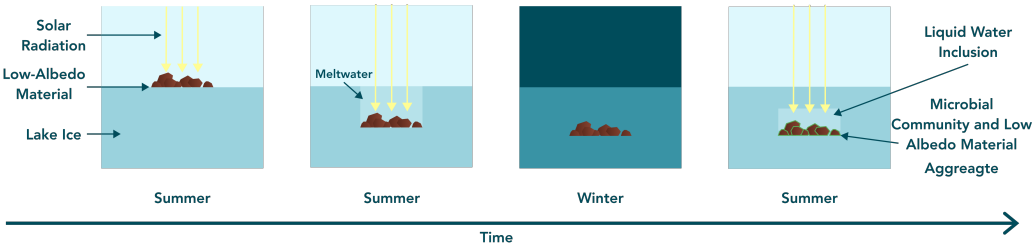

Figure 6.1: Formation of Inhabited Fluid Inclusion Environments in Antarctic Lake Ice. Solar radiation heats the low-albedo material, melting the subjacent ice and forming a habitat in which microorganisms can proliferate. The cycle repeats annually, forming fluid inclusions within the ice cover and causing the sediment and associated microbial community to migrate down through the ice until an equilibrium depth is reached. Aggregates can be up to multi-cm in size. Diagram is not to scale.

in this state for years [300]. These lake-ice environments have been identified as potential analogues for extraterrestrial ice environments such as the Martian polar ice caps [51, 292] but there have not been any physical experiments exploring the formation and persistence of such environments under Martian polar conditions.

Cryoconite Holes

On the ablation zone of glaciers in many locations about the terrestrial cryosphere, a spectacular landscape of countless water-filled holes can be observed [301–304]. In the base of these holes is a layer of sediment known as cryoconite (meaning 'cold rock dust'), a dark material of mineral and biological composition. It is via the solar-heating of this material and consequential melting of glacial ice that these 'cryoconite holes' form [305]. They are typically cylindrical and range in size from cm-scale to over a meter in diameter. Similar to the Antarctic lake ice environments, cryoconite holes reach a dynamic equilibrium depth, where the melt rate of the cryoconite hole is in equilibrium with the ablation rate of the glacier surface [306, 307]. These depths are typically tens of centimetres but depths of several meters have been observed [308]. The holes can form protective ice lids in the winter as shown in Figure 6.2. Some ice-lidded cryoconite holes are thought to persist for years or even decades [308, 309]. These holes are home to many diverse organisms including some invertebrates [284, 310, 311]. The relative warmth of the water that accumulates inside the holes allows microbes associated with the cryoconite to proliferate and develop co-operative relationships [285,

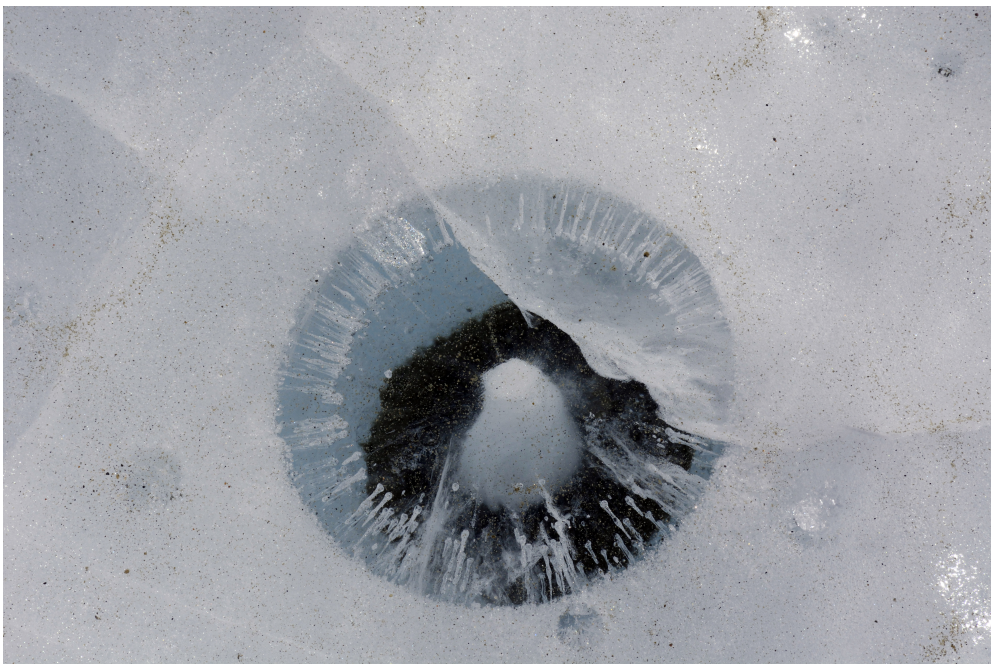

Figure 6.2: An Ice-Lidded Cryoconite Hole on Taylor Glacier, Antarctica. (Peter Rejcek, Public domain).

287, 312–314]. The communities inhabiting these microenvironments have been observed and studied on alpine [283, 315], Antarctic [284, 303, 310, 316], Arctic [284, 316, 317] and, Himalayan [285] glaciers. The melt caused by cryoconite has been estimated to significantly contribute to glacier melt-water runoff in Antarctica [308]. Though these environments have been studied in many locations on Earth, and suggested as potential analogues to Martian polar habitats [318, 319], no physical simulations have been performed to determine whether they may be able to form under Martian polar conditions.

Algae on Ice Sheets

Microorganisms themselves can also have a significant effect on the albedo of ice environments. Algae and other microorganisms grow directly on the surface of the Greenland ice sheet [320] causing darkening as shown in Figure 6.3. The algal blooms responsible for this albedo increase [321–324] absorb solar radiation, causing melt so significant that it may have implications for global sea level rise [325–327].

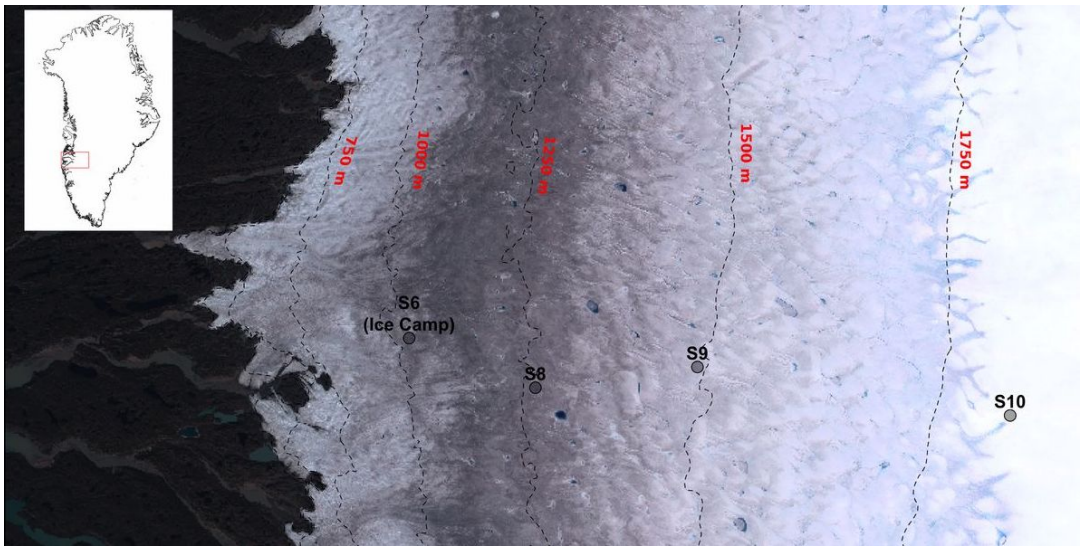

(a)

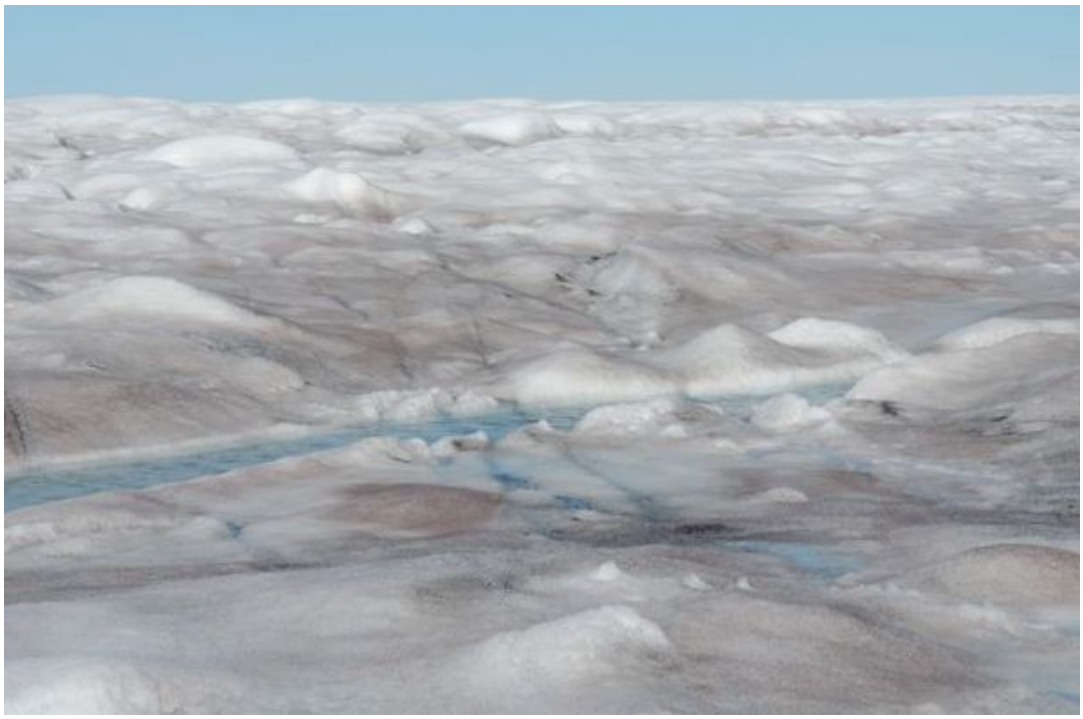

(b)

Figure 6.3: Algal Bloom on the Greenland Ice Sheet. (a) Satellite image of the southwestern Greenland ice sheet margin. The dark zone at the 1250 m marker is thought to be caused by algal blooms. (b) The surface of the Greenland ice sheet covered in dark algae (From Williamson et al. 2020 [326]).

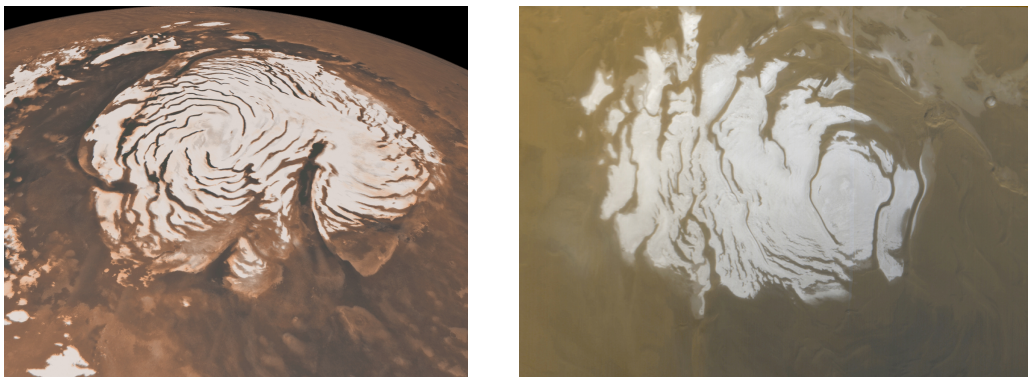

(a) (b)

Figure 6.4: Mars Global Surveyor Images of the Martian Poles. (a) North polar region and (b) south polar region (Credit: NASA/JPL-Caltech/MSSS)

6.2.2 The Martian Cryosphere

First observed in the 17th century by Huygens and Cassini, the polar caps of Mars are fascinating and beautiful landscapes (Figure 6.4). Both regions have a wealth of potential regarding the climatological history of the planet stored in the layered deposits beneath the caps. There is evidence at both poles that phenomena related to the solar-heating of low-albedo material occurs.

The North Pole

The north polar region of Mars has a striking landscape of chasms, scarps and spiralling troughs (Figure 6.4a) with depths up to 2 km exposing sections of the north polar layered deposits (NPLD) which lie beneath a bright, pure-water ice cap known as the north polar residual cap (NPRC). The region has an approximate diameter of ∼1000 km with its outer edges beginning around 80°N [282]. During the winter months, frigid temperatures cause CO_2 from the atmosphere to condense onto the NPRC, covering it in a layer of dry ice. The temperatures in the summer rise enough that the CO_2 layer sublimates away, revealing the water ice cap beneath [277, 328–330]. The exposed layer is ∼1 m thick [276], is composed of pure, large-grained water ice [281, 331], and has a pitted texture [282, 332]. This texture could allow for the accumulation of material deposited by wind as is the case with the initiation of cryoconite holes and lake ice fluid inclusions on Earth [297, 305]. The layered deposits beneath are also composed primarily of water ice [333] and have a cumulative depth of ∼2

km [281] from the surface to the basal unit (Figure 6.5)[282, 334]. The resolvable individual layers range in thickness from ∼10 cm [335] to a few meters [336] and vary in albedo, potentially containing up to ∼50% dust [337]. Dust storms are a well documented phenomenon on Mars with some encircling the entire planet [338–341]. These storms represent a mechanism for the global redistribution of material [342, 343]. The differences in albedo and thickness of the layers are thought to be caused by climatic variations causing different amounts of dust to be incorporated into each layer [344]. During periods of high obliquity, dust storms may be more common and consequently more dust could be deposited at the polar region compared to periods of low obliquity where lower temperatures would make ice deposition more prevalent [345]. Variations in obliquity and Mars' orbital parameters over periodic cycles drive changes in the Martian climate which may be recorded in these layers [346, 347]. These layers could therefore contain an archive of the atmospheric and climatological conditions during Mars' recent history. The upper ∼100 m of the NPLD have been estimated to have accumulated over the past 400,000 years [348, 349]. The troughs in the NPLD interior expose these upper layers [282, 350, 351]. On Earth, biosignatures and reportedly viable microorganisms have been extracted from ancient terrestrial ice environments [61, 352–356], some of which are older than the exposed upper layers of the NPLD [59, 357–363].

Perchlorate Salts In the North Polar Region Martian soil at the Phoenix lander site has been measured to have up to 0.6% wt perchlorate salts present [75]. Hydrated mineral deposits with spectral signatures consistent with perchlorate have also been observed on the north polar cap [364]. Perchlorate salts are highly soluble deliquescent salts which can significantly depress the freezing point of water to as low as -74°C when in solution [274]. Their highly hygroscopic nature allows them to absorb moisture from the atmosphere [365]. If the deliquescent relative humidity of the perchlorate salt is reached, it can absorb sufficient water to re-dissolve itself into solution [27, 366, 367]. Fischer et al (2014) found that perchlorate in direct contact with ice deliquesced rapidly under -50°C temperature conditions. Therefore perchlorate in direct contact with ice could contribute to the melt-migration of low albedo material through ice under Mars surface conditions.

Significant work has been done on characterising the composition, formation mechanisms and age of the north polar cap and deposits. Such research has

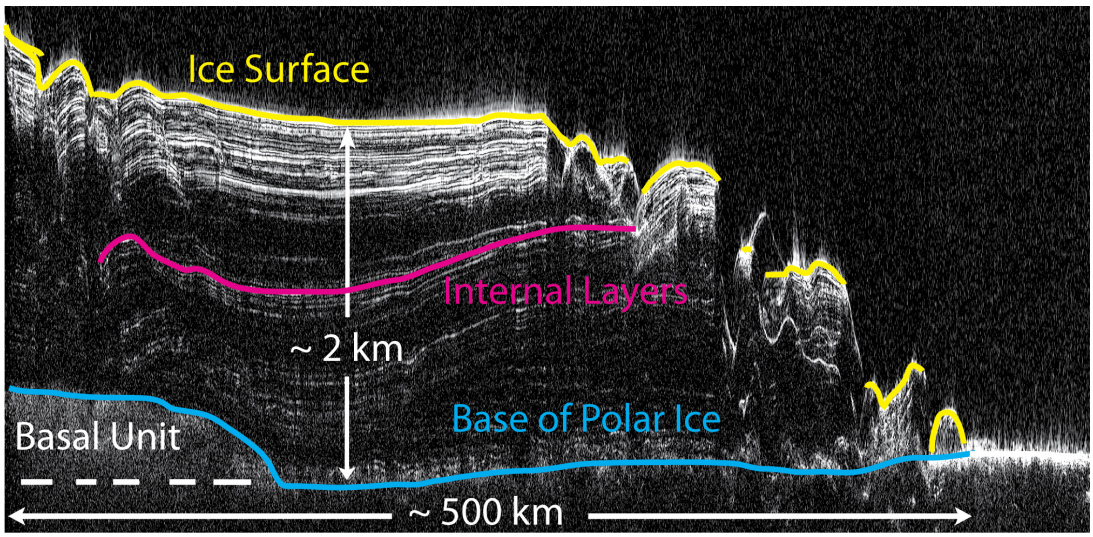

Figure 6.5: Radargram Showing North Polar Layered Deposits. Shallow radar (SHARAD) radargram showing the NPLD and basal unit (BU) of Planum Boreum. (NASA/JPL-Caltech/ASI/UT)

looked at determining how inferences on past climatological conditions can be made from the layers [276, 368, 369]. By understanding if the north polar cap could have formed habitats and constraining the conditions under which putative habitats could form - combined with the ongoing work on unlocking the climate record stored in the NPLD - particular layers could be targeted for sampling in future missions focused on the search for habitats and biosignatures on Mars.

The South Pole

There is also evidence of phenomena related to the solar-heating of low-albedo material at the Martian south pole. The south polar layered deposits (SPLD) are also composed predominately of water [370, 371] but, due to low average summer temperatures is topped with a perennial, several-meter-thick CO_2 cap [372–375]. Spectacular patterns of dark material have been observed on the CO_2 cap surface like in Figure 6.6. It has been proposed that these fans of dark material are expelled from the cap in a geyser-like eruption caused by the solar-heating of dust beneath the CO_2 cap which then sublimates the superjacent CO_2, increasing pressure, and eventually erupting [376, 377]. Additionally, fracturing of the SPRC surface may be driven by CO_2 sublimation induced by solar-heated dust beneath the CO_2 ice layer [378].

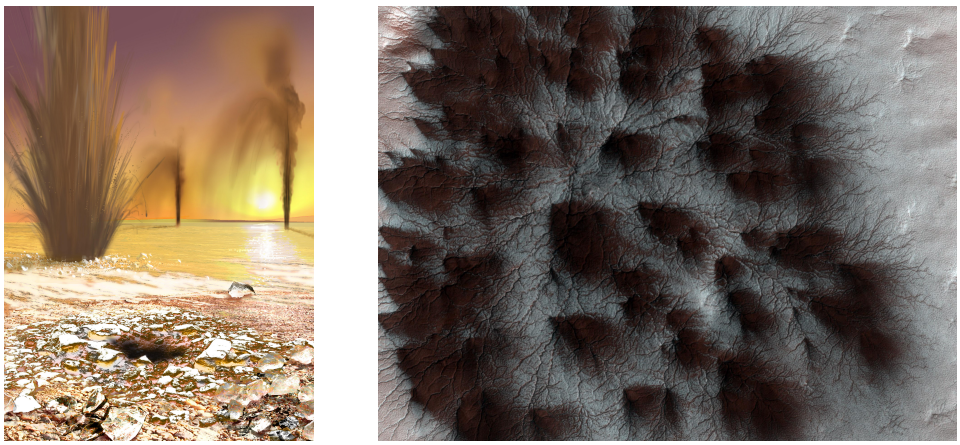

(a) (b)

Figure 6.6: South Polar Eruptions. (a) Artists impression of a potential Martian south-polar geyser as a mechanism for the deposition of observed dark material fans (Source:Arizona State University/Ron Miller). (b) Approximately 1 km across HiRISE image of fan deposits of dark material, potentially deposited by geysers like those imagined in (a). (Source: NASA/JPL-Caltech/University of Arizona).

6.2.3 Liquid Water on the NPRC

Despite the freezing conditions experienced in the north polar region of Mars, the presence of substantial gypsum deposits that require liquid water to form suggest the presence of liquid water in the relatively recent past [44–46]. A model produced by Losiak et al. (2015) suggests that enough liquid water can be produced on the Martian NPRC to explain the formation of these deposits [44]. The model simulates the irradiation of a monolayer of dust particles of sizes 2-200 μm on south-facing slopes of the NPRC under favourable environmental conditions - a surface temperature of 215 K and solar irradiation of 265-450 Wm^{-2}. They found that dust particles could melt depths of up to $\sim$20 mm into the ice, that melt could take place for up to $\sim$500 minutes, and that bulk water could form by the heating of sediment (Figure 6.7). However, this has not been experimentally verified. The work presented in this chapter seeks to address this.

We aimed to explore whether aqueous environments could have formed and in principle provided a habitable space on the Martian north polar ice cap under extremely harsh recent Martian surface conditions and during periods of elevated solar flux caused by Mars' changing orbital parameters. The experiments presented here further our understanding of the conditions under which aqueous

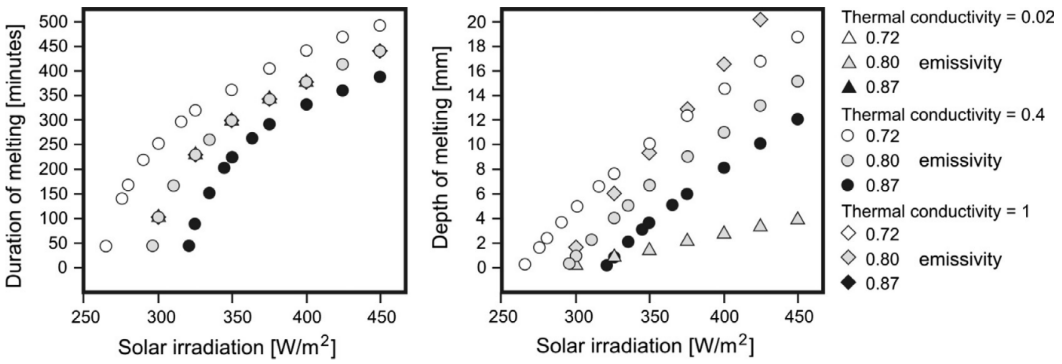

Figure 6.7: Duration and Depth of Melt From Losiak Model. Model results for the duration and depth of melting for a monolayer of Mars dust on the NPRC for various solar irradiation levels, ice thermal conductivities [$\mathrm{Wm^{-1}K^{-1}}$] and, dust emissivities. The left figure is a plot of melt duration vs received solar irradiation. The right figure is a plot of melt depth of grains into the ice surface vs received solar irradiation (from Losiak et al. (2015) [44]).

environments may form and hence the habitability of Martian ice environments. These findings may be used to contribute to the process of identifying sites on Mars that are of interest to biosignature seeking missions.

Table 6.1: Parameters and Nomenclature

Parameter	Symbol	Units
Diameter	$\varnothing$	mm
Albedo	α	-
Thickness	t	mm
Irradiance	S	Wm^{-2}
Temperature	T	°C
Mass	m	g
Density	ρ	g mm^{-3}
Volume	V	mm^3
Total Volume of Ice Melted by Analogue Material	V_{tot}	mm^3
Mean Radius of Melt Hole	r	mm
Mean Depth of Melt Hole	d	mm
Melt Rate	v	mm $hour^{-1}$

6.3 Materials and Methods

6.3.1 Materials and Experimental Parameters

Low-Albedo Material

Sand nearby perennially ice-covered lakes harbouring fluid inclusion environments in the MDV of Antarctica has been found to have an albedo of 0.14 [379]. The albedo of Martian dune material near to the NPRC has been found to be ∼0.13, but can be as low as 0.05 [44, 277, 380].

Discs of diameter 22 mm were cut from sheet aluminium, chosen due to its high thermal conductivity. The discs were primed by lightly filing the surface then painted matte black using acrylic spray paint (RS PRO) to reduce their albedo (aluminium coated with black acrylic paint has an albedo of ∼0.04 [381]). The result was black discs of thickness 1 mm that were used to simulate low-albedo material in ice environments.

JSC Mars-1 regolith, a Martian analogue regolith was also used [382, 383]. The albedo of the 25-63 μm grain size fraction of JSC Mars-1 has been measured to be ∼0.13, decreasing to ∼0.05 when moistened to 40% wt water [384]. In the preliminary experiments, the grain sizes were <500 μm. In the Mars ice experiments, the regolith was sieved such that the <63 μm grain fraction was used. The regolith was also mixed with $Mg(ClO_4)_2$ salt for the ideal Martian temperature experiments. Perchlorate ions in association with Mg^{2+} ions have

been detected in the Martian north polar region [75] and perchlorate signatures have been detected on the NPRC [364]. These highly deliquescent salts may contribute to ice melting [385].

Water Ice

The NPRC is composed of water ice, topped with CO_2 ice in the winter which sublimates in warmer months leaving the water ice cap exposed [328, 329]. The uppermost layer of the NPRC is almost pure water ice, beneath which are layered deposits of dusty ice and relatively pure water ice [281, 333, 337]. Lakes in the dry valleys are topped with perennial water ice up to 6 m thick [294]. The ice blocks produced for this work were composed of pure, deionised (DI) and degassed water. The ice was produced to be as bubble and impurity free as possible in order to maximise the transmission of light through the ice in the case of embedded material and for ease of melt depth measurement and consistency between experiments.

Simulated Solar Irradiation

For preliminary experiments, the received flux was $\sim$100 Wm^{-2} as this was the maximum output achieved by the lamp until a new bulb was procured.

Antarctic Irradiation During the time period that the fluid inclusions in the McMurdo dry valleys were studied, climatological data was also taken. The mean annual solar flux in the dry valleys was between 73 Wm^{-2} to 117 Wm^{-2} [288]. Hourly averages in December 1994 were between 100 Wm^{-2} and 600 Wm^{-2} [386]. The fluid inclusion environments reported by Priscu et al. (1998) were sampled from a number of perennially ice-capped lakes, one of which was Lake Bonney [51]. Typical solar irradiance on the ice of Lake Bonney was over 300 Wm^{-2} for around 12 hours a day [386]. To allow for daily variation, cover due to local geographical features and considering the maximum output of the solar simulator lamp used, for the Antarctic analogue experiments 300 Wm^{-2} was chosen.

Mars North Polar Irradiation Typical solar irradiation received by horizontal surfaces at the edge of the Mars NPRC during the summer and in a low-dust atmospheric ranges from 100 to 260 Wm^{-2} [44, 278]. However during periods

of higher obliquity the received flux may have been as high as 400 Wm^{-2} [346]. Additionally, on south-facing inclines at the edge of the NPRC, the received flux could be as high as 460 Wm^{-2} and above 300 Wm^{-2} for more than 6 hours [278]. The solar simulator used in this work had a maximum received flux of approximately 300 Wm^{-2}, so this value was chosen for the Martian environment experiments. The irradiation period for the Martian experiments was 6 hours.

Ice Temperature Conditions

Antarctic Ice During the time period that the fluid inclusions in the dry valleys were studied, the average temperature of the lake ice during the summer months where liquid water existed in the ice was 0°C [298]. For the experiments under Antarctic conditions, the ice was prepared to 0°C and the temperature maintained at ∼0°C using water ice chips.

Martian Ice Typical temperatures on the surface of the NPRC are ∼150 K (-123°C) but models suggest temperatures greater than ∼200 K (-73°C) can be reached during the summer [279]. For low atmospheric dust scenarios, the Mars Climatological Database has modelled surface temperatures on the edge of the NPRC up to 230 K (-43°C) [278]. During periods of high obliquity temperatures may even reach up to 250 K (-23°C) [387]. The Mars NPRC environment experiments were performed at -74°C and -42°C to reflect more typical summer temperatures and ideal summer temperatures respectively.

6.3.2 Protocol Development and Apparatus

Ice Production

The development of ice with minimal presence of impurities and bubbles was important to minimise scattering - ensuring that light could pass through the ice sufficiently to transfer energy to the sample - and maintain consistency between experiments.

A directional freezing method was used. This method is commonly employed by bartenders to produce large blocks of clear ice to be cut down and shaped for beverages. It has also been employed to produce clear blocks of ice for scientific research purposes [388]. Deionised (DI) water was used to minimise the presence of impurities (Nanopure, Thermofisher). An insulated cooler box containing two hollow perspex cylinders (outer diameter $\varnothing$ = 100 mm, inner diameter $\varnothing$ = 90 mm, height h = 300 mm) was filled with DI water. The base and sides of the box were surrounded with insulation board then placed in a -15°C freezer. The insulated walls of the box force the water to freeze from the top downwards, pushing any remaining gas, ions and impurities to the bottom as shown in Figure 6.8.

Initially, the DI water was used directly in the directional-freezing method. However, copious bubble formation occurred as the water froze to the extent which would significantly affect the traversal of light through the ice (Figure 6.9a). The water was henceforth degassed in a vacuum chamber (manufactured in-house [389]) at 10 mb pressure for two hours before freezing, reducing the formation of bubbles (Figure 6.9b). Although fewer bubbles formed, they were still prevalent enough that further reduction was required. The temperature of the freezer was increased to its maximum of -5°C. By increasing the freezer temperature, the duration of the directional freezing method was increased from 3-5 days to 7-10 days. Minimising the freezing rate reduced the number of bubbles becoming trapped in the ice matrix as downward freezing occurs (Figure 6.9c). In most ice blocks it was not possible to completely eliminate bubbles so each block was individually assessed for its experimental suitability. If the central column of ice was relatively bubble-free, it could be used for any of the experiments. More bubbly blocks were suitable for use in experiments where the analogue regolith material was atop the ice, such that the radiative transfer through the ice itself was of lesser importance. The final protocol for producing ice cylinders was as

follows. The ice was prepared by degassing 6 litres of DI water at 10 mb pressure for two hours in a vacuum chamber. The water was carefully poured into two cylindrical cooler boxes, each containing a single hollow perspex cylinder. The base and sides of the cooler were surrounded with insulation board and placed in a -5°C freezer for 7-10 days or until most of the water had frozen (Figure 6.10). The box was removed from the freezer before the freezing process completed. This reduced the risk of fractures and apparatus breakage caused by the water at the bottom freezing, expanding and exerting pressure on the container and the ice above. The ice blocks were removed from the cool box and allowed to warm up enough to slip the ice cylinders out of the perspex moulds. The ice was examined for bubbles and cracks to determine its suitability for experiments. The ice was trimmed using a hack saw, evening the surface and removing any remaining bubbles. The ice surface was polished by abrading on a flat sheet of copper, ensuring a flat and pit-free surface. The ice blocks were stored at -5°C, -15°C or -80°C. Some fractures occurred throughout the ice during cooling to -80°C. To minimise this, the ice was prepared to the highest quality possible, minimising the embedding of any contaminants or particles using the aforementioned directional freezing method. After the ice was produced, it was handled with care to minimise the risk of forming cracks which could be exacerbated during the cooling process. The ice was also cooled gradually from -5°C to -15°C and then to -80°C. Even with these processes in place, significant cracking sometimes occurred. The cracks were assessed visually to determine whether their placement or severity was such that they should be precluded from the experiment (i.e. if a lateral crack formed which would reflect the incident light, the ice was used for the surface irradiation experiments or discarded).

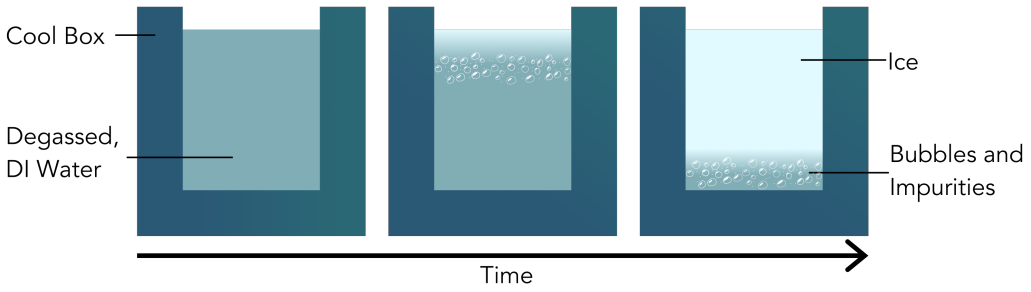

Figure 6.8: Directional Freezing Method. Bubbles and impurities in the water are concentrated downward by the freezing front, resulting in clear ice. This process is carried out in a freezer.



(a) Bubbly ice **(b)** Partially bubbly ice **(c)** Clear ice

Figure 6.9: Bubbly Ice Comparison Photographs. Comparison of the presence of bubbles in ice produced using different preparation methods. Each ice block is approximately 85 mm in diameter. (a) -15°C freezer and no degassing resulting in very bubbly ice. (b) -15°C freezer with degassing resulting in partially bubbly ice. (c) -5°C freezer with degassing resulting in clear ice.

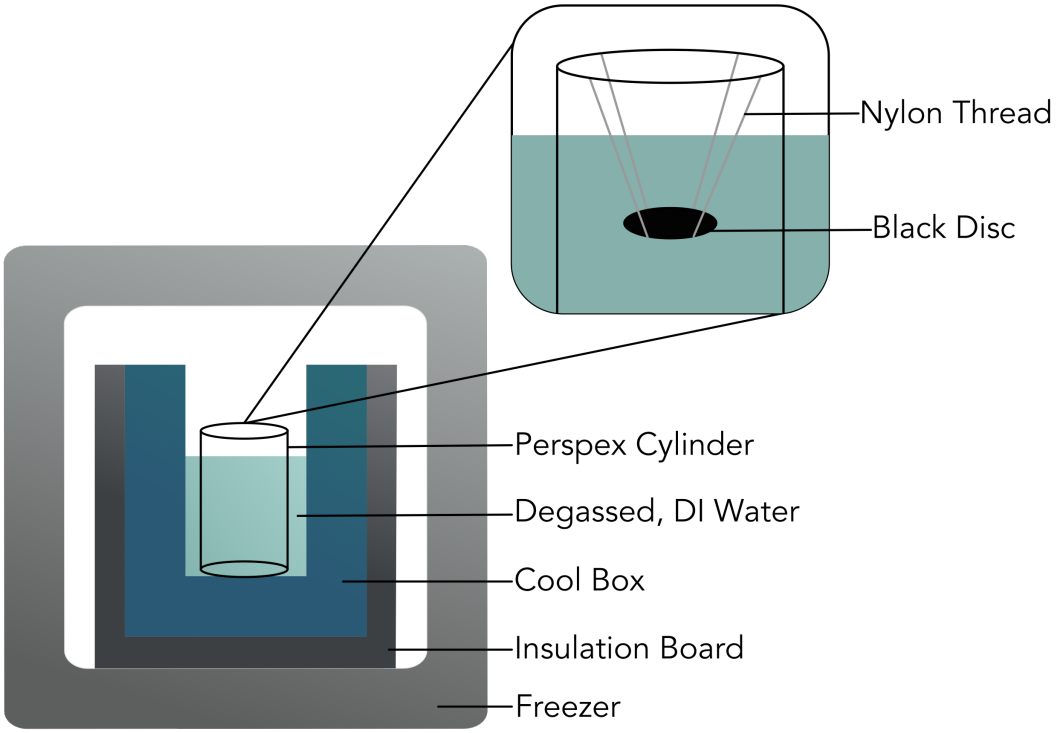

Figure 6.10: Ice Production Apparatus. The apparatus was used to produce bubble-free ice blocks. The insulated box forced the ice to freeze from the top down, forcing bubbles and impurities to the bottom, resulting in clear ice. The inset figure depicts the production of an ice block embedded with a black disc. Diagram is not to scale.

Embedding Material into Ice

Black Discs In the case of the embedded discs, 'invisible' nylon thread (Manufacturer: Hemline) was attached to one side of the disc and the opposite end wrapped around a rod which was then rested upon grooves cut into the top of the perspex tubes, in order to prevent the rod becoming dislodged. The thread suspended the disc into the ice by approximately 25 mm. In later experiments, the thread was tied around the disc and attached to four points on the perspex tubes (Figure 6.10), resulting in a more level and consistent placement of the disc within the ice blocks . This method consistently produced sufficiently bubble-free ice with a disc embedded within it like the example in Figure 6.11.

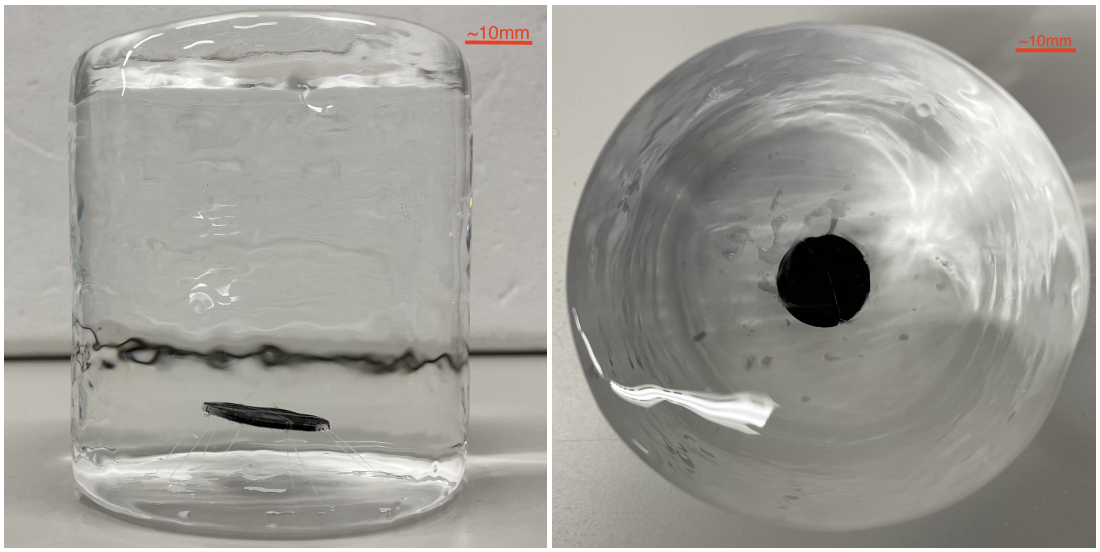

(a) **(b)**

Figure 6.11: Bubble-Free Ice Block Embedded with Black Disc. Perspective from the side (a) and the top (b) of the block. The ice block is approximately 85 mm in diameter.

Regolith Embedded regolith could not be prepared in the process described above due to its granularity. The regolith was prepared by compacting 0.2 g of regolith mixed with 0.2 g DI water into a cylindrical mould with the same diameter as the black disc ($\varnothing = 22$ mm) and freezing. This produced a regolith disc of diameter 22 mm and thickness 1 mm, consistent with the black aluminium disc. A cylindrical depression was melted into the ice using a copper cylinder heated in hot water. To minimise melting outwith the desired area, melt-water was pipetted away as it formed. The frozen disc was then inserting into the cavity in the ice block. One mL of chilled DI water ($\sim$0°C) was added to the cavity and

frozen to secure the regolith disc in place while minimising melting which may disrupt and redistribute the grains. The rest of the cavity was then filled with chilled DI water and frozen. This resulted in a disc of regolith embedded within the ice and clearly visible from the top of the ice (Figure 6.12).

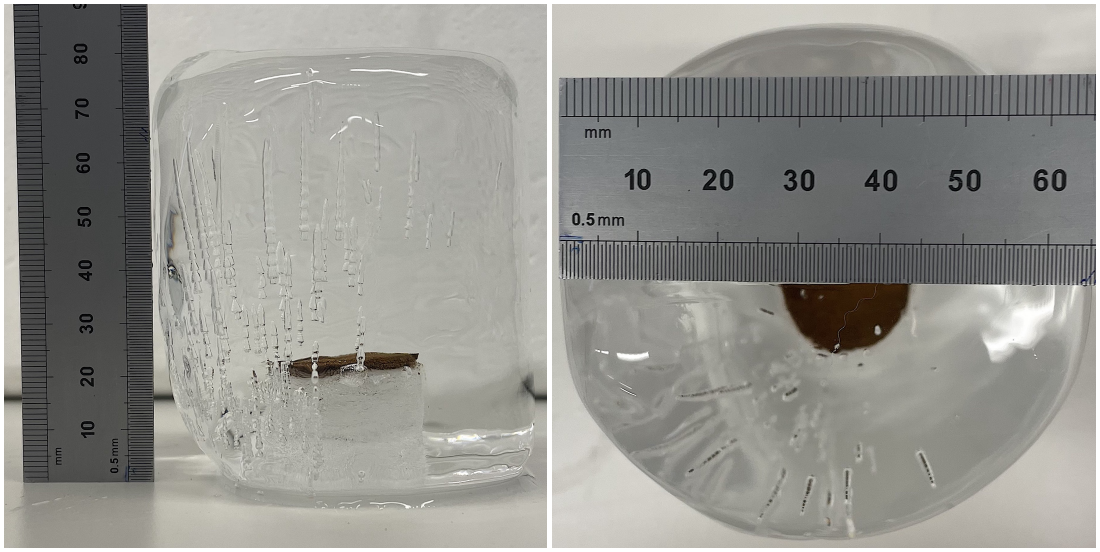

(a) **(b)**

Figure 6.12: Ice Block Embedded with JSC Mars-1 Regolith. Perspective from the side (a) and the top (b) of the block.

Cooling System

The experiments presented here used a cooling system consisting of an insulated polystyrene box filled with dry ice pellets, water ice chips or a combination of both to maintain the necessary environmental temperature conditions. Attempts were made to develop a more versatile and consistent cooling system. A cold plate connected to a liquid recirculating chiller (G50 ThermoFisher) with silicone oil circulator fluid (SIL100, Thermo Fisher) was tested. An insulating polystyrene box surrounded the cold plate. An ice block (-15°C) was placed on the centre of the cold plate and surrounded with (-15°C) ice chips. The circulator was set to (-42°C). After one hour a significant amount of melt from the block had occurred. This was repeated with a coil of copper piping, fed into a insulating polystyrene box. The ice block was slotted into the centre of the coil, such that the copper piping was in contact with the ice. The box could then be filled with ice as usual. This strategy was more effective than the cold plate, however, ongoing issues with the consistency of the circulator temperature and difficulties retrieving the ice sample from the coil meant the most effective cooling system for the purpose of

these experiments was the insulated box filled with dry ice pellets/water ice chips. To monitor the consistency of this cooling system, two holes were drilled 10 mm deep into the ice blocks. One hole 15 mm from the upper surface and one 15 mm from the lower surface. Type-K thermocouples were frozen into the drill-holes. The thermocouples were input into a dual probe digital thermometer (Fluke, 52 II). During irradiation experiments, temperature readings were taken hourly for 4 or 6 hours for the Antarctic and Mars temperature experiments respectively. The mean temperature remained relatively consistent for the duration of the experiments and ice chips or dry ice pellets were added to the system to maintain the temperature when necessary (Figure 6.13).

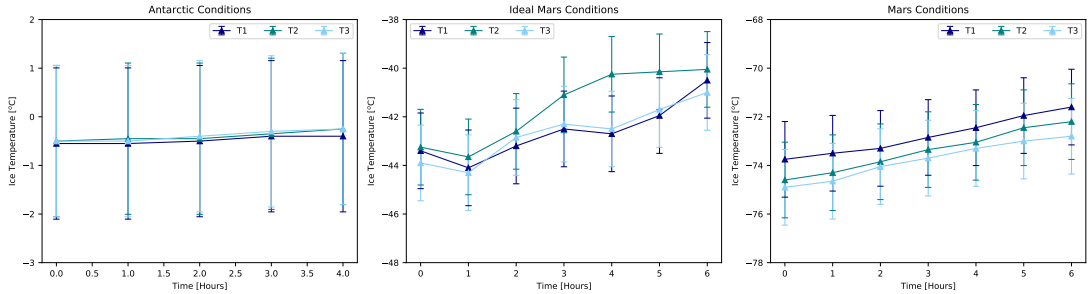

Figure 6.13: Mean Ice Temperature Plots. Mean temperature measurements taken from thermocouples embedded in the ice blocks. Mean temperature was obtained by taking the mean of the upper and lower thermocouple measurements at each time point. T1-T3 label each of the triplicate experiments. (a) Antarctic ice (0°C), (b) ideal Mars ice (-42°C) and (c) typical Mars ice (-74°C).

Ice Irradiation Apparatus

A 150 W Xe arc lamp (λ=200-2500 nm, Quantum Designs) was used to simulate solar irradiation. The ice blocks were put into an insulating polystyrene box filled with crushed water ice, dry ice or a mixture of the two to maintain the ice blocks at ∼0°C, ∼-74°C and ∼-42°C respectively. The polystyrene box was placed within a protective steel chamber. The ice block was centred beneath the collimated beam of the lamp such that the low-albedo material would receive the maximum flux. The experimental apparatus is depicted in Figure 6.14. The maximum flux received by the top of the ice was 300 Wm^{-2}. This flux was suitable for both Antarctic and Mars polar irradiation. Before the procurement of a new solar simulator bulb, the maximum measured irradiation was ∼100 Wm^{-2}.

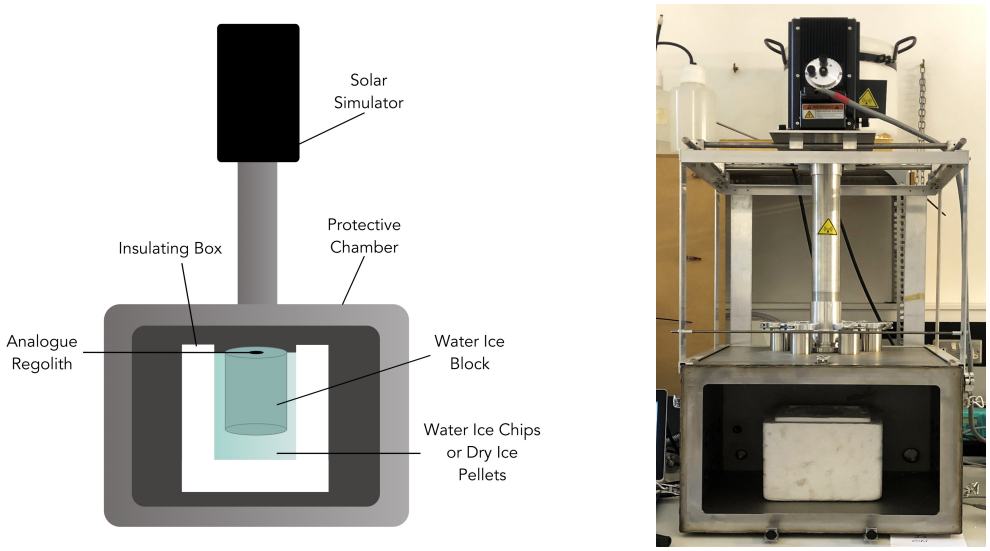

Figure 6.14: Ice Irradiation Experiment Apparatus. A solar simulator irradiated dark-coloured material on or within ice. Dry ice or water ice chips were used to maintain the experimental temperature. (a) Apparatus schematic (not to scale). (b) Apparatus photograph.

6.3.3 Experimental Methods

Measurements of the dimensions of the ice blocks were taken before and after irradiation to measure vertical ablation rate of the ice block.

Preliminary Experiments

The preliminary experiments were performed to test the viability of the experimental protocol. They were performed before the procurement of a new bulb for the solar simulator and during the clear ice development process resulting in a maximum irradiance of 100 Wm^{-2} and the use of bubbly ice blocks.

Antarctic Temperature The temperature of the ice blocks was maintained at ~0°C using water ice chips in a polystyrene insulating box.

A black disc was placed on the surface of an ice block and irradiated for 5 hours. The maximum depth of melt caused by the heating of the disc was measured using a depth gauge and calipers.

A block of ice with an embedded black disc was irradiated for 6 hours. The block was split in half and the maximum melt depth of the fluid inclusion measured using a depth gauge and calipers.

A mass of 0.05 g of JSC Mars-1 regolith (grain size <500 μm) was placed on the surface of an ice block and irradiated for 3 hours. The maximum depth of melt was measured using a depth gauge and calipers.

A block of ice with a disc of JSC Mars-1 regolith (grain size <500 μm) was irradiated for 6 hours. The block was split in half and the maximum melt depth of the fluid inclusion measured using a depth gauge and calipers.

.

Martian Temperature The temperature of the ice blocks was maintained at ~-74°C using dry ice pellets in a polystyrene insulating box.

The preliminary Mars environment experiments were performed once each for a black disc atop and embedded within the ice block. Each ice block was irradiated for 6 hours. Each ice block was then examined for the presence of melt water.

During initial -74°C experiments it was observed that moisture from the air was condensing onto the ice and simulant regolith surfaces, diminishing the received flux of the simulant regolith. This condensation was minimised by adding a tray of silica beads to the chamber and applying a thin layer of ethanol (cooled to -80°C) to the ice surface for experiments where material was embedded into the ice. However, it was not possible to completely prevent condensation onto the ice surface or the simulant material.

Antarctic Temperature Experiments

The experiments under Antarctic conditions were performed at approximately 0°C. Within the insulated box, water ice chips surrounded the ice block to maintain the temperature for the duration of the experiment. Before the experiment, the dimensions of the ice block were measured. For the surface disc experiments, the disc was chilled in the freezer with the ice such that they were the same temperature at the experiment start. For the disc atop ice experiments, the disc was placed on the centre of the exposed surface of the ice block just before commencing exposure to the solar simulator. The ice block was exposed to the solar simulator at 300 Wm^{-2} for 4 hours, which provided sufficient time for melt to occur but was limited by the longevity of the ice chips. Directly after the experiment concluded, the dimensions of the ice block and the dimensions of the melt hole were measured using a ruler, depth gauge and calipers. Each experiment (disc atop ice and disc embedded within ice) was repeated in triplicate.

Measuring Melt-Water Volume: Disc Atop Ice To measure the approximate volume of ice melted by the disc, directly after the completion of irradiation, melt-water was extracted from the melt-hole and measured using a stripette (Corning, 10 mL ± 2%). However, in most cases, the melt-water had escaped through channels in the ice so this method of measurement could not be used. The dimensions of the melt holes were measured using vernier calipers and a depth gauge. The approximate volume of the melt hole was calculated using the measured dimensions.

Measuring Melt-Water Volume: Embedded Disc To measure the approximate melt volume produced by the embedded disc, the block was cut in half using a saw and the dimensions of the inclusion measured using vernier calipers

and a depth gauge. Attempts were made initially to drill through the ice block into the fluid inclusion and extract the melt-water using a syringe, however, this method was inconsistent in its efficacy due to the tendency of the melt-water to exit through the drill hole the moment the drill bit made contact. The volume of the inclusion was calculated and the volume of the disc subtracted, leaving the approximate volume of ice melted by the disc.

Control Experiment One ice block without any analogue regolith material was irradiated for 4 hours. Another block with a black disc atop was not irradiated for 4 hours. A third block embedded with a black disc was not irradiated for 4 hours. Before the experiment, the dimensions of the blocks were measured. Directly after the experiment, the blocks were visually examined for melt-water and the dimensions measured. Each control experiment was performed in triplicate.

Martian Temperature Experiments - Ideal Conditions

Black Disc Ideal Mars NPRC temperature conditions are the warmest that are likely to occur under favourable climate conditions and are therefore the most potentially supportive of melting. The experiments under ideal Mars conditions were performed at approximately -42°C. Within the insulated box, a layer of dry ice pellets below a layer of water ice chips surrounded the ice block to maintain the temperature for the duration of the experiment. The duration of the exposure to the solar simulator was 6 hours, which was limited by the longevity of the dry ice/water ice mixture. Before the experiment, the dimensions of the ice block were measured. For the surface disc experiments, the disc was chilled to the same temperature as the ice and placed on the centre of the exposed surface of the ice block just before commencing exposure to the solar simulator. Directly after the experiment concluded, the ice block was visually examined for the presence of melt-water. For embedded discs, the ice block was broken in half as above to determine if any melt-water formed. Each experiment (disc atop ice and disc embedded within ice) was performed in triplicate.

Regolith and $Mg(ClO_4)_2$ The JSC Mars-1 was sieved (Fisherbrand stainless steel test sieve, 63μm pores) such that the grains were $\leq$63 μm. Though atmospheric dust is on average $\sim$3 μm in diameter [390], aeolian processes on Mars can move particles over 100 μm in diameter [391–394]. To have a layer

Table 6.2: Regolith Material Parameters. To produce discs of regolith and a salt-regolith mixture approximately one grain thick, the density of each material was calculated. The required mass of material could then be calculated.

Material	Triplicate	Mean Mass of 200 mm^3 of Material (m_m) [g]	Bulk Density (ρ) [g mm^{-3}]	Mass of 24.95 mm^3 Disc of Material (m) [g]
≤ 63 μm Grain Regolith	T1	0.121±0.005	$(6.05\pm0.94)\times10^{-4}$	0.014±0.002
	T2	0.122±0.005	$(6.10\pm0.95)\times10^{-4}$	0.015±0.002
	T3	0.121±0.005	$(6.05\pm0.94)\times10^{-4}$	0.014±0.002
	Mean	0.121±0.003	$(6.07\pm0.54)\times10^{-4}$	0.014±0.001
1:1 Mixture of $Mg(ClO_4)_2$ and ≤ 63 μm Grain Regolith	T1	0.152±0.005	$(7.60\pm1.17)\times10^{-4}$	0.019±0.003
	T2	0.149±0.005	$(7.45\pm1.15)\times10^{-4}$	0.019±0.003
	T3	0.150±0.005	$(7.50\pm1.15)\times10^{-4}$	0.019±0.003
	Mean	0.150±0.003	$(7.52\pm0.67)\times10^{-4}$	0.019±0.002

approximately one regolith grain thick, the required mass of the material was calculated. The density of the regolith and salt-regolith mixture was calculated by filling an Eppendorf tube with the material up to the 0.2 mL graduation line then measuring the mass of that volume of regolith or salt-regolith mixture. The density ρ [g mm^{-3}] could then be calculated using

$$\rho = \frac{m_m}{V_m} \tag{6.1}$$

where m_m [g] is the measured mass of $V_m = (200 \pm 30)$ mm^3 (0.2 mL) of regolith or salt-regolith mixture. The volume of the required disc of material, V [mm^3] was calculated using

$$V = \pi r_d^2 t_d \tag{6.2}$$

where r_d [mm] and t_d [mm] are the radius (11 mm) and thickness (63 μm) of the material disc respectively, resulting in a volume of 24.95 mm^3. The mass of regolith or salt-regolith mixture, m [g] needed for the material disc was then calculated using

$$m = V\rho = \pi r_d^2 t_d \frac{m_m}{V_m}. \tag{6.3}$$

These calculations resulted in a necessary mass of (0.014 ± 0.001) g of $\leq$63 μm

grain regolith to produce a disc of regolith of mean thickness of 63 μm. For the 1:1 mixture of $Mg(ClO_4)_2$ and $\leq$63 μm regolith, a mass of (0.019 $\pm$ 0.002) g was calculated using the same method. The parameters are presented in Table 6.2.

A 1:1 mixture by mass of $Mg(ClO_4)_2$ and sieved regolith was prepared. The mixture was separated into (0.019 $\pm$ 0.002) g quantities and cooled to -80°C. The ice was prepared as in the ideal Mars conditions section. Extra care was taken to ensure the ice surface was level and smooth and there were no pits present. The salt-regolith mixture was poured onto the ice surface and spread into a circle of $\varnothing = \sim$22 mm using a chilled plastic spreader tool. The ice was then irradiated at 300 Wm^{-2} for 6 hours. Directly after the experiment concluded, the ice block was visually examined for the presence of melt-water and for grains sinking into the ice surface. The ice block was broken in half to measure the depth of any sunken grains/grain clumps. This experiment was performed in triplicate.

This was repeated for an ice block with (0.014 $\pm$ 0.001) g of only $\leq$63 μm regolith atop to investigate the role of $Mg(ClO_4)_2$ in melt-water formation. Another ice block with a 1:1 mixture by weight of $\leq$63 μm regolith and $Mg(ClO_4)_2$ was not irradiated for 6 hours to investigate the role of solar radiation in melt-water. Directly after the experiment, the blocks were visually examined for melt-water and the dimensions measured. These blocks were split in half in order to more thoroughly examine for melt and make measurements.

Martian Temperature Experiments - Typical Conditions

Black Disc The experiments under Martian temperature conditions were performed at approximately -74°C. Within the insulated box, dry ice pellets surrounded the ice block to maintain the temperature for the duration of the experiment. The duration of the exposure to the solar simulator was 6 hours. Before the experiment, the dimensions of the ice block were measured. For the surface disc experiments, the disc was chilled to the same temperature as the ice and placed on the centre of the exposed surface of the ice block just before commencing exposure to the solar simulator. Directly after the experiment concluded, the ice block was visually examined for the presence melt-water. For embedded discs, the ice block was broken in half to determine if any melt-water had formed. This was done by sawing close to the region where the disc was embedded, then using a hammer and chisel to cleave the block in half. This minimised the chance of melt-water formed from the sawing of the ice reaching

the embedded disc and being mistaken for melt-water resulting from irradiation. Each experiment (disc atop ice and disc embedded within ice) was performed in triplicate.

6.3.4 Measurements and Calculations

Discs Atop Ice

The volumes of the melt holes were calculated by approximating them to cylinders. Several measurements of the radius and depth of the melt hole were taken to calculate their respective means. The mean depth and mean radius were then used to calculate the approximate volume of melted ice. These measurements were taken using vernier calipers and a depth gauge. The volume V_c of the approximated cylindrical melt hole was calculated using

$$V_c = \pi r^2 d \tag{6.4}$$

where r is the mean radius of the cylinder and d is the mean depth of the cylinder. The depth of the melt hole was measured from the bottom of the concave depression (caused by the lamp melting the ice surface directly) and the bottom of the melt hole caused by the disc itself (Figure 6.15)

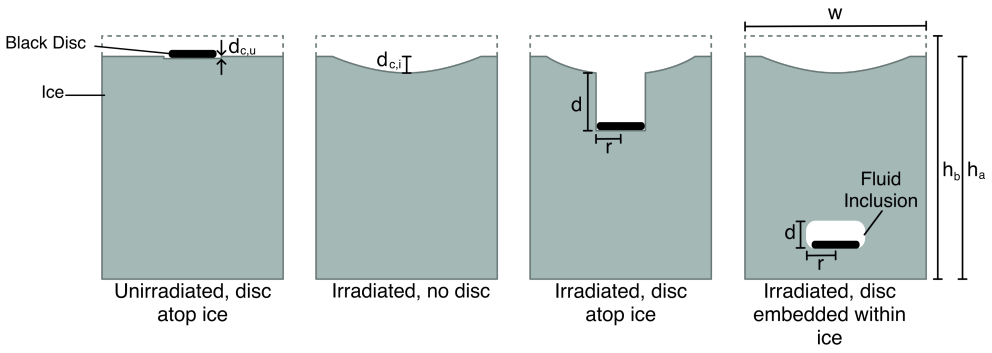

Figure 6.15: Ice Block and Melt Measurements. w is the width of the ice block, h_b and h_a are the height of the ice block before and after irradiation respectively, d and r are the mean depth and radius of the melt hole respectively, $d_{c,u}$ is the mean depth of the melt hole for the unirradiated control ice and $d_{c,i}$ is the maximum depth of the concave melt pool on the irradiated control ice.

Discs Embedded Within Ice

To measure the melt hole produced by embedded disc, the ice blocks were split in half. Several measurements of the depth and radius of the melt hole (Figure 6.15) were taken and the respective means calculated. On each section of the split block the volume of the melt holes were estimated by approximating each hole to a half-cylinder of volume

$$V_{hc} = \frac{1}{2}\pi r^2 d \tag{6.5}$$

This was done for each of the ice block halves. The two volumes added together and the volume of the disc subtracted to V_{tot}

$$V_{tot} = V_{hc,1} + V_{hc,2} - V_{disc} \tag{6.6}$$

where $V_{hc,1}$ and $V_{hc,2}$ are the volumes of the two half-cylinders and V_{disc} is the volume of the black disc.

6.4 Results

6.4.1 Preliminary Experiments

Antarctic Conditions

Disc Atop Ice Significant melt due to heating of the black disc occurred as shown in Figure 6.16. The maximum depth of melt after 5 hours of irradiation at 100 Wm^{-2} was (10 ± 1) mm, melting at a maximum rate of (2.0 ± 0.2) mm $hour^{-1}$ (Table 6.3). The approximate volume of ice melted was (4.91 ± 0.63)×10^3 mm^3.

Disc Embedded Within Ice Significant melt also occurred due to heating of the embedded disc, forming a fluid inclusion of maximum depth (10 ± 1) mm, melting at a maximum rate of (1.67 ± 0.17) mm $hour^{-1}$ (Table 6.3). The inclusions were clearly visible from outside the block. Manual agitation of the block caused the disc to float around in the liquid water within the inclusion. The block was split open and the fluid inclusions highlighted as shown in Figure 6.17. The approximate volume of ice melted was (3.14 ± 0.44)×10^3 mm^3.

Regolith Atop Ice The majority of the regolith melted down into the ice to a maximum depth of (5 ± 1) mm. A small amount of regolith migrated much further into the ice - as shown in Figure 6.18 - to a maximum depth of (35 ± 1) mm resulting in a maximum melt rate of (11.7 ± 0.3) mm $hour^{-1}$ (Table 6.3). The conduit which produced this particularly deep migration may have been a gas bubble or ice grain boundary.

Regolith Embedded Within Ice Significant melt also occurred due to heating of the embedded regolith, forming a substantial fluid inclusion visible in Figure 6.19. The inclusion was clearly visible from outside the block. Manual agitation of the block caused the regolith to float around in the liquid water within the inclusion. The maximum depth of the inclusions was (11 ± 1) mm, resulting in a maximum melt rate of (1.83 ± 0.17) mm $hour^{-1}$. The approximate volume of ice melted was (4.17 ± 0.59)×10^3 mm^3 (Table 6.3).

Martian Conditions

Disc Atop Ice The presence of melt-water was determined by visual examination of the ice surface and disc after irradiation. The ice surface remained completely intact as shown in Figure 6.20 and no detectable melt occurred (Table 6.3).

Disc Embedded Within Ice The presence of melt-water was determined by visual examination of the ice after irradiation (Figure 6.21) and by splitting the ice in half to examine the disc site. No detectable melt of the ice occurred (Table 6.3).

Table 6.3: Results of Preliminary Ice Experiments Under Antarctic and Mars Temperature Conditions: Depth, Rate and Volume of Ice Melt. All experiments were irradiated at 100 Wm^{-2}. Maximum depth refers to the maximum depth of melt achieved by the low albedo material. Max rate refers to the maximum melt-migration rate. Melt volume is the approximate volume of ice melted by the low albedo material.

Simulated Environment	Analogue Material	Position	Duration [hours]	Max Depth [mm]	Max Rate [mm $hour^{-1}$]	Melt Volume [mm^3]
Antarctic (0°C)	Disc	atop	5	10 ± 1	2.0 ± 0.2	$(4.91 \pm 0.63) \times 10^3$
	Disc	embedded	6	10 ± 1	1.67 ± 0.17	$(3.14 \pm 0.44) \times 10^3$
	Regolith	atop	3	35 ± 1	11.7 ± 0.3	-
	Regolith	embedded	6	11 ± 1	1.83 ± 0.17	$(4.17 \pm 0.59) \times 10^3$
Martian (-74°C)	Disc	atop	6	0	0	0
	Disc	embedded	6	0	0	0



(a) **(b)** **(c)**

Figure 6.16: Results of Preliminary Antarctic Temperature Experiment: Black Disc Atop Ice Block. The disc has melted ∼10 mm into the ice block after a 5 hour irradiation at 100 Wm^{-2} under Antarctic temperature conditions ($\sim 0°C$). Perspectives of the ice block from the side (a) and top (b) and (c).

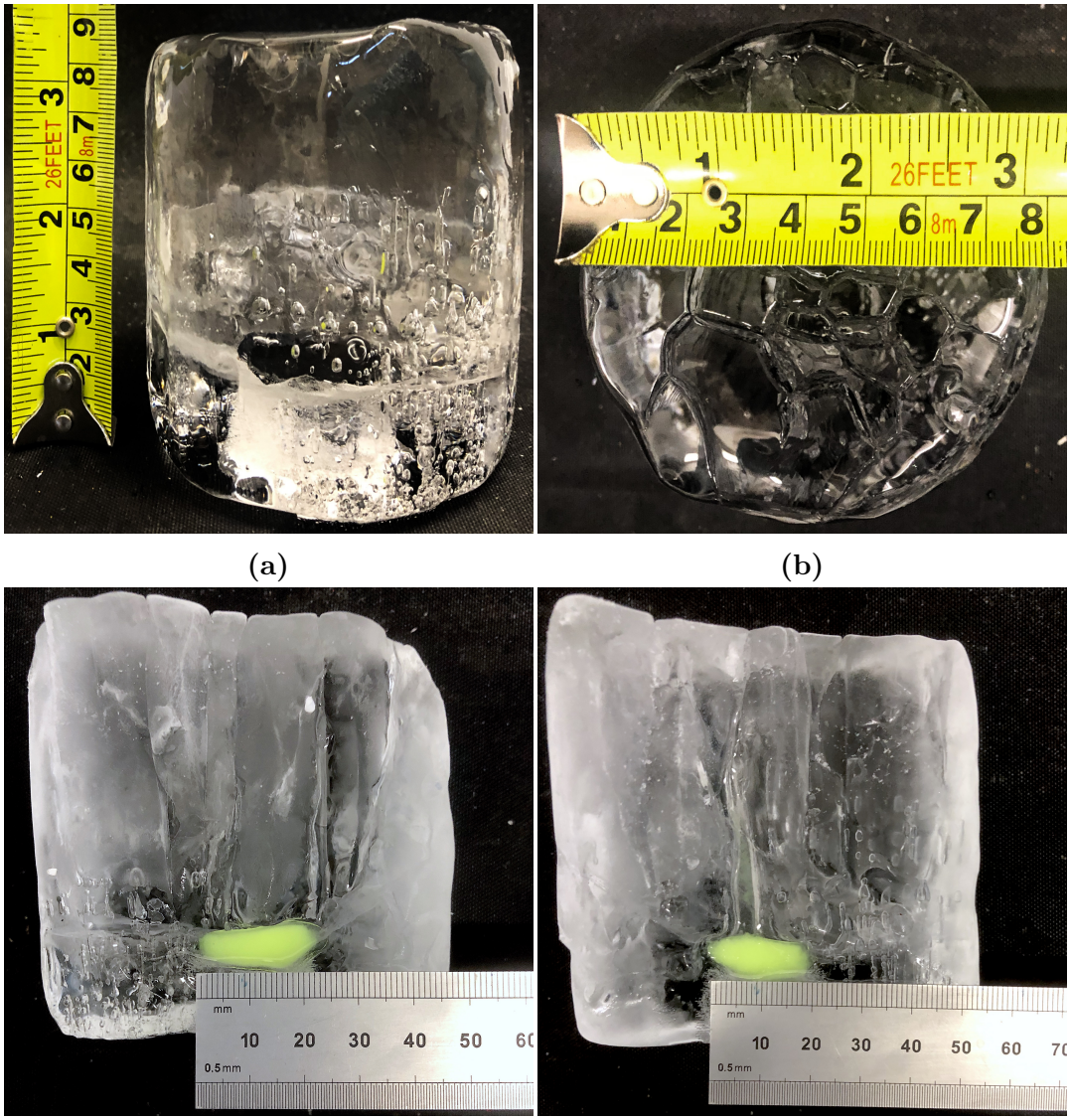

Figure 6.17: Results of Preliminary Antarctic Temperature Experiment: Black Disc Embedded Within Ice Block. A fluid inclusion formed within the ice during 6 hours of irradiation at 100 Wm^{-2} under Antarctic temperature conditions (∼0°C). Exterior of the ice after irradiation from the side (a) and the top (a) perspectives. The block was split in half and the fluid inclusion filled with coloured, -15°C ethanol to highlight the inclusion (c) and (d).



(a) (b) (c)

Figure 6.18: Results of Preliminary Antarctic Temperature Experiment: Regolith Atop Ice Block. JSC Mars-1 regolith melting into ice block after 3 hour irradiation at 100 Wm^{-2} under Antarctic temperature conditions ($\sim$0°C). Perspectives of the ice block from the side (a) and (b) and top (c).



(a) (b)

Figure 6.19: Results of Preliminary Antarctic Temperature Experiment: Regolith Embedded Within Ice Block. A fluid inclusion formed within 6 hours of irradiation at 100 Wm^{-2} under Antarctic temperature conditions ($\sim$0°C). The block was split in half to measure inclusion dimensions. Perspectives from the side (a) and top (b).

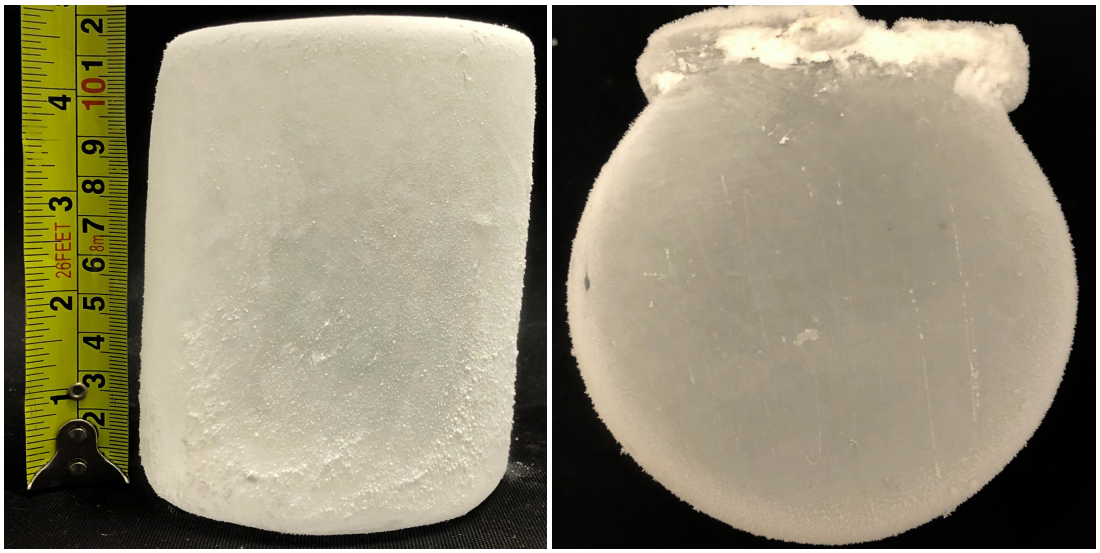

(a) (b)

Figure 6.20: Results of Preliminary Mars Temperature Experiment: Black Disc Atop Ice Block. Ice block after 6 hour irradiation at 100 Wm^{-2} under Mars temperature conditions (-74°C) from side (a) and top (b) perspectives. No visible melt occurred on the ice surface that the disc was on (b).

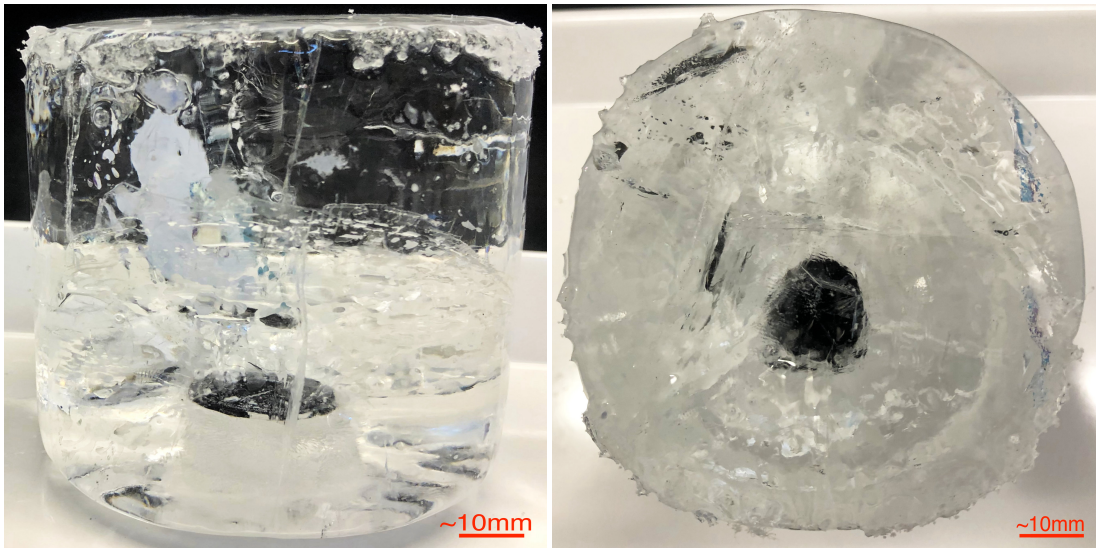

(a) (b)

Figure 6.21: Results of Preliminary Mars Temperature Experiment: Black Disc Embedded Within Ice Block. Ice block after 6 hour irradiation at 100 Wm^{-2} under Mars temperature conditions (-74°C) from side (a) and top (b) perspectives. No measurable melt occurred.

Table 6.4: Results of Melt Caused by a Black Disc Atop Ice Under Each Experimental Temperature Condition. The experiments were performed for 4 hours and 6 hours for the Antarctic and Martian temperatures respectively. All experiments were conducted at an irradiation of 300 Wm^{-2}. T1-T3 are labels for each triplicate in an experiment set.

Simulated Environment	Triplicate	Mean Depth [mm]	Max depth [mm]	Melt Volume [mm^3]	Mean Melt Rate [mm $hour^{-1}$]	Max Melt Rate [mm $hour^{-1}$]
Antarctic (0°C)	T1	18 ± 1	25 ± 1	(10.4 ± 0.7)×10^3	4.50 ± 0.18	6.25 ± 0.25
	T2	15 ± 1	15 ± 1	(7.40 ± 0.8)×10^3	3.75 ± 0.25	3.75 ± 0.25
	T3	19 ± 1	23 ± 1	(11.3 ± 0.7)×10^3	4.75 ± 0.18	5.75 ± 0.25
	Mean	17.6 ± 0.4	21 ± 1	(9.80 ± 0.40)×10^3	4.40 ± 0.11	5.25 ± 0.14
Ideal Mars (-42°C)	T1	0	0	0	0	0
	T2	0	0	0	0	0
	T3	0	0	0	0	0
	Mean	0	0	0	0	0
Mars (-74°C)	T1	0	0	0	0	0
	T2	0	0	0	0	0
	T3	0	0	0	0	0
	Mean	0	0	0	0	0

Table 6.5: Results of Melt Caused by a Black Disc Embedded in Ice Under Each Experimental Temperature Condition. The experiments were performed for 4 hours and 6 hours for the Antarctic and Martian temperatures respectively. All experiments were conducted at an irradiation of 300 Wm^{-2}. T1-T3 are labels for each triplicate in an experiment set.

Simulated Environment	Triplicate	Mean Depth [mm]	Max depth [mm]	Melt Volume [mm^3]	Mean Melt Rate [mm $hour^{-1}$]	Max Melt Rate [mm $hour^{-1}$]
Antarctic (0°C)	T1	11.0 ± 0.7	15 ± 1	(4.96 ± 0.29)×10^3	2.75 ± 0.18	3.75 ± 0.25
	T2	8.5 ± 0.7	9 ± 1	(4.56 ± 0.30)×10^3	2.13 ± 0.18	2.25 ± 0.25
	T3	12.0 ± 0.7	13 ± 1	(5.18 ± 0.33)×10^3	3.0 ± 0.18	3.25 ± 0.25
	Mean	10.5 ± 0.4	13 ± 1	(5.17 ± 0.18)×10^3	2.63 ± 0.10	3.08 ± 0.14
Ideal Mars (-42°C)	T1	0	0	0	0	0
	T2	0	0	0	0	0
	T3	0	0	0	0	0
	Mean	0	0	0	0	0
Mars (-74°C)	T1	0	0	0	0	0
	T2	0	0	0	0	0
	T3	0	0	0	0	0
	Mean	0	0	0	0	0

Table 6.6: Mean Ablation Rate of Uncovered Ice Surface at Each Experimental Temperature Condition. T1-T3 are labels for each triplicate in an experiment set.

		Ablation Rate [mm hour^{-}1]	
Simulated Environment	Triplicate	Atop	Embedded
Antarctic (0°C)	T1	1.25 ± 0.25	2.38 ± 0.25
	T2	2.5 ± 0.25	1.25 ± 0.25
	T3	1.25 ± 0.25	2.5 ± 0.25
	Mean	1.67 ± 0.14	2.04 ± 0.14
Ideal Mars (-42°C)	T1	0	0
	T2	0	0
	T3	0	0
	Mean	0	0
Mars (-74°C)	T1	0	0
	T2	0	0
	T3	0	0
	Mean	0	0

6.4.2 Antarctic Temperature Experiments

Black Disc Atop Ice

For each of the three experiments, significant melt due to heating of the black disc occurred as shown in Figure 6.22. For each experiment, the results of mean and maximum melt depth and melt rate, and approximate volume of ice melted are presented in Table 6.4. The mean maximum depth of melt across the triplicates for a four hour irradiation was (21 ± 1) mm, melted at a mean maximum rate of (5.25 ± 0.14) mm hour^{-1}. The overall mean approximate ice volume melted was (9.80 ± 0.40)×10^3 mm^3.

Black Disc Embedded in Ice

Significant melt also occurred due to heating of the embedded disc, forming a fluid inclusion for each of the triplicates as shown in Figure 6.23 and Figure 6.24. The inclusions were clearly visible from outside the block. Manual agitation of the block caused the disc to float around in the liquid water within the inclusion. For each experiment, the results of mean and maximum melt depth and melt rate, and approximate volume of ice melted are presented in Table 6.5. The

mean maximum depth of the inclusions across the triplicates was (13 ± 1) mm, melted at a mean maximum rate of (3.08 ± 0.14) mm hour^{-1}. The overall mean approximate volume of ice melted was (5.17 ± 0.18)×10^3 mm^3.

Irradiated Ice Without Black Discs

After 4 hours of irradiation at 300 Wm^{-2}, the ice blocks without a disc present on or within them all had shallow (∼4 mm deep) concave melt pools on the ice surface. Measurements of the dimensions of the melt pools were taken (Table 6.7). The concave pool diameters were consistent with the width of the collimated beam from the solar simulator lamp (Figure 6.25). The presence of a wide, shallow melt pool in contrast to the deep melt hole caused by the disc confirms that the heated disc is the cause of the melt holes observed in Figure 6.22 and not just the incident light itself.

Unirradiated Ice With Black Discs

The unirradiated ice blocks with a superjacent disc had a melt hole depth of up to <0.1 mm (Table 6.7 and Figure 6.26). The unirradiated ice with an embedded disc formed no visible melt-water (Figure 6.27). This indicates that even without irradiation, the surface disc can facilitate a small amount of melting, possibly through transfer of heat from the atmosphere, but this melt is not significant compared to the that which occurs when the system is irradiated. The embedded disc will receive little energy transfer from the environment as it is encased in the ice. These results confirm that the majority of the melting which occurred to form the melt-holes was generated by the solar-heating of the disc and not by energy transfer from the atmosphere.

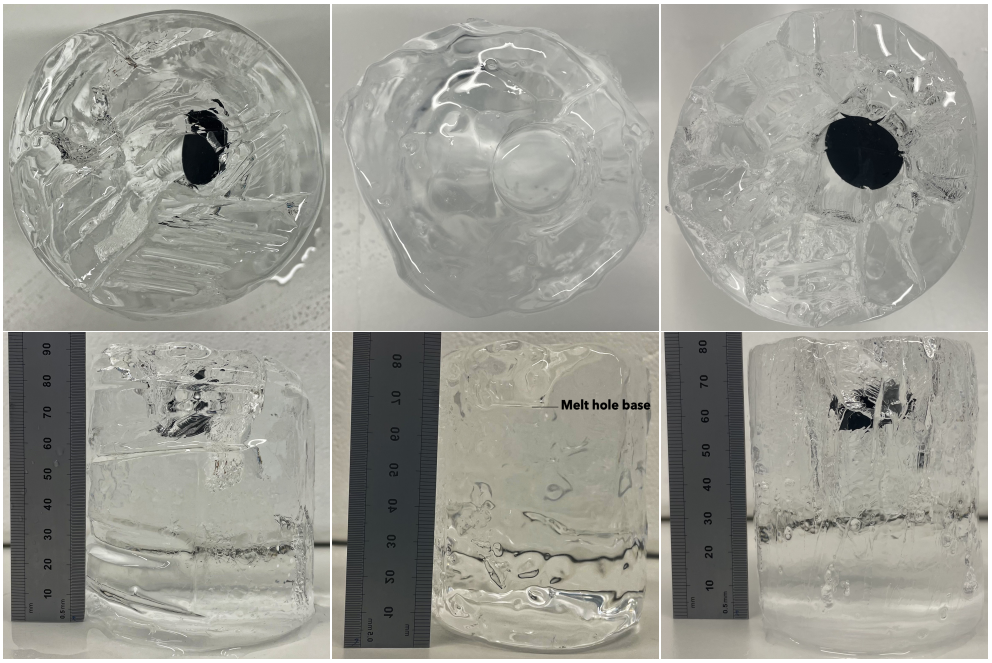

(a) T1 **(b)** T2 **(c)** T3

Figure 6.22: Results of Antarctic Temperature Experiments: Black Disc Atop Ice. Black disc melted into ice block during 4 hour irradiation at 300 Wm^{-2} under Antarctic temperature conditions (∼0°C). (a)-(c) triplicate experiments T1-T3.

Table 6.7: Results of Antarctic Temperature Control Experiments. Maximum depth refers to the depth of the concave melt depression formed by the lamp beam and the depth of melt caused by the heating of the black disc in the irradiated and unirradiated control experiments respectively. C1-C3 are labels for the three triplicates in each control experiment set.

Experiment	Triplicate	Max depth [mm]	Melt Rate [mm $hour^{-1}$]
Irradiated, No Disc	C1	3 ± 1	0.75 ± 0.25
	C2	5 ± 1	1.25 ± 0.25
	C3	5 ± 1	1.25 ± 0.25
	Mean	4 ± 1	1.08 ± 0.14
Unirradiated, Disc Atop	C1	0	0
	C2	<0.1	<0.025
	C3	0	0
Unirradiated, Embedded Disc	C1	0	0
	C2	0	0
	C3	0	0

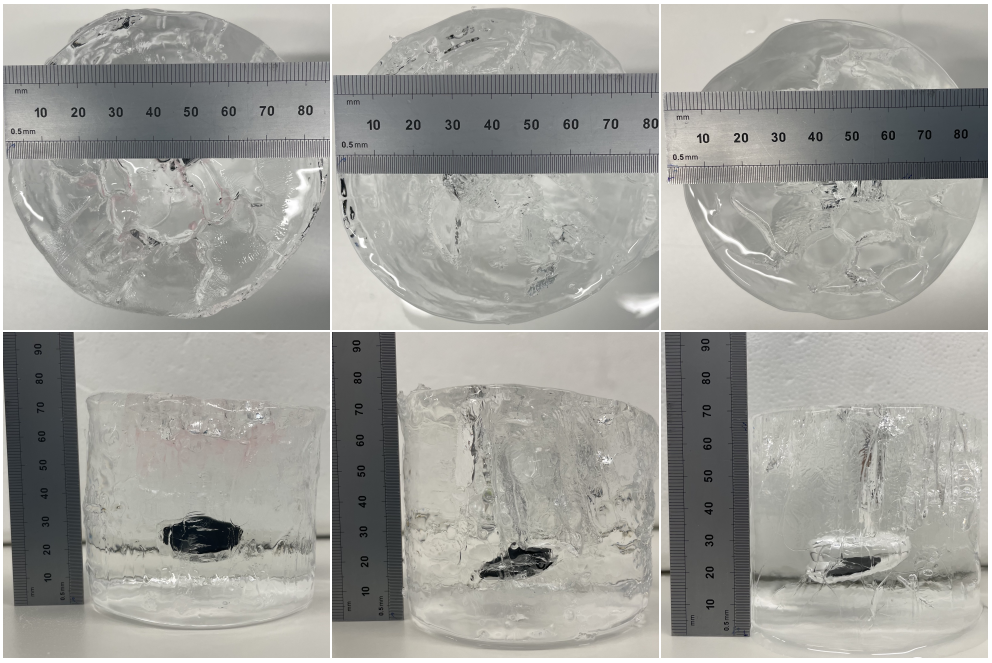

(a) T1 **(b)** T2 **(c)** T3

Figure 6.23: Results of Antarctic Temperature Experiments: Black Disc Embedded Within Ice. Black disc melted into ice block during 4 hour irradiation at 300 Wm^{-2} under Antarctic temperature conditions (∼0°C). Fluid inclusions formed within the ice due to the heating of the disc. The inclusions were clearly visible from outside the ice block. (a)-(c) triplicate experiments T1-T3.

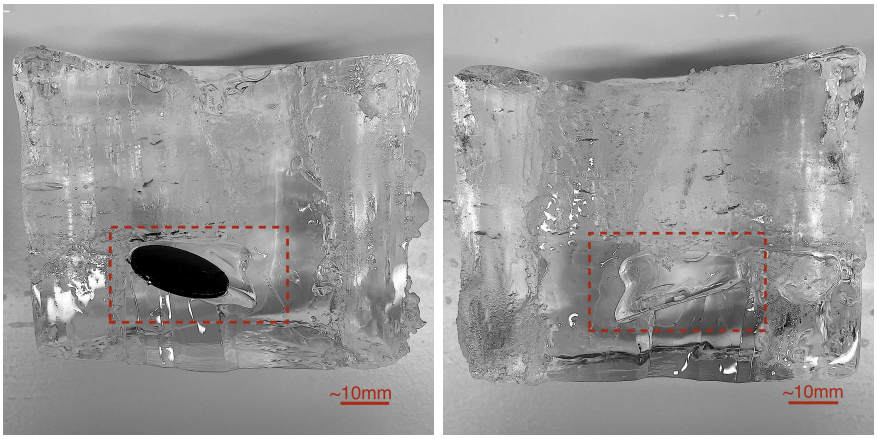

(a) T1

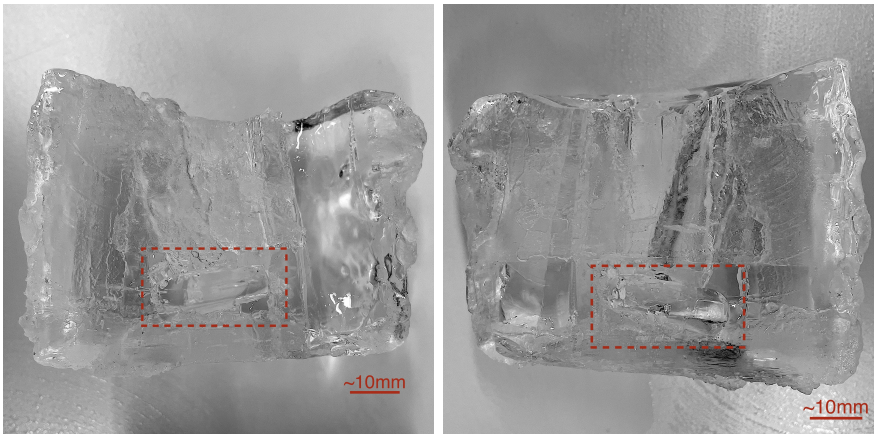

(b) T2

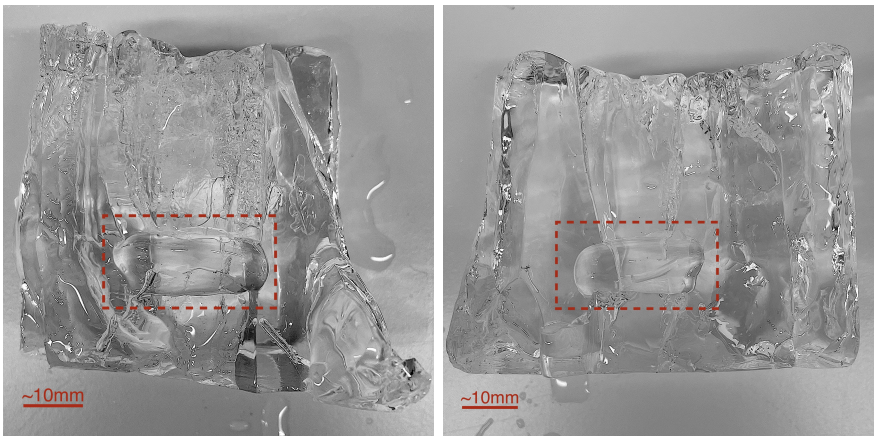

(c) T3

Figure 6.24: Results of Antarctic Temperature Experiments: Black Disc Embedded Within Ice - Halved Ice Blocks. Fluid inclusions formed by black disc embedded into ice block during 4 hour irradiation at 300 Wm^{-2} under Antarctic temperature conditions (∼0°C). The blocks (shown in Figure 6.23) were split in half to measure the inclusion dimensions. The inclusions are within the dashed red boxes. (a)-(c) triplicate experiments T1-T3.

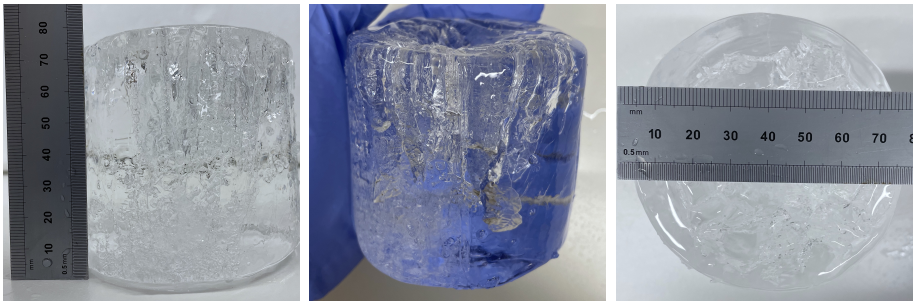

(a) C1

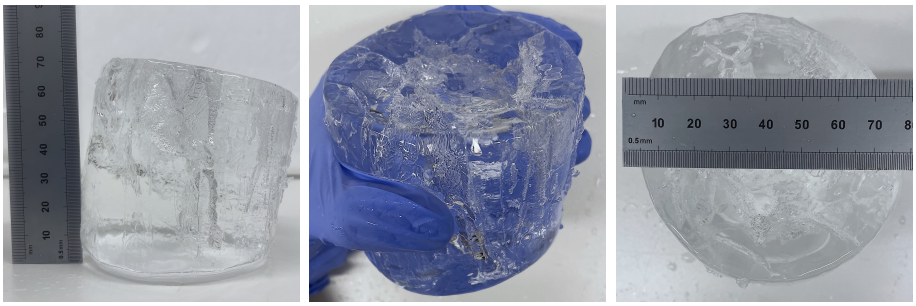

(b) C2

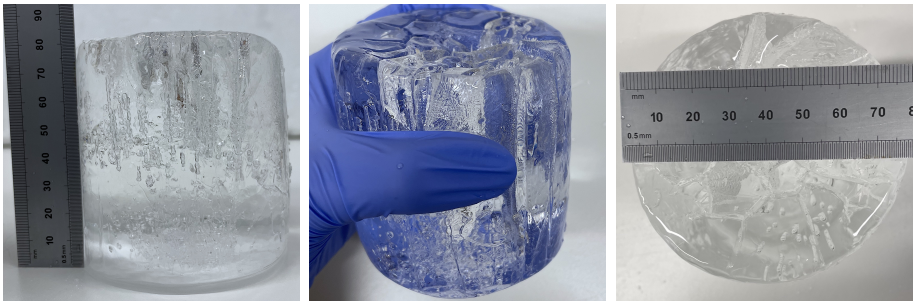

(c) C3

Figure 6.25: Results of Antarctic Temperature Control Experiments: Irradiated Without Black Disc. Irradiated control ice blocks after 4 hours of 300 Wm^{-2} irradiation under Antarctic temperature conditions ($\sim$0°C) with no low-albedo material present. Some melting occurred where the lamp beam was incident on the ice. (a)-(c) Control experiments C1-C3.

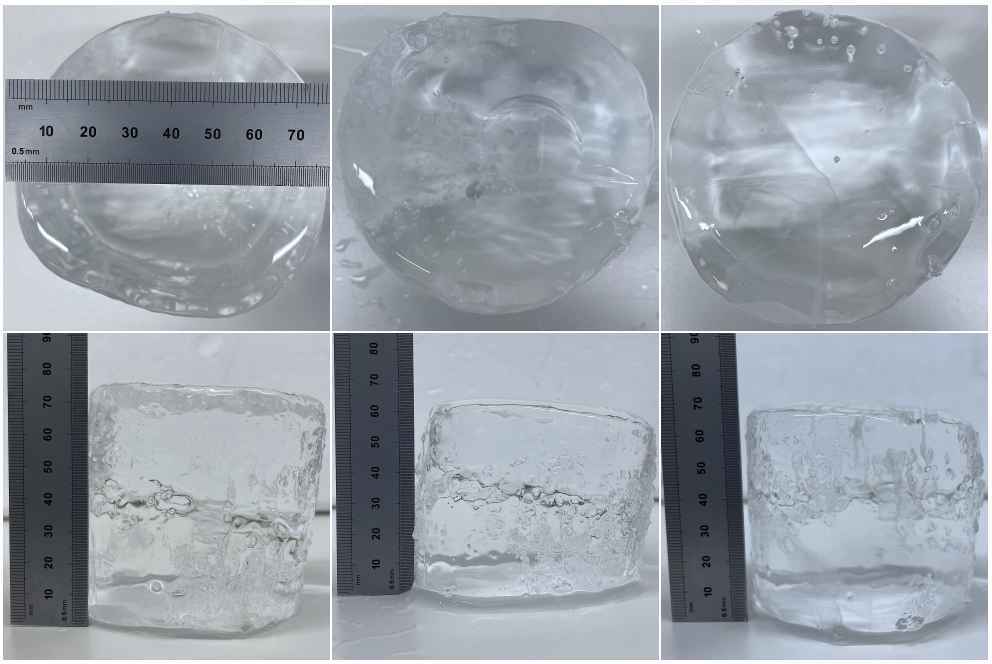

(a) C1 **(b)** C2 **(c)** C3

Figure 6.26: Results of Antarctic Temperature Control Experiments: Unirradiated Black Disc Atop Ice. Unirradiated control ice blocks after 4 hours under Antarctic temperature conditions (∼0°C) with black disc atop. All blocks had very little melt due to the black disc atop the ice. (a)-(c) Control experiments C1-C3.

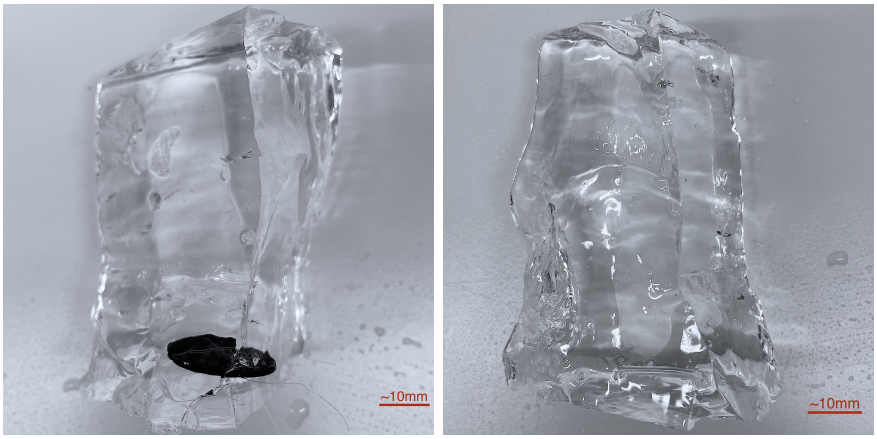

(a) C1

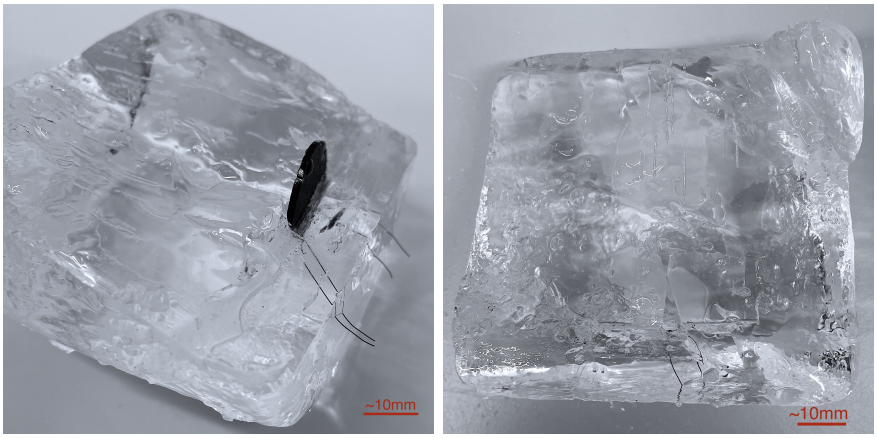

(b) C2

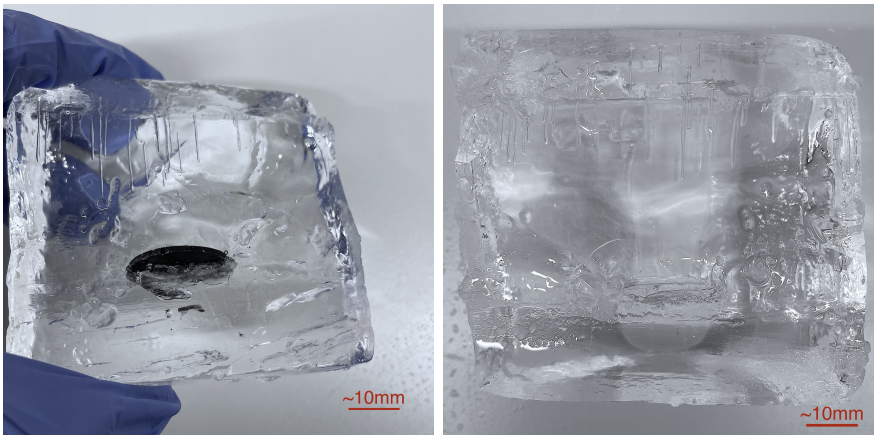

(c) C3

Figure 6.27: Results of Antarctic Temperature Control Experiments: Unirradiated Black Disc Embedded Within Ice. Unirradiated control ice blocks after 4 hours under Antarctic temperature conditions (∼0°C) with black disc embedded. The blocks were split in half to check for melt water. All blocks had no measurable melt due to the black disc embedded within the ice. (a)-(c) Control experiments C1-C3.

6.4.3 Martian Temperature Experiments - Ideal Conditions

Disc Atop Ice After 6 hours of 300 Wm^{-2} irradiation under ideal Mars temperature conditions (-42°C) no detectable bulk melting of the water ice had occurred (Table 6.4). The ice blocks after irradiation are shown in Figure 6.28.

Disc Embedded in Ice After 6 hours of 300 Wm^{-2} irradiation under ideal Mars temperature conditions (-42°C) the ice block was examined from the outside and no fluid inclusion was observed (Figure 6.29). The block was split open to confirm that no detectable bulk melting of the water ice had occurred. Fluid inclusions had not formed and no measurable melting had occurred.

Regolith & $Mg(ClO_4)_2$ Atop Ice After 6 hours of 300 Wm^{-2} irradiation under ideal Mars temperature conditions (-42°C) some of the grains had sunk a very slight but visually detectable amount into the ice. Some of the grains appeared darkened as if saturated with liquid. Furthermore, some of the grains had spread outwards from the original 22 mm diameter circle, indicating the presence of liquid to facilitate this migration (Figure 6.30). To measure the depth of the melt, the blocks had to be split open. Some grains had clearly sunk into the ice surface as shown in Figure 6.31. The depth measurements were taken with calipers. The maximum melt depth measured on each of the three ice block was (0.5 ± 0.1) mm.

Irradiated Ice With 63 μm Regolith Atop Ice

After 6 hours of 300 Wm^{-2} irradiation under the ideal Mars conditions of -42°C the ice block with only 63 μm regolith atop was split in half and examined and no visible melt or regolith migration had occurred. The halved ice block is shown in Figure 6.32.

Unirradiated Ice With 63 μm Regolith & $Mg(ClO_4)_2$ Atop Ice

After 6 hours with no irradiation under the ideal Mars conditions of -42°C the ice block with 63 μm regolith & $Mg(ClO_4)_2$ atop was split in half and examined and no visible melt or regolith migration had occurred. The halved ice block is

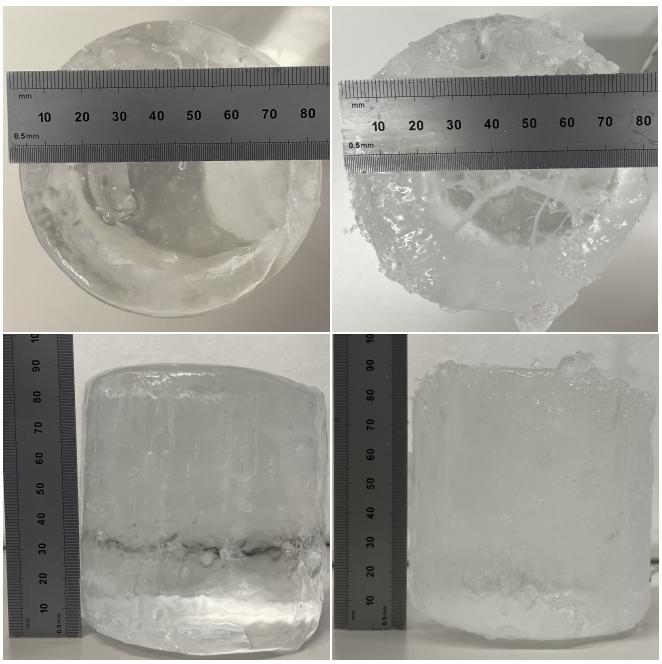

(a) T1 **(b)** T2

Figure 6.28: Results of Ideal Martian Temperature Experiments: Black Disc Atop Ice. Photographs of ice blocks after 6 hour irradiation at 300 Wm^{-2} under ideal Mars temperature conditions (-42°C). No measurable melt occurred. (a)-(b) Triplicate experiments T1-T2.

shown in Figure 6.33.

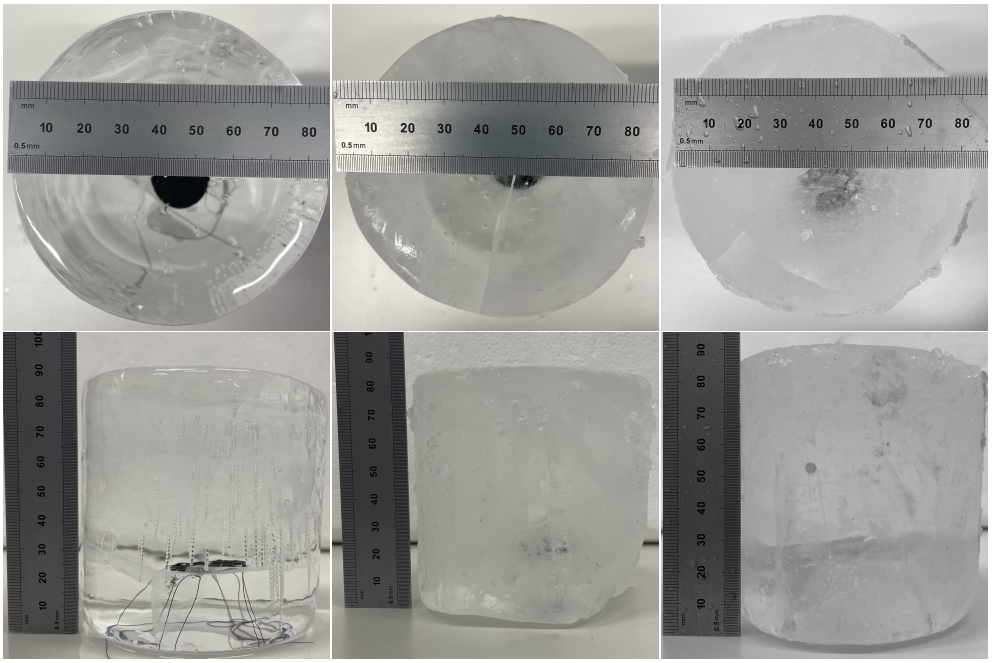

(a) T1 **(b)** T2 **(c)** T3

Figure 6.29: Results of Ideal Martian Temperature Experiments: Black Disc Embedded Within Ice. Photographs of ice blocks after 6 hour irradiation at 300 Wm^{-2} under ideal Mars temperature conditions (-42°C). No measurable melt occurred. (a)-(c) Triplicate experiments T1-T3.

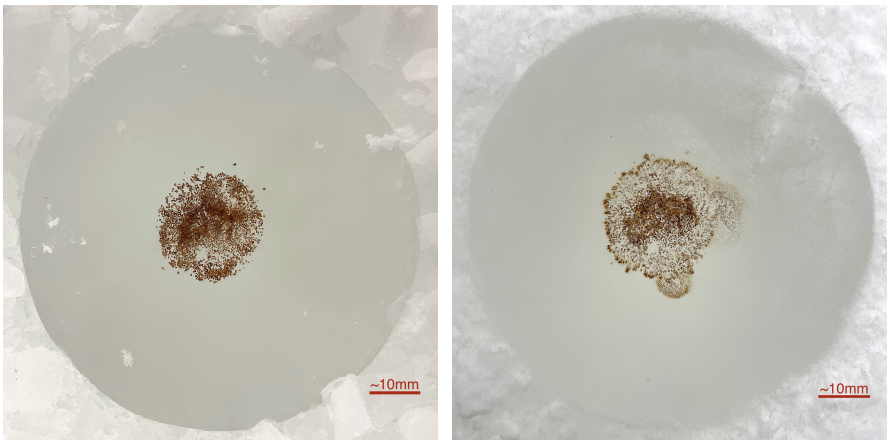

(a) **(b)**

Figure 6.30: Results of Ideal Martian Temperature Experiments: JSC Mars-1 Regolith and $Mg(ClO_4)_2$ Atop Ice Surface Before and After Irradiation. Photograph of ice surface surface (a) before and (b) after 6 hour irradiation at 300 Wm^{-2} under ideal Mars temperature conditions (-42°C). The spreading of the grains is evidence that melting has taken place.

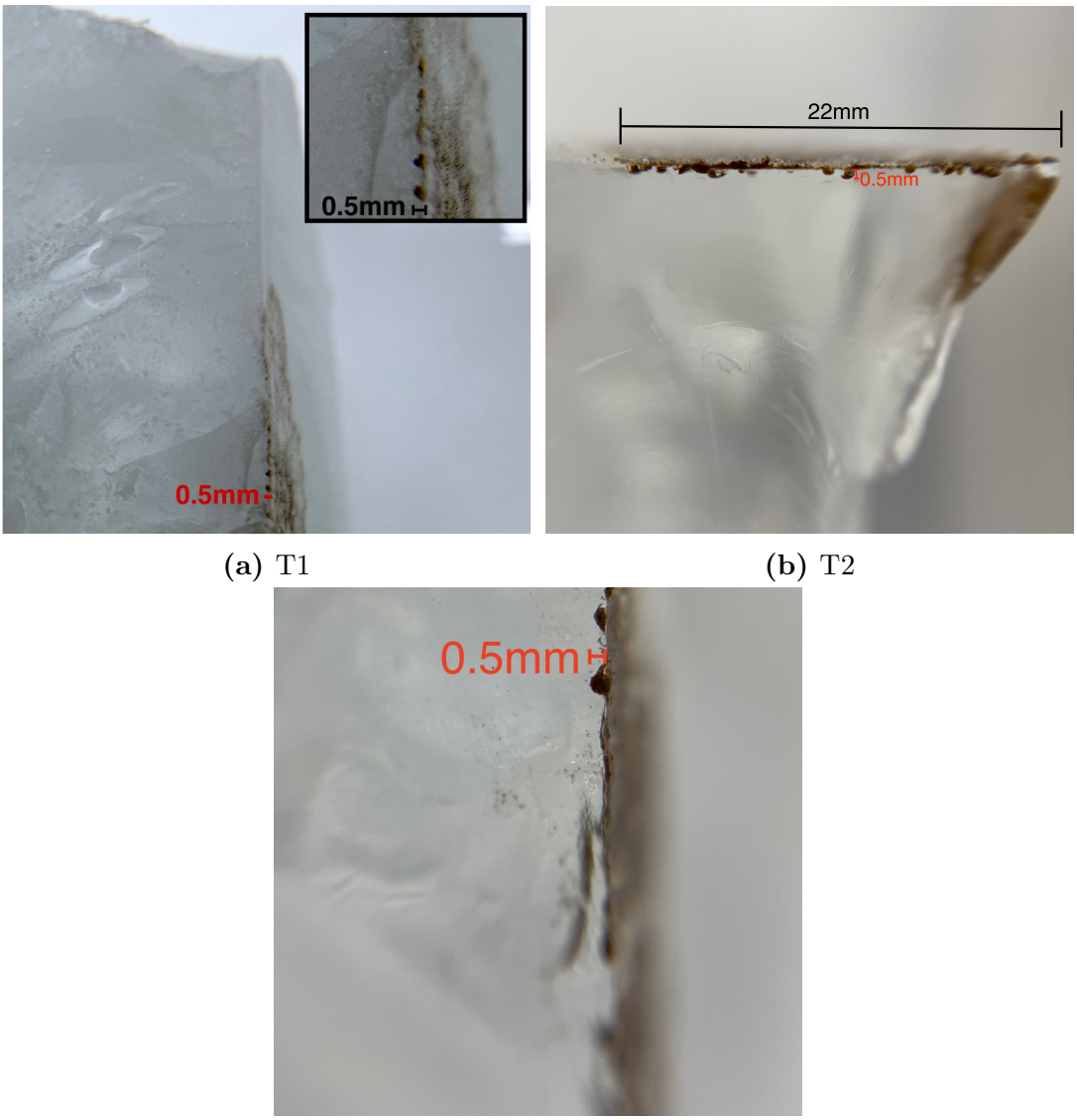

(a) T1 **(b)** T2

(c) T3

Figure 6.31: Results of Ideal Martian Temperature Experiments: JSC Mars-1 Regolith and $Mg(ClO_4)_2$ Atop Halved Ice Block. Photographs of halved ice blocks after 6 hour irradiation at 300 Wm^{-2} under ideal Mars temperature conditions (-42°C). A small amount of sediment migration into the ice surface occurred, suggesting melting took place. T1-T3 refers to each experiment in the set of triplicates.

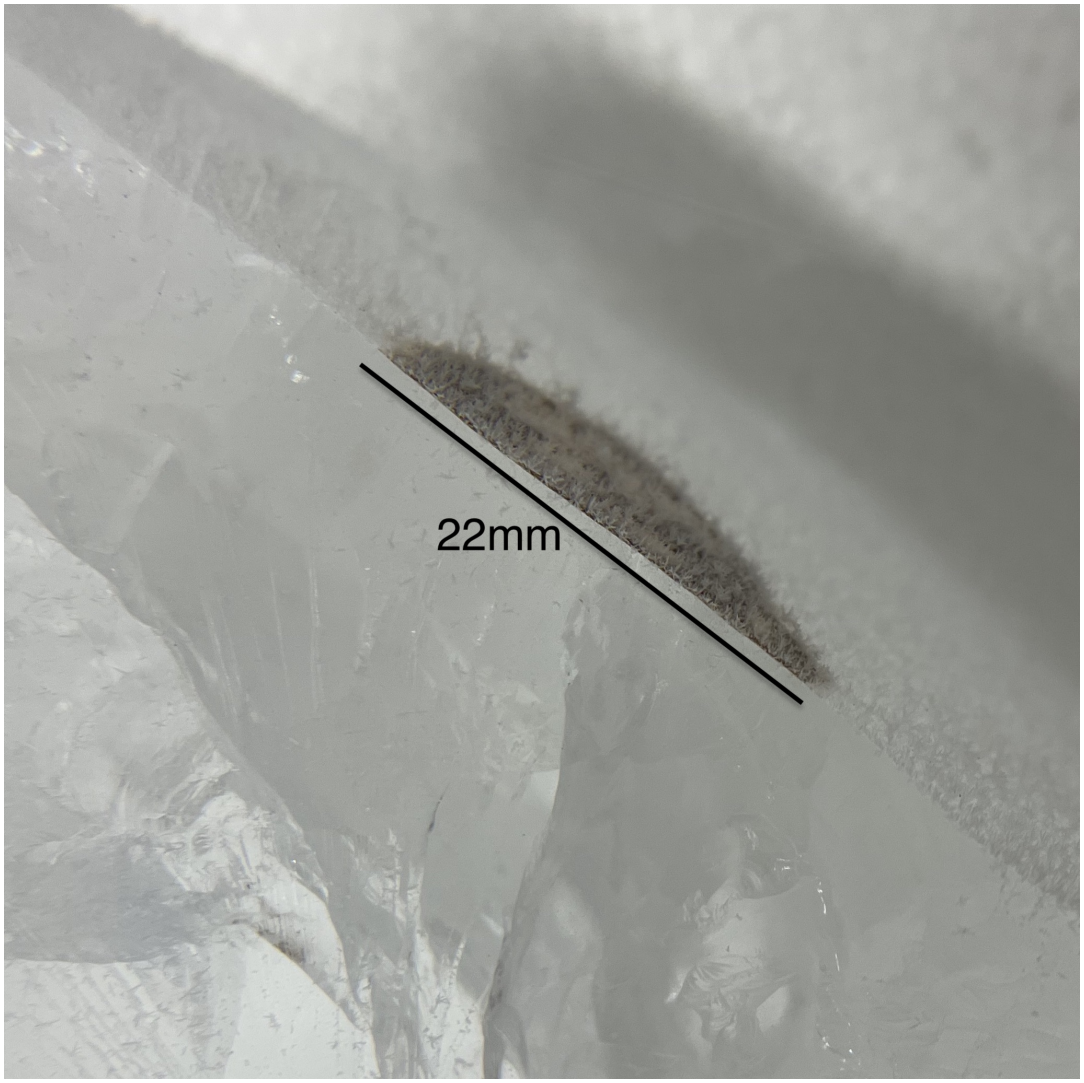

Figure 6.32: Results of Ideal Martian Temperature Control Experiments: JSC Mars-1 Regolith Atop Halved Ice. Photograph of halved ice block after 6 hour Irradiation at 300 Wm^{-2} under ideal Mars temperature conditions (-42°C). No visible melt or sediment migration occurred.

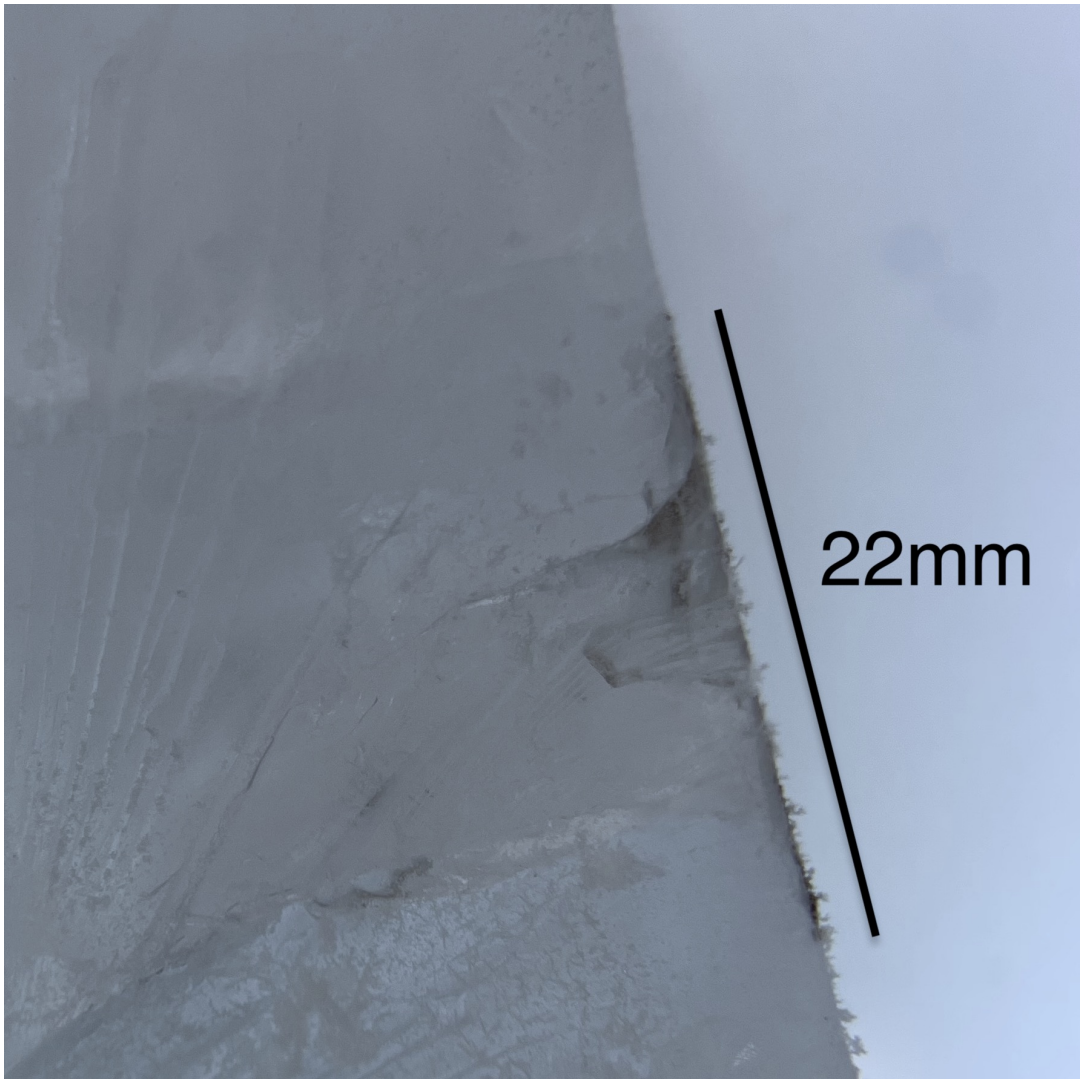

Figure 6.33: Results of Ideal Martian Temperature Control Experiments: Unirradiated JSC Mars-1 Regolith and $Mg(ClO_4)_2$ Atop Ice Photograph of halved ice block after 6 hours under ideal Mars temperature conditions (-42°C). No visible melt or sediment migration occurred.

6.4.4 Martian Temperature Experiments - Typical Conditions

Black Disc Atop Ice

The presence of melt-water was determined by visual examination of the ice surface after irradiation. For each of the three -74°C experiments, no detectable melt of the ice occurred (Table 6.4 and Figure 6.34).

Black Disc Embedded Within Ice

For embedded discs, the blocks were cut open to determine whether any melt had occurred and formed a fluid inclusion. For each of the triplicates, no detectable melt occurred and no fluid inclusions formed (Table 6.5, Figure 6.35 and Figure 6.36).

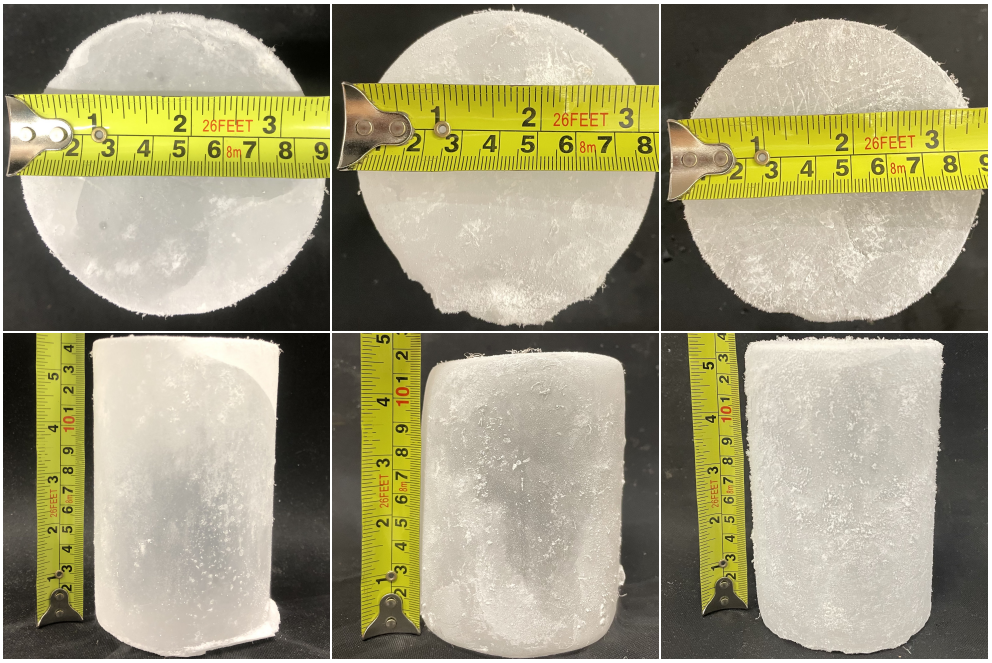

(a) T1 **(b)** T2 **(c)** T3

Figure 6.34: Results of Typical Martian Temperature Experiments: Black Disc Atop Ice. Photographs of ice blocks after 6 hour irradiation at 300 Wm^{-2} under Mars temperature conditions (∼-74°C) with black disc atop the ice. No visible melt occurred.T1-T3 label each experiment in the set of triplicates.

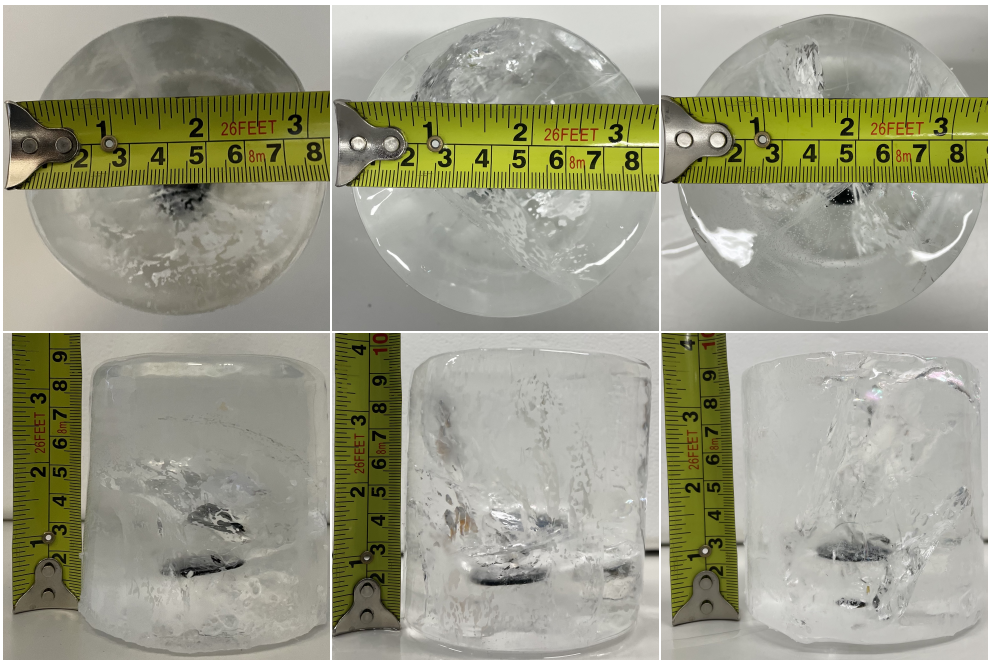

(a) T1 **(b)** T2 **(c)** T3

Figure 6.35: Results of Typical Martian Temperature Experiments: Black Disc Embedded Within Ice. Photographs of ice blocks after 6 hour irradiation at 300 Wm^{-2} under Mars temperature conditions (∼-74°C) with black disc embedded in the ice. No fluid inclusion formed. T1-T3 label each experiment in the set of triplicates.

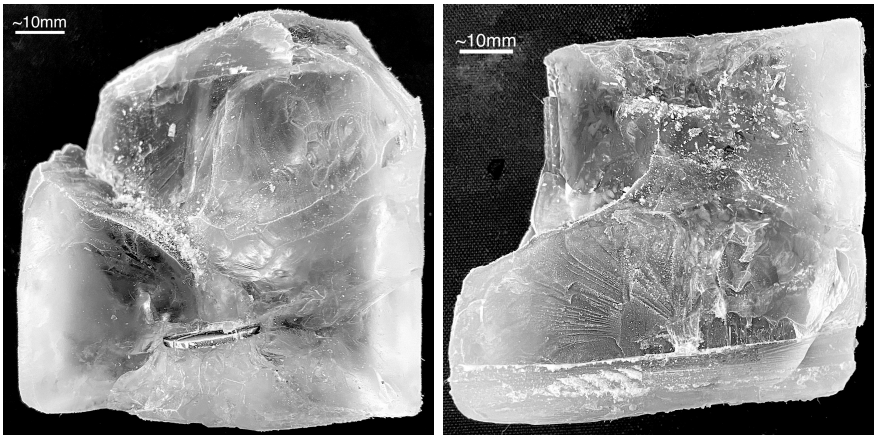

(a) T1

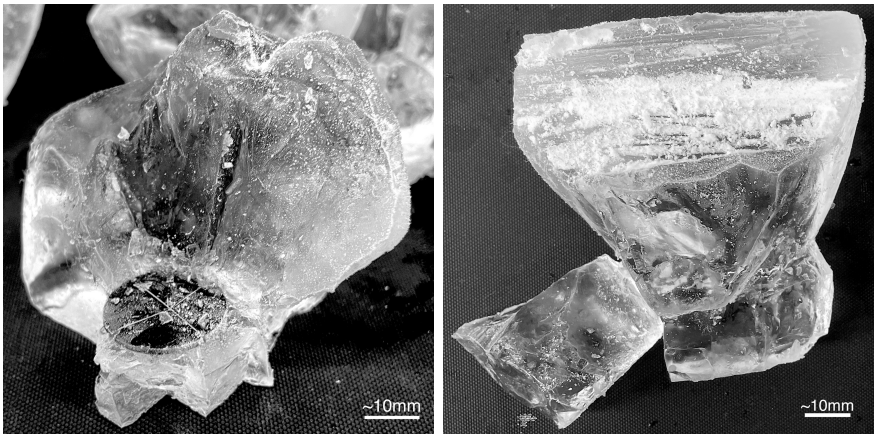

(b) T2

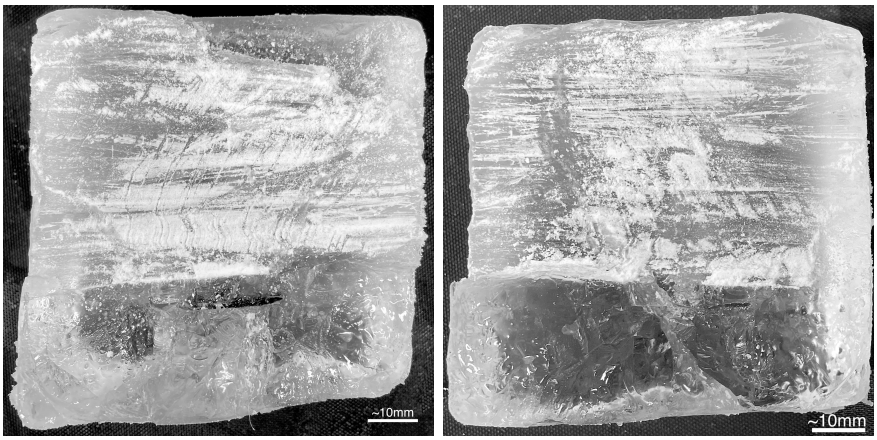

(c) T3

Figure 6.36: Results of Typical Martian Temperature Experiments: Black Disc Embedded Within Ice - Halved Ice Blocks. Photographs of halved ice blocks after 6 hour irradiation at 300 Wm^{-2} under Mars temperature conditions (∼-74°C) with black disc embedded in the ice. The blocks (shown in Figure 6.35) were split in half to examine for melt. No visible melt occurred. T1-T3 label each experiment in the set of triplicates.

6.5 Discussion

The presence of liquid water is imperative for the existence of life as we know it. It is therefore important that we understand the physical limits under which liquid water can exist, particularly under polyextreme conditions like those experienced on the Martian surface. The work presented in this chapter explores whether bulk liquid water formation can occur as a consequence of the solar-heating of low albedo material on analogue Martian polar ice. This exploration contributes to our understanding of the physical limits under which liquid water can exist, and hence our understanding of where habitats could exist or have existed on Mars.

A procedure for the production of suitably clear ice and experimental protocols for irradiating low-albedo material atop and embedded within ice were developed. Under Antarctic temperature conditions, significant melt occurred as a consequence of the solar-heating of a black aluminium disc superjacent to and embedded within ice. These results are consistent with previous experimental work and fieldwork measurements, substantiating the efficacy of the experimental apparatus and procedure. Under ideal (-42°C) and more typical (-74°C) Martian polar summer temperatures, no measurable melt occurred via the solar-heating of a black aluminium disc in either the superjacent or embedded positions. At -42°C, A small amount of melting occurred when $Mg(ClO_4)_2$ salt was mixed with $\leq$63 μm grain regolith.

The results presented in this chapter highlight the challenge of forming bulk liquid water under Martian north polar temperature and solar conditions. Only when highly-deliquescent magnesium perchlorate salt was added to fine-grained ($\leq$63 μm) JSC Mars-1 simulant regolith did visible melt occur under ideal Mars north polar temperature and solar conditions.

6.5.1 Antarctic Temperature Conditions

The Antarctic temperature experiments successfully reproduced the mechanism that forms lake ice fluid inclusion environments similar to those observed by Priscu et al. (1998) in the McMurdo dry valleys, Antarctica [51]. The melt that occurred in the experiments presented in this chapter is consistent with a similar experiment performed by Jepsen et al. (2010). They found that a 1 mm layer

of regolith atop water ice under Antarctic solar and temperature conditions (589 Wm^{-2}, ∼-1°C ice temperature, ∼-5°C air temperature) measured a melt rate between (∼3.5 ± 0.5) mm hr^{-1} and (∼6 ± 2) mm hr^{-1}, corresponding to 14-24 mm of melt after 4 hours [379]. The maximum melt depths and maximum melt rates of the experiments presented here were d = (21 ± 1) mm, v_{max} = (5.25 ± 0.14) mm hr^{-1} and d = (13 ± 1) mm, v_{max} = (3.08 ± 0.14) mm hr^{-1} for a black aluminium disc positioned atop and embedded within the ice respectively. Jepsen et al. (2010) also found that their experimentally and computationally obtained melt-migration rates resulted in an equilibrium depth of ∼2 m, which is consistent with field observations [51, 298]. The consistency of the rate and depth of ice melt as a consequence of the solar-heating of low albedo material under Antarctic solar and temperature conditions presented here with those presented in previous work and with observations of environments in the field indicates that the experimental protocol used here is efficacious. It may therefore be reasonably expected that applying the same protocol under low temperature conditions will yield accurate results.

6.5.2 Martian Temperature Conditions

The experiments performed at ideal and more typical Mars north polar summer temperatures produced no visible melt in either the embedded or surficial black disc cases. Under ideal Martian polar temperature conditions (-42°C) fine-grained regolith (≤63 μm) atop the ice did not produce any visible melt-water. However, when $Mg(ClO_4)_2$ salt was mixed with ≤63 μm grain regolith in a 1:1 ratio by weight and exposed to simulated solar irradiation atop a -42°C ice block for 6 hours, a small amount of melting occurred, causing grains to sink into the ice up to 0.5 mm deep.

Conversely, Losiak et al (2014) modelled the melt-migration of dust particles on the Martian NPRC, generating a melt depth of up to 5 mm for irradiation of 300 Wm^{-2} (Figure 6.7). There are several factors that could explain this discrepancy. Firstly, the regolith model is a layer grains of thickness 2-200 μm. Here, the disc experiments used a solid 1 mm thick aluminium disc as analogue regolith. Although aluminium has a much higher thermal conductivity than the model dust grains, the thickness of the layer may have had an effect on the production of melt-water, although it is noted by Losiak et al. (2015) that the thickness of the layer had little effect on the melt depth. It is possible that the disc may

have actually been acting as an insulator due to its thickness, however studies of sediment on ice demonstrate that this insulation effect occurs at thicknesses greater than 1 mm and where there is some contribution of interstitial air to the insulating property, which is not the case with solid aluminium [395] [305]. For the layer of JSC Mars-1 regolith, the mean thickness of the layer was ∼63 μm, which is within the parameters of the model. The regolith was, however, very unevenly distributed, which may be a factor contributing to the discrepancy between the model and the experimental results. Despite this uneven distribution, per the results of the model, it would still be expected to observe some grains in the thinner sections of the regolith layer melting into the ice. It would be beneficial to repeat these experiments with a more evenly distributed layer of regolith analogue of varying thicknesses to probe this parameter.

The melt produced by the JSC Mars-1 regolith mixed with $Mg(ClO_4)_2$ suggests that the presence of perchlorate salts cause or contribute to the melt process. The control experiment with regolith but no $Mg(ClO_4)_2$ did not have any measurable resultant melt, suggesting that the presence of perchlorate salt is an important factor. Fischer et al. (2014) found that when perchlorate salts are in contact with ice, the highly hygroscopic salts deliquesce within minutes, producing liquid brine, despite taking a long time to deliquesce at the same temperature when not in contact with ice [385]. Other deliquescent salts in contact with ice behave similarly, but perchlorates have the added benefit of extremely low eutectic temperatures allowing stability at Martian temperatures [396].

Ice in contact with brine would not have to heat up to 0°C in order to change state, instead only to the eutectic temperature of the brine, provided the deliquescence relative humidity is also reached. Once incorporated into the ice matrix, the regolith would need less energy to heat up sufficiently to melt the ice as less energy would be lost to the atmosphere. The eutectic temperature and concentration of $Mg(ClO_4)_2$ solution is 206 K and 44% wt ([28]). The $Mg(ClO_4)_2$ phase diagram constructed by Chevrier et al. (2009) suggests that at above about -67°C, $Mg(ClO_4)_2$ has a liquid component for concentrations below ∼65% wt. This suggests that at -42°C, the temperature at which the ideal Mars experiments took place, once the perchlorate salt grains have deliquesced, there should be some persistent liquid component until either the water in the brine evaporates away or the temperature drops below -67°C . This brine could have soaked into the regolith grains, some of which did appear to darken throughout the experiment, decreasing its albedo [397–399]. Maturilli et al (2012) found that JSC Mars-1 regolith, when

sufficiently moistened, had its visual albedo reduced from ∼0.13 to ∼0.05 [384]. The soaking of regolith with brine would also increase its thermal conductivity [397]. Both of these factors could contribute to increasing the temperature of the irradiated regolith through more effective absorption and conduction of solar energy, increasing the likelihood of further melting. If liquid-perchlorate soaked regolith becomes incorporated into the ice matrix, the solution would no longer have to contend with the low pressure Martian atmosphere under which liquid water is unstable. Additionally, it should be easier for melt due to solar radiation to occur, assuming relatively clear superjacent ice, as less energy would be lost to the atmosphere. In this case, the regolith now only has to heat surrounding ice to above the eutectic temperature of the perchlorate in order for melt to occur and initiate further downward migration. The hysteresis of crystallisation effect would also allow for the greater longevity of the transient liquid brine environment, as the perchlorate brine would not recrystallise until the relative humidity drops below the efflorescent relative humidity of the salt, which for $Mg(ClO_4)_2$ is ∼19% [166].

6.5.3 Implications for Habitability

The presence of liquid water is essential for life as we know it. The results presented in this chapter show that the presence of $Mg(ClO_4)_2$ salt appears to contribute to the generation of transient liquid water and cause sediment melt-migration under favourable Martian north polar temperature and solar conditions. Though the presence of water is essential, in this case any putative organisms would have to contend with extremely high concentrations of perchlorate, extreme freeze-thaw cycles and temperatures lower than the current known limit for life. Some organisms have been shown to grow in relatively high concentrations of perchlorate solutions [142, 144] and low temperatures can enhance growth in concentrated chloride brines [400]. Putative Martian organisms exposed to high concentrations of perchlorate over long time frames could have adapted to higher concentrations than the limits measured on Earth [144].

This work suggests that under favourable environmental conditions and in the presence of $Mg(ClO_4)_2$ salt, melt could occur on the Martian north polar ice cap. Combined with the ongoing research into unlocking the climate record stored in the NPLD, these results could contribute to the determination of the eligibility of sites for future biosignature-seeking missions. Additionally, biosignatures and

reportedly viable microorganisms have been extracted from ancient terrestrial ice environments, several of which are older than some layers of the Martian north polar layered deposits (NPLD) [59, 357–359]. There are regions where the NPLD are exposed and could be sampled by a craft. If a good understanding of the conditions under which each layer of the NPLD formed can be established, layers that formed during periods of more favourable climate and that have indications of the presence of perchlorate salts could be sampled for biosignatures.

6.5.4 Limitations and Future Work

The experimental protocol and apparatus developed here could be used as a basis for future experiments exploring melt-water formation in Mars and other extraterrestrial ice environments. The experimental apparatus would benefit from the addition of atmospheric pressure and composition control, relative humidity control, and precise and sustained refrigeration. It would be particularly interesting to characterise the behaviour of irradiated perchlorate salts and regolith in contact with ice over a range of temperatures, relative humidities, and pressures in order to systematically understand the role they could play in habitat formation in Martian polar environments.

Air temperature

The chamber in which the experiment took place was not capable of consistent and sustained refrigeration. The air temperature in the chamber during the experiments was therefore close to the ambient temperature of the room. The materials used to maintain the temperature of the ice blocks did cause a drop in the chamber air temperature. However, this was not sufficient to bring the air close to the temperatures of the environments being simulated. In Jepsen et al. (2010) modelling and fieldwork observations showed that surficial sediment sinks at a lower rate than embedded sediment due to losing more heat to the atmosphere - which was colder than the ice - as well as to the shallower, colder ice. This is not the case in the Antarctic condition experiments presented here, where the mean maximum melt rate for the surficial discs ((5.25 ± 0.14) mm hr^{-1}) is greater than for the embedded discs ((3.08 ± 0.14) mm hr^{-1}) . This discrepancy is likely due to the lack of atmospheric refrigeration in the experiment causing heat transfer from the surrounding air to the surficial disc and melt-water. For the regolith & $Mg(ClO_4)_2$ experiments, where only a very small quantity of melt occurred this could have affected the results. As the eutectic point of $Mg(ClO_4)_2$ is -67°C [28, 29], even if the air had been cooled to ideal Martian temperatures, it is likely that liquid brine would have formed anyway. However, it would be prudent to repeat the $Mg(ClO_4)_2$ experiment in an air temperature and relative humidity controlled environment.

Grain Size, Composition and Distribution

In the regolith-perchlorate experiment, the regolith mixture was spread unevenly on the surface of the ice. In future, it would be beneficial to develop a method of evenly depositing the analogue regolith material for more consistent melting. This would have the added benefit of allowing the exploration of the parameter of layer thickness, which is a parameter that could have contributed to the difference between the results reported here and the Losiak et al. (2015) model [44]. In future, smaller regolith grains that are more likely to be deposited in bulk onto the Mars north polar cap could be used - though smaller grains present the challenge of being difficult to handle and distribute under the current method. Although JSC Mars-1 is a spectral analogue, its thermal properties may vary from regolith on the Martian surface. The effect of the composition of regolith grains on melt formation is another parameter that could be explored in future.

Received Flux

This work was limited by the power output of the solar simulator lamp used. Some models suggests that the maximum flux received by the NPRC during periods of high obliquity could be 400 Wm^{-2} [278, 346]. Increasing the received flux could allow the analogue regolith material alone to heat up sufficiently to melt the ice. These experiments could be repeated in future with a more powerful lamp to explore this possibility.

Atmospheric Pressure

These experiments were performed under ambient atmospheric pressure conditions. At lower pressures, the thermal properties of regolith material can be affected [401]. Additionally, heat transfer between regolith material and the atmosphere is lower at Martian pressure due to lower atmospheric density [44]. It would therefore be prudent to perform these experiments under low pressure conditions to more accurately reflect the thermal properties of the system under Martian surface conditions.

The experiments presented in this chapter could not be performed at low pressure due to the use of dry ice as a coolant. At the Mars-relevant temperatures at which these experiments were performed (-74°C and -42°C) the CO_2 would rapidly

sublimate under low pressure conditions [402].

Melt-Water detection

Detection of melt-water was performed by visual inspection of the sample site and by thoroughly examining the site for grains which may have sunk into the ice, particularly in regions where darkening has occurred suggesting liquid has soaked into the grains. This method does not account for the formation of microscopic quantities of water which can form around regolith grains and ice grain boundaries at temperatures of $\sim$-20°C [387]. In soil science, instruments that detect the presence of liquid water in frozen soil are available, but require much higher volumes of soil than the volumes used in this work. If a similar instrument could be acquired or developed for use in the experiments presented in this chapter, the experiments performed with JSC Mars-1 and $Mg(ClO_4)_2$ should be repeated to robustly confirm the presence of liquid brine.

6.6 Conclusions

Although the north polar region of Mars appears highly inhospitable due to the extreme and freezing temperature conditions, the presence of abundant water and the preservation potential of ice make it a potential region of astrobiological interest. With regard to the search for life on Mars it is important to establish likely locations for the discovery of biosignatures, to help determine where future missions should take place. This work investigated a potential aqueous environment on the surface of the Martian north polar residual cap.

A protocol for the irradiation of ice was developed and tested under Antarctic conditions to establish its efficacy. Under Antarctic conditions, abundant melting due to the solar-heating of a black disc took place. Under more typical and ideal Martian north polar summer temperature conditions, no melting took place. When fine-grained JSC Mars-1 regolith was mixed with the highly hygroscopic salt $Mg(ClO_4)_2$ and irradiated under ideal Martian temperature conditions, a small amount of melting took place and grains to sunk into the ice surface.

These findings highlight the inhospitable conditions that any Martian organisms would have to contend with on the north polar cap. The results suggest that even under highly favourable temperature conditions, bulk melt of ice does not occur solely due to solar-heating of low-albedo material. However the presence of perchlorate salt can facilitate the formation of transient liquid water under these conditions. This makes layers of the north polar layered deposits that formed during periods of favourable climate sites of interest for future biosignature seeking missions, particularly if they host perchlorate salts that could have contributed to the generation of liquid water environments.

Chapter 7

Conclusions

The aim of this thesis was to contribute to our understanding of the astrobiological potential of a selection of putative aqueous Martian microenvironments by investigating the formation and lifetime of liquid water and the interactions between water, salts and lithic material in laboratory based analogue environment experiments. The principal results of this thesis are as follows.

- Saturated solutions of salts comprising ions observed on Mars' surface, and binary mixtures of such solutions, produce distinct evaporite structures with different astrobiological implications for potential Martian microenvironments. Interfacial salt crusts have the ability to inhibit evaporation under ambient and low pressure conditions, significantly extending the lifetime of sub-crust liquid brine. Creeping structures can transport micron-sized objects, facilitating putative habitat expansion over small scales. Creeping structures also have the potential to be used as environmental indicators due to their maximum extent being limited at low pressure.
- The reduction in evaporative surface area by the introduction of porous media leads to a reduction in the mass loss rate of a test volume of water compared to the same volume of free water. When saturated with soluble sulphate salts that plug pore openings this inhibitive effect was enhanced, preserving liquid brine within some porous media over several days under current Martian surface pressure conditions.
- The solar heating of low-albedo material alone did not cause measurable ice melt under Martian north polar temperature and solar irradiation

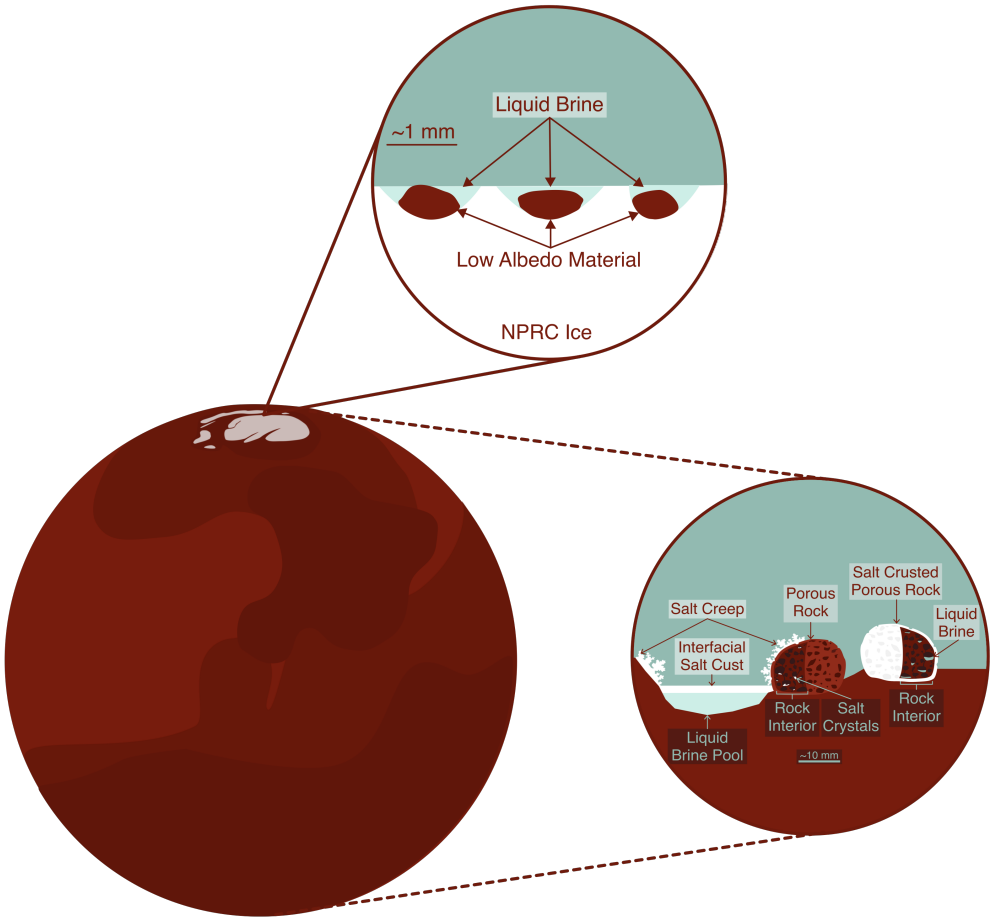

Figure 7.1: Summary Representation of Potential Aqueous Microenvironments on the Surface of Mars. The putative microenvironments discussed in this thesis are represented together in this diagram. The evaporite and rock pore environments discussed in Chapters 4 and 5 respectively are shown in the lower inset. An interfacial salt crust on a shallow brine pool extends the lifetime of the aqueous environment. A rock contains salt crystals within its interior pores, providing a protected environment where biosignatures could be preserved. Habitat-expanding salt creeping structures emerge from the brine pool and from the rock surface. A salt-crusted rock extends the lifetime of liquid brine within it porous interior. The north polar ice-melt microenvironment discussed in Chapter 6 is shown in the upper inset. Solar heated low albedo material associated with deliquescent salt melts into the surface of North Polar Residual Cap ice creating transient liquid brine environments.

conditions. However, the addition of a hygroscopic perchlorate salt to fine-grained regolith material caused downward melt migration of the grains into the ice surface and facilitated small-scale transient liquid water formation.

These results are summarised in Figure 7.1, which represents the potential Martian surface microenvironments discussed in this work. The results show that the presence of salts in high concentrations can influence the habitability of environments by contributing to the formation of liquid water or prolonging its lifetime under extreme conditions relevant to the surface of Mars. This chapter will summarise the key findings of each chapter of this thesis.

7.1 Chapter 4: The Astrobiological Potential of Brine Evaporites

The typical evaporite morphologies of 10 Mars-relevant brines and their binary mixtures were characterised in order to determine what properties of astrobiological interest each evaporite may have. The following general trends were observed. Sulphate brines form interfacial surface crusts that can preserve the sub-crust solution. Chloride brines form creeping structures that rapidly deplete the solution. Perchlorate brines form both crusting and creeping evaporite structures where the crust can temporarily preserve the sub-crust solution but the gradual formation of creeping structures eventually deplete the solution. The evaporite structures formed by binary mixtures of saturated brines generally reflected a combination of the evaporite structures of the constituent brines. A notable exception to this is when Na_2SO_4 is mixed with another high-solubility sulphate salt, resulting in distinctive dendritic creeping structures despite both constituent brines typically producing crusts.

$MgSO_4$, Na_2SO_4, and their binary mixture $MgSO_4$ & Na_2SO_4 were selected to investigate the effect of low pressure on evaporite formation. It was found that $MgSO_4$ formed an interfacial crust that inhibited evaporation effectively. Na_2SO_4 formed a crust that was not effective at preventing evaporation. $MgSO_4$ & Na_2SO_4 did not form the distinctive creeping structure that it formed at ambient pressure, instead forming a crust that was effective at inhibiting evaporation.

$MgSO_4$ was selected to investigate the efficacy of evaporite crusts in inhibiting evaporation from the sub-crust solution and consequently extending liquid water

lifetime at ambient and low pressure. The crust was found to be highly effective at inhibiting evaporation under ambient and low pressure conditions.

The binary mixture of $MgSO_4$ & Na_2SO_4 was selected to investigate whether porous media can facilitate the formation of creeping structures at low pressure, and if so whether pressure affects the extent to which these structures can grow. The introduction of porous media allowed the formation of small creeping structures at low pressure. The maximum extent of the structures formed decreased with decreasing pressure. This suggests that distinctive evaporite structures have the potential to be used as environmental indicators.

The binary mixture of $MgSO_4$ & Na_2SO_4 was also used to explore the potential self-expansion of habitat space. It was found that microspheres could be transported via the salt creeping mechanism, becoming incorporated into the creep structure and transported into rock pore spaces. This shows that brine environments are capable of the transport of analogue microorganisms to potentially new microhabitats with more favourable local conditions for growth and/or preservation.

This chapter showed that diverse Mars-relevant brine evaporites have properties that can improve the conditions for habitability at small scales. These results have implications for the habitability potential of briny environments on Mars as evaporite environments may have been locations of the last vestiges of liquid water as the planet's surface became more hostile.

7.2 Chapter 5: The Lifetime of Liquid Water in Porous Media at Low Pressure

The results presented in this chapter show that the presence of porous media can increase the lifetime of liquid water under ambient and low pressure conditions due to the reduction in surface area through which evaporation can take place. The effect of this lifetime extension lessened with decreasing pressure.

The results in this chapter also highlighted the dependency of mass loss rate on the length of the porous media and the position of the water within the media.

The presence of salts dissolved in water significantly increased the lifetime of liquid water within porous media under present-day Martian pressure conditions

due to the precipitation of pore obstructing salt crystals. This suggests that porous rocks in the presence of crusting salts such as $MgSO_4$, which is abundant on Mars, could be environments of interest for Martian habitat and biosignature-seeking missions.

7.3 Chapter 6: A Potential Aqueous Environment on the Martian North Polar Residual Cap

The results presented in this chapter highlight the challenge of forming liquid water the under extreme low-temperature conditions experienced by the Martian north polar residual cap. A protocol for the production and irradiation of ice blocks wa developed. Under Antarctic temperature conditions, fluid inclusions similar to those observed in terrestrial ice environments, formed through the solar-heating of low-albedo material. However, under typical and ideal Martian polar summer temperatures, no melt occurred via the solar heating of low-albedo material alone. Only when highly deliquescent $Mg(ClO_4)_2$ salt was incorporated into analogue regolith did melting of ice occur under ideal Martian polar temperature conditions. This resulted in a small melt-migration of the regolith material into the ice and presents a potential pathway for transient liquid water formation on the north polar residual cap. This suggests that layers of the north polar layered deposits that formed during periods of favourable climate could be sites of interest for future biosignature seeking missions, particularly if they host perchlorate salts that could have contributed to the generation of liquid water environments.

7.4 Closing Remarks

The results presented here show that, although liquid water is usually unstable under current Martian surface conditions, there are microenvironments where aspects of the extreme conditions experienced on the surface of Mars may be buffered, allowing for the formation or persistence of liquid water.

These results highlight that, despite the challenges high concentrations of salts can pose for living organisms, their presence can contribute to the generation of habitat space and prolong the lifetime of liquid water under some current Mars

surface conditions.

Appendix A

Appendix

A.1 Pure Brines

A.1.1 No Evaporite Macrostructure Formation

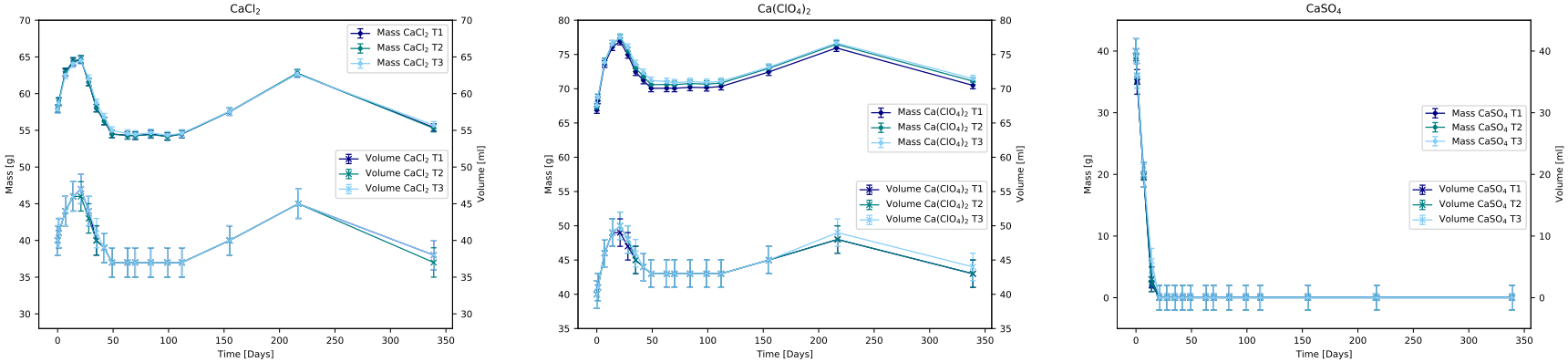

(a) $CaCl_2$ **(b)** $Ca(ClO_4)_2$ **(c)** $CaSO_4$

Figure A.1: Results of Main Evaporite Experiment: Plots of Mass and Bulk Volume of Pure Brines That Did Not Form Evaporite Macrostructures Over 11 Months. Bulk volume refers to the volume of liquid brine and any precipitated salt within the body of the brine.

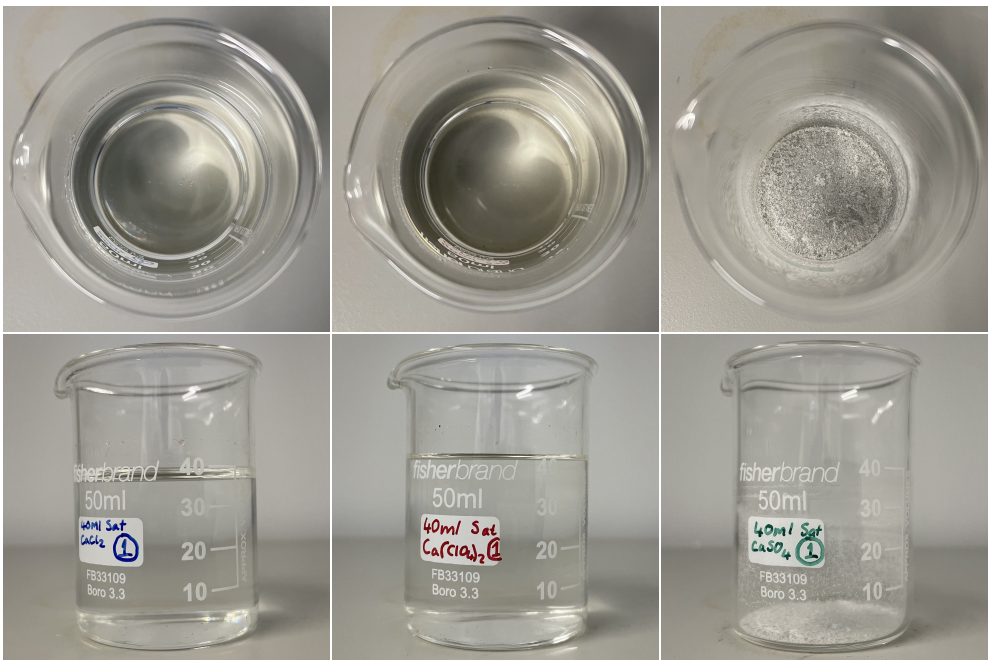

(a) $CaCl_2$ **(b)** $Ca(ClO_4)_2$ **(c)** $CaSO_4$

Figure A.2: Results of Main Evaporite Experiment: Photographs of Pure Brines That Did Not Form Evaporite Macrostructures Over 11 Months. The figures show one example of each solution at the end of the 11 month experimental period. $CaCl_2$ and $Ca(ClO_4)_2$ did not evaporate sufficiently to form evaporite structures. $CaSO_4$ did not form macrostructures due to being highly insoluble.

A.1.2 Crusts

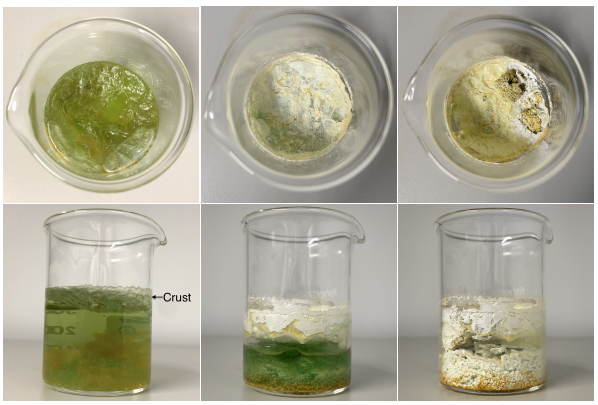

(a) 7 Days **(b)** 112 Days **(c)** 339 Days

Figure A.3: Results of Main Evaporites Experiment: Evaporites Forming From $FeSO_4$ Brine (Sample T3) Over 11 months.

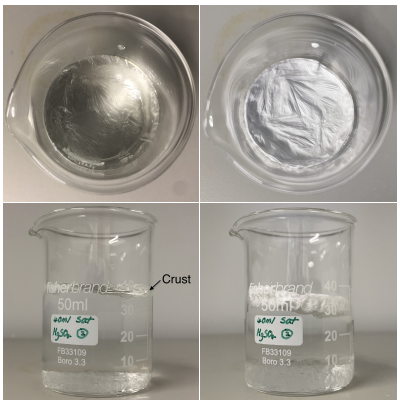

(a) 1 Day **(b)** 339 Days

Figure A.4: Results of Main Evaporites Experiment: Evaporites Forming From $MgSO_4$ Brine (Sample T2) Over 11 months.

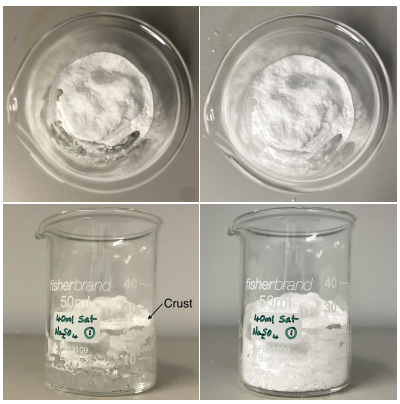

(a) 14 Days **(b)** 49 Days

Figure A.5: Results of Main Evaporites Experiment: Evaporites Forming From Na_2SO_4 Brine (Sample T1) Over 49 days.

A.1.3 Creeping Structures

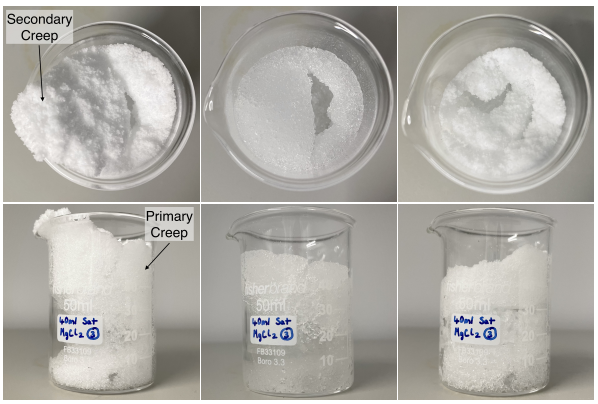

(a) 49 Days **(b)** 216 Days **(c)** 339 Days

Figure A.6: Results of Main Evaporites Experiment: Evaporites Forming From $MgCl_2$ Brine (Sample T3) Over 11 months.

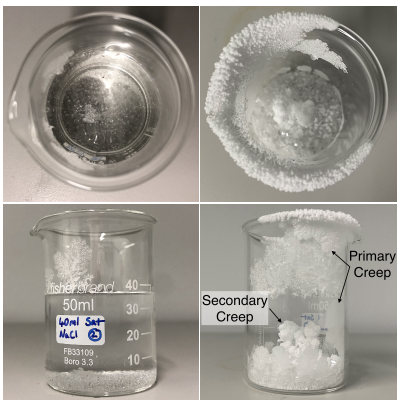

(a) 1 Day **(b)** 28 Days

Figure A.7: Results of Main Evaporites Experiment: Evaporites Forming From NaCl Brine (Sample T2) Over 28 days.

A.1.4 Crusts & Creeping Structures

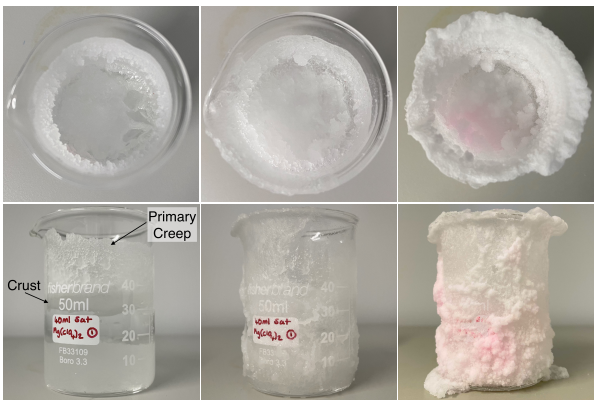

(a) 28 Days **(b)** 216 Days **(c)** 339 Days

Figure A.8: Results of Main Evaporites Experiment: Evaporites Forming From $Mg(ClO_4)_2$ Brine (Sample T1) Over 11 months.

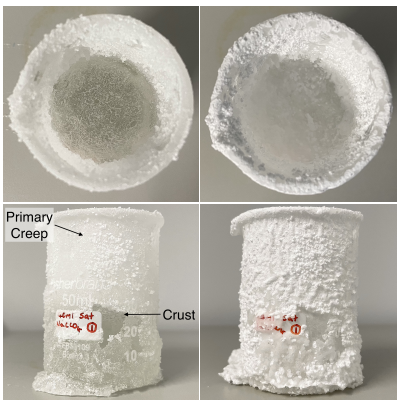

(a) 28 Days **(b)** 339 Days

Figure A.9: Results of Main Evaporites Experiment: Evaporites Forming From $NaClO_4$ Brine (Sample T1) Over 11 months.

A.2 Mixed Brines

A.2.1 Crusts

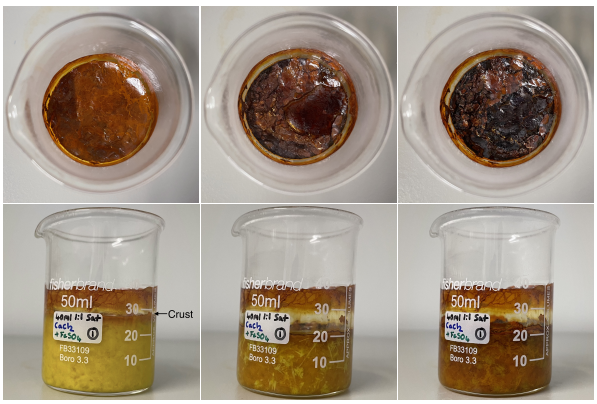

(a) 28 Days **(b)** 216 Days **(c)** 339 Days

Figure A.10: Results of Main Evaporites Experiment: Evaporites Forming From $CaCl_2$ & $FeSO_4$ Brine (Sample T1) Over 11 months.

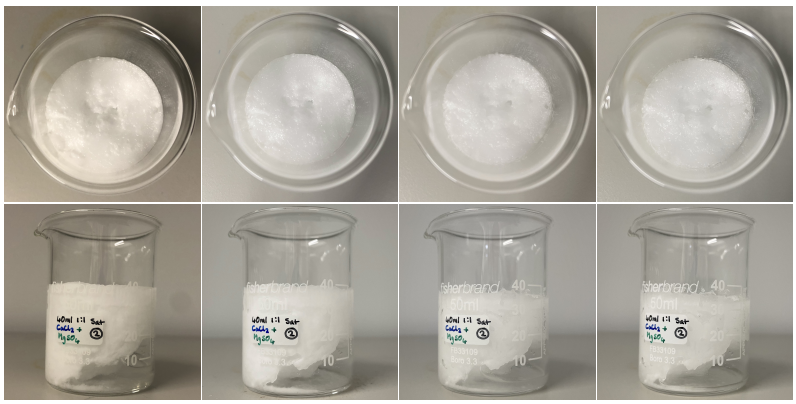

(a) 2 Days **(b)** 21 Day **(c)** 216 Days **(d)** 339 Days

Figure A.11: Results of Main Evaporites Experiment: Evaporites Forming From $CaCl_2$ & $MgSO_4$ Brine (Sample T2) Over 11 months.

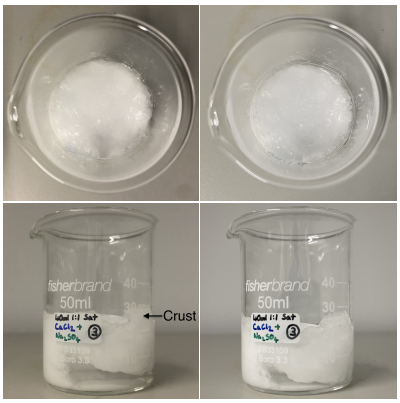

(a) 14 Days **(b)** 339 Days

Figure A.12: Results of Main Evaporites Experiment: Evaporites Forming From $CaCl_2$ & Na_2SO_4 Brine (Sample T3) Over 11 months.

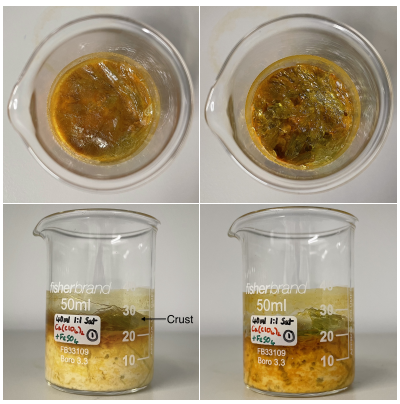

(a) 35 Days **(b)** 339 Days

Figure A.13: Results of Main Evaporites Experiment: Evaporites Forming From $Ca(ClO_4)_2$ & $FeSO_4$ Brine (Sample T1) Over 11 months.

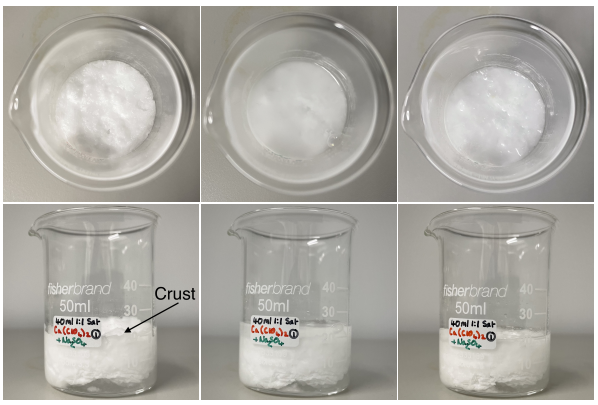

(a) 49 Days **(b)** 216 Days **(c)** 339 Days

Figure A.14: Results of Main Evaporites Experiment: Evaporites Forming From $Ca(ClO_4)_2$ & Na_2SO_4 Brine (Sample T1) Over 11 months.

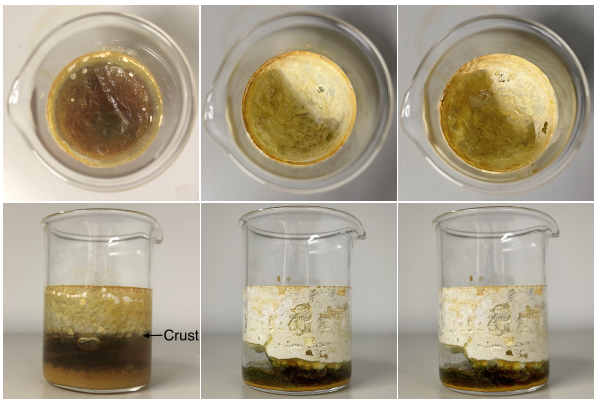

(a) 14 Days **(b)** 216 Days **(c)** 339 Days

Figure A.15: Results of Main Evaporites Experiment: Evaporites Forming From $CaSO_4$ & $FeSO_4$ Brine (Sample T2) Over 11 months.

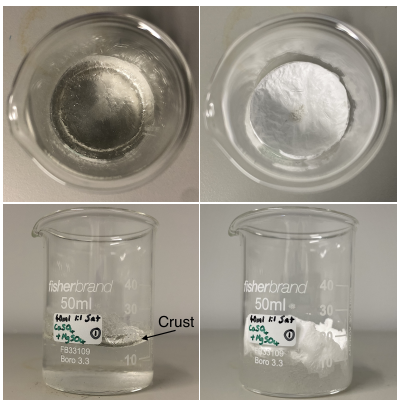

(a) 14 Days **(b)** 339 Days

Figure A.16: Results of Main Evaporites Experiment: Evaporites Forming From $CaSO_4$ & $MgSO_4$ Brine (Sample T1) Over 11 months.



(a) 14 Days **(b)** 63 Days

Figure A.17: Results of Main Evaporites Experiment: Evaporites Forming From $CaSO_4$ & Na_2SO_4 Brine (Sample T2) Over 63 Days.

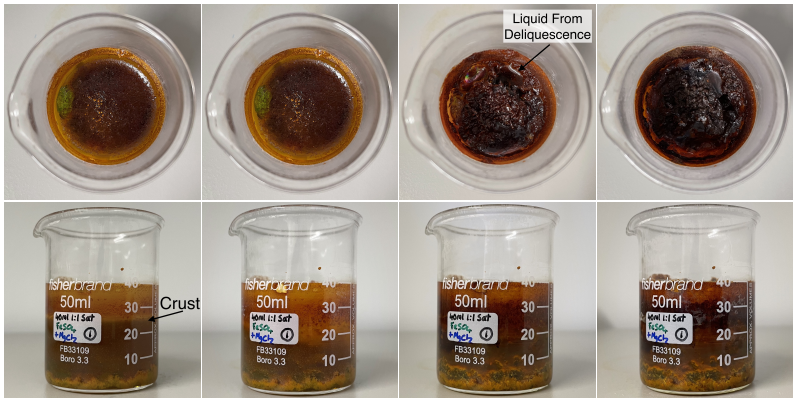

(a) 28 Days **(b)** 49 Days **(c)** 216 Days **(d)** 339 Days

Figure A.18: Results of Main Evaporites Experiment: Evaporites Forming From $FeSO_4$ & $MgCl_2$ Brine (Sample T1) Over 11 months.

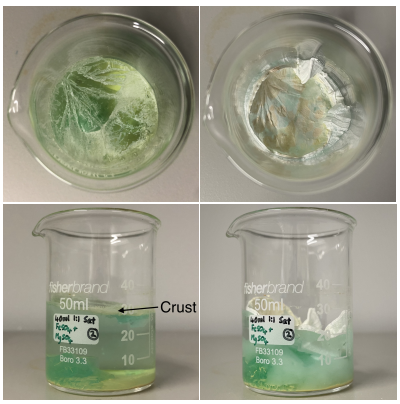

(a) 7 Days **(b)** 339 Days

Figure A.19: Results of Main Evaporites Experiment: Evaporites Forming From $FeSO_4$ & $MgSO_4$ Brine (Sample T2) Over 11 months.

A.2.2 Creeping Structures



(a) 63 Days **(b)** 216 Days **(c)** 339 Days

Figure A.20: Results of Main Evaporites Experiment: Evaporites Forming From $CaSO_4$ & $MgCl_2$ Brine (Sample T2) Over 11 months.

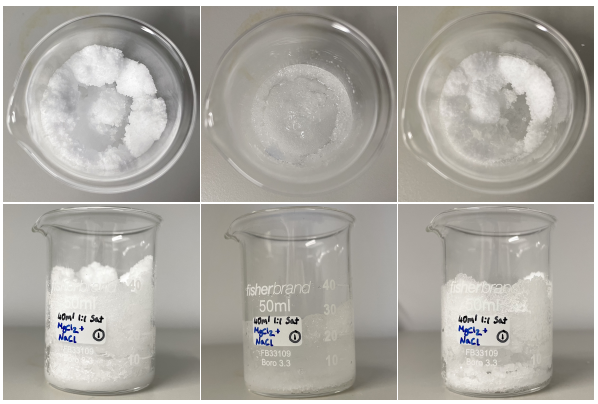

(a) 63 Days **(b)** 216 Days **(c)** 339 Days

Figure A.21: Results of Main Evaporites Experiment: Evaporites Forming From $MgCl_2$ & NaCl Brine (Sample T1) Over 11 months.

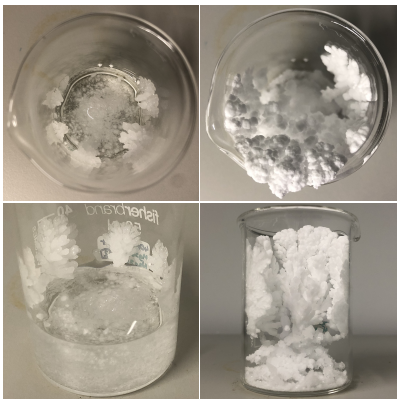

(a) 7 Days **(b)** 21 Days

Figure A.22: Results of Main Evaporites Experiment: Evaporites Forming From $MgSO_4$ & Na_2SO_4 Brine (Sample T2) Over 21 days.

A.2.3 Crusts & Creeping Structures

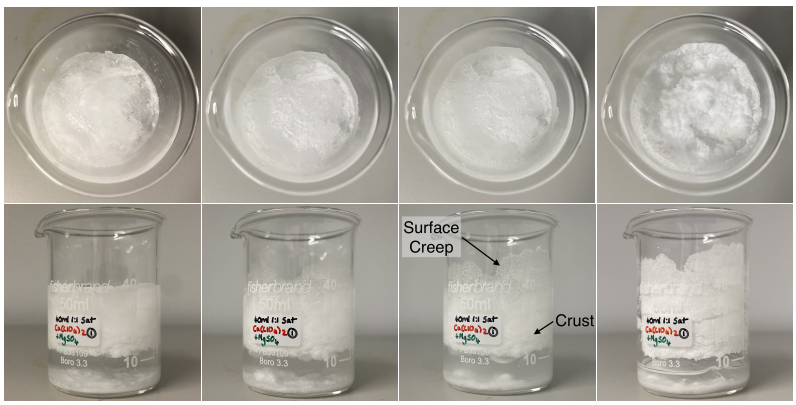

(a) 1 Day **(b)** 21 Days **(c)** 28 Days **(d)** 339 Days

Figure A.23: Results of Main Evaporites Experiment: Evaporites Forming From $Ca(ClO_4)_2$ & $MgSO_4$ Brine (Sample T1) Over 11 months.

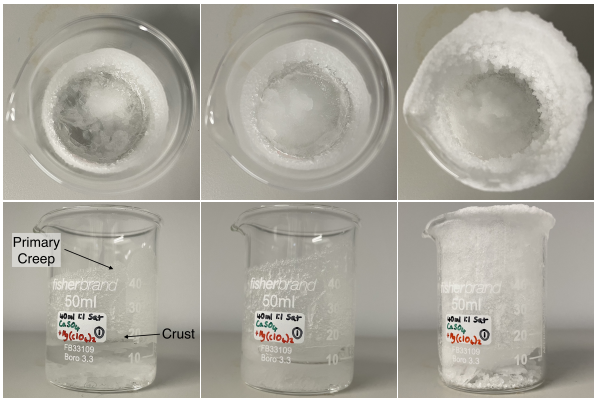

(a) 28 Days **(b)** 216 Days **(c)** 339 Days

Figure A.24: Results of Main Evaporites Experiment: Evaporites Forming From $CaSO_4$ & $Mg(ClO_4)_2$ Brine (Sample T1) Over 11 months.

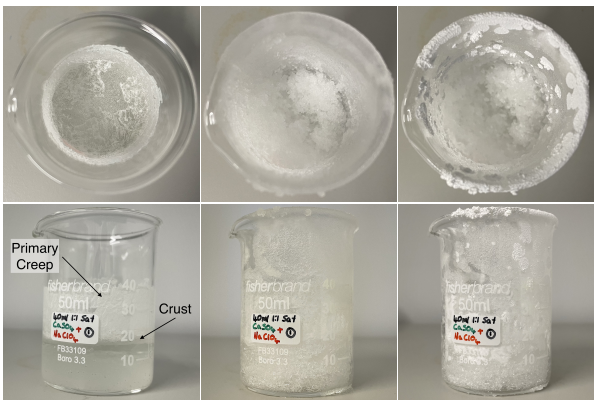

(a) 35 Days **(b)** 216 Days **(c)** 339 Days

Figure A.25: Results of Main Evaporites Experiment: Evaporites Forming From $CaSO_4$ & $NaClO_4$ Brine (Sample T1) Over 11 Months.



(a) 28 Days **(b)** 216 Days **(c)** 339 Days

Figure A.26: Results of Main Evaporites Experiment: Evaporites Forming From $FeSO_4$ & $Mg(ClO_4)_2$ Brine (Sample T1) Over 11 months.

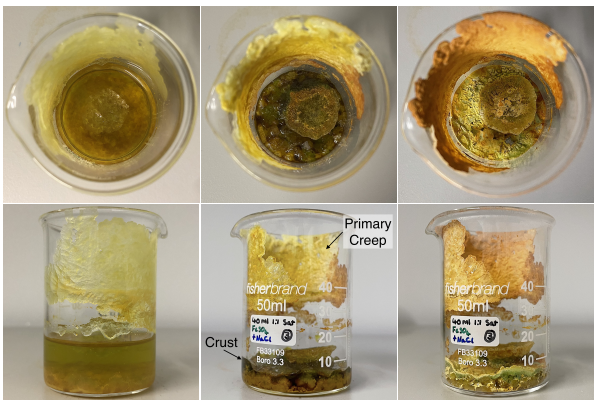

(a) 14 Days **(b)** 28 Days **(c)** 339 Days

Figure A.27: Results of Main Evaporites Experiment: Evaporites Forming From $FeSO_4$ & NaCl Brine (Sample T3) Over 11 months.

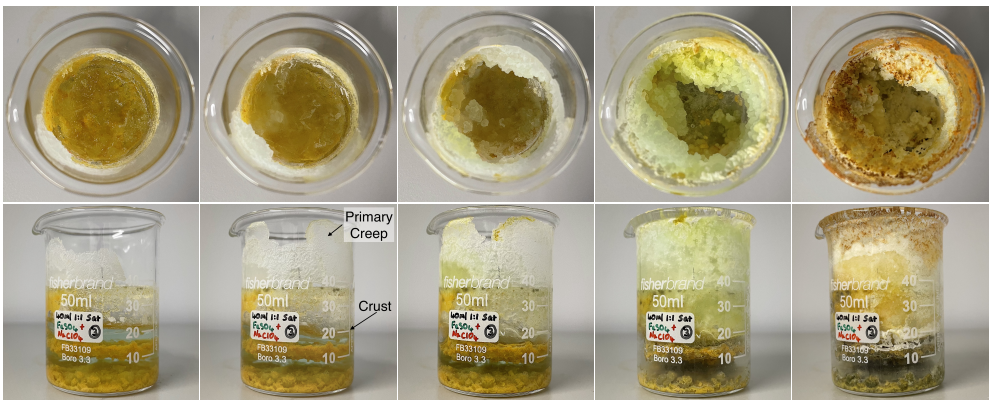

(a) 28 Days **(b)** 35 Days **(c)** 42 Days **(d)** 63 Days **(e)** 339 Days

Figure A.28: Results of Main Evaporites Experiment: Evaporites Forming From $FeSO_4$ & $NaClO_4$ Brine (Sample T3) Over 11 months.

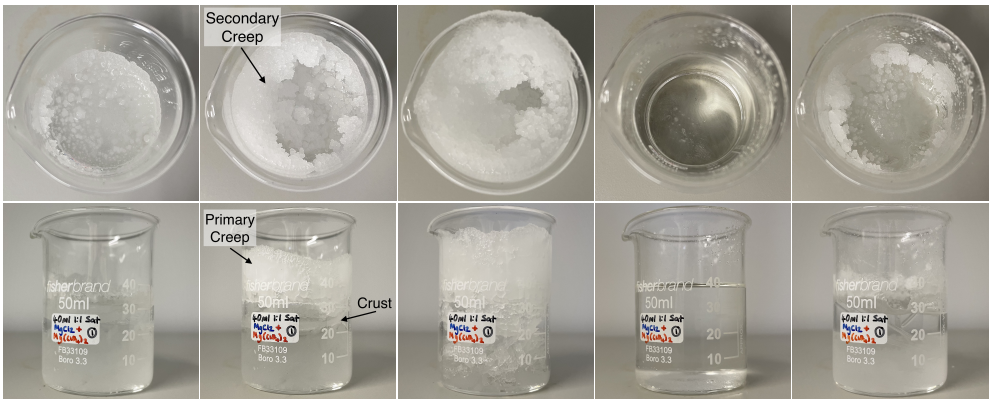

(a) 49 Days **(b)** 63 Days **(c)** 99 Days **(d)** 216 Days **(e)** 339 Days

Figure A.29: Results of Main Evaporites Experiment: Evaporites Forming From $MgCl_2$ & $Mg(ClO_4)_2$ Brine (Sample T1) Over 11 months.

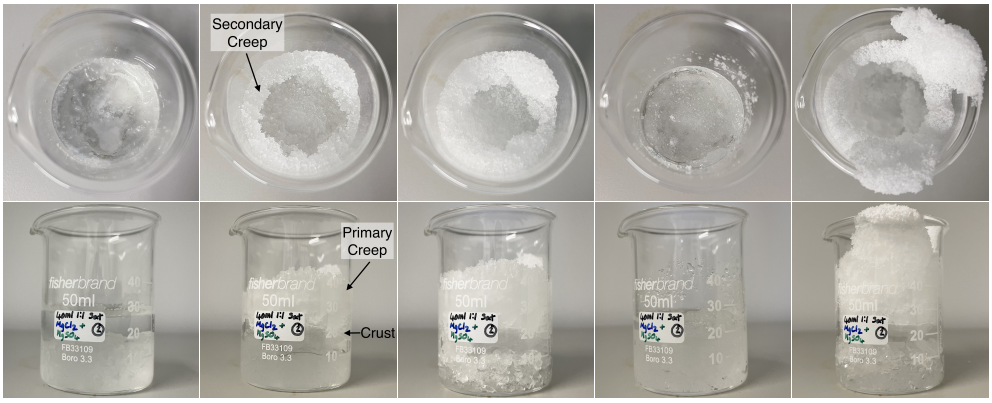

(a) 35 Days **(b)** 63 Days **(c)** 84 Days **(d)** 216 Days **(e)** 339 Days

Figure A.30: Results of Main Evaporites Experiment: Evaporites Forming From $MgCl_2$ & $MgSO_4$ Brine (Sample T2) Over 11 months.

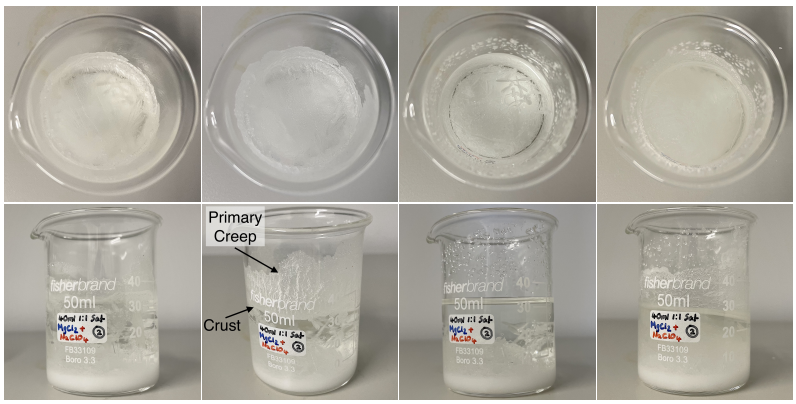

(a) 35 Days **(b)** 122 Days **(c)** 216 Days **(d)** 339 Days

Figure A.31: Results of Main Evaporites Experiment: Evaporites Forming From $MgCl_2$ & $NaClO_4$ Brine (Sample T2) Over 11 months.

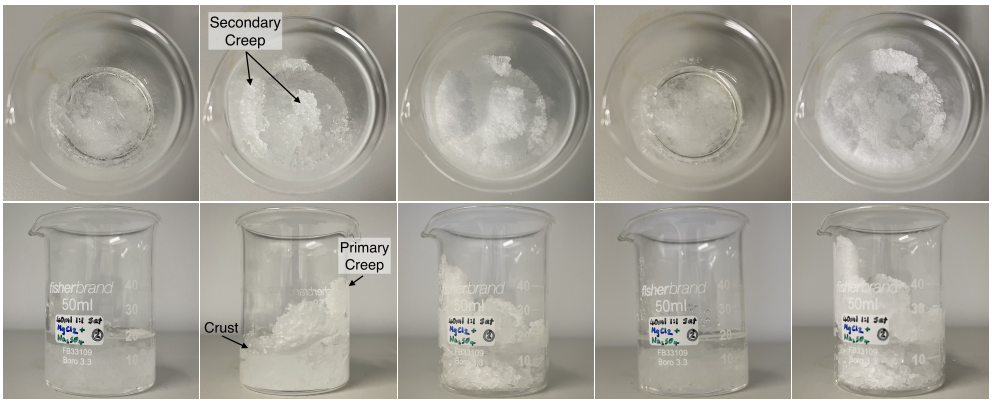

(a) 35 Days **(b)** 49 Days **(c)** 112 Days **(d)** 216 Days **(e)** 339 Days

Figure A.32: Results of Main Evaporites Experiment: Evaporites Forming From $MgCl_2$ & Na_2SO_4 Brine (Sample T2) Over 11 months.

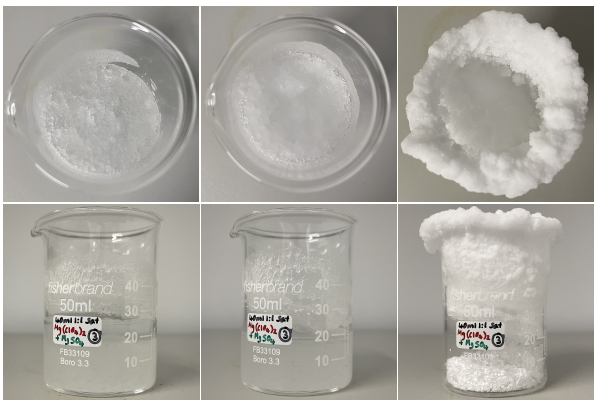

(a) 21 Days **(b)** 155 Days **(c)** 339 Days

Figure A.33: Results of Main Evaporites Experiment: Evaporites Forming From $Mg(ClO_4)_2$ & $MgSO_4$ Brine (Sample T3) Over 11 months.

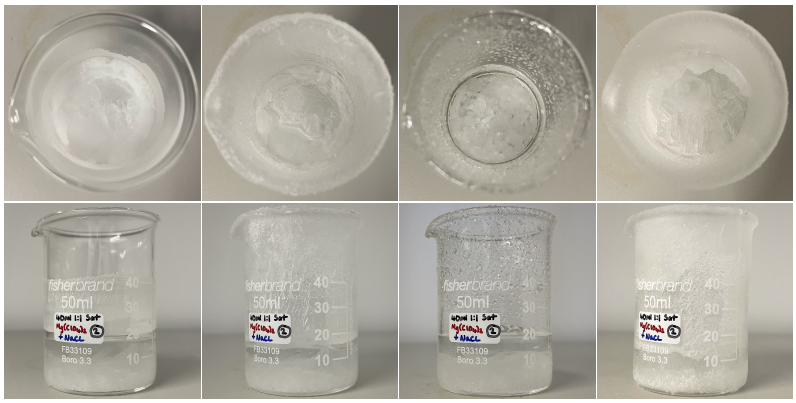

(a) 35 Days **(b)** 155 Days **(c)** 216 Days **(d)** 339 Days

Figure A.34: Results of Main Evaporites Experiment: Evaporites Forming From $Mg(ClO_4)_2$ & NaCl Brine (Sample T2) Over 11 months.

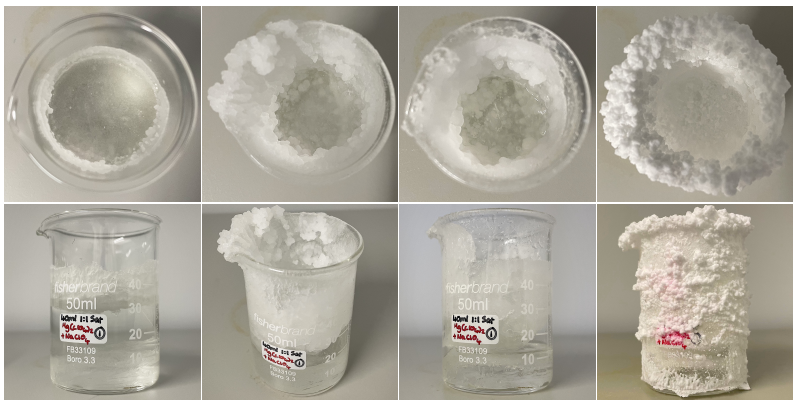

(a) 35 Days **(b)** 155 Days **(c)** 216 Days **(d)** 339 Days

Figure A.35: Results of Main Evaporites Experiment: Evaporites Forming From $Mg(ClO_4)_2$ & $NaClO_4$ Brine (Sample T1) Over 11 months.

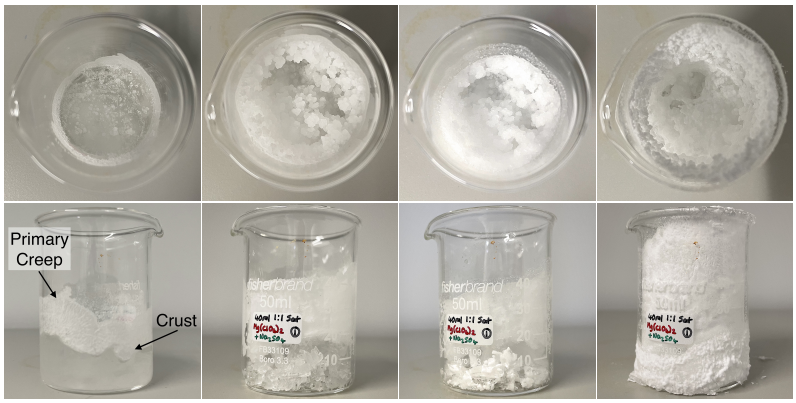

(a) 35 Days **(b)** 70 Days **(c)** 216 Days **(d)** 339 Days

Figure A.36: Results of Main Evaporites Experiment: Evaporites Forming From $Mg(ClO_4)_2$ & Na_2SO_4 Brine (Sample T1) Over 11 months.

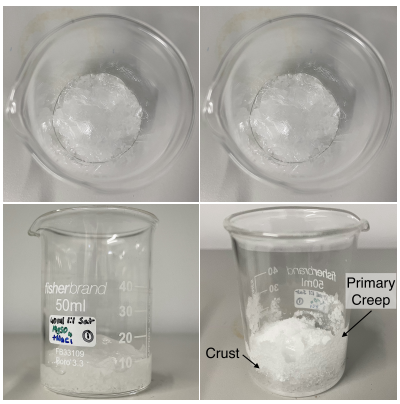

(a) 21 Days **(b)** 35 Days

Figure A.37: Results of Main Evaporites Experiment: Evaporites Forming From $MgSO_4$ & NaCl Brine (Sample T1) Over 35 days.

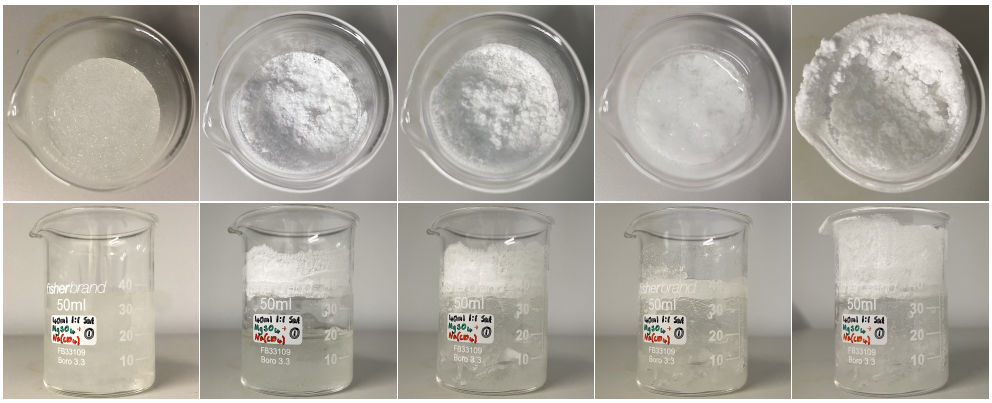

(a) Days **(b)** 63 Days **(c)** 112 Days **(d)** 216 Days **(e)** 339 Days

Figure A.38: Results of Main Evaporites Experiment: Evaporites Forming From $MgSO_4$ & $NaClO_4$ Brine (Sample T1) Over 11 months.

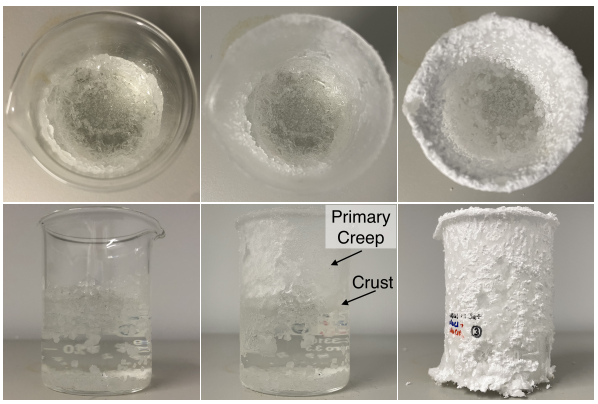

(a) 7 Days **(b)** 21 Days **(c)** 339 Days

Figure A.39: Results of Main Evaporites Experiment: Evaporites Forming From NaCl & $NaClO_4$ Brine (Sample T3) Over 11 months.

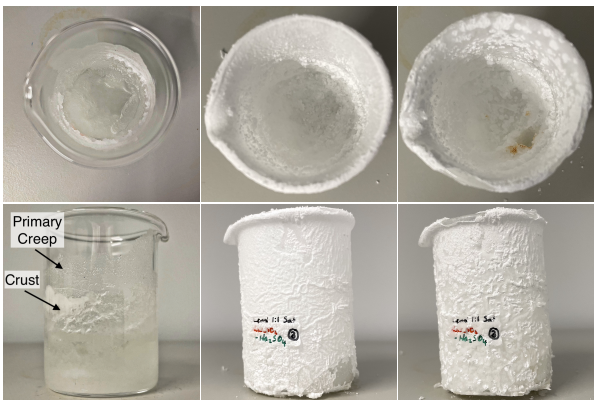

(a) 28 Days **(b)** 155 Days **(c)** 339 Days

Figure A.40: Results of Main Evaporites Experiment: Evaporites Forming From $NaClO_4$ & Na_2SO_4 Brine (Sample T3) Over 11 months.

Bibliography

[1] W. Herschel, "On the Remarkable Appearances at the Polar Regions of the Planet Mars, the Inclination of Its Axis, the Position of Its Poles, and Its Spheroidical Figure; With a Few Hints Relating to Its Real Diameter and Atmosphere." *Philosophical Transactions of the Royal Society of London*, vol. 74, no. 1784, 1784.

[2] P. Lowell, *Mars*. The Riverside Press, Cambridge, 1895.

[3] G. M. Martínez and N. O. Renno, "Water and brines on mars: Current evidence and implications for MSL," *Space Science Reviews*, vol. 175, no. 1-4, pp. 29–51, 2013.

[4] B. L. Ehlmann, J. F. Mustard, S. L. Murchie, J.-p. Bibring, A. Meunier, A. A. Fraeman, and Y. Langevin, "Subsurface water and clay mineral formation during the early history of Mars," *Nature*, pp. 53–60, 2011.

[5] R. P. Irwin, A. D. Howard, R. A. Craddock, and J. M. Moore, "An intense terminal epoch of widespread fluvial activity on early Mars : 2 . Increased runoff and paleolake development," *Journal of Geophysical Research*, vol. 110, pp. 1–38, 2005.

[6] A. D. Howard, J. M. Moore, and P. Rossman, "An intense terminal epoch of widespread fluvial activity on early Mars : 1 . Valley network incision and associated deposits," *Journal of Geophysical Research*, vol. 110, pp. 1–20, 2005.

[7] K. P. Harrison and R. E. Grimm, "Groundwater-controlled valley networks and the decline of surface runoff on early Mars," *Journal of Geophysical Research*, vol. 110, pp. 1–17, 2005.

[8] T. D. Glotch and P. R. Christensen, "Geologic and mineralogic mapping of Aram Chaos : Evidence for a water-rich history," *Journal of Geophysical Research*, vol. 110, pp. 1–21, 2005.

[9] A. S. McEwan, C. J. Hansen, W. A. Delamere, E. Eliason, and K. E. Herkenhoff, "A closer look at Water-Related Geologic Activity on Mars," *Science*, vol. 37, pp. 1706–1710, 2007.

[10] H. Hiesinger and J. W. H. Iii, "Topography and morphology of the Argyre Basin , Mars : implications for its geologic and hydrologic history," *Planetary and Space Science*, vol. 50, pp. 939–981, 2002.

[11] J. I. Lunine, J. Chambers, A. Morbidelli, and L. A. Leshin, "The origin of water on Mars," *Icarus*, vol. 165, pp. 1–8, 2003.

[12] J.-p. Bibring, Y. Langevin, J. F. Mustard, and R. Arvidson, "Global Mineralogical and Aqueous Mars History Derived from OMEGA / Mars Express Data," *Science*, vol. 312, no. 5772, pp. 400–405, 2006.

[13] F. Salese, G. D. Achille, A. Neesemann, G. G. Ori, and E. Hauber, "Hydrological and sedimentary analyses of well-preserved paleofluvial-paleolacustrine systems at Moa Valles, Mars," *Journal of Geophysical Research: Planets*, vol. 121, no. 2, pp. 194–232, 2016.

[14] N. J. Tosca, A. H. Knoll, and S. M. McLennan, "Water Activity and the Challenge for Life on Early Mars," *Science*, vol. 320, no. May, pp. 1204–1208, 2008.

[15] B. M. Jakosky, "Atmospheric loss to space and the history of water on mars," *Annual Review of Earth and Planetary Sciences*, vol. 49, pp. 71–93, 2021.

[16] S. A. Wilson, A. M. Morgan, A. D. Howard, and J. A. Grant, "The Global Distribution of Craters With Alluvial Fans and Deltas on Mars," *Geophysical Research Letters*, vol. 48, pp. 1–10, 2021.

[17] A. M. Morgan, S. A. Wilson, and A. D. Howard, "The global distribution and morphologic characteristics of fan-shaped sedimentary landforms on Mars," *Icarus*, vol. 385, 2022. [Online]. Available: https://doi.org/10.1016/j.icarus.2022.115137

[18] B. M. Hynek, M. Beach, and M. R. T. Hoke, "Updated global map of Martian valley networks and implications for climate and hydrologic processes," *Journal of Geophysical Research*, vol. 115, no. November 2009, 2010.

[19] A. Howard, J. M. Moore, and P. I. Rossman, "An intense terminal epoch of widespread fluvial activity on early Mars : 1 . Valley network incision and associated deposits," *Journal of Geophysical Research*, vol. 110, 2005.

[20] A. S. McEwen, L. Ojha, C. M. Dundas, S. S. Mattson, S. Byrne, J. J. Wray, S. C. Cull, S. L. Murchie, N. Thomas, and V. C. Gulick, "Seasonal flows on warm Martian slopes," *Science*, vol. 333, no. 6043, pp. 740–743, 2011.

[21] N. O. Rennó, B. J. Bos, D. Catling, B. C. Clark, L. Drube, D. Fisher, W. Goetz, S. F. Hviid, H. U. Keller, J. F. Kok, S. P. Kounaves, K. Leer, M. Lemmon, M. B. Madsen, W. J. Markiewicz, J. Marshall, C. McKay, M. Mehta, M. Smith, M. P. Zorzano, P. H. Smith, C. Stoker, and S. M.

Young, "Possible physical and thermodynamical evidence for liquid water at the Phoenix landing site," *Journal of Geophysical Research E: Planets*, vol. 114, no. 10, pp. 1–11, 2009.

[22] E. Fischer, G. Martínez, and N. Rennó, "Formation and Persistence of Brine on Mars: Experimental Simulations throughout the Diurnal Cycle at the Phoenix Landing Site," *Astrobiology*, vol. 16, no. 12, pp. 937–948, 2016.

[23] E. G. Rivera-Valentín, V. F. Chevrier, A. Soto, G. Martínez, and N. A. Author, "DISTRIBUTION AND HABITABILITY OF (META)STABLE BRINES ON PRESENT-DAY MARS," *Nature Astronomy*, vol. 4, pp. 756–761, 2020. [Online]. Available: https://pds-geosciences.wustl.edu/missions/phoenix/martinez.htm

[24] E. Fischer, G. M. Martínez, H. M. Elliott, and N. O. Rennõ, "Experimental evidence for the formation of liquid saline water on Mars," *Geophysical Research Letters*, vol. 41, no. 13, pp. 4456–4462, 7 2014.

[25] L. Ojha, M. B. Wilhelm, S. L. Murchie, A. S. Mcewen, J. J. Wray, J. Hanley, M. Massé, and M. Chojnacki, "Spectral evidence for hydrated salts in recurring slope lineae on Mars," *Nature Geoscience*, vol. 8, pp. 829–833, 2015. [Online]. Available: www.nature.com/naturegeoscience

[26] F. J. Martín-Torres, M.-P. Zorzano, P. Valentín-Serrano, A.-M. Harri, M. Genzer, O. Kemppinen, E. G. Rivera-Valentin, I. Jun, J. Wray, M. Bo Madsen, W. Goetz, A. S. McEwen, C. Hardgrove, N. Renno, V. F. Chevrier, M. Mischna, R. Navarro-González, J. Martínez-Frías, P. Conrad, T. McConnochie, C. Cockell, G. Berger, A. R. Vasavada, D. Sumner, and D. Vaniman, "Transient liquid water and water activity at Gale crater on Mars," *Nature Geoscience*, vol. 8, no. 5, pp. 357–361, 5 2015. [Online]. Available: http://www.nature.com/articles/ngeo2412

[27] R. V. Gough, V. F. Chevrier, K. J. Baustian, M. E. Wise, and M. A. Tolbert, "Laboratory studies of perchlorate phase transitions: Support for metastable aqueous perchlorate solutions on Mars," *Earth and Planetary Science Letters*, vol. 312, no. 3-4, pp. 371–377, 2011. [Online]. Available: http://dx.doi.org/10.1016/j.epsl.2011.10.026

[28] V. F. Chevrier, J. Hanley, and T. S. Altheide, "Stability of perchlorate hydrates and their liquid solutions at the Phoenix landing site, mars," *Geophysical Research Letters*, vol. 36, no. 10, pp. 1–6, 2009.

[29] O. N. Pestova, L. A. Myund, M. K. Khripun, and A. V. Prigaro, "Polythermal Study of the Systems Mg(ClO4)2-H20," *Russian Journal of Applied Chemistry*, vol. 78, no. 3, pp. 409–413, 2005.

[30] F. Schmidt, F. Andrieu, F. Costard, M. Kocifaj, and A. G. Meresescu, "Formation of recurring slope lineae on Mars by rarefied gas-triggered granular flows," *Nature Geoscience*, vol. 10, no. 4, pp. 270–273, 2017.

[31] C. M. Dundas, A. S. McEwen, M. Chojnacki, M. P. Milazzo, S. Byrne, J. N. McElwaine, and A. Urso, "Granular flows at recurring slope lineae on Mars indicate a limited role for liquid water," *Nature Geoscience*, vol. 10, no. 12, pp. 903–907, 2017. [Online]. Available: http://dx.doi.org/10.1038/s41561-017-0012-5

[32] S. E. Ackiss and J. J. Wray, "Occurrences of possible hydrated sulfates in the southern high latitudes of Mars," *Icarus*, vol. 243, pp. 311–324, 2014. [Online]. Available: http://dx.doi.org/10.1016/j.icarus.2014.08.016

[33] W. C. Feldman, M. T. Mellon, S. Maurice, T. H. Prettyman, J. W. Carey, D. T. Vaniman, D. L. Bish, C. I. Fialips, S. J. Chipera, J. S. Kargel, R. C. Elphic, H. O. Funsten, D. J. Lawrence, and R. L. Tokar, "Hydrated states of MgSO4 at equatorial latiudes on Mars," *Geophysical Research Letters*, vol. 31, no. 16, pp. 3–6, 2004.

[34] A. Gendrin, N. Mangold, J.-P. Bibring, Y. Langevin, B. Gondet, F. Poulet, G. Bonello, C. Quantin, J. Mustard, R. Arvidson, and S. Lemouélic, "Sulfates in Martian Layered Terrains: The OMEGA/Mars Express View," *Science*, vol. 307, no. 5715, pp. 1587–1591, 2005. [Online]. Available: http://science.sciencemag.org/

[35] J.-P. Bibring, Y. Langevin, A. Gendrin, B. Gondet, and F. Poulet, "Mars Surface Diversity as Revealed by the OMEGA/Mars Express Observations," *J. Geophys. Res*, vol. 307, p. 75, 2005.

[36] E. L. Scheller, B. L. Ehlmann, R. Hu, D. J. Adams, and Y. L. Yung, "Long-term drying of Mars by sequestration of ocean-scale volumes of water in the crust," *Science*, vol. 372, no. 6537, pp. 56–62, 2021.

[37] J. F. Mustard, *Sequestration of volatiles in the Martian crust through hydrated minerals: A significant planetary reservoir of water.* Elsevier Inc., 2018, no. 2015. [Online]. Available: http://dx.doi.org/10.1016/B978-0-12-804191-8.00008-8

[38] D. W. Mittlefehldt, R. Gellert, S. vanBommel, R. E. Arvidson, J. W. Ashley, B. C. Clark, L. S. Crumpler, W. H. Farrand, M. P. Golombek, J. A. Grant, R. V. Morris, and C. Schröder, "Geology and Geochemistry of Noachian Bedrock and Alteration Events, Meridiani Planum, Mars: MER Opportunity Observations," *Journal of Geophysical Research: Planets*, vol. 126, no. 9, 2021.

[39] E. L. Scheller, J. R. Hollis, E. L. Cardarelli, A. Steele, L. W. Beegle, R. Bhartia, P. Conrad, K. Uckert, S. Sharma, B. L. Ehlmann, W. J. Abbey, S. A. Asher, and K. C. Benison, "Aqueous alteration processes in Jezero crater, Mars — implications for organic geochemistry," *Science*, vol. 378, pp. 1105–1110, 2022.

[40] K. A. Farley, K. M. Stack, D. L. Shuster, B. H. N. Horgan, J. A. Hurowitz, J. D. Tarnas, J. I. Simon, V. Z. Sun, E. L. Scheller, K. R. Moore, S. M. McLennan, P. M. Vasconcelos, R. C. Wiens, A. H. Treiman, L. E. Mayhew, O. Beyssac, T. V. Kizovski, N. J. Tosca, K. H. Williford, L. S. Crumpler, L. W. Beegle, J. F. Bell, B. L. Ehlmann, Y. Liu, J. N. Maki, M. E. Schmidt, A. C. Allwood, H. E. F. Amundsen, R. Bhartia, T. Bosak, A. J. Brown, B. C. Clark, A. Cousin, O. Forni, T. S. J. Gabriel, Y. Goreva, S. Gupta, S.-E. Hamran, C. D. K. Herd, K. Hickman-Lewis, J. R. Johnson, L. C. Kah, P. B. Kelemen, K. B. Kinch, L. Mandon, N. Mangold, C. Quantin-Nataf, M. S. Rice, P. S. Russell, S. Sharma, S. Siljeström, A. Steele, R. Sullivan, M. Wadhwa, B. P. Weiss, A. J. Williams, B. V. Wogsland, P. A. Willis, T. A. Acosta-Maeda, P. Beck, K. Benzerara, S. Bernard, A. S. Burton, E. L. Cardarelli, B. Chide, E. Clavé, E. A. Cloutis, B. A. Cohen, A. D. Czaja, V. Debaille, E. Dehouck, A. G. Fairén, D. T. Flannery, S. Z. Fleron, T. Fouchet, J. Frydenvang, B. J. Garczynski, E. F. Gibbons, E. M. Hausrath, A. G. Hayes, J. Henneke, J. L. Jørgensen, E. M. Kelly, J. Lasue, S. Le Mouélic, J. M. Madariaga, S. Maurice, M. Merusi, P.-Y. Meslin, S. M. Milkovich, C. C. Million, R. C. Moeller, J. I. Núñez, A. M. Ollila, G. Paar, D. A. Paige, D. A. K. Pedersen, P. Pilleri, C. Pilorget, P. C. Pinet, J. W. Rice, C. Royer, V. Sautter, M. Schulte, M. A. Sephton, S. K. Sharma, S. F. Sholes, N. Spanovich, M. St. Clair, C. D. Tate, K. Uckert, S. J. VanBommel, A. G. Yanchilina, and M.-P. Zorzano, "Aqueously altered igneous rocks sampled on the floor of Jezero crater, Mars," *Science*, vol. 377, no. 6614, 2022.

[41] N. Stein, J. P. Grotzinger, J. Schieber, N. Mangold, B. Hallet, H. Newsom, K. M. Stack, J. A. Berger, L. Thompson, K. L. Siebach, A. Cousin, S. L. Mouélic, M. Minitti, D. Sumner, C. Fedo, C. House, S. Gupta, A. R. Vasavada, R. Gellert, R. C. Wiens, J. Frydenvang, O. Forni, P. Meslin, V. Payré, and E. Dehouck, "Desiccation cracks provide evidence of lake drying on Mars, Sutton Island member, Murray formation, Gale Crater," *Geology*, vol. 46, no. 6, pp. 515–518, 2018.

[42] M. R. El-Maarry, A. Pommerol, and N. Thomas, "Analysis of polygonal cracking patterns in chloride-bearing terrains on Mars: Indicators of ancient playa settings," *Journal of Geophysical Research: Planets*, vol. 118, no. 11, pp. 2263–2278, 2013.

[43] M. S. Phillips, M. Mcinenly, M. H. Hofmann, N. W. Hinman, K. Warren-rhodes, E. G. Rivera-Valenitn, and N. A. Cabrol, "Salt Constructs in Paleo-Lake Basins as High-Priority Astrobiology Targets," *Remote Sensing*, vol. 15, no. 314, 2023.

[44] A. Losiak, L. Czechowski, and M. A. Velbel, "Ephemeral liquid water at the surface of the martian North Polar Residual Cap: Results of numerical modelling," *Icarus*, vol. 262, pp. 131–139, 12 2015.

[45] K. L. Tanaka, J. A. P. Rodriguez, J. A. Skinner, M. C. Bourke, C. M.

Fortezzo, K. E. Herkenhoff, E. J. Kolb, and C. H. Okubo, "North polar region of Mars: Advances in stratigraphy, structure, and erosional modification," *Icarus*, vol. 196, no. 2, pp. 318–358, 8 2008.

[46] Y. Langevin, F. Poulet, J. P. Bibring, and B. Gondet, "Sulfates in the north polar region of Mars detected by OMEGA/Mars express," *Science*, vol. 307, no. 5715, pp. 1584–1586, 2005.

[47] M. T. Mellon, R. E. Arvidson, H. G. Sizemore, M. L. Searls, D. L. Blaney, S. Cull, M. H. Hecht, T. L. Heet, H. U. Keller, M. T. Lemmon, W. J. Markiewicz, D. W. Ming, R. V. Morris, W. T. Pike, and A. P. Zent, "Ground ice at the Phoenix landing site: Stability state and origin," *Journal of Geophysical Research: Planets*, vol. 114, no. 12, pp. 1–15, 2009.

[48] S. Piqueux, J. Buz, C. S. Edwards, J. L. Bandfield, A. Kleinböhl, D. M. Kass, and P. O. Hayne, "Widespread Shallow Water Ice on Mars at High Latitudesand Midlatitudes," *Geophysical Research Letters*, vol. 46, no. 24, pp. 14 290–14 298, 2019.

[49] H. D. Smith, M. Baqué, A. G. Duncan, C. R. Lloyd, C. P. McKay, and D. Billi, "Comparative analysis of cyanobacteria inhabiting rocks with different light transmittance in the Mojave Desert: A Mars terrestrial analogue," *International Journal of Astrobiology*, vol. 13, no. 3, pp. 271–277, 2014.

[50] H. Dong, J. A. Rech, H. Jiang, H. Sun, and B. J. Buck, "Endolithnic cyanobacteria in soil gypsum: Occurences in Atacama (Chile), Mojave (United States), and Al-Jafr Basin (Jordan) Deserts," *Journal of Geophysical Research: Biogeosciences*, vol. 112, no. 2, 2007.

[51] J. C. Priscu, C. H. Fritsen, E. E. Adams, S. J. Giovannoni, H. W. Paerl, C. P. McKay, P. T. Doran, D. A. Gordon, B. D. Lanoil, J. L. Pinckney, C. H. Fristen, E. E. Adams, S. J. Giovannoni, H. W. Paerl, C. P. McKay, P. T. Doran, D. A. Gordon, B. D. Lanoil, and J. L. Pinckney, "Perennial antarctic lake ice: An oasis for life in a polar desert," *Science*, vol. 280, no. 5372, pp. 2095–2098, 1998.

[52] W. Vincent, *Microbial Ecosystems of Antarctica*. Cambridge University Press, 1988.

[53] E. I. Friedmann and R. Ocampo, "Endolithic blue-green algae in the dry valleys: Primary producers in the Antarctic desert ecosystem," *Science*, vol. 193, no. 4259, pp. 1247–1249, 1976.

[54] J. Cook, A. Edwards, N. Takeuchi, and T. Irvine-Fynn, "Cryoconite: The dark biological secret of the cryosphere," *Progress in Physical Geography*, vol. 40, no. 1, pp. 66–111, 2016.

[55] J. J. Walker and N. R. Pace, "Phylogenetic Composition of Rocky Mountain Endolithic Microbial Ecosystems," *Applied and Environmental Microbiology*, vol. 73, no. 11, pp. 3497–3504, 2007. [Online]. Available: http://aem.asm.org/

[56] R. A. Bell, "Endolithic Algae of Semi-Desert Sandstones: Systematic, Biogeographic and Ecophysiologic Investigations," Ph.D. dissertation, Arizona State University, 1986.

[57] R. J. Palmer and E. I. Friedmann, "Water relations and photosynthesis in the cryptoendolithic microbial habitat of hot and cold deserts," *Microbial Ecology*, vol. 19, no. 1, pp. 111–118, 1990.

[58] R. H. Vreeland, W. D. Rosenzweig, and D. W. Powers, "Isolation of a 250 million-year-old halotolerant bacterium from a primary salt crystal," *Nature*, vol. 407, no. 6806, pp. 897–900, 2000.

[59] S. Abyzov, "Microorganisms in the Antarctic Ice," in *Antarctic Microbiology*, E. Friedmann, Ed. Wiley, 1993.

[60] D. C. Zhang, A. Brouchkov, G. Griva, F. Schinner, and R. Margesin, "Isolation and characterization of bacteria from ancient Siberian permafrost sediment," *Biology*, vol. 2, no. 1, pp. 85–106, 2013.

[61] V. I. Miteva and J. E. Brenchley, "Detection and Isolation of Ultrasmall Microorganisms from a 120,000-Year-Old Greenland Glacier Ice Core," *Applied and Environmental Microbiology*, vol. 71, no. 12, pp. 7806–7818, 2005.

[62] M. Ivarsson, H. Drake, A. Neubeck, T. Sallstedt, S. Bengtson, N. M. Roberts, and B. Rasmussen, "The fossil record of igneous rock," *Earth-Science Reviews*, vol. 210, p. 103342, 11 2020.

[63] M. Sakakibara, H. Sugawara, T. Tsuji, and M. Ikehara, "Filamentous microbial fossil from low-grade metamorphosed basalt in northern Chichibu belt, central Shikoku, Japan," *Planetary and Space Science*, vol. 95, pp. 84–93, 2014. [Online]. Available: http://dx.doi.org/10.1016/j.pss.2013.05.008

[64] S. Mcmahon, "Earth's earliest and deepest purported fossils may be iron-mineralized chemical gardens," *Proc. R. Soc. B*, vol. 286, 2019.

[65] S. Mcmahon and S. F. Jordan, "A fundamental limit to the search for the oldest," *Nature Ecology & Evolution*, vol. 6, pp. 832–834, 2022.

[66] C. S. Cockell, T. Bush, C. Bryce, S. Direito, M. Fox-Powell, J. P. Harrison, H. Lammer, H. Landenmark, J. Martin-Torres, N. Nicholson, L. Noack, J. O'Malley-James, S. J. Payler, A. Rushby, T. Samuels, P. Schwendner, J. Wadsworth, and M. P. Zorzano, "Habitability: A Review," *Astrobiology*, vol. 16, no. 1, pp. 89–117, 2016.

[67] C. Cockell, *Astrobiology: Understanding Life in The Universe.* John Wiley & Sons, Ltd, 2015.

[68] Microsoft Corporation, "Microsoft Excel," 2023.

[69] G. Van Rossum and F. L. Drake, *Python 3 Reference Manual.* Create Space, 2009.

[70] J. Taylor, *An Introduction to Error Analysis: The Study of Uncertainties in Physical Measurements*, 2nd ed., A. McGuire, Ed. University Science Books, 1997.

[71] B. C. Clark and D. C. Van Hart, "The salts of Mars," *Icarus*, vol. 45, no. 2, pp. 370–378, 2 1981. [Online]. Available: https://www.sciencedirect.com/science/article/pii/0019103581900415

[72] B. C. Clark, A. Baird, H. Rose, K. Keil, A. Castro, W. Kelliher, C. Rowe, and P. Evans, "Inorganic Analyses of Martian Surface Samples at the Viking Landing Sites," *Science*, vol. 194, pp. 1283–1288, 1976.

[73] A. K. Baird, P. Toulmin, B. C. Clark, H. J. Rose, K. Keil, R. P. Christian, and J. L. Gooding, "Mineralogic and petrologic implications of Viking geochemical results from Mars: Interim report," *Science*, vol. 194, no. 4271, pp. 1288–1293, 1976.

[74] B. Clark, "Chemical and physical Microenvironments at the Viking Landing Sites," *Journal of Molecular Evolution*, vol. 14, pp. 13–31, 1979.

[75] M. H. Hecht, S. P. Kounaves, R. C. Quinn, S. J. West, S. M. M. Young, D. W. Ming, D. C. Catling, B. C. Clark, W. V. Boynton, J. Hoffman, L. P. DeFlores, K. Gospodinova, J. Kapit, and P. H. Smith, "Detection of Perchlorate and the Soluble Chemistry of Martian Soil at the Phoenix Lander Site," *Science*, vol. 325, no. 5936, pp. 64–67, 2009.

[76] N. Mangold, A. Gendrin, B. Gondet, S. Lemouelic, C. Quantin, V. Ansan, J.-P. Bibring, Y. Langevin, P. Masson, and G. Neukum, "Spectral and geological study of the sulfate-rich region of West Candor Chasma, Mars," *Icarus*, vol. 194, pp. 519–543, 2008. [Online]. Available: www.elsevier.com/locate/icarus

[77] M. M. Osterloo, V. E. Hamilton, J. L. Bandfield, T. D. Glotch, A. M. Baldridge, P. R. Christensen, L. L. Tornabene, and F. S. Anderson, "Chloride Bearing Materials in the Southern Highlands of Mars," *Science*, vol. 319, no. March, pp. 1651–1654, 2008.

[78] W. Rapin, B. L. Ehlmann, G. Dromart, J. Schieber, N. H. Thomas, W. W. Fischer, V. K. Fox, N. T. Stein, M. Nachon, B. C. Clark, L. C. Kah, L. Thompson, H. A. Meyer, T. S. Gabriel, C. Hardgrove, N. Mangold, F. Rivera-Hernandez, R. C. Wiens, and A. R. Vasavada, "An interval of high salinity in ancient Gale crater lake on Mars," *Nature Geoscience*, vol. 12, no. 11, pp. 889–895, 11 2019.

[79] I. Friedmann, Y. Lipkin, and R. Ocampo-Paus, "Desert Algae of the Negev (Israel)," *Phycologia*, vol. 6, no. 4, pp. 185–200, 1967.

[80] E. I. Friedmann and M. Galun, "Desert Algae, Lichens, and Fungi," in *Desert Biology*. ACADEMIC PRESS, INC., 1974, vol. 6, pp. 165–212. [Online]. Available: http://dx.doi.org/10.1016/B978-0-12-135902-7.50011-X

[81] R. H. Vreeland, J. Jones, A. Monson, W. D. Rosenzweig, T. K. Lowenstein, M. Timofeeff, C. Satterfield, B. C. Cho, J. S. Park, A. Wallace, and W. D. Grant, "Isolation of live cretaceous (121-112 million years old) halophilic Archaea from primary salt crystals," *Geomicrobiology Journal*, vol. 24, no. 3-4, pp. 275–282, 2007.

[82] L. J. Rothschild, "Earth analogs for Martian life. Microbes in evaporites, a new model system for life on Mars," *Icarus*, vol. 88, no. 1, pp. 246–260, 1990.

[83] C. Pontefract, T. F. Zhu, V. K. Walker, H. Hepburn, C. Lui, M. T. Zuber, and G. Ruvkun, "Microbial Diversity in a Hypersaline Sulfate Lake: A Terrestrial Analog of Ancient Mars," *Frontiers in Microbiology*, vol. 8, no. 1, p. 1819, 2017.

[84] H. M. Sapers, J. Ronholm, I. Raymond-Bouchard, R. Comrey, G. R. Osinski, and L. G. Whyte, "Biological characterization of microenvironments in a hypersaline cold spring mars analog," *Frontiers in Microbiology*, vol. 8, no. DEC, 12 2017.

[85] J. D. Crisler, F. Chen, B. C. Clark, and M. A. Schneegurt, "Cultivation and characterization of the bacterial assemblage of epsomic Basque Lake, BC," *Antonie van Leeuwenhoek, International Journal of General and Molecular Microbiology*, vol. 112, no. 7, pp. 1105–1119, 2019. [Online]. Available: https://doi.org/10.1007/s10482-019-01244-0

[86] M. G. Fox-Powell and C. S. Cockell, "Building a geochemical view of microbial salt tolerance: Halophilic adaptation of Marinococcus in a natural magnesium sulfate brine," *Frontiers in Microbiology*, vol. 9, no. APR, pp. 1–10, 2018.

[87] L. Steinle, K. Knittel, N. Felber, C. Casalino, G. De Lange, C. Tessarolo, A. Stadnitskaia, J. S. Sinninghe Damsté, J. Zopfi, M. F. Lehmann, T. Treude, and H. Niemann, "Life on the edge: Active microbial communities in the Kryos MgCl2-brine basin at very low water activity," *ISME Journal*, vol. 12, no. 6, pp. 1414–1426, 2018.

[88] E. Zaikova, K. C. Benison, M. R. Mormile, and S. S. Johnson, "Microbial communities and their predicted metabolic functions in a desiccating acid salt lake," *Extremophiles*, vol. 22, no. 3, pp. 367–379, 2018. [Online]. Available: https://doi.org/10.1007/s00792-018-1000-4

[89] J. M. McGonigle, J. A. Bernau, B. B. Bowen, and W. J. Brazelton, "Robust Archaeal and Bacterial Communities Inhabit Shallow Subsurface Sediments of the Bonneville Salt Flats," *mSphere*, vol. 4, no. 4, 8 2019.

[90] A. B. Martin-Cuadrado, E. Senel, M. Martínez-García, A. Cifuentes, F. Santos, C. Almansa, M. Moreno-Paz, Y. Blanco, M. García-Villadangos, M. G. del Cura, M. E. Sanz-Montero, J. P. Rodríguez-Aranda, R. Rosselló-Móra, J. Antón, and V. Parro, "Prokaryotic and viral community of the sulfate-rich crust from Peñahueca ephemeral lake, an astrobiology analogue," *Environmental Microbiology*, vol. 21, no. 10, pp. 3577–3600, 2019.

[91] F. Gómez, B. Cavalazzi, N. Rodríguez, R. Amils, G. G. Ori, K. Olsson-Francis, C. Escudero, J. M. Martínez, and H. Miruts, "Ultra-small microorganisms in the polyextreme conditions of the Dallol volcano, Northern Afar, Ethiopia," *Scientific Reports*, vol. 9, no. 1, pp. 1–9, 2019.

[92] B. R. Kilmer, T. C. Eberl, B. Cunderla, F. Chen, B. C. Clark, and M. A. Schneegurt, "Molecular and phenetic characterization of the bacterial assemblage of hot lake, wa, an environment with high concentrations of magnesium sulphate, and its relevance to Mars," *International Journal of Astrobiology*, vol. 13, no. 1, pp. 69–80, 2014.

[93] G. Meyer, M. Morrow, O. Wyss, T. Berg, and J. Littlepage, "Antarctica: The Microbiology of an Unfrozen Saline Pond," *Science*, vol. 138, pp. 1103–1104, 1962.

[94] B. Siegel, G. McMurty, S. Siegel, J. Chen, and P. LaRock, "Life in the calcium chloride environment of Don Juan Pond, Antarctica," *Nature*, vol. 280, no. 20, pp. 828–829, 1979.

[95] K. A. Hughes and B. Lawley, "A novel Antarctic microbial endolithic community within gypsum crusts," *Environmental Microbiology*, vol. 5, no. 7, pp. 555–565, 2003.

[96] J. D. Clarke, "Antiquity of aridity in the Chilean Atacama Desert," *Geomorphology*, vol. 73, no. 1-2, pp. 101–114, 2006.

[97] G. Michalski, J. K. Böhlke, and M. Thiemens, "Long term atmospheric deposition as the source of nitrate and other salts in the Atacama Desert, Chile: New evidence from mass-independent oxygen isotopic compositions," *Geochimica et Cosmochimica Acta*, vol. 68, no. 20, pp. 4023–4038, 2004.

[98] J. Flahaut, M. Martinot, J. L. Bishop, G. R. Davies, and N. J. Potts, "Remote sensing and in situ mineralogic survey of the Chilean salars: An analog to Mars evaporate deposits?" *Icarus*, vol. 282, pp. 152–173, 2017.

[99] D. C. Catling, M. W. Claire, K. J. Zahnle, R. C. Quinn, B. C. Clark, M. H. Hecht, and S. Kounaves, "Atmospheric origins of perchlorate on mars and in

the atacama," *Journal of Geophysical Research E: Planets*, vol. 115, no. 1, pp. 1–15, 2010.

[100] R. R. Cordero, G. Seckmeyer, A. Damiani, S. Riechelmann, J. Rayas, F. Labbe, and D. Laroze, "The world's highest levels of surface UV," *Photochemical and Photobiological Sciences*, vol. 13, no. 1, pp. 70–81, 2014.

[101] R. R. Cordero, A. Damiani, J. Jorquera, E. Sepúlveda, M. Caballero, S. Fernandez, S. Feron, P. J. Llanillo, J. Carrasco, D. Laroze, and F. Labbe, "Ultraviolet radiation in the Atacama Desert," *Antonie van Leeuwenhoek, International Journal of General and Molecular Microbiology*, vol. 111, no. 8, pp. 1301–1313, 2018.

[102] R. Navarro-González, F. A. Rainey, P. Molina, D. R. Bagaley, B. J. Hollen, J. De La Rosa, A. M. Small, R. C. Quinn, F. J. Grunthaner, L. Cáceres, B. Gomez-Silva, and C. P. McKay, "Mars-Like Soils in the Atacama Desert, Chile, and the Dry Limit of Microbial Life," *Science*, vol. 302, no. 5647, pp. 1018–1021, 11 2003. [Online]. Available: http://science.sciencemag.org/

[103] K. M. Finstad, A. J. Probst, B. C. Thomas, G. L. Andersen, C. Demergasso, A. Echeverría, R. G. Amundson, and J. F. Banfield, "Microbial Community Structure and the Persistence of Cyanobacterial Populations in Salt Crusts of the Hyperarid Atacama Desert from Genome-Resolved Metagenomics," *Frontiers in Microbiology*, vol. 8, no. 1435, 2017. [Online]. Available: www.frontiersin.org

[104] J. Wierzchos, C. Ascaso, and C. P. McKay, "Endolithic cyanobacteria in halite rocks from the hyperarid core of the Atacama Desert," *Astrobiology*, vol. 6, no. 3, pp. 415–422, 2006.

[105] J. Wierzchos, B. Camara, A. De Los Ríos, and A. F. Davila, "Microbial colonization of Ca-sulfate crusts in the hyperarid core of the Atacama Desert : implications for the search for life on Mars," *Geobiology*, vol. 9, pp. 44–60, 2011.

[106] J. E. Hallsworth, "Microbial unknowns at the saline limits for life," *Nature Ecology and Evolution*, vol. 3, no. 11, pp. 1503–1504, 2019. [Online]. Available: http://dx.doi.org/10.1038/s41559-019-1021-0

[107] J. Belilla, D. Moreira, L. Jardillier, G. Reboul, K. Benzerara, J. M. López-García, P. Bertolino, A. I. López-Archilla, and P. López-García, "Hyperdiverse archaea near life limits at the polyextreme geothermal Dallol area," *Nature Ecology and Evolution*, vol. 3, no. 11, pp. 1552–1561, 2019. [Online]. Available: http://dx.doi.org/10.1038/s41559-019-1005-0

[108] B. Cavalazzi and S. Filippidou, "Microbial Survival and Adaptation in Extreme Terrestrial Environments—The Case of the Dallol Geothermal Area in Ethiopia," in *Planet Formation and Panspermia: New Prospects for the Movement of Life through Space*, 2021, pp. 93–117.

[109] B. Cavalazzi, R. Barbieri, F. Gómez, B. Capaccioni, K. Olsson-Francis, M. Pondrelli, A. P. Rossi, K. Hickman-Lewis, A. Agangi, G. Gasparotto, M. Glamoclija, G. G. Ori, N. Rodriguez, and M. Hagos, "The Dallol Geothermal Area, Northern Afar (Ethiopia) - An Exceptional Planetary Field Analog on Earth," *Astrobiology*, vol. 19, no. 4, pp. 553–578, 2019.

[110] E. Kotopoulou, A. Delgado Huertas, J. M. Garcia-Ruiz, J. M. Dominguez-Vera, J. M. Lopez-Garcia, I. Guerra-Tschuschke, and F. Rull, "A Polyextreme Hydrothermal System Controlled by Iron: The Case of Dallol at the Afar Triangle," *ACS Earth and Space Chemistry*, vol. 3, no. 1, pp. 90–99, 2019.

[111] C. P. Mckay, J. C. Rask, A. M. Detweiler, B. M. Bebout, R. Craig Everroad, J. Z. Lee, J. P. Chanton, M. H. Mayer, A. A. L. Caraballo, B. Kapili, M. Al-Awar, and A. Al-Farraj, "An Unusual Inverted Saline Microbial Mat Community in an Interdune Sabkha in the Rub' al Khali (the Empty Quarter), United Arab Emirates," *PLoS ONE*, vol. 11, no. 3, 2016.

[112] P. Forti, "Chemical deposits in evaporite caves: An overview," *International Journal of Speleology*, vol. 46, no. 2, pp. 109–135, 2017.

[113] J. De Waele, C. Carbone, L. Sanna, M. Vattano, E. Galli, F. Sauro, and P. Forti, "Secondary minerals from salt caves in the Atacama Desert (Chile): A hyperarid and hypersaline environment with potential analogies to the Martian subsurface," *International Journal of Speleology*, vol. 46, no. 1, pp. 51–66, 2017.

[114] J. R. Gat and Y. Levy, "Isotope hydrology of inland sabkhas in the Bardawil area, Sinai," *Limnology and Oceanography*, vol. 23, no. 5, pp. 841–850, 1978.

[115] P. M. Driessen and R. Schoorl, "Mineralogy And Morphology Of Salt Efflorescences On Saline Soils In The Great Konya Basin, Turkey," *Journal of Soil Science*, vol. 24, no. 4, pp. 436–442, 1973.

[116] E. Malek, G. E. Bingham, and G. D. Mccurdy, "Evapotranspiration From The Margin And Moist Playa Of A Closed Desert Valley," Utah State University, Tech. Rep., 1990.

[117] A. F. Davila, I. Hawes, C. Ascaso, and J. Wierzchos, "Salt deliquescence drives photosynthesis in the hyperarid Atacama Desert," *Environmental Microbiology Reports*, vol. 5, no. 4, pp. 583–587, 8 2013.

[118] C. S. Cockell and J. A. Raven, "Zones of photosynthetic potential on Mars and the early Earth," *Icarus*, vol. 169, no. 2, pp. 300–310, 2004.

[119] A. Oren, M. Kuhl, and U. Karsten, "An endoevaporitic microbial mat within a gypsum crust: zonation of phototrophs, photopigments, and light penetration," *MARINE ECOLOGY PROGRESS SERIES*, vol. 128, pp. 151–159, 1995.

[120] C. F. Norton and W. D. Grant, "Survival of Halobacteria Within Fluid Inclusions in Salt Crystals," *Journal of General Microbiology*, vol. 134, pp. 1365–1366, 1988.

[121] C. F. Norton, T. J. McGenity, and W. D. Grant, "Archaeal halophiles (halobacteria) from two British salt mines," *Journal of General Microbiology*, vol. 139, no. 5, pp. 1077–1081, 1993.

[122] H. Stan-Lotter, T. J. McGenity, A. Legat, E. B. Denner, K. Glaser, K. O. Stetter, and G. Wanner, "Very similar strains of Halococcus salifodinae are found in geographically separated Permo-Triassic salt deposits," *Microbiology*, vol. 145, no. 12, pp. 3565–3574, 1999.

[123] B. A. Schubert, T. K. Lowenstein, and M. N. Timofeeff, "Microscopic identification of prokaryotes in modern and ancient halite, Saline Valley and Death Valley, California," *Astrobiology*, vol. 9, no. 5, pp. 467–482, 2009.

[124] B. A. Schubert, T. K. Lowenstein, M. N. Timofeeff, and M. A. Parker, "Halophilic archaea cultured from ancient halite, Death Valley, California," *Environmental Microbiology*, vol. 12, no. 2, pp. 440–454, 2010.

[125] T. J. McGenity, R. T. Gemmell, W. D. Grant, and H. Stan-Lotter, "Origins of halophilic microorganisms in ancient salt deposits," *Environmental Microbiology*, vol. 2, no. 3, pp. 243–250, 2000.

[126] C. L. Satterfield, T. K. Lowenstein, R. H. Vreeland, W. D. Rosenzweig, and D. W. Powers, "New evidence for 250 Ma age of halotolerant bacterium from a Permian salt crystal," *Geology*, vol. 33, no. 4, pp. 265–268, 2005.

[127] S. A. Bowden, R. Wilson, C. Taylor, J. M. Cooper, and J. Parnell, "The extraction of intracrystalline biomarkers and other organic compounds from sulphate minerals using a microfluidic format - A feasibility study for remote fossil-life detection using a microfluidic H-cell," *International Journal of Astrobiology*, vol. 6, no. 1, pp. 27–36, 2007.

[128] T. K. Lowenstein, B. A. Schubert, and M. N. Timofeeff, "Microbial communities in fluid inclusions and long-term survival in halite," *GSA TODAY*, vol. 21, no. 1, pp. 4–9, 2011.

[129] M. Nachon, N. Mangold, O. Forni, L. C. Kah, A. Cousin, R. C. Wiens, R. Anderson, D. Blaney, J. G. Blank, F. Calef, S. M. Clegg, C. Fabre, M. R. Fisk, O. Gasnault, J. P. Grotzinger, R. Kronyak, N. L. Lanza, J. Lasue, L. L. Deit, S. L. Mouélic, S. Maurice, P. Y. Meslin, D. Z. Oehler, V. Payré, W. Rapin, S. Schröder, K. Stack, and D. Sumner, "Chemistry of diagenetic features analyzed by ChemCam at Pahrump Hills, Gale crater, Mars," *Icarus*, vol. 281, pp. 121–136, 1 2017.

[130] L. C. Kah, R. Kronyak, J. V. Beek, M. Nachon, N. Mangold, L. Thompson, R. Wiens, J. Grotzinger, M. Minitti, J. Shieber, D. Oehler, P. Scienc, M. Space, S. Systems, S. Diego, N. Brunswick, and L. Alamos, "Diagenetic Crystal Clusters and Dendrites, Lower Mount Sharp, Gale Crater." *46th Lunar and Planetary Science Conference (2015)*, no. March, pp. 1–2, 2015.

[131] M. J. Qazi, H. Salim, C. A. W. Doorman, E. Jambon-Puillet, and N. Shahidzadeh, "Salt creeping as a self-amplifying crystallization process," *Science Advances*, vol. 5, no. 12, p. eaax1853, 2019.

[132] B. E. Roger Washburn, "The Creeping of Solutions," *J. Phys. Chem.*, vol. 31, no. 8, pp. 1246–1248, 1927. [Online]. Available: https://pubs.acs.org/sharingguidelines

[133] H. T., H. C. Martin, and L. Brewer, "The Creeping of Saturated Salt Solutions," *The Journal of Physical Chemistry*, no. 1935, pp. 439–452, 1936.

[134] W. J. Van Enckevort and J. H. Los, "On the creeping of saturated salt solutions," *Crystal Growth and Design*, vol. 13, no. 5, pp. 1838–1848, 2013.

[135] D. Hurle, Ed., *Handbook of Crystal Growth 2*. Amsterdam: North Holland, 1993.

[136] R. Hienonen and R. Lahtinen, *Corrosion and climatic effects in electronics*. VTT Publications, 2007, no. 626.

[137] C. Lepinay, A. Mihajlovski, S. Touron, D. Seyer, F. Bousta, and P. Di Martino, "Bacterial diversity associated with saline efflorescences damaging the walls of a French decorated prehistoric cave registered as a World Cultural Heritage Site," *International Biodeterioration and Biodegradation*, vol. 130, no. April, pp. 55–64, 2018. [Online]. Available: https://doi.org/10.1016/j.ibiod.2018.03.016

[138] J. Adamiak, A. Otlewska, and B. Gutarowska, "Halophilic microbial communities in deteriorated buildings," *World Journal of Microbiology and Biotechnology*, vol. 31, no. 10, pp. 1489–1499, 2015.

[139] L. Laiz, D. Recio, B. Hermosin, and C. Saiz-jimenez, "Microbial Communities in Salt Efflourescences," in *Of Microbes and Art*, 2000, pp. 77–88.

[140] C. J. Lee, P. E. McMullan, C. J. O'Kane, A. Stevenson, I. C. Santos, C. Roy, W. Ghosh, R. L. Mancinelli, M. R. Mormile, G. McMullan, H. L. Banciu, M. A. Fares, K. C. Benison, A. Oren, M. L. Dyall-Smith, and J. E. Hallsworth, "NaCl-saturated brines are thermodynamically moderate, rather than extreme, microbial habitats," *FEMS Microbiology Reviews*, vol. 42, no. 5, pp. 672–693, 2018.

[141] A. H. Stevens and C. S. Cockell, "A Systematic Study of the Limits of Life in Mixed Ion Solutions : Physicochemical Parameters Do Not Predict Habitability," *Frontiers in Microbiology*, vol. 11, pp. 1–10, 2020.

[142] J. Heinz, J. Doellinger, D. Maus, A. Schneider, P. Lasch, H. P. Grossart, and D. Schulze-Makuch, "Perchlorate-specific proteomic stress responses of Debaryomyces hansenii could enable microbial survival in Martian brines," *Environmental Microbiology*, vol. 24, no. 11, pp. 5051–5065, 2022.

[143] J. Heinz, V. Rambags, and D. Schulze-Makuch, "Physicochemical parameters limiting growth of debaryomyces hansenii in solutions of hygroscopic compounds and their effects on the habitability of martian brines," *Life*, vol. 11, no. 11, 2021.

[144] J. Heinz, T. Krahn, and D. Schulze-Makuch, "A new record for microbial perchlorate tolerance: fungal growth in naclo4 brines and its implications for putative life on mars," *Life*, vol. 10, no. 5, pp. 4–11, 2020.

[145] J. Heinz, A. C. Waajen, A. Airo, A. Alibrandi, J. Schirmack, and D. Schulze-Makuch, "Bacterial Growth in Chloride and Perchlorate Brines: Halotolerances and Salt Stress Responses of Planococcus halocryophilus," *Astrobiology*, vol. 19, no. 11, pp. 1377–1387, 2019.

[146] B. L. Ehlmann and C. S. Edwards, "Mineralogy of the Martian surface," *Annual Review of Earth and Planetary Sciences*, vol. 42, pp. 291–315, 2014.

[147] B. C. Clark, R. V. Morris, S. M. Mclennan, R. Gellert, B. Jolliff, A. H. Knoll, S. W. Squyres, T. K. Lowenstein, D. W. Ming, N. J. Tosca, A. Yen, P. R. Christensen, S. Gorevan, J. Brü Ckner D, W. Calvin, G. Dreibus, W. Farrand, G. Klingelhoefer, H. Waenke, J. Zipfel, J. F. B. Iii, J. Grotzinger, H. Y. Mcsween, and R. Rieder, "Chemistry and mineralogy of outcrops at Meridiani Planum," *Earth and Planetary Science Letters*, vol. 140, no. 1, pp. 73–94, 2005. [Online]. Available: www.elsevier.com/locate/epsl

[148] G. Klingelhöfer, R. V. Morris, B. Bernhardt, C. Schröder, D. S. Rodionov, P. A. De Souza, A. Yen, R. Gellert, E. N. Evlanov, B. Zubkov, J. Foh, U. Bonnes, E. Kankeleit, P. Gütlich, D. W. Ming, F. Renz, T. Wdowiak, S. W. Squyres, and R. E. Arvidson, "Jarosite and hematite at Meridiani Planum from opportunity's Mössbauer spectrometer," *Science*, vol. 306, no. 5702, pp. 1740–1745, 2004.

[149] S. M. McLennan, J. F. Bell, W. M. Calvin, P. R. Christensen, B. C. Clark, P. A. de Souza, J. Farmer, W. H. Farrand, D. A. Fike, R. Gellert, A. Ghosh, T. D. Glotch, J. P. Grotzinger, B. Hahn, K. E. Herkenhoff, J. A. Hurowitz, J. R. Johnson, S. S. Johnson, B. Jolliff, G. Klingelhöfer, A. H. Knoll, Z. Learner, M. C. Malin, H. Y. McSween, J. Pocock, S. W. Ruff, L. A. Soderblom, S. W. Squyres, N. J. Tosca, W. A. Watters, M. B. Wyatt, and A. Yen, "Provenance and diagenesis of the evaporite-bearing Burns

formation, Meridiani Planum, Mars," *Earth and Planetary Science Letters*, vol. 240, no. 1, pp. 95–121, 2005.

[150] M. Nachon, S. M. Clegg, N. Mangold, S. Schröder, L. C. Kah, G. Dromart, A. Ollila, and J. Johnson, "Calcium sulfate veins characterized by ChemCam/Curiosity at Gale crater, Mars," *Journal of Geophysical Research: Planets*, vol. 119, pp. 1991–2016, 2014.

[151] D. T. Vaniman, G. M. Martínez, E. B. Rampe, T. F. Bristow, D. F. Blake, A. S. Yen, D. W. Ming, W. Rapin, P. Y. Meslin, J. M. Morookian, R. T. Downs, S. J. Chipera, R. V. Morris, S. M. Morrison, A. H. Treiman, C. N. Achilles, K. Robertson, J. P. Grotzinger, R. M. Hazen, R. C. Wiens, and D. Y. Sumner, "Gypsum, bassanite, and anhydrite at Gale crater, Mars," *American Mineralogist*, vol. 103, no. 7, pp. 1011–1020, 7 2018.

[152] N. H. Thomas, B. L. Ehlmann, P. Y. Meslin, W. Rapin, D. E. Anderson, F. Rivera-Hernández, O. Forni, S. Schröder, A. Cousin, N. Mangold, R. Gellert, O. Gasnault, and R. C. Wiens, "Mars Science Laboratory Observations of Chloride Salts in Gale Crater, Mars," *Geophysical Research Letters*, vol. 46, no. 19, pp. 10 754–10 763, 10 2019.

[153] P. E. Martin, K. A. Farley, P. Douglas Archer, J. V. Hogancamp, K. L. Siebach, J. P. Grotzinger, and S. M. McLennan, "Reevaluation of Perchlorate in Gale Crater Rocks Suggests Geologically Recent Perchlorate Addition," *Journal of Geophysical Research: Planets*, vol. 125, no. 2, pp. 1–15, 2020.

[154] K. A. Farley, P. Martin, P. D. Archer, S. K. Atreya, P. G. Conrad, J. L. Eigenbrode, A. G. Fairén, H. B. Franz, C. Freissinet, D. P. Glavin, P. R. Mahaffy, C. Malespin, D. W. Ming, R. Navarro-Gonzalez, and B. Sutter, "Light and variable 37Cl/35Cl ratios in rocks from Gale Crater, Mars: Possible signature of perchlorate," *Earth and Planetary Science Letters*, vol. 438, pp. 14–24, 3 2016.

[155] J. R. Johnson, I. F. Bell, E. Cloutis, M. Staid, W. H. Farrand, T. McCoy, M. Rice, A. Wang, and A. Yen, "Mineralogic constraints on sulfur-rich soils from Pancam spectra at Gusev crater, Mars," *Geophysical Research Letters*, vol. 34, no. 13, 7 2007.

[156] A. Wang, L. A. Haskin, S. W. Squyres, B. L. Jolliff, L. Crumpler, R. Gellert, C. Schröder, K. Herkenhoff, J. Hurowitz, N. J. Tosca, W. H. Farrand, R. Anderson, and A. T. Knudson, "Sulfate deposition in subsurface regolith in Gusev crater, Mars," *Journal of Geophysical Research: Planets*, vol. 111, no. 2, 2006.

[157] D. W. Ming, D. W. Mittlefehldt, R. V. Morris, D. C. Golden, R. Gellert, A. Yen, B. C. Clark, S. W. Squyres, W. H. Farrand, S. W. Ruff, R. E. Arvidson, G. Klingelhöfer, H. Y. McSween, D. S. Rodionov, C. Schröder, J. A. de Souza, and A. Wang, "Geochemical and mineralogical indicators

for aqueous processes in the Columbia Hills of Gusev crater, Mars," *Journal of Geophysical Research: Planets*, vol. 111, no. 2, 2006.

[158] L. A. Haskin, A. Wang, B. L. Jolliff, H. Y. McSween, B. C. Clark, D. J. Des Marais, S. M. McLennan, N. J. Tosca, J. A. Hurowitz, J. D. Farmer, A. Yen, S. W. Squyres, R. E. Arvidson, G. Klingelhöfer, C. Schröder, P. A. De Souza, D. W. Ming, R. Gellert, J. Zipfel, J. Brückner, J. F. Bell, K. Herkenhoff, P. R. Christensen, S. Ruff, D. Blaney, S. Gorevan, N. A. Cabrol, L. Crumpler, J. Grant, and L. Soderblom, "Water alteration of rocks and soils on Mars at the Spirit rover site in Gusev crater," *Nature*, vol. 436, no. 7047, pp. 66–69, 2005.

[159] J. I. Simon, K. Hickman-Lewis, B. A. Cohen, L. Mayhew, D. Shuster, V. Debaille, E. M. Hausrath, B. Weiss, T. Bosak, M. Zorzano, H. E. F. Amundsen, L. Beegle, J. Bell, K. C. Benison, E. L. Berger, O. Beyssac, A. Brown, F. Calef, T. M. Casademont, B. Clark, E. Clavé, L. Crumpler, A. D. Czaja, A. G. Fairén, K. A. Farley, D. T. Flannery, T. Fornaro, O. Forni, F. Gómez, Y. Goreva, A. Gorin, K. P. Hand, S. Hamran, J. Henneke, C. D. K. Herd, B. H. N. Horgan, J. R. Johnson, J. Joseph, R. E. Kronyak, J. M. Madariaga, J. N. Maki, L. Mandon, F. M. McCubbin, S. M. McLennan, R. C. Moeller, C. E. Newman, J. I. Núñez, A. C. Pascuzzo, D. A. Pedersen, G. Poggiali, P. Pinet, C. Quantin-Nataf, M. Rice, J. W. Rice, C. Royer, M. Schmidt, M. Sephton, S. Sharma, S. Siljeström, K. M. Stack, A. Steele, V. Z. Sun, A. Udry, S. VanBommel, M. Wadhwa, R. C. Wiens, A. J. Williams, and K. H. Williford, "Samples Collected from the Floor of Jezero Crater with the Mars 2020 Perseverance Rover," *Journal of Geophysical Research: Planets*, 2023.

[160] S. W. Squyres, J. P. Grotzinger, R. E. Arvidson, J. F. Bell, W. Calvin, P. R. Christensen, B. C. Clark, J. A. Crisp, W. H. Farrand, K. E. Herkenhoff, J. R. Johnson, G. Klingelhöfer, A. H. Knoll, S. M. McLennan, H. Y. McSween, R. V. Morris, J. W. Rice, R. Rieder, and L. A. Soderblom, "In situ evidence for an ancient aqueous environment at Meridiani Planum, Mars," *Science*, vol. 306, no. 5702, pp. 1709–1714, 2004.

[161] S. W. Squyres and A. H. Knoll, "Sedimentary rocks at Meridiani Planum: Origin, diagenesis, and implications for life on Mars," *Earth and Planetary Science Letters*, vol. 240, no. 1, pp. 1–10, 2005.

[162] S. L. Murchie, J. F. Mustard, B. L. Ehlmann, R. E. Milliken, J. L. Bishop, N. K. McKeown, E. Z. Noe Dobrea, F. P. Seelos, D. L. Buczkowski, S. M. Wiseman, R. E. Arvidson, J. J. Wray, G. Swayze, R. N. Clark, D. J. Des Marais, A. S. McEwen, and J. P. Bibring, "A synthesis of Martian aqueous mineralogy after 1 Mars year of observations from the Mars Reconnaissance Orbiter," *Journal of Geophysical Research: Planets*, vol. 114, no. 9, pp. 1–30, 2009.

[163] M. M. Osterloo, F. S. Anderson, V. E. Hamilton, and B. M. Hynek,

"Geologic context of proposed chloride-bearing materials on Mars," *Journal of Geophysical Research E: Planets*, vol. 115, no. 10, pp. 1–29, 2010.

[164] E. K. Leask and B. L. Ehlmann, "Evidence for Deposition of Chloride on Mars From Small-Volume Surface Water Events Into the Late Hesperian-Early Amazonian," *AGU Advances*, vol. 3, no. 1, 2022.

[165] T. Altheide, V. Chevrier, C. Nicholson, and J. Denson, "Experimental investigation of the stability and evaporation of sulfate and chloride brines on Mars," *Earth and Planetary Science Letters*, vol. 282, no. 1-4, pp. 69–78, 2009.

[166] R. V. Gough, V. F. Chevrier, and M. A. Tolbert, "Formation of aqueous solutions on Mars via deliquescence of chloride-perchlorate binary mixtures," *Earth and Planetary Science Letters*, vol. 393, pp. 73–82, 5 2014.

[167] C. S. Cockell, "Biological effects of high ultraviolet radiation on early earth - A theoretical evaluation," *Journal of Theoretical Biology*, vol. 193, no. 4, pp. 717–729, 8 1998.

[168] C. S. Cockell, D. C. Catling, W. L. Davis, K. Snook, R. L. Kepner, P. Lee, and C. P. McKay, "The Ultraviolet Environment of Mars: Biological Implications Past, Present, and Future," *Icarus*, vol. 146, no. 2, pp. 343–359, 2000.

[169] P. J. Godin, A. C. Schuerger, and J. E. Moores, "Salt Tolerance and UV Protection of Bacillus subtilis and Enterococcus faecalis under Simulated Martian Conditions," *Astrobiology*, vol. 21, no. 4, pp. 1–11, 2020.

[170] P. J. Godin, H. Stone, R. Bahrami, A. C. Schuerger, and J. E. Moores, "UV attenuation by Martian brines," *Canadian Journal of Physics*, vol. 98, no. 6, pp. 567–570, 2020.

[171] K. M. Cannon, L. A. Fenwick, and R. C. Peterson, "Spotted Lake: Mineralogical Clues For The Formation Of Authigenic Sulfates In Ancient Lakes On Mars," in *43rd Lunar and Planetary Science Conference*, ser. Advances in Astrobiology and Biogeophysics. Berlin, Heidelberg: Springer Berlin Heidelberg, 2012. [Online]. Available: http://link.springer.com/10.1007/978-3-540-75679-8

[172] C. S. Cockell, R. Santomartino, K. Finster, A. C. Waajen, L. J. Eades, R. Moeller, P. Rettberg, F. M. Fuchs, R. Van Houdt, N. Leys, I. Coninx, J. Hatton, L. Parmitano, J. Krause, A. Koehler, N. Caplin, L. Zuijderduijn, A. Mariani, S. S. Pellari, F. Carubia, G. Luciani, M. Balsamo, V. Zolesi, N. Nicholson, C. M. Loudon, J. Doswald-Winkler, M. Herová, B. Rattenbacher, J. Wadsworth, R. Craig Everroad, and R. Demets, "Space station biomining experiment demonstrates rare earth element extraction in microgravity and Mars gravity," *Nature Communications*, vol. 11, no. 1, pp. 1–11, 2020. [Online]. Available: http://dx.doi.org/10.1038/s41467-020-19276-w

[173] T. L. Hudson and O. Aharonson, "Diffusion barriers at Mars surface conditions: Salt crusts, particle size mixtures, and dust," *Journal of Geophysical Research*, vol. 113, no. E9, 2008.

[174] B. Gómez-Silva, F. A. Rainey, K. A. Warren-Rhodes, C. P. McKay, and R. Navarro-González, "Atacama Desert Soil Microbiology," in *Microbiology of Extreme Soils*. Springer, Berlin, Heidelberg, 2008, pp. 117–132. [Online]. Available: https://link.springer.com/chapter/10.1007/978-3-540-74231-9_6

[175] J. Wierzchos, A. F. Davila, O. Artieda, B. Cámara-Gallego, A. de los Ríos, K. H. Nealson, S. Valea, M. Teresa García-González, and C. Ascaso, "Ignimbrite as a substrate for endolithic life in the hyper-arid Atacama Desert: Implications for the search for life on Mars," *Icarus*, vol. 224, no. 2, pp. 334–346, 6 2013.

[176] G. Panieri, S. Lugli, V. Manzi, K. A. Palinska, and M. Roveri, "Microbial communities in Messinian evaporite deposits of the Vena del Gesso (northern Apennines, Italy)," *Stratigraphy*, vol. 5, no. 3-4, pp. 343–352, 2008.

[177] G. Panieri, S. Lugli, V. Manzi, M. Roveri, B. C. Schreiber, and K. A. Palinska, "Ribosomal RNA gene fragments from fossilized cyanobacteria identified in primary gypsum from the late Miocene, Italy," *Geobiology*, vol. 8, no. 2, pp. 101–111, 2010.

[178] N. B. Vargaftik, B. N. Volkov, and L. D. Voljak, "International Tables of Water Surface Tension," *J. Phys. Chem. Ref. Data*, vol. 12, no. 3, pp. 817–820, 1983.

[179] W. V. Kayser, "Temperature Dependence of the Surface Tension of Water in Contact with Its Saturated Vapor," *Journal of Colloid and Interface Science*, vol. 56, no. 3, 1976.

[180] W. D. Harkins and H. M. McLaughlin, "The Structure of Films on Salt Solutions I. Surface Tension and Adsorption for Aqeuous Solutions of Sodium Chloride," *Journal of the American Chemical Society American*, vol. 47, no. 8, 1925.

[181] K. Ali, Anwar-il-Haq, S. Bilal, and S. Siddiqi, "Concentration and temperature dependence of surface parameters of some aqueous salt solutions," *Colloids and Surfaces*, vol. 272, pp. 105–110, 2006.

[182] P. K. Weissenborn and R. J. Pugh, "Surface Tension of Aqueous Solutions of Electrolytes: Relationship with Ion Hyradtion, Oxygen Solubility, and Bubble Coalescence," *Journal of Col*, vol. 184, pp. 550–563, 1996.

[183] J. Nyvlt, "Kinetics of Nucleation in Solutions," *Journal of Crystal Growth*, vol. 3, no. 4, pp. 377–383, 1968.

[184] J. Nyvlt, "Nucleation and Growth Rate in Mass Crystallization," *Prog. Crystal Growth and Charact.*, vol. 9, pp. 335–370, 1984.

[185] A. F. Davila, L. G. Duport, R. Melchiorri, J. Jänchen, S. Valea, A. De Los Rios, A. G. Fairén, D. Möhlmann, C. P. McKay, C. Ascaso, and J. Wierzchos, "Hygroscopic salts and the potential for life on mars," *Astrobiology*, vol. 10, no. 6, pp. 617–628, 2010.

[186] R. F. Scott, *The Voyage of Discovery: Volume II.* Cambridge University Press, 1905.

[187] N. H. Horowitz, R. E. Cameron, and J. S. Hubbard, "Microbiology of the dry valleys of Antarctica," *Science*, vol. 176, no. 4032, pp. 242–245, 1972.

[188] L. Kappen, E. Friedmann, and J. Garty, "Ecophysiology of Lichens in the Dry Valleys of Southern Victoria Land, Antarctica I. Microclimate of the Cryptoendolithic Lichen Habitat," *Flora*, vol. 171, no. 3, pp. 216–235, 1981.

[189] R. E. Arvidson, S. W. Squyres, R. V. Morris, A. H. Knoll, R. Gellert, B. C. Clark, J. G. Catalano, B. L. Jolliff, S. M. McLennan, K. E. Herkenhoff, S. Vanbommel, D. W. Mittlefehldt, J. P. Grotzinger, E. A. Guinness, J. R. Johnson, J. F. Bell, W. H. Farrand, N. Stein, V. K. Fox, M. P. Golombek, M. A. Hinkle, W. M. Calvin, and P. A. De Souza, "High concentrations of manganese and sulfur in deposits on Murray Ridge, Endeavour Crater, Mars," *American Mineralogist*, vol. 101, no. 6, pp. 1389–1405, 2016.

[190] S. Golubic, I. Friedmann, and J. Schneider, "The Lithobiontic Ecological Niche, With Special Reference To Microorganisms," *Journal of Sedimentary Petrology*, vol. 51, pp. 475–478, 1981.

[191] V. Meslier and J. DiRuggiero, "Endolithic microbial communities as model systems for ecology and astrobiology," in *Model Ecosystems in Extreme Environments*. Elsevier Inc., 2019, pp. 145–168. [Online]. Available: http://dx.doi.org/10.1016/B978-0-12-812742-1.00007-6

[192] J.-B. Ramond and D. Cowan, Eds., *Microbiology of Hot Deserts*. Springer, 2022.

[193] E. I. Friedmann, "Light and scanning electron microscopy of the endolithic desert algal habitat," *Phycologia*, vol. 10, no. 4, pp. 411–428, 1971.

[194] V. Meslier, M. C. Casero, M. Dailey, J. Wierzchos, C. Ascaso, O. Artieda, P. R. McCullough, and J. DiRuggiero, "Fundamental drivers for endolithic microbial community assemblies in the hyperarid Atacama Desert," *Environmental Microbiology*, vol. 20, no. 5, pp. 1765–1781, 2018.

[195] E. I. Friedmann, "Endolithic Microorganisms in the Antarctic Cold Desert," *Science*, vol. 215, no. 4536, pp. 1045–1053, 1982.

[196] P. Hirsch, B. Hoffmann, C. C. Gallikowski, U. Mevs, J. Siebert, and M. Sittig, "Diversity and Identification of Heterotrophs from Antarctic Rocks of the McMurdo Dry Valleys (Ross Desert)," *Polarforschung*, vol. 58, no. 2/3, pp. 261–269, 1988.

[197] C. R. Omelon, "Endolithic microbial communities in polar desert habitats," *Geomicrobiology Journal*, vol. 25, no. 7-8, pp. 404–414, 2008.

[198] S. D. Archer, A. de los Ríos, K. C. Lee, T. S. Niederberger, S. C. Cary, K. J. Coyne, S. Douglas, D. C. Lacap-Bugler, and S. B. Pointing, "Endolithic microbial diversity in sandstone and granite from the McMurdo Dry Valleys, Antarctica," *Polar Biology*, vol. 40, no. 5, pp. 997–1006, 2017.

[199] D. A. Fike, C. Cockell, D. Pearce, and P. Lee, "Heterotrophic microbial colonization of the interior of impact-shocked rocks from Haughton impact structure, Devon Island, Nunavut, Canadian High Arctic," *International Journal of Astrobiology*, vol. 1, no. 4, pp. 311–323, 2002.

[200] C. S. Cockell, C. P. Mckay, and C. Omelon, "Polar endoliths – an anti-correlation of climatic extremes and microbial biodiversity," *International Journal of Astrobiology*, vol. 1, no. 4, pp. 305–310, 2003.

[201] A. Herrera, C. S. Cockell, S. Self, M. Blaxter, J. Reitner, T. Thorsteinsson, G. Arp, W. Dröse, and A. G. Tindle, "A cryptoendolithic community in volcanic glass," *Astrobiology*, vol. 9, no. 4, pp. 369–381, 2009.

[202] C. S. Cockell, K. Olsson, F. Knowles, L. Kelly, A. Herrera, T. Thorsteinsson, and V. Marteinsson, "Bacteria in weathered basaltic glass, Iceland," *Geomicrobiology Journal*, vol. 26, no. 7, pp. 491–507, 2009.

[203] S. E. Jorge Villar, H. G. Edwards, and L. G. Benning, "Raman spectroscopic and scanning electron microscopic analysis of a novel biological colonisation of volcanic rocks," *Icarus*, vol. 184, no. 1, pp. 158–169, 2006.

[204] H. Y. Holman, D. L. Perry, and J. C. Hunter-Cevera, "Surface-enhanced infrared absorption-reflectance (SEIRA) microspectroscopy for bacteria localization on geologic material surfaces," *Journal of Microbiological Methods*, vol. 34, no. 1, pp. 59–71, 1998.

[205] P. Bergsten, P. Vannier, A. M. Klonowski, S. Knobloch, M. T. Gudmundsson, M. D. Jackson, and V. T. Marteinsson, "Basalt-Hosted Microbial Communities in the Subsurface of the Young Volcanic Island of Surtsey, Iceland," *Frontiers in Microbiology*, vol. 12, no. September, 2021.

[206] B. Cavalazzi, F. Westall, R. Barbieri, U. Bologna, and V. Zamboni, "(Crypto-) endoliths from vesicular oceanic basaltic crust , Coral Patch Seamount , North Atlantic Ocean," *Acta Geol.*, vol. 83, no. January, pp. 177–182, 2008.

[207] K. J. Edwards, C. G. Wheat, and J. B. Sylvan, "Under the sea: Microbial life in volcanic oceanic crust," *Nature Reviews Microbiology*, vol. 9, no. 10, pp. 703–712, 2011.

[208] J. Wierzchos, M. C. Casero, O. Artieda, and C. Ascaso, "Endolithic microbial habitats as refuges for life in polyextreme environment of the Atacama Desert," *Current Opinion in Microbiology*, vol. 43, pp. 124–131, 2018. [Online]. Available: https://doi.org/10.1016/j.mib.2018.01.003

[209] R. Bell, "Cryptoendolithic Algae of Hot Semiarid Lands and Deserts," *Journal of Phycology*, vol. 29, no. 2, pp. 133–139, 1993.

[210] E. I. Friedmann, C. P. Mckay, and J. A. Nienow, "The Cryptoendolithic Microbial Environment in the Ross Desert of Antarctica: Satellite-Transmitted Continuous Nanoclimate Data, 1984 to 1986," *Polar Biol*, vol. 7, pp. 273–287, 1987.

[211] C. Cockell, P. Rettberg, G. Horneck, K. Scherer, and M. D. Stokes, "Measurements of microbial protection from ultraviolet radiation in polar terrestrial microhabitats," *Polar Biology*, vol. 26, no. 1, pp. 62–69, 2003.

[212] B. L. Carrier, W. J. Abbey, L. W. Beegle, R. Bhartia, and Y. Liu, "Attenuation of Ultraviolet Radiation in Rocks and Minerals: Implications for Mars Science," *Journal of Geophysical Research: Planets*, vol. 124, no. 10, pp. 2599–2612, 2019.

[213] U. Matthes, S. J. Turner, and D. W. Larson, "Light Attenuation by Limestone Rock and Its Constraint on the Depth Distribution of Endolithic Algae and Cyanobacteria," *International Journal of Plant Sciences*, vol. 162, no. 2, pp. 263–270, 2001.

[214] C. P. McKay, "Full solar spectrum measurements of absorption of light in a sample of the Beacon Sandstone containing the Antarctic cryptoendolithic microbial community," *Antarctic Science*, vol. 24, no. 3, pp. 243–248, 2012.

[215] E. I. Friedmann, "Endolithic Microbial Life in Hot and Cold Deserts," *Origins of Life*, vol. 10, no. 3, pp. 223–235, 1980.

[216] C. P. McKay and E. I. Friedmann, "The cryptoendolithic microbial environment in the Antarctic cold desert: Temperature variations in nature," *Polar Biology*, vol. 4, no. 1, pp. 19–25, 1985.

[217] J. Peckmann, W. Bach, K. Behrens, and J. Reitner, "Putative cryptoendolithic life in Devonian pillow basalt, Rheinisches Schiefergebirge, Germany," *Geobiology*, vol. 6, no. 2, pp. 125–135, 2008.

[218] B. Eickmann, W. Bach, S. Kiel, J. Reitner, and J. Peckmann, "Evidence for cryptoendolithic life in Devonian pillow basalts of Variscan orogens, Germany," *Palaeogeography, Palaeoclimatology, Palaeoecology*, vol. 283, no. 3-4, pp. 120–125, 2009. [Online]. Available: http://dx.doi.org/10.1016/j.palaeo.2009.09.006

[219] S. Bengtson, B. Rasmussen, M. Ivarsson, J. Muhling, C. Broman, F. Marone, M. Stampanoni, and A. Bekker, "Fungus-like mycelial fossils in 2.4-billion-year-old vesicular basalt," *Nature Ecology and Evolution*, vol. 1, no. 6, p. 41559, 2017.

[220] G. Schumann, W. Manz, J. Reitner, and M. Lustrino, "Ancient Fungal Life in North Pacific Eocene Oceanic Crust," *Geomicrobiology Journal*, vol. 21, no. 4, pp. 241–246, 6 2004. [Online]. Available: https://www.tandfonline.com/doi/abs/10.1080/01490450490438748

[221] M. Ivarsson, J. Lausmaa, S. Lindblom, C. Broman, and N. G. Holm, "Fossilized microorganisms from the emperor seamounts: Implications for the search for a subsurface fossil record on earth and mars," *Astrobiology*, vol. 8, no. 6, pp. 1139–1157, 2008.

[222] D. T. Carlsson, M. Ivarsson, and A. Neubeck, "Fossilized Endolithic Microorganisms in Pillow Lavas from the Troodos Ophiolite, Cyprus," *Geosciences*, vol. 9, p. 456, 10 2019. [Online]. Available: https://www.mdpi.com/2076-3263/9/11/456/htmhttps://www.mdpi.com/2076-3263/9/11/456

[223] S. McMahon, J. Parnell, J. Ponicka, M. Hole, and A. Boyce, "The Habitability of Vesicles in Martian Basalt," *Astronomy and Geophysics*, vol. 54, no. 1, pp. 17–1, 2013.

[224] B. Cavalazzi, F. Westall, and S. Cady, "Vesicular Basalts as a Niche for Microbial Life," in *Life on Earth and other Planetary Bodies*. Springer, 2012, pp. 29–43.

[225] L. N. Schaefer, J. E. Kendrick, T. Oommen, Y. Lavallée, and G. Chigna, "Geomechanical rock properties of a basaltic volcano," *Frontiers in Earth Science*, vol. 3, no. June, pp. 1–15, 2015.

[226] A. A. Al-Harthi, R. M. Al-Amri, and W. M. Shehata, "The porosity and engineering properties of vesicular basalt in Saudi Arabia," *Engineering Geology*, vol. 54, no. 3-4, pp. 313–320, 1999.

[227] B. Bailey, A. Templeton, H. Staudigel, and B. M. Tebo, "Utilization of substrate components during basaltic glass colonization by Pseudomonas and Shewanella Isolates," *Geomicrobiology Journal*, vol. 26, no. 8, pp. 648–656, 2009.

[228] M. R. Fisk and S. J. Giovannoni, "Sources of nutrients and energy for a deep biosphere on Mars," *Journal of Geophysical Research: Planets*, vol. 104, no. E5, pp. 11 805–11 815, 5 1999. [Online]. Available: http://doi.wiley.com/10.1029/1999JE900010

[229] S. W. Squyres, O. Aharonson, B. Clark, B. A. Cohen, L. S. Crumpler, P. A. De Souza, W. H. Farrand, R. Gellert, J. Grant, J. P. Grotzinger, A. Haldemann, J. R. Johnson, G. Klingelhöfer, K. W. Lewis, R. Li,

T. McCoy, A. S. McEwan, H. Y. McSween, D. W. Ming, J. Moore, R. Morris, T. Parker, J. Rice, S. Ruff, M. Schmidt, C. Schröder, L. A. Soderblom, and A. Yen, "Pyroclastic Activity at Home Plate in Gusev Crater, Mars," *Science*, vol. 316, no. May, pp. 738–742, 2007.

[230] R. B. Singer, T. B. McCord, R. N. Clark, J. B. Adams, and R. L. Huguenin, "Mars surface composition from reflectance spectroscopy: a summary." *Journal of Geophysical Research*, vol. 84, no. B14, pp. 8415–8426, 1979.

[231] F. Poulet, C. Gomez, J. P. Bibring, Y. Langevin, P. Pinet, G. Belluci, and J. Mustard, "Martian surface mineralogy from Observatoire pour la Minéralogie, l'Eau, les Glaces et l'Activité on board the Mars Express spacecraft (OMEGA/MEx): Global mineral maps," *Journal of Geophysical Research: Planets*, vol. 112, no. 8, pp. 1–15, 2007.

[232] J. L. Bandfield, V. E. Hamilton, and P. R. Christensen, "A global view of martian surface compositions from MGS-TES," *Science*, vol. 287, no. 5458, pp. 1626–1630, 2000.

[233] S. R. Taylor and S. McLennan, "Mars: crustal composition and evolution," in *Planetary Crusts: Their Composition, Origin and Evolution.* Cambridge University Press, 2009, pp. 141–180.

[234] J. P. Bibring and S. Erard, "The Martian surface composition," *Space Science Reviews*, vol. 96, pp. 293–316, 2001.

[235] M. B. Wyatt and H. Y. McSween, "Spectral evidence for weathered basalt as an alternative to andesite in the northern lowlands of Mars," *Nature*, vol. 417, no. 6886, pp. 263–266, 2002.

[236] T. Mutch, R. Arvidson, A. Binder, E. Guinness, and E. Morris, "The geology of the Viking Lander 2 site revisited," *Journal of Geophysical Research*, vol. 82, no. 28, pp. 4452–4467, 1977.

[237] M. E. Schmidt, S. W. Ruff, T. J. McCoy, W. H. Farrand, J. R. Johnson, R. Gellert, D. W. Ming, R. V. Morris, N. Cabrol, K. W. Lewis, and C. Schroeder, "Hydrothermal origin of halogens at Home Plate, Gusev Crater," *Journal of Geophysical Research: Planets*, vol. 113, no. 6, pp. 1–21, 2008.

[238] L. S. Crumpler, T. McCoy, and M. E. Schmidt, "Spirit: Observations of Very Vesicular Basalts in the Columbia Hills, Mars and Significance for Primary Lava Textures, Volatiles and Paleoenvironment," in *Lunar and Planetary Science XXXVIII*, 2007.

[239] H. Y. McSween, R. E. Arvidson, J. F. Bell, D. Blaney, N. A. Cabrol, P. R. Christensen, B. C. Clark, J. A. Crisp, L. S. Crumpler, D. J. Des Marias, J. D. Farmer, R. Gellert, A. Ghosh, S. Gorevan, T. Graff, J. Grant, L. A. Haskin, K. E. Herkenhoff, J. R. Johnson, B. L. Jolliff, G. Klingelhoefer, A. T. Knudson, S. McLennan, K. A. Milam, J. E. Moersch, R. V. Morris,

R. Rieder, S. W. Ruff, P. A. De Souza, S. W. Squyres, H. Wänke, A. Wang, M. B. Wyatt, A. Yen, and J. Zipfel, "Basaltic rocks analyzed by the Spirit rover in Gusev crater," *Science*, vol. 305, no. 5685, pp. 842–845, 2004.

[240] D. W. Mittlefehldt, R. Gellert, S. vanBommel, D. W. Ming, A. S. Yen, B. C. Clark, R. V. Morris, C. Schröder, L. S. Crumpler, J. A. Grant, B. L. Jolliff, R. E. Arvidson, W. H. Farrand, K. E. Herkenhoff, J. F. Bell, B. A. Cohen, G. Klingelhöfer, C. M. Schrader, and J. W. Rice, "Diverse Lithologies and Alteration Events on the Rim of Noachian-Aged Endeavour Crater, Meridiani Planum, Mars: In Situ Compositional Evidence," *Journal of Geophysical Research: Planets*, vol. 123, no. 5, pp. 1255–1306, 2018.

[241] A. W. Tait, C. Schröder, W. H. Farrand, J. W. Ashley, B. A. Cohen, R. Gellert, J. Rice, L. C. Crumpler, and B. Jolliff, "Exploring Origins Of Pitted/Vesicular Rocks In Perseverance Valley, Endeavour Crater," in *50th Lunar and Planetary Science Conference*, 2019.

[242] J. F. Bell, J. N. Maki, S. Alwmark, B. L. Ehlmann, S. A. Fagents, J. P. Grotzinger, S. Gupta, A. Hayes, K. E. Herkenhoff, B. H. Horgan, J. R. Johnson, K. B. Kinch, M. T. Lemmon, M. B. Madsen, J. I. Núñez, G. Paar, M. Rice, J. W. Rice, N. Schmitz, R. Sullivan, A. Vaughan, M. J. Wolff, A. Bechtold, T. Bosak, L. E. Duflot, A. G. Fairén, B. Garczynski, R. Jaumann, M. Merusi, C. Million, E. Ravanis, D. L. Shuster, J. Simon, M. St Clair, C. Tate, S. Walter, B. Weiss, A. M. Bailey, T. Bertrand, O. Beyssac, A. J. Brown, P. Caballo-Perucha, M. A. Caplinger, C. M. Caudill, F. Cary, E. Cisneros, E. A. Cloutis, N. Cluff, P. Corlies, K. Crawford, S. Curtis, R. Deen, D. Dixon, C. Donaldson, M. Barrington, M. Ficht, S. Fleron, M. Hansen, D. Harker, R. Howson, J. Huggett, S. Jacob, E. Jensen, O. B. Jensen, M. Jodhpurkar, J. Joseph, C. Juarez, L. C. Kah, O. Kanine, J. Kristensen, T. Kubacki, K. Lapo, A. Magee, M. Maimone, G. L. Mehall, L. Mehall, J. Mollerup, D. Viúdez-Moreiras, K. Paris, K. E. Powell, F. Preusker, J. Proton, C. Rojas, D. Sallurday, K. Saxton, E. Scheller, C. H. Seeger, M. Starr, N. Stein, N. Turenne, J. Van Beek, A. G. Winhold, and R. Yingling, "Geological, multispectral, and meteorological imaging results from the Mars 2020 Perseverance rover in Jezero crater," *Science Advances*, vol. 8, no. 47, 2022.

[243] A. Udry, A. Ostwald, V. Sautter, A. Cousin, O. Beyssac, O. Forni, G. Dromart, K. Benzerara, M. Nachon, B. Horgan, L. Mandon, E. Clavé, E. Dehouck, E. Gibbons, S. Alwmark, E. Ravanis, R. C. Wiens, C. Legett, R. Anderson, P. Pilleri, N. Mangold, M. Schmidt, Y. Liu, J. I. Núñez, K. Castro, J. M. Madariaga, T. Kizovski, P. Beck, S. Bernard, T. Bosak, A. Brown, S. Clegg, E. Cloutis, B. Cohen, S. Connell, L. Crumpler, V. Debaille, D. Flannery, T. Fouchet, T. S. J. Gabriel, O. Gasnault, C. D. K. Herd, J. Johnson, J. A. Manrique, S. Maurice, F. M. McCubbin, S. McLennan, A. Ollila, P. Pinet, C. Quantin-Nataf, C. Royer, S. Sharma, J. I. Simon, A. Steele, N. Tosca, and A. Treiman, "A Mars 2020 Perseverance SuperCam Perspective on the Igneous Nature of the Máaz

formation at Jezero crater and link with Séítah, Mars," *Journal of Geophysical Research: Planets*, 2022.

[244] A. Cousin, V. Sautter, V. Payré, O. Forni, N. Mangold, O. Gasnault, L. Le Deit, J. Johnson, S. Maurice, M. Salvatore, R. C. Wiens, P. Gasda, and W. Rapin, "Classification of igneous rocks analyzed by ChemCam at Gale crater, Mars," *Icarus*, vol. 288, pp. 265–283, 2017. [Online]. Available: http://dx.doi.org/10.1016/j.icarus.2017.01.014

[245] V. Sautter, M. J. Toplis, R. C. Wiens, A. Cousin, C. Fabre, O. Gasnault, S. Maurice, O. Forni, J. Lasue, A. Ollila, J. C. Bridges, N. Mangold, S. Le Mouélic, M. Fisk, P. Y. Meslin, P. Beck, P. Pinet, L. Le Deit, W. Rapin, E. M. Stolper, H. Newsom, D. Dyar, N. Lanza, D. Vaniman, S. Clegg, and J. J. Wray, "In situ evidence for continental crust on early Mars," *Nature Geoscience*, vol. 8, no. 8, pp. 605–609, 2015.

[246] M. E. Schmidt, J. L. Campbell, R. Gellert, G. M. Perrett, A. H. Treiman, D. L. Blaney, A. Olilla, F. J. Calef, L. Edgar, B. E. Elliott, J. Grotzinger, J. Hurowitz, P. L. King, M. E. Minitti, V. Sautter, K. Stack, J. A. Berger, J. C. Bridges, B. L. Ehlmann, O. Forni, L. A. Leshin, K. W. Lewis, S. M. McLennan, D. W. Ming, H. Newsom, I. Pradler, S. W. Squyres, E. M. Stolper, L. Thompson, S. Vanbommel, and R. C. Wiens, "Geochemical diversity in first rocks examined by the curiosity rover in gale crater: Evidence for and significance of an alkali and volatile-rich igneous source," *Journal of Geophysical Research: Planets*, vol. 119, no. 1, pp. 64–81, 2014.

[247] R. J. Pender, "The behaviour of water in porous building materials and structures," *Studies in Conservation*, vol. 49, no. 1, pp. 49–62, 2004.

[248] D. McAllister, P. Warke, S. McCabe, and M. Gomez-Heras, "Evaporative moisture loss from heterogeneous stone: Material-environment interactions during drying," *Geomorphology*, vol. 273, pp. 308–322, 2016. [Online]. Available: http://dx.doi.org/10.1016/j.geomorph.2016.08.008

[249] C. Franzen and P. W. Mirwald, "Moisture content of natural stone: Static and dynamic equilibrium with atmospheric humidity," *Environmental Geology*, vol. 46, no. 3-4, pp. 391–401, 2004.

[250] G. E. Harbeck, "The Effect of Salinity on Evaporation," United States Department of the Interior, Tech. Rep., 1955.

[251] A. M. Salhotra, E. E. Adams, and D. R. Harleman, "Effect of Salinity and Ionic Composition on Evaporation: Analysis of Dead Sea Evaporation Pans," *Water Resources Research*, vol. 21, no. 9, pp. 1336–1344, 1985.

[252] D. W. G. Sears and J. D. Chittenden, "On laboratory simulation and the temperature dependence of the evaporation rate of brine on Mars," *Geophysical Research Letters*, vol. 32, no. 23, pp. 1–4, 12 2005.

[253] J. Todorović and H. Janssen, "The impact of salt pore clogging on the hygric properties of bricks," *Construction and Building Materials*, vol. 164, pp. 850–863, 3 2018.

[254] C. Rodriguez-Navarro and E. Doehne, "Salt Weathering: Influence Of Evaporation Rate, Supersaturation And Crystallization Pattern," *Earth Surface Processes and Landforms*, vol. 24, pp. 191–209, 1999.

[255] S. Gupta, H. P. Huinink, M. Prat, L. Pel, and K. Kopinga, "Paradoxical drying of a fired-clay brick due to salt crystallization," *Chemical Engineering Science*, vol. 109, no. 2014, pp. 204–211, 2014. [Online]. Available: http://dx.doi.org/10.1016/j.ces.2014.01.023

[256] R. M. Espinosa-Marzal and G. W. Scherer, "Impact of in-pore salt crystallization on transport properties," *Environmental Earth Sciences*, vol. 69, no. 8, pp. 2657–2669, 2013.

[257] M. M. Al-Doury, "A discussion about hydraulic permeability and permeability," *Petroleum Science and Technology*, vol. 28, no. 17, pp. 1740–1749, 2010.

[258] H. K. Dahle, M. A. Celia, and S. M. Hassanizadeh, "Bundle-of-Tubes Model for Calculating Dynamic Effects in the Capillary-Pressure-Saturation Relationship," *Transp Porous Med*, vol. 58, pp. 5–22, 2005. [Online]. Available: http://link.springer.com/10.1007/1-4020-3604-3_2

[259] M. O. Saar and M. Manga, "Permeability-porosity relationship in vesicular basalts," *Geophysical Research Letters*, vol. 26, no. 1, pp. 111–114, 1999.

[260] I. M. Coulson, M. Beech, and W. Nie, "Physical properties of Martian meteorites: Porosity and density measurements," *Meteoritics and Planetary Science*, vol. 42, no. 12, pp. 2043–2054, 2007.

[261] J. R. Michalski, T. C. Onstott, S. J. Mojzsis, J. Mustard, Q. H. Chan, P. B. Niles, and S. S. Johnson, "The Martian subsurface as a potential window into the origin of life," *Nature Geoscience*, vol. 11, no. 1, pp. 21–26, 2018. [Online]. Available: http://dx.doi.org/10.1038/s41561-017-0015-2

[262] G. J. Consolmagno, D. T. Britt, and R. J. Macke, "The significance of meteorite density and porosity," *Chemie der Erde Geochemistry*, vol. 68, no. 1, pp. 1–29, 2008.

[263] C. Hall and W. Hoff, *Water Transport in Brick, Stone and Concrete*, 3rd ed. Taylor and Francis, 2021.

[264] E. Keita, P. Faure, S. Rodts, D. Weitz, and P. Coussot, "Evaporation from a capillary tube: Experiment and modelization," in *5th International Conference on Porous Media and Their Applications in Science, Engineering and Industry.* ECI Symposium Series, 2014. [Online]. Available: http://dc.engconfintl.org/porous_media_V/48

[265] J. M. Wilks, F. Chen, B. C. Clark, and M. A. Schneegurt, "Bacterial growth in saturated and eutectic solutions of magnesium sulphate and potassium chlorate with relevance to Mars and the ocean worlds," *International Journal of Astrobiology*, vol. 18, no. 6, pp. 502–509, 2019.

[266] M. Ivarsson and P. Lindgren, "The Search for Sustainable Subsurface Habitats on Mars, and the Sampling of Impact Ejecta," *Sustainability*, vol. 2, pp. 1969–1990, 2010.

[267] C. S. Cockell and N. G. Barlow, "Impact Excavation and the Search for Subsurface Life on Mars," *Icarus*, vol. 155, pp. 340–349, 2002.

[268] G. Horneck, "Bacterial Spores Survive Simulated Meteorite Impact," *Icarus*, vol. 149, pp. 285–290, 2001.

[269] J. Parnell, S. Bowden, P. Lindgren, M. Burchell, D. Milner, M. Price, E. C. Baldwin, and I. A. Crawford, "The preservation of fossil biomarkers during meteorite impact events : Experimental evidence from biomarker-rich projectiles and target rocks," *Meteoritics & Planetary Science*, vol. 45, no. 8, pp. 1340–1358, 2010.

[270] B. L. Barney, S. N. Pratt, and D. E. Austin, "Survivability of bare , individual Bacillus subtilis spores to high-velocity surface impact : Implications for microbial transfer through space," *Planetary and Space Science*, vol. 125, pp. 20–26, 2016. [Online]. Available: http://dx.doi.org/10.1016/j.pss.2016.02.010

[271] R. S. Thombre, F. Gomez, R. Parkhe, K. Kaur, P. Vaishampayan, and E. Shivakarthik, "Effect of impact shock on extremophilic Halomonas gomseoemensis EP-3 isolated from hypersaline sulphated lake Laguna de Peña Hueca, Spain," *Planetary and Space Science*, vol. 192, no. May, 2020. [Online]. Available: https://doi.org/10.1016/j.pss.2020.105041

[272] M. J. Burchell, K. H. Mcdermott, M. C. Price, and L. Yolland, "Survival of fossils under extreme shocks induced by hypervelocity impacts," *Philosophical Transactions of the Royal Society A*, vol. 372, 2014.

[273] J. F. Mustard, F. Poulet, B. L. Ehlmann, R. Milliken, and A. Fraeman, "Sequestration Of Volatiles In The Martian Crust Through Hydrated Minerals: Implications For Planetary Evolution," in *Third Conference on Early Mars*, 2012.

[274] J. D. Toner, D. C. Catling, and B. Light, "The formation of supercooled brines, viscous liquids, and low-temperature perchlorate glasses in aqueous solutions relevant to Mars," *Icarus*, vol. 233, pp. 36–47, 2014. [Online]. Available: http://dx.doi.org/10.1016/j.icarus.2014.01.018

[275] I. Mitrofanov, D. Anfimov, A. Kozyrev, M. Litvak, A. Sanin, V. Tret'yakov, A. Krylov, V. Shvetsov, W. Boynton, C. Shinohara, D. Hamara, and R. S.

Saunders, "Maps of subsurface hydrogen from the High Energy Neutron Detector, Mars Odyssey," *Science*, vol. 297, no. 5578, pp. 78–81, 2002.

[276] I. B. Smith, P. O. Hayne, S. Byrne, P. Becerra, M. Kahre, W. Calvin, C. Hvidberg, S. Milkovich, P. Buhler, M. Landis, B. Horgan, A. Kleinböhl, M. R. Perry, R. Obbard, J. Stern, S. Piqueux, N. Thomas, K. Zacny, L. Carter, L. Edgar, J. Emmett, T. Navarro, J. Hanley, M. Koutnik, N. Putzig, B. L. Henderson, J. W. Holt, B. Ehlmann, S. Parra, D. Lalich, C. Hansen, M. Hecht, D. Banfield, K. Herkenhoff, D. A. Paige, M. Skidmore, R. L. Staehle, and M. Siegler, "The Holy Grail: A road map for unlocking the climate record stored within Mars' polar layered deposits," *Planetary and Space Science*, vol. 184, no. January, 2020.

[277] D. A. Paige, J. E. Bachman, and K. D. Keegan, "Thermal and albedo mapping of the polar regions of Mars using Viking thermal mapper observations," *Journal of Geophysical Research*, vol. 99, no. 12, pp. 959–25, 1994.

[278] E. Millour, F. Forget, A. Spiga, M. Vals, V. Zakharov, L. Montabone, F. Montmessin, P. L. Read, and F. Cipriani, "The Mars Climate Database (Version 5 . 3)," in *Scientific Workshop: "From Mars Express to ExoMars"*, 2018, pp. 27–28.

[279] J. Larsen and D. Dahl-Jensen, "Interior Temperatures of the Northern Polar Cap on Mars," *Icarus*, vol. 144, no. 2, pp. 456–462, 2000.

[280] J. Bapst, S. Byrne, J. L. Bandfield, and P. O. Hayne, "Thermophysical Properties of the North Polar Residual Cap using Mars Global Surveyor Thermal Emission Spectrometer," *Journal of Geophysical Research: Planets*, vol. 124, no. 5, pp. 1315–1330, 2019.

[281] R. J. Phillips, M. T. Zuber, S. E. Smrekar, M. T. Mellon, J. W. Head, K. L. Tanaka, N. E. Putzig, S. M. Milkovich, B. A. Campbell, J. J. Plaut, A. Safaeinili, R. Seu, D. Biccari, L. M. Carter, G. Picardi, R. Orosei, P. Surdas Mohit, E. Heggy, R. W. Zurek, A. F. Egan, E. Giacomoni, F. Russo, M. Cutigni, E. Pettinelli, J. W. Holt, C. J. Leuschen, and L. Marinangeli, "Mars North Polar Deposits: Stratigraphy, Age, and Geodynamical Response," *Science*, vol. 320, pp. 1182–1185, 2008. [Online]. Available: https://www.science.org

[282] S. Byrne, "The Polar Deposits of Mars," *Annual Review of Earth and Planetary Sciences*, vol. 37, pp. 535–560, 2009. [Online]. Available: www.annualreviews.org

[283] A. Edwards, J. A. Pachebat, M. Swain, M. Hegarty, A. J. Hodson, T. D. L Irvine-Fynn, S. M. E Rassner, and B. Sattler, "A metagenomic snapshot of taxonomic and functional diversity in an alpine glacier cryoconite ecosystem," *Environmental Research Letters*, vol. 8, no. 3, 2013.

[284] K. A. Cameron, A. J. Hodson, and A. M. Osborn, "Structure and diversity of bacterial, eukaryotic and archaeal communities in glacial cryoconite holes from the Arctic and the Antarctic," *FEMS Microbiology Ecology*, vol. 82, no. 2, pp. 254–267, 2012.

[285] N. Takeuchi, S. Kohshima, and K. Seko, "Structure, Formation, and Darkening Process of Albedo-reducing Material (Cryoconite) on a Himalayan Glacier: A Granular Algal Mat Growing on the Glacier," *Arctic, Antarctic, and Alpine Research*, vol. 33, no. 2, pp. 115–122, 2001.

[286] P. Singh, M. Tsuji, S. M. Singh, and N. Takeuchi, "Contrasting patterns of microbial communities in glacier cryoconite of Nepali Himalaya and Greenland, Arctic," *Sustainability*, vol. 12, 2020.

[287] S. Lutz, L. A. Ziolkowski, and L. G. Benning, "The biodiversity and geochemistry of cryoconite holes in queen maud land, East Antarctica," *Microorganisms*, vol. 7, no. 6, pp. 1–16, 2019.

[288] P. T. Doran, C. P. McKay, G. D. Clow, G. L. Dana, A. G. Fountain, T. Nylen, and W. B. Lyons, "Valley floor climate observations from the McMurdo dry valleys, Antarctica, 1986-2000," *Journal of Geophysical Research Atmospheres*, vol. 107, no. 24, pp. 13–1, 2002.

[289] M. Tranter, L. Bagshaw, A. G. Fountain, and C. Foreman, "The biogeochemistry and hydrology of McMurdo Dry Valley glaciers: is there life on martian ice now?" *Life in Antarctic Deserts and other Cold Dry Environments*, pp. 195–220, 2010.

[290] P. T. Doran, B. W. Lyons, and D. M. McKnight, Eds., *Life in Antarctic Deserts and Other Cold Dry Environments: Astrobiological Analogs*. Cambridge University Press, 2010.

[291] A. Cassaro, C. Pacelli, L. Aureli, I. Catanzaro, P. Leo, and S. Onofri, "Antarctica as a reservoir of planetary analogue environments," *Extremophiles*, vol. 25, no. 5-6, pp. 437–458, 2021. [Online]. Available: https://doi.org/10.1007/s00792-021-01245-w

[292] D. Gordon, B. Lanoil, S. Giovannoni, and J. Priscu, "Cyanobacterial communities associated with mineral particles in antarctic lake ice," *Antarctic Journal of the United States*, vol. 31, no. 2, pp. 224–225, 1996.

[293] J. L. Pinckney and H. W. Paerl, "Lake-ice algal phototroph community composition and growth rates, Lake Bonney, dry valley lakes, Antarctica," *Antarctic Journal of the United States*, vol. 31, no. 2, pp. 215–216, 1996.

[294] C. P. McKay, G. D. Clow, R. A. Wharton, and S. W. Squyres, "Thickness of ice on perennially frozen lakes," *Nature*, vol. 313, pp. 561–562, 1985.

[295] K. T. Wing and J. C. Priscu, "Microbial Communities in the Permanent Ice Cap of Lake Bonney, Antarctica: Relationships Among Chlorophyll-a, Gravel and Nutrients," *Antarctic Journal*, pp. 247–249, 1993.

[296] D. A. Gordon, J. Priscu, and S. Giovannoni, "Origin and Phylogeny of Microbes Living in Permanent Antarctic Lake Ice," *§Microbial Ecology*, vol. 39, pp. 197–202, 2000.

[297] H. Paerl and J. Priscu, "Microbial Phototrophic, Heterotrophic, and Diazotrophic Activities Associated with Aggregates in the Permanent Ice Cover of Lake Bonney, Antarctica," *Microbial Ecology*, vol. 36, pp. 221–230, 1998.

[298] C. H. Fritsen, E. E. Adams, C. P. Mckay, and J. C. Priscu, "Permanent Ice Covers Of The Mcmurdo Dry Valleys Lakes, Antarctica: Liquid Water Contents," in *Ecosystem Dynamics in a Polar Desert: the Mcmurdo Dry Valleys, Antarctica*, J. C. Priscu, Ed. American Geophysical Union, 1998, pp. 269–280. [Online]. Available: https://agupubs.onlinelibrary.wiley.com/doi/pdf/10.1029/AR072p0269

[299] J. Priscu and C. Fritsen, "Antarctic lake-ice microbial consortia: Origin, distribution, and growth physiology," *Antarctic Journal of the United States*, vol. 31, no. 2, pp. 223–224, 1996.

[300] A. M. Grue, C. H. Fristen, and J. C. Priscu, "Nitrogen fixation within permanent ice covers on lakes in the McMurdo dry valleys, Antarctica," *Antarctic Journal of the United States*, vol. 31, no. 2, pp. 218–220, 1996.

[301] R. W. Gerdel and F. Drouet, "The Cryoconite of the Thule Area, Greenland," *Transactions of the American Microscopical Society*, vol. 79, no. 3, pp. 256–272, 1960.

[302] N. Takeuchi, S. Kohshima, Y. Yoshimura, K. Seko, and K. Fujita, "Characteristics of cryoconite holes on a Himalayan glacier, Yala Glacier Central Nepal," *Bulletin of glaciological research*, vol. 17, no. September 2014, pp. 51–59, 2000.

[303] R. A. Wharton, W. Vinyard, B. C. Parker, G. M. Simmons, and K. Seaburg, "Algae in Cryoconite Holes on Canda Glacier in Southern Victorialand, Antarctica," *Phycologia*, vol. 20, no. 2, pp. 208–211, 1981.

[304] R. A. Wharton, C. P. McKay, G. M. Simmons, and B. C. Parker, "Cryoconite holes on glaciers." *Bioscience*, vol. 35, no. 8, pp. 499–503, 1985.

[305] N. F. McIntyre, "Cryoconite hole thermodynamics." *Canadian Journal of Earth Sciences*, vol. 21, no. 2, pp. 152–156, 1984.

[306] P. Gribbon, "Cryoconite Holes on Sermikavsak, West Greenland," *Journal of Glaciology*, vol. 22, no. 86, pp. 177–181, 1979.

[307] A. G. Fountain, T. H. Nylen, M. Tranter, and E. Bagshaw, "Temporal variations in physical and chemical features of cryoconite holes on Canada Glacier, McMurdo Dry Valleys, Artarctica," *Journal of Geophysical Research: Biogeosciences*, vol. 113, no. 1, pp. 1–11, 2008.

[308] A. G. Fountain, M. Tranter, T. H. Nylen, K. J. Lewis, and D. R. Mueller, "Evolution of cryoconite holes and their contribution to meltwater runoff from glaciers in the McMurdo Dry Valleys, Antarctica," *Journal of Glaciology*, vol. 50, no. 168, pp. 35–45, 2004.

[309] M. Tranter, A. G. Fountain, C. H. Fritsen, W. B. Lyons, J. C. Priscu, P. J. Statham, and K. A. Welch, "Extreme hydrochemical conditions in natural microcosms entombed within Antarctic ice," *Hydrological Processes*, vol. 18, no. 2, pp. 379–387, 2004.

[310] D. L. Porazinska, A. G. Fountain, T. H. Nylen, M. Tranter, R. A. Virginia, and D. H. Wall, "The biodiversity and biogeochemistry of cryoconite holes from McMurdo Dry Valley glaciers, Antarctica," *Arctic, Antarctic, and Alpine Research*, vol. 36, no. 1, pp. 84–91, 2004.

[311] K. Zawierucha, M. Kolicka, N. Takeuchi, and L. Kaczmarek, "What animals can live in cryoconite holes? A faunal review," *Journal of Zoology*, vol. 295, no. 3, pp. 159–169, 2015.

[312] C. M. Foreman, B. Sattler, J. A. Mikucki, D. L. Porazinska, and J. C. Priscu, "Metabolic activity and diversity of cryoconites in the Taylor Valley, Antarctica," *Journal of Geophysical Research: Biogeosciences*, vol. 112, no. 4, 2007.

[313] T. R. Vonnahme, M. Devetter, J. D. Žárský, M. Šabacká, and J. Elster, "Controls on microalgal community structures in cryoconite holes upon high-Arctic glaciers, Svalbard," *Biogeosciences*, vol. 13, no. 3, pp. 659–674, 2016.

[314] J. K. Gokul, A. J. Hodson, E. R. Saetnan, T. D. Irvine-Fynn, P. J. Westall, A. P. Detheridge, N. Takeuchi, J. Bussell, L. A. Mur, and A. Edwards, "Taxon interactions control the distributions of cryoconite bacteria colonizing a High Arctic ice cap," *Molecular ecology*, vol. 25, no. 15, pp. 3752–3767, 2016.

[315] R. Margesin, G. Zacke, and F. Schinner, "Characterization of Heterotrophic Microorganisms in Alpine Glacier Cryoconite," *Arctic, Antarctic, and Alpine Research*, vol. 34, no. 1, pp. 88–93, 2002.

[316] D. R. Mueller, W. F. Vincent, W. H. Pollard, and C. H. Fritsen, "Glacial cryoconite ecosystems: A bipolar comparison of algal communities and habitats," *Nova Hedwigia*, vol. 123, pp. 173–197, 2001.

[317] C. Säwström, P. Mumford, W. Marshall, A. Hodson, and J. Laybourn-Parry, "The microbial communities and primary productivity of cryoconite holes in an Arctic glacier (Svalbard 79°N)," *Polar Biology*, vol. 25, no. 8, pp. 591–596, 2002.

[318] D. Corenblit, J. Darrozes, F. Julien, T. Otto, E. Roussel, J. Steiger, and H. Viles, "The Search for a Signature of Life on Mars: A Biogeomorphological Approach," *Astrobiology*, vol. 19, no. 10, pp. 1279–1291, 2019.

[319] C. P. McKay and C. R. Stoker, "The early environment and its evolution on Mars: Implication for life," *Reviews of Geophysics*, vol. 27, no. 2, pp. 189–214, 1989.

[320] S. Lutz, J. McCutcheon, J. B. McQuaid, and L. G. Benning, "The diversity of ice algal communities on the Greenland Ice Sheet as revealed by oligotyping," *Microbial genomics*, vol. 4, no. 3, pp. 1–10, 2018.

[321] M. L. Yallop, A. M. Anesio, R. G. Perkins, J. Cook, J. Telling, D. Fagan, J. MacFarlane, M. Stibal, G. Barker, C. Bellas, A. Hodson, M. Tranter, J. Wadham, and N. W. Roberts, "Photophysiology and albedo-changing potential of the ice algal community on the surface of the Greenland ice sheet," *ISME Journal*, vol. 6, no. 12, pp. 2302–2313, 2012.

[322] L. Perini, C. Gostinčar, A. M. Anesio, C. Williamson, M. Tranter, and N. Gunde-Cimerman, "Darkening of the Greenland ice sheet: Fungal abundance and diversity are associated with algal bloom," *Frontiers in Microbiology*, vol. 10, no. MAR, 2019.

[323] J. M. Cook, A. J. Hodson, A. S. Gardner, M. Flanner, A. J. Tedstone, C. Williamson, T. D. Irvine-Fynn, J. Nilsson, R. Bryant, and M. Tranter, "Quantifying bioalbedo: A new physically based model and discussion of empirical methods for characterising biological influence on ice and snow albedo," *Cryosphere*, vol. 11, no. 6, pp. 2611–2632, 2017.

[324] C. J. Williamson, A. M. Anesio, J. Cook, A. Tedstone, E. Poniecka, A. Holland, D. Fagan, M. Tranter, and M. L. Yallop, "Ice algal bloom development on the surface of the Greenland Ice Sheet," *FEMS Microbiology Ecology*, vol. 94, no. 3, pp. 1–10, 2018.

[325] J. M. Cook, A. J. Tedstone, C. Williamson, J. McCutcheon, A. J. Hodson, A. Dayal, M. Skiles, S. Hofer, R. Bryant, O. McAree, A. McGonigle, J. Ryan, A. M. Anesio, T. D. Irvine-Fynn, A. Hubbard, E. Hanna, M. Flanner, S. Mayanna, L. G. Benning, D. Van As, M. Yallop, J. B. McQuaid, T. Gribbin, and M. Tranter, "Glacier algae accelerate melt rates on the south-western Greenland Ice Sheet," *Cryosphere*, vol. 14, no. 1, pp. 309–330, 2020.

[326] C. J. Williamson, J. Cook, A. Tedstone, M. Yallop, J. McCutcheon, E. Poniecka, D. Campbell, T. Irvine-Fynn, J. McQuaid, M. Tranter, R. Perkins, and A. Anesio, "Algal photophysiology drives darkening and melt of the Greenland Ice Sheet," *Proceedings of the National Academy of Sciences*, vol. 117, no. 11, pp. 5694–5705, 3 2020. [Online]. Available: https://pnas.org/doi/full/10.1073/pnas.1918412117

[327] A. J. Tedstone, J. L. Bamber, J. M. Cook, C. J. Williamson, X. Fettweis, A. J. Hodson, and M. Tranter, "Dark ice dynamics of the south-west Greenland Ice Sheet," *Cryosphere*, vol. 11, no. 6, pp. 2491–2506, 2017.

[328] J. L. Benson and P. B. James, "Yearly comparisons of the martian polar caps : 1999 – 2003 Mars Orbiter Camera observations," *Icarus*, vol. 174, pp. 513–523, 2005.

[329] S. Piqueux, A. Kleinböhl, P. O. Hayne, D. M. Kass, J. T. Schofield, and D. J. Mccleese, "Variability of the martian seasonal CO2 cap extent over eight Mars Years," *Icarus*, vol. 251, pp. 164–180, 2015.

[330] H. H. Kieffer, S. C. Chase, T. Z. Martin, E. D. Miner, and F. D. Palluconi, "Martian north pole summer temperatures: Dirty water ice," *Science*, vol. 194, no. 4271, pp. 1341–1343, 1976.

[331] Y. Langevin, F. Poulet, J. P. Bibring, B. Schmitt, S. Douté, and B. Gondet, "Summer evolution of the north polar cap of Mars as observed by OMEGA/Mars express," *Science*, vol. 307, no. 5715, pp. 1581–1584, 3 2005. [Online]. Available: https://www.science.org/doi/10.1126/science.1109438

[332] P. C. Thomas, M. C. Malin, K. S. Edgett, M. H. Carr, W. K. Hartmann, A. P. Ingersoll, P. B. James, L. A. Soderblom, J. Veverka, and R. Sullivan, "North-south geological differences between the residual polar caps on Mars," *Letters to Nature*, vol. 404, no. March, pp. 161–164, 2000.

[333] C. Grima, W. Kofman, J. Mouginot, R. J. Phillips, A. Hérique, D. Biccari, R. Seu, and M. Cutigni, "North polar deposits of Mars: Extreme purity of the water ice," *Geophysical Research Letters*, vol. 36, no. 3, pp. 2–5, 2009.

[334] D. E. Smith, M. T. Zuber, H. V. Frey, J. B. Garvin, J. W. Head, D. O. Muhleman, G. H. Pettengill, R. J. Phillips, S. C. Solomon, H. J. Zwally, W. B. Banerdt, T. C. Duxbury, M. P. Golombek, F. G. Lemoine, G. A. Neumann, D. D. Rowlands, O. Aharonson, P. G. Ford, A. B. Ivanov, C. L. Johnson, P. J. McGovern, J. B. Abshire, R. S. Afzal, and X. Sun, "Mars Orbiter Laser Altimeter: Experiment summary after the first year of global mapping of Mars," *Journal of Geophysical Research: Planets*, vol. 106, no. E10, pp. 23 689–23 722, 2001.

[335] K. E. Herkenhoff, S. Byrne, P. S. Russell, K. E. Fishbaugh, and A. McEwen, "Meter-Scale Morphology of the North Polar Region of Mars," *Science*, vol. 317, no. September, pp. 1711–1715, 2007.

[336] A. B. Limaye, O. Aharonson, and J. T. Perron, "Detailed stratigraphy and bed thickness of the Mars north and south polar layered deposits," *Journal of Geophysical Research: Planets*, vol. 117, no. 6, pp. 1–15, 2012.

[337] D. E. Lalich and J. W. Holt, "New Martian climate constraints from radar reflectivity within the north polar layered deposits," *Geophysical Research Letters*, vol. 44, no. 2, pp. 657–664, 2017.

[338] W. Fernández, "Martian dust storms: A review," *Earth, Moon and Planets*, vol. 77, no. 1, pp. 19–46, 1997.

[339] P. R. Christensen, D. L. Anderson, S. C. Chase, R. T. Clancy, R. N. Clark, B. J. Conrath, H. H. Kieffer, R. O. Kuzmin, M. C. Malin, J. C. Pearl, T. L. Roush, and M. D. Smith, "Results from the Mars global surveyor thermal emission spectrometer," *Science*, vol. 279, no. 5357, pp. 1692–1696, 1998.

[340] O. B. Toon, J. B. Pollack, and C. Sagan, "Physical properties of the particles composing the Martian dust storm of 1971-1972," *Icarus*, vol. 30, no. 4, pp. 663–696, 1977.

[341] L. J. Martin and R. W. Zurek, "An analysis of the history of dust activity on Mars," *Journal of Geophysical Research*, vol. 98, no. E2, pp. 3221–3246, 1993.

[342] H. H. Kieffer, B. M. Jakosky, C. W. Snyder, and M. S. Matthews, Eds., *Mars*, ser. The University of Arizona Space Science Series. University of Arizona Press, 2018. [Online]. Available: https://books.google.co.uk/books?id=AT9IDwAAQBAJ

[343] J. R. Barnes, "Mars atmospheric dynamics as simulated by the NASA Ames general circulation model. 2. Transient baroclinic eddies," *Journal of Geophysical Research*, vol. 98, no. E2, pp. 3125–3148, 1993.

[344] K. R. Blasius, J. A. Cutts, and A. D. Howard, "Topography and stratigraphy of Martian polar layered deposits," *Icarus*, vol. 50, no. 2-3, pp. 140–160, 1982.

[345] R. M. Haberle, J. R. Murphy, and J. Schaeffer, "Orbital change experiments with a Mars general circulation model," *Icarus*, vol. 161, no. 1, pp. 66–89, 2003.

[346] J. Laskar, B. Levrard, and J. F. Mustard, "Orbital Forcing, Paleoclimates, and the Martian Polar Layered Deposits." *Letters to Nature*, vol. 419, pp. 375–377, 2002.

[347] J. Laskar, A. C. Correia, M. Gastineau, F. Joutel, B. Levrard, and P. Robutel, "Long term evolution and chaotic diffusion of the insolation quantities of Mars," *Icarus*, vol. 170, no. 2, pp. 343–364, 2004.

[348] I. B. Smith, N. E. Putzig, J. W. Holt, and R. J. Phillips, "An ice age recorded in the polar deposits of mars," *Science*, vol. 352, no. 6289, pp. 1075–1078, 2016.

[349] B. Levrard, F. Forget, F. Montmessin, and J. Laskar, "Recent formation and evolution of northern Martian polar layered deposits as inferred from a Global Climate Model," *Journal of Geophysical Research: Planets*, vol. 112, no. 6, pp. 1–18, 2007.

[350] S. M. Milkovich and J. W. Head, "North polar cap of Mars: Polar layered deposit characterization and identification of a fundamental climate signal," *Journal of Geophysical Research: Planets*, vol. 110, no. 1, pp. 1–21, 2005.

[351] K. E. Fishbaugh and C. S. Hvidberg, "Martian north polar layered deposits stratigraphy: Implications for accumulation rates and flow," *Journal of Geophysical Research: Planets*, vol. 111, no. 6, pp. 1–21, 2006.

[352] Z. P. Zhong, F. Tian, S. Roux, M. C. Gazitúa, N. E. Solonenko, Y. F. Li, M. E. Davis, J. L. Van Etten, E. Mosley-Thompson, V. I. Rich, M. B. Sullivan, and L. G. Thompson, "Glacier Archives Nearly 15,000-year-old microbes and phages," *Microbiome*, vol. 9, no. 1, pp. 1–23, 2021.

[353] V. I. Miteva, P. P. Sheridan, and J. E. Brenchley, "Phylogenetic and Physiological Diversity of Microorganisms Isolated from a Deep Greenland Glacier Ice Core," *Applied and Environmental Microbiology*, vol. 70, no. 1, pp. 202–213, 2004.

[354] J. K. Jansson and N. Taş, "The microbial ecology of permafrost," *Nature Reviews Microbiology*, vol. 12, no. 6, pp. 414–425, 2014.

[355] P. P. Sheridan, V. I. Miteva, and J. E. Brenchley, "Phylogenetic analysis of anaerobic psychrophilic enrichment cultures obtained from a Greenland glacier ice core," *Applied and Environmental Microbiology*, vol. 69, no. 4, pp. 2153–2160, 2003.

[356] R. Liang, Z. Li, M. C. Lau Vetter, T. A. Vishnivetskaya, O. G. Zanina, K. G. Lloyd, S. M. Pfiffner, E. M. Rivkina, W. Wang, J. Wiggins, J. Miller, R. L. Hettich, and T. C. Onstott, "Genomic reconstruction of fossil and living microorganisms in ancient Siberian permafrost," *Microbiome*, vol. 9, no. 1, pp. 1–20, 2021.

[357] T. Shi, R. H. Reeves, D. A. Gilichinsky, and E. I. Friedmann, "Characterization of viable bacteria from siberian permafrost by 16S rDNA sequencing," *Microbial Ecology*, vol. 33, no. 3, pp. 169–179, 1997.

[358] B. C. Christner, E. Mosley-Thompson, L. G. Thompson, and J. N. Reeve, "Bacterial recovery from ancient glacial ice," *Environmental Microbiology*, vol. 5, no. 5, pp. 433–436, 2003.

[359] B. C. Christner, J. A. Mikucki, C. M. Foreman, J. Denson, and J. C. Priscu, "Glacial ice cores: A model system for developing extraterrestrial decontamination protocols," *Icarus*, vol. 174, no. 2 SPEC. ISS., pp. 572–584, 2005.

[360] D. A. Gilichinsky, G. S. Wilson, E. I. Friedmann, C. P. McKay, R. S. Sletten, E. M. Rivkina, T. A. Vishnivetskaya, L. G. Erokhina, N. E. Ivanushkina, G. A. Kochkina, V. A. Scherbakova, V. S. Soina, E. V. Spirina, E. A. Vorobyova, D. G. Frodorov-Davydov, B. Hallet, S. M. Ozerskaya, V. A. Sorokovikov, K. S. Laurinavichyus, A. V. Shatilovich, J. P. Chanton,

V. E. Ostroumov, and J. M. Tiedje, "Microbial populations in Antarctic permafrost: Biodiversity, stage, age, and implication for astrobiology," *Astrobiology*, vol. 7, no. 2, pp. 275–311, 2007.

[361] K. D. Bidle, S. H. Lee, D. R. Marchant, and P. G. Falkowski, "Fossil genes and microbes in the oldest ice on Earth," *Proceedings of the National Academy of Sciences of the United States of America*, vol. 104, no. 33, pp. 13 455–13 460, 2007.

[362] S. S. Johnson, M. B. Hebsgaard, T. R. Christensen, M. Mastepanov, R. Nielsen, K. Munch, T. Brand, M. T. P. Gilbert, M. T. Zuber, M. Bunce, R. Rønn, D. Gilichinsky, D. Froese, and E. Willerslev, "Ancient bacteria show evidence of DNA repair," *Proceedings of the National Academy of Sciences of the United States of America*, vol. 104, no. 36, pp. 14 401–14 405, 2007.

[363] R. Liang, M. Lau, T. Vishnivetskay, K. G. Lloyd, W. Wang, J. Wiggins, J. Miller, S. Pfiffner, E. M. Rivkina, and T. C. Onstott, "Predominance of anaerobic, spore-forming bacteria in metabolically active microbial communities from ancient Siberian permafrost," *Applied and Environmental Microbiology*, vol. 85, no. 15, pp. 1–15, 2019.

[364] M. Massé, O. Bourgeois, S. Le Mouélic, C. Verpoorter, L. Le Deit, and J. P. Bibring, "Martian polar and circum-polar sulfate-bearing deposits: Sublimation tills derived from the North Polar Cap," *Icarus*, vol. 209, no. 2, pp. 434–451, 2010.

[365] M. P. Zorzano, E. Mateo-Martí, O. Prieto-Ballesteros, S. Osuna, and N. Renno, "Stability of liquid saline water on present day Mars," *Geophysical Research Letters*, vol. 36, no. 20, pp. 2–5, 2009.

[366] V. F. Chevrier, A. Fitting, A. Elsenousy, and E. G. Rivera-Valentín, "Thermodynamic modelling of perchlorate/chloride and perchlorate/chlorate deliquescence at Mars-relevant temperatures," *Geochimica et Cosmochimica Acta*, vol. 333, pp. 56–74, 9 2022.

[367] X. Jia, W. Gu, Y. J. Li, P. Cheng, Y. Tang, L. Guo, X. Wang, and M. Tang, "Phase Transitions and Hygroscopic Growth of Mg(ClO4)2, NaClO4, and NaClO4·H2O: Implications for the Stability of Aqueous Water in Hyperarid Environments on Mars and on Earth," *ACS Earth and Space Chemistry*, vol. 2, no. 2, pp. 159–167, 2018.

[368] C. S. Hvidberg, K. E. Fishbaugh, M. Winstrup, A. Svensson, S. Byrne, and K. E. Herkenhoff, "Reading the climate record of the martian polar layered deposits," *Icarus*, vol. 221, no. 1, pp. 405–419, 2012. [Online]. Available: http://dx.doi.org/10.1016/j.icarus.2012.08.009

[369] K. E. Fishbaugh, S. Byrne, K. E. Herkenhoff, R. L. Kirk, C. Fortezzo, P. S. Russell, and A. McEwen, "Evaluating the meaning of "layer" in

the martian north polar layered deposits and the impact on the climate connection," *Icarus*, vol. 205, no. 1, pp. 269–282, 2010. [Online]. Available: http://dx.doi.org/10.1016/j.icarus.2009.04.011

[370] J. J. Plaut, G. Picardi, A. Safaeinili, A. B. Ivanov, S. M. Milkovich, A. Cicchetti, W. Kofman, J. Mouginot, W. M. Farrell, R. J. Phillips, S. M. Clifford, A. Frigeri, R. Orosei, C. Federico, I. P. Williams, D. A. Gurnett, E. Nielsen, T. Hagfors, E. Heggy, E. R. Stofan, D. Plettemeier, T. R. Watters, C. J. Leuschen, and P. Edenhofer, "Subsurface radar sounding of the south polar layered deposits of Mars," *Science*, vol. 316, no. 5821, pp. 92–95, 2007.

[371] M. T. Zuber, R. J. Phillips, J. C. Andrews-Hanna, S. W. Asmar, S. Konopliv, F. G. Lemoine, J. J. Plaut, D. E. Smith, and S. E. Smrekar, "Density of Mars' South Polar Layered Deposits," *Science*, vol. 317, pp. 1718–1720, 2007.

[372] P. C. Thomas, P. B. James, W. M. Calvin, R. Haberle, and M. C. Malin, "Residual south polar cap of Mars: Stratigraphy, history, and implications of recent changes," *Icarus*, vol. 203, no. 2, pp. 352–375, 2009. [Online]. Available: http://dx.doi.org/10.1016/j.icarus.2009.05.014

[373] M. C. Malin, M. A. Caplinger, and S. D. Davis, "Observational evidence for an active surface reservoir of solid carbon dioxide on Mars," *Science*, vol. 294, no. 5549, pp. 2146–2148, 2001.

[374] S. Byrne and A. P. Ingersoll, "A Sublimation Model for Martian South Polar Ice Features," *Science*, vol. 299, pp. 1051–1053, 2003.

[375] T. H. Prettyman, W. C. Feldman, M. T. Mellon, G. W. McKinney, W. V. Boynton, S. Karuantillake, D. J. Lawrence, S. Maurice, A. E. Metzger, J. R. Murphy, S. W. Squyres, R. D. Starr, and R. L. Tokar, "Composition and structure of the Martian surface at high southern latitudes from neutron spectroscopy," *Journal of Geophysical Research: Planets*, vol. 109, no. 5, pp. 1–28, 2004.

[376] H. H. Kieffer, P. R. Christensen, and T. N. Titus, "CO2 jets formed by sublimation beneath translucent slab ice in Mars' seasonal south polar ice cap," *Nature*, vol. 442, no. 7104, pp. 793–796, 2006.

[377] S. Piqueux, S. Byrne, and M. I. Richardson, "Sublimation of Mar's southern seasonal CO2 ice cap and the formation of spiders," *Journal of Geophysical Research: Planets*, vol. 108, no. 8, pp. 1–9, 2003.

[378] P. B. Buhler, A. P. Ingersoll, B. L. Ehlmann, C. I. Fassett, and J. W. Head, "How the martian residual south polar cap develops quasi-circular and heart-shaped pits, troughs, and moats," *Icarus*, vol. 286, pp. 69–93, 2017. [Online]. Available: http://dx.doi.org/10.1016/j.icarus.2017.01.012

[379] S. M. Jepsen, E. E. Adams, and J. C. Priscu, "Sediment melt-migration dynamics in perennial antarctic lake ice," *Arctic, Antarctic, and Alpine Research*, vol. 42, no. 1, pp. 57–66, 2010.

[380] D. Tyler and J. R. Barnes, "Atmospheric mesoscale modeling of water and clouds during northern summer on Mars," *Icarus*, vol. 237, pp. 388–414, 2014. [Online]. Available: http://dx.doi.org/10.1016/j.icarus.2014.04.020

[381] H. Taha, D. Sailor, and H. Akbari, "High-Albedo Materials for Reducing Building Cooling Energy Use." *California Institute for Energy Efficiency (CIEE).*, pp. 1–75, 1992.

[382] C. C. Allen, K. M. Jager, R. V. Morris, D. J. Lindstrom, M. M. Lindstrom, and J. P. Lockwood, "JSC Mars-1: A Martian Soil Simulant," in *Sixth ASCE Specialty Conference and Exposition on Engineering, Construction, and Operations in Space*, 1998. [Online]. Available: https://ascelibrary.org/doi/10.1061/40339%28206%2954

[383] C. C. Allen, R. V. Morris, K. M. Jager, D. C. Golden, D. J. Lindstrom, M. Lindstrom, and J. P. Lockwood, "Martian Regolith Simulant JSC Mars-1," in *29th Annual Lunar and Planetary Science Conference*, 1998.

[384] A. Maturilli, J. Helbert, T. L. Roush, and M. D'Amore, "Influence of moisture content on albedo changes of JSC Mars-1 Martian simulant: a lesson for HiRISE? A." in *43rd Lunar and Planetary Science Conference*, 2012.

[385] E. Fischer, G. M. Martinez, H. M. Elliott, and N. O. Renno, "Experimental Evidence for the Formation of Liquid Saline Water on Mars," *Geophysical Research Letters*, vol. 41, pp. 4456–4462, 2014.

[386] G. L. Dana, R. A. Wharton, and R. Dubayah, "Solar Radiation In The Mcmurdo Dry Valleys, Antarctica," in *Ecosystem Dynamics in a Polar Desert: the Mcmurdo Dry Valleys, Antarctica*, J. Priscu, Ed. American Geophysical Union, 1998, pp. 39–64.

[387] B. M. Jakosky, K. H. Nealson, C. Bakermans, R. E. Ley, and M. T. Mellon, "Subfreezing activity of microorganisms and the potential habitability of Mars' polar regions," *Astrobiology*, vol. 3, no. 2, pp. 343–350, 2003.

[388] J. C. Priscu, C. H. Fritsen, S. R. Smith, and S. L. Brackman, "Permanent Ice Covers Of The Mcmurdo Dry Valley Lakes, Bubble Formation And Metamorphism," *Ecosystem Dynamics in a Polar Desert: the Mcmurdo Dry Valleys, Antarctica*, vol. 72, 1998.

[389] D. Martin and C. S. Cockell, "PELS (Planetary Environmental Liquid Simulator): A New Type of Simulation Facility to Study Extraterrestrial Aqueous Environments," *Astrobiology*, vol. 15, no. 2, pp. 111–118, 2 2015. [Online]. Available: http://online.liebertpub.com/doi/abs/10.1089/ast.2014.1240

[390] M. T. Lemmon, M. J. Wolff, M. D. Smith, R. T. Clancy, D. Banfield, G. A. Landis, A. Ghosh, P. H. Smith, N. Spanovich, B. Whitney, P. Whelley, R. Greeley, S. Thompson, J. F. Bell, and S. W. Squyres, "Atmospheric imaging results from the Mars exploration rovers: Spirit and opportunity," *Science*, vol. 306, no. 5702, pp. 1753–1756, 2004.

[391] R. Greeley, "Saltation impact as a means for raising dust on Mars," *Planetary and Space Science*, vol. 50, no. 2, pp. 151–155, 2002.

[392] J. D. Iverson and B. R. White, "Saltation threshold on Earth, Mars and Venus," *Sedimentology*, vol. 29, no. 1, pp. 111–119, 1982.

[393] R. Greeley, R. Leach, B. White, J. Iversen, and J. Pollack, "Threshold windspeeds for sand on Mars: Wind tunnel simulations," *Geophysical Research Letters*, vol. 7, no. 2, pp. 121–124, 1980.

[394] M. P. Almeida, E. J. Parteli, J. S. Andrade, and H. J. Herrmann, "Giant saltation on Mars," *Proceedings of the National Academy of Sciences of the United States of America*, vol. 105, no. 17, pp. 6222–6226, 2008.

[395] G. Östrem, "Ice Melting under a Thin Layer of Moraine, and the Existence of Ice Cores in Moraine Ridges," *Geografiska Annaler*, vol. 41, no. 4, pp. 228–230, 1959.

[396] G. W. Brass, "Stability of Brines on Mars," *ICARUS*, vol. 42, pp. 20–28, 1980.

[397] S. Piqueux and P. R. Christensen, "A model of thermal conductivity for planetary soils : 2 . Theory for cemented soils," *Journal of Geophysical Research*, vol. 114, pp. 1–12, 2009.

[398] C. S. Edwards and S. Piqueux, "The water content of recurring slope lineae on Mars," *Geophysical Research Letters*, vol. 43, pp. 8912–8919, 2016.

[399] M. T. Mellon, R. L. Fergason, and N. E. Putzig, "The thermal inertia of the surface of Mars," in *The Martian Surface: Composition, Mineralogy, and Physical Properties*, J. Bell, Ed. Cambridge University Press, 2008.

[400] J. Heinz, J. Schirmack, A. Airo, S. P. Kounaves, and D. Schulze-Makuch, "Enhanced microbial survivability in subzero brines," *Astrobiology*, vol. 18, no. 9, pp. 1171–1180, 2018.

[401] A. E. Wechsler and A. P. E. Glaser, "Pressure Effects on Postulated Lunar Materials," *ICARUS*, vol. 4, pp. 335–352, 1965.

[402] J. Longhi, "Phase equilibrium in the system CO2-H2O: Application to Mars," *Journal of Geophysical Research: Planets*, vol. 111, no. 6, pp. 1–16, 2006.